Uniwersytet Warszawski

Wydział Fizyki
Instytut Fizyki Doświadczalnej
Zakład Cząstek i Oddziaływań Fundamentalnych

Kaon production in mid-rapidity in Be+Be collisions at the CERN SPS.

ROZPRAWA DOKTORSKA

mgr inż. Magdalena Kuich

Promotor:
Prof. dr hab. Wojciech Dominik

Warszawa, 2019

Acknowledgements

I would like to express my sincere gratitude to my supervisor, Prof. dr hab. Wojciech Dominik, for his (probably) infinite patience, constant motivation and inspiration. His support along the bumpy road of the analysis process up to the results and, in the end, completing this thesis is invaluable. I could not have imagined having a better mentor.

I am very appreciative to Prof. dr hab. Marek Gaździcki, dr Szymon Puławski, dr Emil Kaptur and other colleagues from the NA61/SHINE Collaboration. This thesis could not have been accomplished without our fruitful discussions and exchange of experience.

With a special mention to Chiara Mazzocchi - thank you for your valuable remarks and all (un-)scientific distractions when these were needed.

Finally, I am not able to express enough gratitude to my family for their never-ending support in every second of my life and completing this thesis in particular.

Abstract

"Kaon production in mid-rapidity in Be+Be collisions at the CERN SPS"

This thesis presents inclusive spectra of identified charged hadrons, namely K^+, K^-, π^+, π^-, proton and anti-proton, produced in inelastic ^{7}Be+^{9}Be collisions at four beam momenta: 30A, 40A, 75A and 150A GeV/c. The data acquisition was performed by the NA61/SHINE Collaboration with the NA61/SHINE fixed target experiment placed at CERN SPS. The hadron production in Be+Be collisions was measured and studied for the first time in SPS energy range.

Charged-hadron identification was obtained with the so-called $tof - dE/dx$ analysis method, based on measurements of hadron mass by Time of Flight detectors and energy loss by Time Projection Chambers. The results were corrected for effects related to the spectrometer acceptance, detection and reconstruction efficiency, contribution of particles originating in weak decays and secondary interactions, as well as the analysis technique.

The double-differential particle spectra were derived as a function of rapidity and transverse momentum. Particular attention was paid to the strangeness production in mid-rapidity by studying the charged K meson spectra. The K^+ and K^- yields in mid-rapidity were calculated and the transverse momentum spectra were parametrised by the inverse slope parameter. This results were further used in the study of the onset of deconfinement and the phenomenon of the light-nuclei collisions at ultra-relativistic energies.

The identification of charged-hadron spectra in Be+Be collisions belongs to the main NA61/SHINE programme of the onset of deconfinement of strongly interacting matter study in collisions of light and intermediate-size ions. The results on strangeness production in mid-rapidity, derived in the framework of this thesis, were compared with the results from p+p interactions and Pb+Pb collisions at the same beam momenta per nucleon, measured by the NA61/SHINE and NA49 experiments, respectively, and also world data in broader collision energy range. Furthermore, the results on charged-kaon spectra in mid-rapidity were compared with the calculation of three microscopic theoretical models of high-energy nuclear collisions and confronted with prediction of the Statistical Model of the Early Stage.

Streszczenie

”Produkcja kaonów w obszarze średnich pośpieszności w zderzeniach Be+Be przy SPS CERN”

Niniejsza rozprawa przedstawia inkluzywne widma naładowanych hadronów, K^+, K^-, π^+, π^-, protonów oraz antyprotonów, wyprodukowanych w nieelastycznych zderzeniach beryl-beryl, zmierzone po raz pierwszy dla czterech pędów wiązki: 30A, 40A, 75A i 150A GeV/c. Dane doświadczalne zostały zmierzone w ramach projektu NA61/SHINE, z wykorzystaniem układu detekcyjnego NA61/SHINE znajdującego się przy akceleratorze SPS w laboratorium CERN.

Identyfikacja hadronów naładowanych została przeprowadzona metodą $tof - dE/dx$, opartą o pomiary masy hadronów w detektorach czasu przelotu (ToF) oraz średnich strat energii na jednostkę drogi w komorach projekcji czasowej (TPC). Wyniki analizy poprawiono, uwzględniając efekty związane z akceptacją detektora, wydajnością detekcji i rekonstrukcji cząstek, przyczynkiem cząstek pochodzących z rozpadów słabych i oddziaływań wtórnych, a także techniką analizy danych.

Dwuwymiarowe widma krotności cząstek naładowanych wyznaczono w funkcji pośpieszności oraz pędu poprzecznego. Szczególną uwagę poświęcono produkcji dziwności w obszarze średnich pośpieszności poprzez analizę widm naładowanych kaonów w tym obszarze. Wyznaczono parametry tych widm: parametry nachylenia rozkładów pędu poprzecznego oraz krotności kaonów naładowanych w danym przedziale pośpieszności. Parametryzacja widm posłużyła dalszym badaniom dotyczącym progu na produkcję plazmy kwarkowo-gluonowej (QGP) oraz zderzeń lekkich jonów przy energiach ultra-relatywistycznych.

Badania zawarte w tej pracy należą do głównego programu NA61/SHINE: poszukiwań progu na produkcję QGP w zderzeniach lekkich i średnich jąder. Widma kaonów i ich parametryzacja zostały zestawione z dostępnymi wynikami z oddziaływań proton-proton i ołów-ołów przy tych samych pędach wiązki na nukleon, zmierzonymi odpowiednio w eksperymentach NA61/SHINE i NA49. Dodatkowo wyniki ujęte w niniejszej pracy zostały porównane z modelami teoretycznymi opisującymi zderzenia jądrowe przy wysokich energiach.

Contents

Chapter 1

Introduction

In the late 19th century, physicists and chemists were convinced that there is not much left to be resolved in science and that physics itself has achieved its final form. Fortunately, they were wrong. The following decades have brought a plenitude of discoveries and breakthrough leading to utterly new physics – studies on radioactivity and the structure of the matter [1].

A vivid development of the technology lead to the construction of instruments allowing for the particle acceleration and detection. Accelerators facilitate performance of particles and nuclei collisions in a controlled way over a broad collision energy range, while more and more sophisticated detection systems and reconstruction procedures allowed for progressively precise measurements. Nowadays, the heavy-ion and hadron collisions are the best tool for the study of the constituents of the matter and interactions between them, which lead to the exploration of the phase diagram of strongly interacting matter and insight into the many-body systems of quarks and gluons including the Quark-Gluon Plasma (QGP).

This thesis is focused, in particular, on the research of the transition between confined matter and QGP via studying the ion-ion collisions at (ultra-)relativistic energies.

1.1 Standard Model of elementary particles

Years of study on lepton, hadron and ion collisions resulted in establishing the theory known as the Standard Model [2]. The Model classifies elementary particles and describes their interactions. The majority of its predictions have been confirmed experimentally, like the existence of the Higgs boson.

The Standard Model predicts the existence of elementary particles: twelve fermions (with corresponding anti-particles) as constituents of matter, and five bosons as the interaction force carriers. Schematic summary of the elementary particles is presented in figure 1.1. As fermions there are six quarks: up – u, down – d, strange – s, charm – c, bottom/beauty – b and top/truth – t, and six leptons: electron – e, electron neutrino – ν_e, muon – μ, muon neutrino – ν_μ, tau – τ and tau neutrino – ν_τ. The lightest quarks, u and d, form the protons and neutron, which constitute the atomic nuclei. Therewith, along with electrons form the atoms. Heavier quarks can create short-lived particles. In normal conditions, quarks are confined in hadrons: baryons (three quarks), anti-baryons (three anti-quarks) and mesons (a pair of quark and anti-quark). Examples of baryons are: protons (uud), neutrons

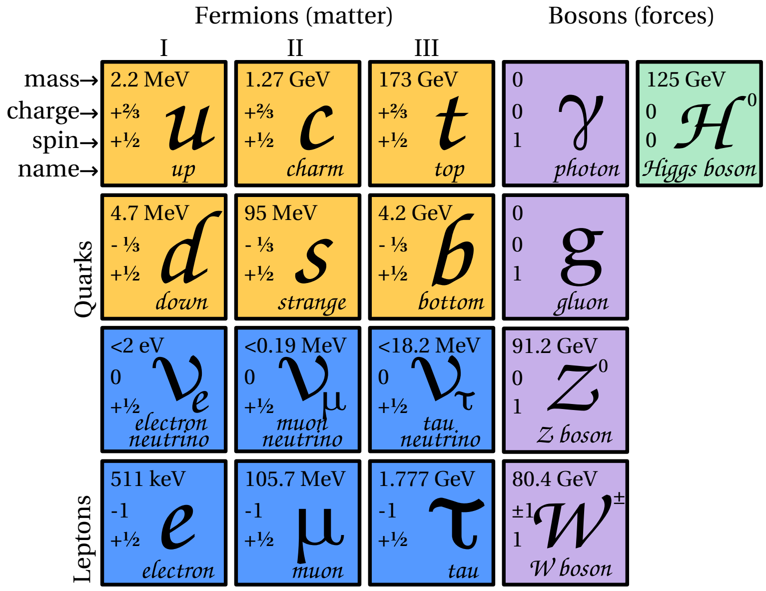

Fig. 1.1: Standard Model of elementary particles. Picture based on Ref. [3–5].

(udd) and Λ (uds). The most common examples of mesons are: pions (meson π) constituted by a light (u, d) quark and anti-quark and kaons (meson K), where one quark (or anti-quark) is replaced by a strange (or anti-strange) quark.

The Standard Model also explains fundamental forces: strong, electromagnetic and weak. Interactions between particles are exchanged by force carriers – bosons. Each type of fundamental force has specific carriers: strong – gluons, electromagnetic – photons, weak – $W^{\pm}$ and Z^0 bosons.

Within Standard Model, strong interactions are defined by quantum field theory – Quantum Chromodynamics, where quarks and gluons carry a strong charge – colour and interact with each other. There are three colour and three anti-colour charges. Each quark (or anti-quark) carries one colour (or anti-colour). Each gluon carries a combination of colours and anti-colours (gluons can have eight independent color states and one colorless state). The strong force is responsible for the quark confinement in hadrons. This force gets stronger with increasing distance between interacting particles until the energy is high enough to produce new $\mathrm{q}-\bar{\mathrm{q}}$ pair. The range of the force is of the order of 10^{-15} m (1 femtometer).

In contrast, the force responsible for electromagnetic interaction has infinite range. It affects all electrically-charged particles. The interaction happens via exchanging photon and is described by Quantum Electrodynamics.

The weak force affects all leptons and quarks and is the only force capable of changing the flavour (e.g., of changing one type of quark into another) and violating basic symmetries (e.g., charge-parity symmetry). Due to the fact that force carriers – $W^{\pm}$ and Z^0 are massive (80.4 GeV and 91.2 GeV respectively), this force has a short range. Above unification energy of 100 GeV, weak and electromagnetic forces can be unified and understood in terms of electro-weak theory.

The Standard Model predicted the existence of another, particularly elementary particle responsible for other particles masses. It is called Higgs boson [6] and was discovered by two experiments at Large Hadron Collider (LHC) in 2012 - Compact Muon Solenoid (CMS) and A Toroidal LHC ApparatuS (ATLAS).

1.2 Quark - gluon plasma

As mentioned above, quarks are confined by the strong force in hadrons. Nevertheless, when quarks reach extreme proximity and the strong force becomes weaker, they behave almost as free particles, which is known as the asymptotic freedom phenomenon. The idea of asymptotic freedom evolved into a concept of a new state of matter, the QGP [7].

It is believed that soon after the Big Bang the matter was in such a phase. As the Universe expanded and cooled down, the QGP turned into hadrons, which further formed the Universe we live in. The QGP is not observed in Nature nowadays, but compact astrophysical objects, as the neutron stars, may contain it in their dense centres. Nevertheless, possibility to study the quark-gluon plasma occurred in the laboratory experiments. The QGP production in a high-energy nuclear collision was confirmed by experiments at the European Organization for Nuclear Research (CERN) [8] and Brookhaven National Laboratory (BNL) [9].

1.3 High-energy collisions

History of particle physics is directly related to the history of accelerators. As the available collision energy increases, heavier particles and new phenomena might be discovered.

Nowadays accelerators can accelerate ions, hadrons or electrons to velocities close to the speed of light. An accelerated bunch of nuclei or hadrons, or in other words beam, (further called projectile particles or projectiles) are forced to interact with a counterflow beam or fixed target (further called target particles or target). If projectile and target collide, they interact. In collisions at high energies, inelastic interactions dominate. A scheme of such a collision is shown the figure 1.2. The

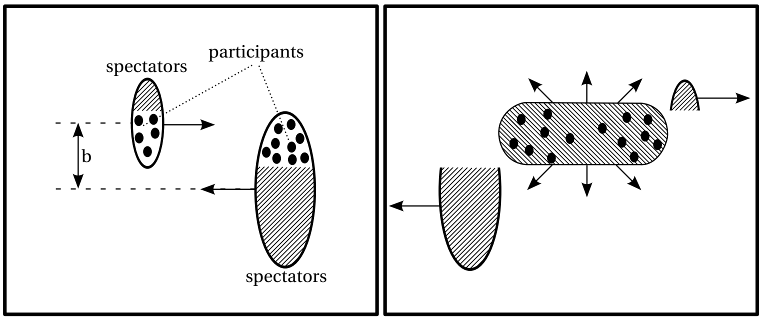

Fig. 1.2: Scheme of an inelastic ion-ion collision. Picture taken from Ref. [10].

higher momentum the accelerated projectile (and target in case of counterflow beams) has, the thinner disc in the laboratory coordinate system it becomes due to Lorentz contraction. Nucleons (or partons), which do not meet any other ones on their way, are called *spectators* of the collision. They do not interact. All those interacting elastically and/or inelastically are named *participants*. The participants of inelastic interactions are termed *wounded nucleons*. The number of spectators (N_{spec}) and participants (N_{part}), as well as number of wounded nucleons (N_W), vary with collision centrality and depend on an *impact parameter*, *b*, which is the distance between centers of colliding projectile and target. *Central collisions* are characterised by small values of b, for strictly central $b \approx 0$. In this case the number of the participants is much larger than the number of spectators and also $N_{part} \cong N_W$ as mostly inelastic interactions happen. Nevertheless, such collisions are not frequent. The most common are *peripheral collisions* – with large impact parameter values. In such collisions, the number of participants is higher than the number of wounded nucleons, since nucleons can also interact elastically.

1.3.1 Evolution of high-energy nuclear collision

During the collision, the energy of the system increases and new particles can be produced. Two possible scenarios of the evolution of relativistic nuclei collisions are presented in Fig. 1.3. In the first scenario, when the energy density after the

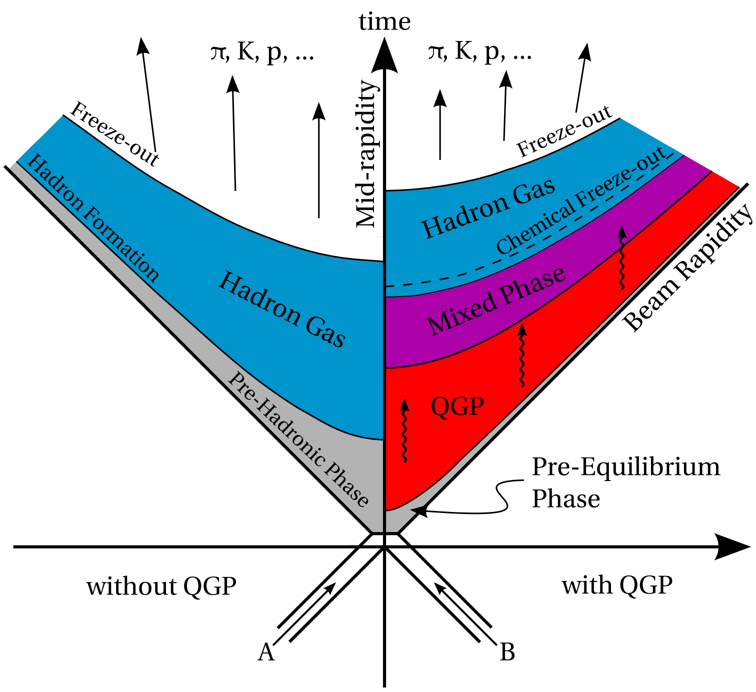

Fig. 1.3: Two scenarios of collision of two relativistic nuclei ('A' and 'B'). On the left side of the diagram - direct formation of hadrons as an outcome of the strong interactions. On the right side - a creation of QGP, and subsequent phase transition and chemical freeze-out. Both scenarios are coped with the hadron gas phase and thermal freeze-out. Picture taken from Ref. [10].

collision is relatively low, a hot and dense hadron gas is formed. In the second case, when the energy density is sufficiently high, the QGP can be created. As the QGP expands and cools down, the hadron formation (*hadronisation*) process takes place. The moment when the inelastic interactions stop and the chemical composition of the system becomes fixed is called *chemical freeze-out*. The particles of hadron gas produced in both scenarios still interact with each other elastically, while the system continues to cool down until the momenta of all particles are fixed and a *thermal (kinetic) freeze-out* occurs. These hadrons and/or the products of their decays can be observed in high-energy experiments.

1.3.2 Phase diagram of strongly interacting matter

The QGP and Hadron Gas (HG), are two distinct phases of strongly interacting matter. Typically, they are presented in a two-dimensional phase diagram with the system temperature, T, on vertical axis and baryonic chemical potential, μ_B, quantifying the change of the system energy caused by the addition or removal of one baryon, on the horizontal axis. The system's T and μ_B can be probed by varying the size of the colliding ions and the collision energy. An example diagram is shown in Fig. 1.4. At low temperatures and relatively low baryonic chemical potential, the

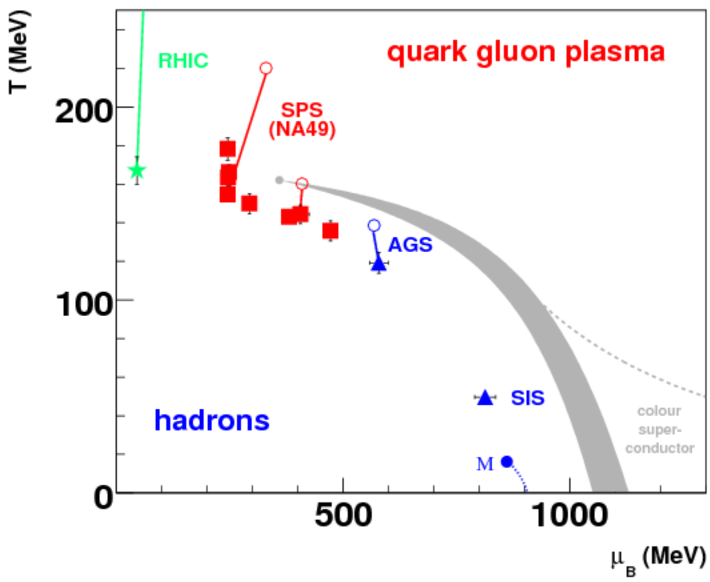

Fig. 1.4: Two-dimensional phase diagram of strongly interacting matter in temperature T and baryonic chemical potential μ_B. The full points present the conditions of the chemical freeze-out calculated in Ref. [11, 12]. The open points and the straight lines indicate a possible evolution of the system from the early stage to the chemical freeze-out. The grey band corresponds to the first order phase transition between hadron gas and QGP, ending with a critical point [13, 14]. Figure taken from Ref. [13].

matter is in HG state. In the opposite conditions, it exists as QGP. The structure of the transition between these two states is still under discussion (as in Ref. [15]), but the most popular approach postulates that increasing the temperature at the lower baryonic chemical potential leads to a phase change via a smooth *crossover* and at the higher baryonic chemical potential - via the *first order phase transition* [16]. Between the postulated 1st order phase transition and a the crossover region the *critical point* (CP) is expected. The CP has not been discovered yet, but lattice calculations (e.g. Ref. [17]) predict that it is located in the $\mu_B - T$ ranges accessible by the studies in the Super Proton Synchrotron (SPS) energy range. The data presented on the plot in Fig. 1.4 corresponds to experimentally probed values of the chemical potential related to the baryonic potential and the temperature of chemical freeze-out.

1.4 Phase transition of strongly interacting matter

The beginning of QGP creation is called the *onset of deconfinement*. The experimental study of this subject was motivated by the predictions of the Statistical Model of the Early Stage (SMES) [18] (recently extended in Ref. [19]), in which a few observables are stated to be sensitive to the transition between hadron gas and QGP. Some of them were measured experimentally in nucleus-nucleus (A+A) collisions and described briefly in the following.

The phenomenon of the onset of deconfinement was originally observed by the NA49 experiment at the SPS [20]. Its discovery was confirmed by the Relativistic Heavy Ion Collider (RHIC) Beam Energy Scan programme [21, 22], which indicates that QGP production can be possible in heavy-ion collisions at energies of several GeV per nucleon. Still, systematic studies in this energy range are needed to understand the characteristics of the transition between confined and deconfined matter.

The SMES assumes that production of matter at the early stage of collisions is entirely defined by the available energy and the volume of the system (Lorentz-contracted volume occupied by the colliding nucleons). Production of new degrees of freedom (new particles) from energy does not produce net charges (e.g. flavour or electric charges). Moreover, only a fraction of the total collision energy is transformed into the energy of new degrees of freedom created at the early stage, as the other part of the energy is carried by the net baryons. SMES is based on the assumption that at early stage of heavy-ion collision, a maximum entropy equilibrium state is always created. For the confined hadron gas SMES uses the ideal gas equation of state to characterise the properties of equilibated matter. The non-strange particles, which dominate the entropy, are assumed to be massless bosons. The mass of strange particles is assumed to be 500 MeV, equal to the kaon mass. The deconfined state, composed with u, d and s quarks and their antiparticles (contribution of heavier quarks is neglected due to their large masses) is characterised by a bag model [23, 24]. In the bag model, the masses of non-strange particles (light quarks, antiquarks and gluons) are set to 0. The s and $\bar{s}$ quarks mass is assumed to be 175 MeV. SMES assumes that the matter created at the early stage expands, then hadronises and freezes-out. It is postulated that the total entropy and a total number of s and $\bar{s}$ quarks created in the early stage are (approximately) conserved. Moreover, the number of degrees of freedom is assumed to be higher in QGP than the HRG.

According to SMES, at low collision energies only pure hadron gas is produced, at higher – pure QGP state. The model assumes also that in the some collision energy region both states coexist forming a mixed-phase. In the model, the onset of deconfinement in central heavy-ion collisions should evince itself in rapid changes of the energy (sometimes expressed as a Fermi's measure, F$\approx \sqrt{s_{NN}}^{1/2}$) dependence of several hadron production properties. Figure 1.5 presents the energy dependence of selected characteristics of hadron production and spectra, which experimentally confirm predictions of the SMES. The results presented in figure 1.5 were obtained in hadron-hadron and ion-ion collisions measured in a broad energy range by various experiments, including NA49 and also NA61/SHINE.

The top left panel of Fig. 1.5 presents so-called *kink* – the energy dependence of the ratio of mean pion multiplicity to the mean number of wounded nucleons. This observable can be considered as energy dependence of the ratio of the total

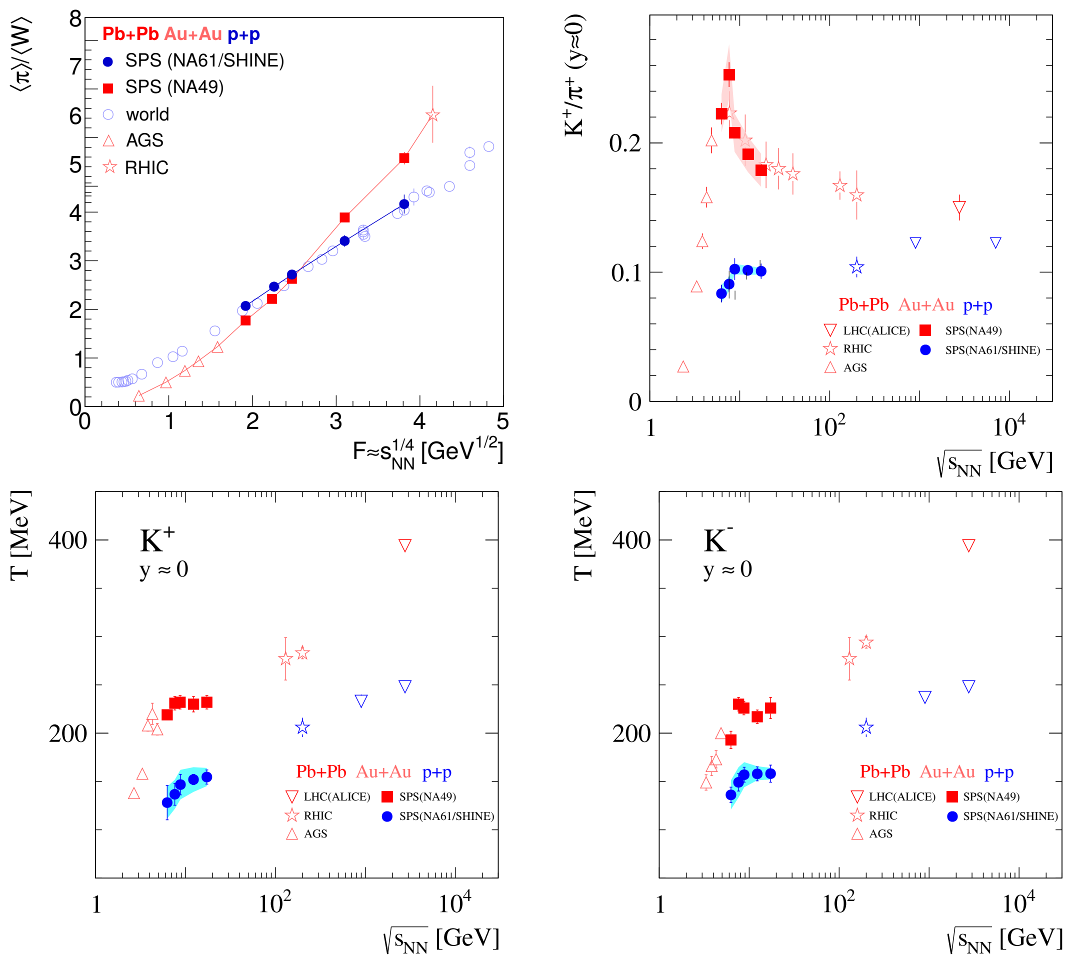

Fig. 1.5: Experimental results on energy dependence of various quantities defined by SMES as the signatures of the onset of deconfinement. *Top left*: ratio of mean pion multiplicity to the mean number of wounded nucleons (*kink*). *Top right*: K^+/π^+ yield ratio in mid-rapidity (proportional to strangeness to entropy ratio) (*horn*). *Bottom*: inverse slope parameter of transverse mass spectra of charges K mesons (related to the early stage temperature) (*step*). Plots based on Refs. [20, 21, 25–41].

entropy to the number of nucleons participating in the collision. In SMES, the ratio is expected to increase linearly with the Fermi energy. As the slope is proportional to the number of effective degrees of freedom, it is steeper for the QGP state. Therefore the slope is much steeper for heavy-ion collisions (red/reddish points on the plot), where QGP production is assumed, than for p+p interactions (blue points).

In the top right panel of Fig. 1.5 the so-called *horn* is shown. It stands for the energy dependence of the strangeness to entropy ratio, expressed by K^+/π^+ yield ratio in mid-rapidity. The ratio obtained in heavy-ion collisions (red/reddish points on the plot) rapidly changes with the collision energy - steeply raises in the hadron phase, reaches the maximum at the onset of deconfinement, decreases in the mixed phase and almost saturate in the QGP phase. A similar behaviour is expected within SMES model. The effect in p+p interactions is significantly reduced.

The bottom row of Fig. 1.5 contains the energy dependence of the inverse slope parameter, T, of transverse mass spectra of charged K mesons, so-called *step* plots. The T measure is associated with temperature of thermal freeze-out. It reminds of a step-like structure: as in the pure phases (HRG phase and QGP phase) the temperature increases linearly with the energy whereas inside the region of the transition, coexistence of both phases, it is constant. The same phenomenon was predicted by SMES.

In figure 1.5 experimental result on nucleus-nucleus collisions for two extreme system sizes are presented: the biggest one – most central Pb+Pb/Au+Au collisions, and the smallest one – p+p interactions. The extended SMES model also provides predictions for intermediate systems, as shown in the left frame of Fig. 1.6. The

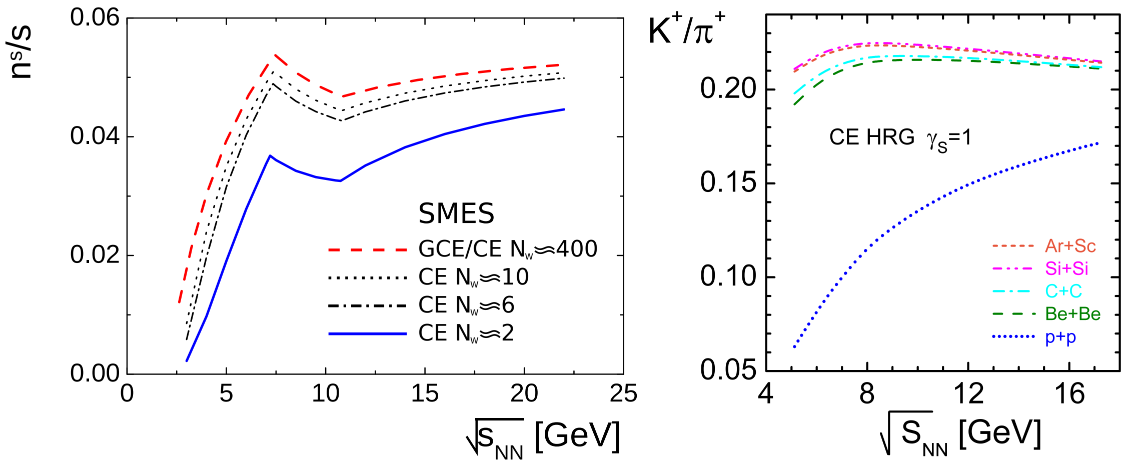

Fig. 1.6: *Left*: Mean strangeness to entropy ratio energy dependence predictions by SMES for various system sizes [19]. *Right*: K^+/π^+ ratio energy dependence predictions by HRG model for various colliding systems [42].

SMES predicts that strangeness-to-entropy ratio, which is proportional to K^+/π^+ ratio, rapidly increases with the system size. According to SMES, the strangeness to entropy ratio enhancement should be present even in such a small system as $N_W \approx 10$, or Be+Be [19, 43]. Calculations of the K^+/π^+ ratio for intermediate system are also being performed within the statistical Hadron-Resonance Gas (HRG) model [42] (for the details of the model see also Refs. [44, 45]), as presented in the right panel of Fig. 1.6. The calculations within HRG model are based on available data from nucleus-nucleus collisions in the SPS energy range. They also reveal expectation of the rapid strangeness-to-entropy ratio enhancement with the colliding system size.

1.5 NA61/SHINE and the study of the phase transition

The conclusions drawn by the NA49 experiment and others, presented and explained in section 1.4, strongly motivated a comprehensive study of the phase transition in the SPS energy range. NA61/SHINE (the sixty-first experiment at the CERN North Area SPS Heavy Ion and Neutrino Experiment) has inherited a big part of the NA49 facility (see chapter 2) and made the study of the onset of deconfinement one of its primary goals. The other one is the search for the critical point of strongly interacting matter. Additionally, the experiment probes a hadron production in hadron-hadron and hadron-nucleus interactions for:

- the study of hadron production at high transverse momenta (p_T of up to 4.5 GeV/c) for an understanding of the nucleus-nucleus reactions,

- the precise hadron production measurements in p+C (a thin target, a replica of the T2K target and a replica of NOνA target) interactions for the neutrino experiments to calculate the initial neutrino fluxes [46–49],
- the precise hadron production measurements in π+C interactions for cosmic ray experiments to reduce systematic uncertainties in simulations of the showers used to reconstruct properties of the initial cosmic ray particles [50, 51].

NA61/SHINE explores a particular region of the phase diagram of strongly interacting matter shown in the right panel of Fig. 1.7. The diagram presents

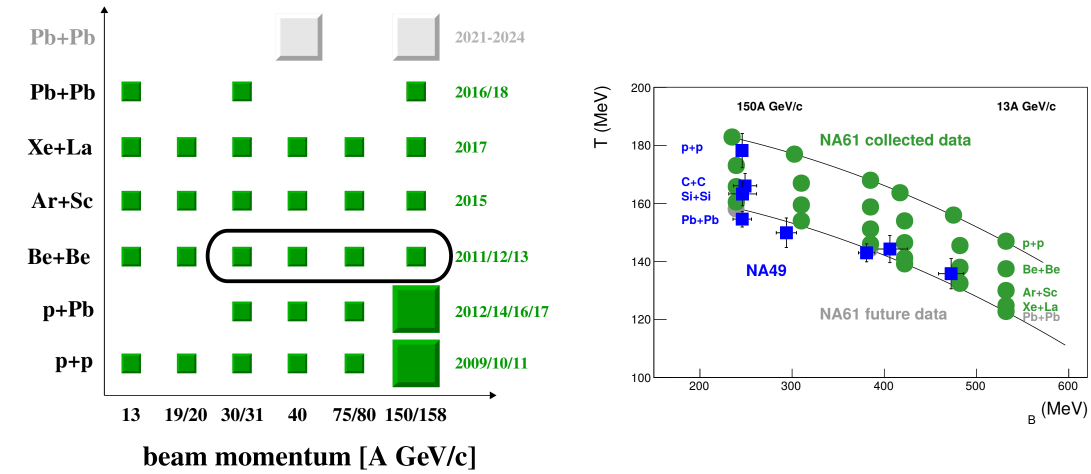

Fig. 1.7: *Left*: Reactions and energies of the two-dimensional scan in system size and beam momenta performed by NA61/SHINE. Size of squares relates to the number of recorded events. Green points indicate data collected gray and red denote future data taking. *Right*: Region of the theoretical phase diagram explored by NA61/SHINE and NA49 experiments. Estimated chemical freeze-out points in NA49 (blue squares) and those expected in NA61/SHINE (circles) according to hadron gas model [12]. Pictures taken from Ref. [10].

chemical freeze-out conditions estimated from NA49 measurements and those expected in NA61/SHINE according to hadron gas model simulation [12]. To achieve its main goals, NA61/SHINE performs systematic two-dimesional scan of the phase space in collision energy and system size by varying the beam momenta as well as projectile and target nuclei. The choice of the nuclei is imposed by the technical capabilities of the ion source and also physical and chemical properties of the target element. NA61/SHINE measures p+p, p+^{208}Pb, ^{7}Be+^{9}Be, ^{40}Ar+^{45}Sc, ^{131}Xe+^{139}La and ^{208}Pb+^{208}Pb collisions at six beam momenta from 13A GeV/c [1] to 150A GeV/c (158 GeV/c for protons). The list of datasets being recorded by the NA61/SHINE is visualised in the left panel of figure 1.7.

A comprehensive scan with various system sizes in a broad momentum range allows for more precise probing of the transition between states of matter and evolution of the system after the collision. Recent results on p+p interactions from NA61/SHINE [28] as well as A Large Ion Collider Experiment at LHC (ALICE) (e.g. Refs. [52, 53]) suggest that some processes related to QGP appearance can take place event in the collisions of light nuclei. That brings up a strong motivation to investigate hadron production also in the collisions of small systems in the SPS energy range, like ^{7}Be+^{9}Be.

[1] 13A GeV/c stands for momentum of 13 GeV/c per nucleon

1.6 Spectra of charged kaons in mid-rapidity

Kaons are the lightest strange (containing strange quark) measurable products of high-energy nuclear collisions. Moreover, due to different properties of strangeness production in hadron gas and QPD, observables based on K mesons (the *horn* and *step*, see Fig. 1.5) spectra are sensitive to phase transition of strongly interacting matter [14].

The main goal of the research presented in the thesis was to study the properties of the onset of deconfinement by charged kaons multiplicity spectra in mid-rapidity in the beam energy scan of beryllium-beryllium collisions recorded by the NA61/SHINE experiment.

The thesis reports results on the inclusive $K^{\pm}$, $\pi^{\pm}$ and (anti-)proton spectra produced in inelastic ^{7}Be+^{9}Be collisions at beam momenta of $30A$, $40A$, $75A$ and $150A$ GeV/c. The multiplicity distributions are presented as a function of rapidity (y) and the transverse momentum (p_{T}). A particular attention is paid to the $K^{\pm}$ spectra in the mid-rapidity region as it directly insight into the study of the onset of deconfinement.

This thesis consists of seven chapters and is organised as follows. After the theoretical introduction and motivation, Chapter 2 describes the NA61/SHINE experiment and the facility used for data collection and Chapter 3 briefly explains the data reconstruction techniques and Monte-Carlo simulation used in the analysis process. The characterisation of the analysed data is presented in Chapter 4. Chapter 5 contains the detailed description of the data analysis followed by the final results presented in Chapter 6. The thesis closes with a summary in Chapter 7.

The appendices include definitions of the coordinate system and kinematic variables used in the analysis (Appendix A), tabulated results (Appendix B) and theoretical calculations used as a comparison for the results (Appendix C) as well as some additional information on the NA61/SHINE gas system (Appendix D).

Author's Contribution

I have been a member of the NA61/SHINE Collaboration since 2013 under the supervision of prof. Wojciech Dominik.

Since the beginning of my PhD studies, I have been actively participating in the data taking campaigns and managing the operation of the Time Projection Chambers (TPCs), the main NA61/SHINE tracking detectors. During this time, I also worked on the operation, maintenance and development of the gas system of the NA61/SHINE TPCs. I was responsible for the upgrade and extension of the TPCs drift velocity monitoring system, including the design and construction of the new drift velocity measuring units, as well as a new readout chain, which allows to measure the drift velocity with precision of order of 1‰. Moreover, I designed and built a separate gas system with gas mixture quality control, which supplies the Forward Time Projection Chambers (FTPCs) installed in the NA61/SHINE facility in 2017.

Despite my passion for hardware, I still worked on many levels of the data calibration and analysis. I was involved in the drift velocity calibration, which is crucial parameter for the precise particle trajectory reconstruction, since discrepancy of the drift velocity in order of 1% can cause vertical displacement of the particle's trace of

1 cm in the NA61/SHINE TPCs. Furthermore, I deeply studied the efficiency of the NA61/SHINE Time Of Flight detectors and improved their calibration methods. I also cooperated with the NA61/SHINE Ion group on the verification of the validity of the experimental data. Finally, I studied the event and track selection-criteria properties and their impact on the charged-particle spectra. I developed the procedures for the data analysis and calculation of uncertainties, which allowed for the comparison of my results with data from other experiments and predictions of the theoretical models, and in the end, finalising this thesis.

Chapter 2

NA61/SHINE detector

This chapter describes the most important parts of the NA61/SHINE facility and detection setup. The detailed information about the NA61/SHINE facility can be found in the Ref. [54], and also [55].

The experiment is a multi-purpose facility measuring hadron production in hadron-proton, hadron-nucleus and nucleus-nucleus collisions. It is a fixed target experiment placed in the North Area of CERN laboratory on H2 beamline of SPS. The NA61/SHINE large acceptance spectrometer is presented in the figure 2.1. Its basics elements, like four large volume Time Projection Chambers

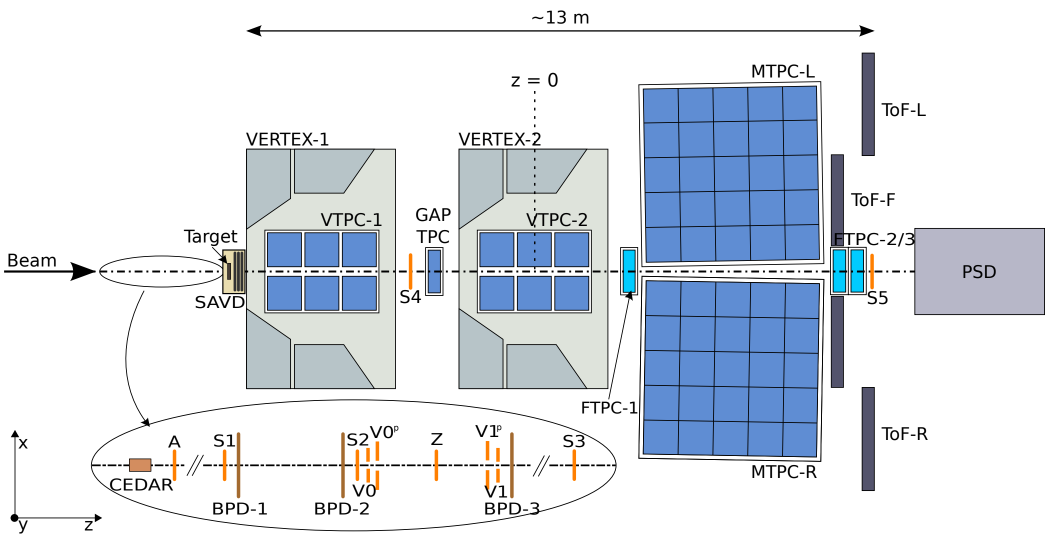

Fig. 2.1: Schematic layout of the NA61/SHINE experiment at the CERN SPS (horizontal cut in the beam plane, not to scale). The beam detectors and trigger counters in zoom. The incoming beam direction is along the z-axis. z=0 is placed in the centre of VTPC-2. The magnetic field bends charged particle trajectories in the x-z (horizontal) plane. Updated schematic from [54]. Description of the NA61/SHINE coordinate system can be found in Appendix A.

(VTPC-1, VTPC-2, MTPC-L and MTPC-R), forward acceptance small volume TPC (Gap-TPC), Time of Flight detectors (ToF-L and ToF-R) and superconducting magnets (VERTEX-1 and VERTEX-2) were inherited from the antecedent experiment NA49 [55]. NA61/SHINE spectrometer is also equipped with a hadronic calorimeter, Projectile Spectator Detector (PSD), forward Time of Flight detector (ToF-F), beamline detectors and upgraded trigger logic based on Field-Programmable Gate Array (FPGA) technology. Moreover, the experimental setup was extended with forward acceptance large volume TPCs (FTPC-1, FTPC-2 and FTPC-3) and Small Acceptance Vertex Detector (SAVD).

2.1 Targets

Realising the two-dimensional scan of the phase space, NA61/SHINE employs target material accordingly to the system size of colliding systems.

Typically, NA61/SHINE uses solid targets made with high purity material, mostly consisting of a single element. Targets of various element kind, like Be, C, Sc, La, Au or Pb, and thickness from 0.5 to 20 mm can be used dependently of measured reaction. The target impurities are measured with Wavelength Dispersive X-Ray Fluorescence (WDXF) to estimate possible bias of the cross-section calculations. Such targets are installed in a dedicated container in a helium atmosphere, to limit possible interactions with materials around the actual target, so-called off-target interactions. The target holder is equipped with a pneumatic movement to enable target inserting in and removing from the beamline. The target position is centred at $z \approx -580cm$.

Lately, SAVD was installed in the NA61/SHINE detection setup and targets described above can be installed inside of this device, close to the SAVD sensors.

NA61/SHINE can also operate with liquid hydrogen target (LHT), as during measurements of p+p interactions. Details on LHT can be found in references [27,28]. Moreover, during reference measurements neutrino experiments the replicas of the T2K and NOνA targets can be used. Such targets are located upstream of the VTPC-1, close to the outside edge of the VERTEX-1 magnet.

2.2 Beams and trigger system

2.2.1 Beams and acceleration chain

NA61/SHINE operates with various beam types – from hadrons to heavy ions, in broad beam momentum range – from several GeV/c to few hundreds GeV/c. It works with primary beams (e.g. Ar, Xe, Pb and primary protons) as well as secondary beams produced via the primary beam fragmentation. NA61/SHINE beams are delivered to the facility after few stages of acceleration performed by the CERN acceleration chain presented in the Fig. 2.2 with components related to the NA61/SHINE beams emphasised.

The primary lead beam is produced by the evaporation of isotopically pure ^{208}Pb sample inserted in a heated crucible, while the beams consisting of nuclei of gases, like hydrogen, argon or xenon, originates from a gas source. A bunch of atoms (H, Ar, Xe or Pb) is transported to electron cyclotron resonance (ECR) source where it is being ionised with electrons accelerated by repetitive microwave pulses. The ions of particular charge state (e.g. p, Pb29+) are electrostatically extracted from the source and injected into the first stage of acceleration.

Primary proton beam acceleration chain is presented in figure 2.2 with the blue colour scheme. It starts with the linear accelerator, LINIAC2, where the beam reaches

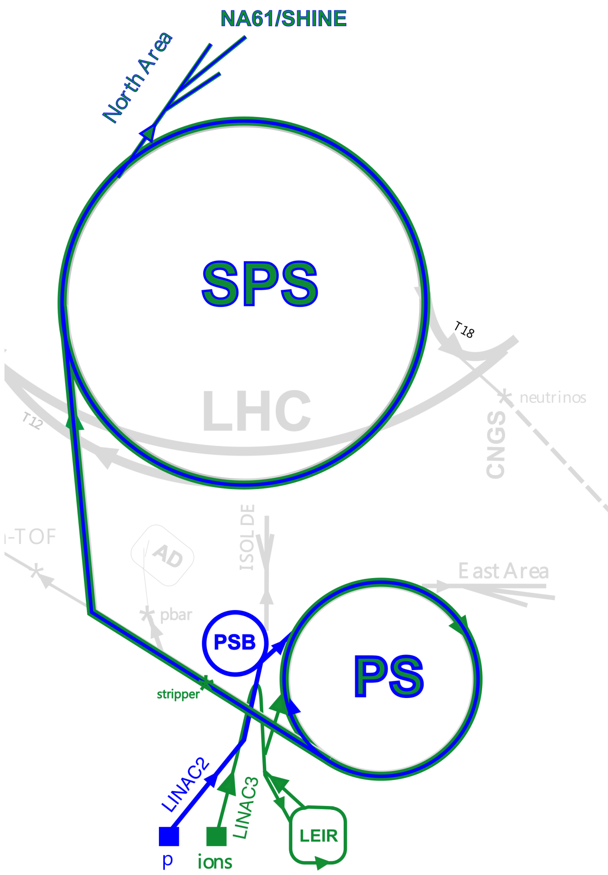

Fig. 2.2: Schematic of the CERN Accelerator Complex detailing components relevant to the NA61/SHINE experiment. Figure taken from Ref. [54].

momentum of 50 MeV/c. Then, the beam is injected to the Proton Synchrotron Booster (PSB), which accelerates protons to the momentum of 1.4 GeV/c, followed by the Proton Synchrotron (PS), which can push the beam to the maximum momentum of 25 GeV/c. Afterwards, protons are sent to the SPS, which supplies CERN North Area as well as LHC with beams.

In case of the primary ion beams, the acceleration chain, marked in figure 2.2 with the green colour scheme, starts with the LINIAC3 linear accelerator, which accelerates ions to momenta of 4.2A MeV/c. Then, acceleration continues in the Low Energy Ion Ring (LEIR), where ions reach momentum of 72A MeV/c. Then, the ions achieve momentum up to 25A GeV/c in the PS accelerator, pass additional stripper to achieve a particular charge state (e.g. Pb82+), and to enter the SPS finally.

The SPS is fed with primary proton beam within momentum range of 13-25 GeV/c and primary ion beam of 13A-25A GeV/c, to supply NA61/SHINE facility with beams within momentum range from 13 GeV/c up to 450 GeV/c (proton beam) and from 13A GeV/c to 150A GeV/c (ion beam).

Secondary beams are gained from the high-intensity (e.g. a few 10^{13} protons or several 10^{8} Pb ions per cycle) primary beams of lead ions or protons interacting with so-called *primary target* (consisting of beryllium plates of 100 mm or 180 mm thickness accordingly to the optimisation of the yield of the requested secondary particle momentum and type) placed 535 m upstream from the NA61/SHINE facility.

2.2.2 Beamline and triggering system

Beams are transported towards the NA61/SHINE experiment with the H2 beamline equipped with devices, which enable to guide and select the requested beam. The beam momentum and type are selected by two large spectrometers of H2 beamline able to separate particles according to their rigidity (roughly A/Z ratio). Each of them consists of six dipole magnets and collimator defining the beam trajectory. The beam intensity is reduced by a set of collimators (placed downstream to the spectrometers) down to a rate of a few 10^5 ions per single spill lasting few seconds.

Besides the magnetic spectrometers, the beamline is equipped with devices providing information of the beam characteristics (e.g. a precise beam particles position, beam profile and intensity), as well as beam particles arrival time and identification. The NA61/SHINE beam monitoring and triggering system consists of various detectors shown in an enlarged part of the Fig. 2.1. Typical parameters of the NA61/SHINE beam detectors are summarized in table 2.1. Detectors based on

detector	dimensions [mm]	hole [mm]	position [m]
S1	60×60		-36.42
S2	$\phi = 20$		-14.42
S3	$\phi = 26$		-5.75
S4	$\phi = 20$		-2.11
S5	$\phi = 20$		9.80
V0	$\phi = 80$	$\phi = 10$	-14.16
$V0^p$	300×300	$\phi = 20$	$\approx$ -14
V1	100×100	$\phi = 8$	-6.72
$V1^p$	300×300	$\phi = 20$	-6.74
A	150×5		$\approx$ -146
Z	160×40		-13.81
BPD-1	$48 \times 48 \times 32.6$		-36.20
BPD-2	$48 \times 48 \times 32.6$		-14.0
BPD-3	$48 \times 48 \times 32.6$		-6.70
Typical thin target (e.g. ^{9}Be) position			-5.80

Tab. 2.1: Summary of typical beam detector parameters: dimensions, positions along the beamline (z coordinates) [54]. Positions of the detectors varied in time due to dismounting and remounting in subsequent runs as well as using various targets. Positions of detectors are surveyed after any change, except the A and $V0^p$ detectors, which were not surveyed, therefore are known only approximately.

plastic scintillation or quartz Cherenkov crystals are equipped with photomultipliers (PMTs) registering photons in selected wavelength range. The beam monitoring system setup is arranged in order to minimise the amount of the material in the beamline the beam particle travels through. Therefore, only a particular selection of beam detectors is installed in the systems depending on the beam type and trigger requirements. The trigger system setup used in ^{7}Be+^{9}Be data taking is described in chapter 4.

The S1 and S2 scintillation counters serve a precise timing reference for the NA61/SHINE triggering system and are used in coincidence in the trigger logic. S1 and S2 measure the energy deposit of the passing ions, which allows for beam particle identification in the off-line analysis. The S1 detector delivers a "start" signal for the time-of-flight (tof) measurement by the NA61/SHINE ToF detectors, described in the section 2.4, and triggers the signals registration in all sub-detectors of the NA61/SHINE detection system.

V0, V0^{p}, V1 and V1^{p} are scintillation counters with holes of a small diameter in the centres. They are working in so-called "veto mode", namely the signals of these detectors are used in anti-coincidence in the trigger logic. They select the core of the beam eliminating the beam halo.

So-called interaction counters: S3, S4 and S5, located downstream of the target, allow for tagging the interactions of the beam particles. They are used in the "veto mode" as well. Signals from them are required to be below some arbitrary threshold adjusted during the preparation of the data-taking.

A-detector and Z-detector were designed to provide the identification of ions in the secondary beam. The first one, a 15 mm thick plastic scintillator, was used to identify the lead beam fragments and verify whether the beryllium contribution is monoisotopic, consisting of ^{7}Be isotope only. It served as the "start" detector of the (tof) measurement of the beam fragments on the distance of 119.32 m, between itself and S1 counter. A-detector measured also the energy deposit of passing ions, what after calibration allowed to derive the charge spectrum of the beam. Time of flight spectra of beryllium and carbon (for comparison) produced in the primary Pb beam fragmentation are presented in the top row of figure 2.3. Carbon tof distribution consists of spectra of two isotopes, ^{11}C and ^{12}C, whereas beryllium spectrum comes from a single isotope, ^{7}Be. Both TDC distributions were obtained after the preliminary charge selection, presented with the blue areas in the charge spectra from A-detector in the bottom row of figure 2.3. Results presented in the left panels of figure 2.3 were measured with a separator set up for the beam B$\rho \approx 2$ (for ^{12}C) and result in the right panels of figure 2.3 - for the beam B$\rho \approx 1.75$ (for ^{7}Be). A-detector operated during the data-taking preparation only and was removed from the beamline for the data taking period.

Z-detector, a quartz Cherenkov counter, was used during all ^{7}Be+^{9}Be data taking campaigns. It measured the Cherenkov photons produced by incoming beam ions. Since, for a given momentum, the amount of Cherenkov light produced by the incident particle is the function of particle charge ($\sim z^{2}$), Z-detector was used to identify the beryllium ions in the beam on-line in a trigger logic in coincidence mode and off-line in further analysis of the beam properties and event selection. An on-line threshold on Z-detector signal was tuned during the preparation of the data-taking.

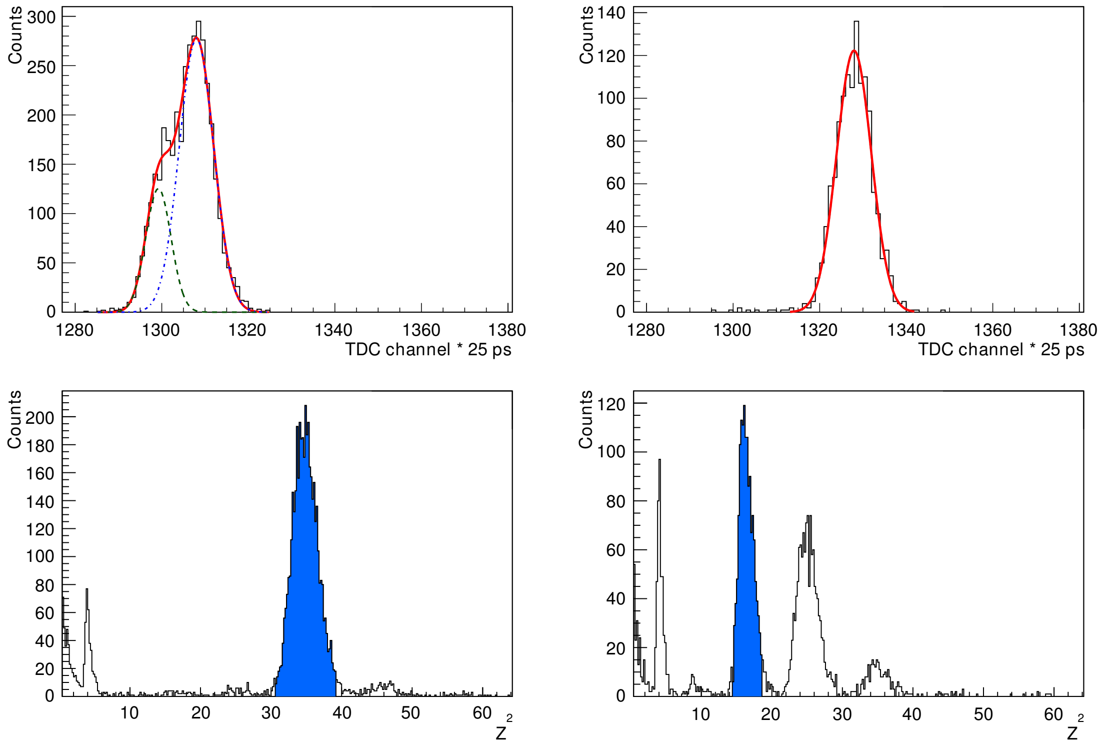

Fig. 2.3: *Top*: The time-of-flight spectra of ions for the carbon (*left*) and beryllium (*right*) beams produced in fragmentation of the primary Pb beam at 13.9A GeV/c. The spectrum of carbon is fitted by a sum of two Gaussian functions due to contributions of two carbon isotopes, ^{11}C and ^{12}C, whereas that of beryllium, ^{7}Be, by a single Gaussian. *Bottom*: The Z^2 spectra with the selected (blue area) contribution of carbon (*left*) and beryllium (*right*). Distributions taken from Ref. [54].

The NA61/SHINE triggering system can also process signals, for example from PSD to tag central, semi-central or minimum bias interactions, or additional device installed in the beam line – Cherenkov Differential Counter with Achromatic Ring Focus (CEDAR) to tag the secondary hadron beam.

The PSD detector is described in the section 2.5. It works in the triggering system in the "veto mode" thus the summed signal from the whole detector is required to be below some arbitrary threshold set up in the preparation of the data taking.

CEDAR, a special Cherenkov counter filled with gas as a radiator, is used in order to identify particles in the secondary hadron beam. It is placed in the beamline only during data taking with hadron beams. Otherwise, it is removed to minimise the material placed in the beamline. It is equipped with an optical system based on eight photomultipliers that collect the Cherenkov photons produced by hadron passing through the radiator. The counter sensitivity can be set to a particular kind of hadrons by setting the appropriate gas pressure (the radiator density). The signal from CEDAR is included in the NA61/SHINE trigger in coincidence mode.

The position of incoming beam particles in the transverse plane is measured by Beam Position Detectors (BPD-1, BPD-2 and BPD-3) placed along the beamline upstream of the target. These detectors are proportional chambers operated with Ar/CO_2 gas mixture in the proportion 85/15. Each BPD measures the position of the trigger-selected beam particle in two orthogonal directions (x-y plane) independently using two planes of orthogonal strips. The scheme of the BPD detector is shown in the figure 2.4. A 3-dimensional point measured by a given BPD, built from

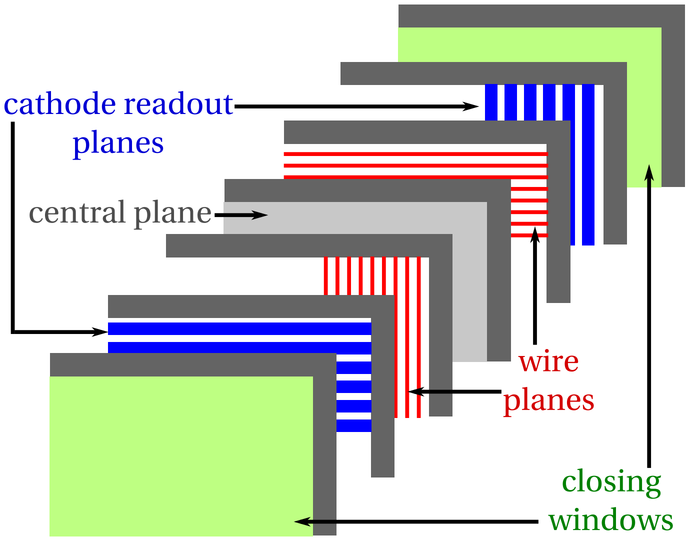

Fig. 2.4: Scheme of BPD detector. Figure taken from Ref. [54].

transverse coordinates and the position of the BPD along the beamline, allows for reconstruction of the beam particle trajectory towards the target.

2.3 Tracking system

The NA61/SHINE tracking system is based on four large volume Time Projection Chambers. Time Projection Chamber allows for measurements of charged particles trajectories in 3-dimensional space and the energy they deposit inside the active volume. Two of NA61/SHINE TPCs, VTPC-1 and VTPC-2, are placed inside superconducting dipole magnets, VERTEX-1 and VERTEX-2 respectively. These two chambers were designed for accurate primary and secondary vertices reconstruction. The measurement of the charged particle trace curvature, by the VTPCs, allows to determine the particle momentum and sign of the electric charge. Two others, MTPC-L and MTPC-R, are situated symmetrically to the beamline downstream to the vertex magnets, outside of the magnetic field. They were built to cover a broad acceptance in the forward hemisphere and also to enhance the energy-loss measurement resolution. An additional smaller chamber, called GAP-TPC, is placed between the two VTPCs, centred on the beamline. It was designed to register particles with small production angles. These five TPCs, marked in blue in the scheme presented in the Fig. 2.1, were exploited during ^{7}Be+^{9}Be data taking campaigns. In 2017 the tracking system was extended with three forward time projection chambers: FTPC-1, FTPC-2 and FTPC-3 (marked in cyan in the Fig. 2.1). The FTPCs improve particle tracking in the very forward region (in region of $0 < \theta < 0.04$ rad in the NA61/SHINE coordinate system, for details see appendix A).

2.3.1 Magnets

The superconducting magnets generate magnetic field oriented vertically, towards negative values of y, to bend trajectories of charged particles in a $x-z$ plane in the NA61/SHINE coordinate system (for details see appendix A). In other words, positively charged particles trajectories are bent towards the left-hand side looking along the beamline and the negatively charged particles in the opposite way.

The maximum magnetic field generated by the VERTEX-1 magnet is 1.5 T, by the VERTEX-2 – 1.1 T. Such magnetic field setting is used for data taking at the highest beam momentum in the NA61/SHINE experiment, namely 150A GeV/c. For lower beam momenta the magnetic field is proportionally scaled down in order to maximise the detector acceptance at forward rapidity hemisphere.

The magnetic field is uniform in the majority of VTPC-1 and VTPC-2 active volumes. An accurate magnetic field map, including inhomogeneities measured at the VTPCs corners, is implemented in NA61/SHINE software used for particle tracks reconstruction.

2.3.2 Time Projection Chambers

General description and principle of operation

A basic TPC design is presented in the figure 2.5. It consists of an active volume of

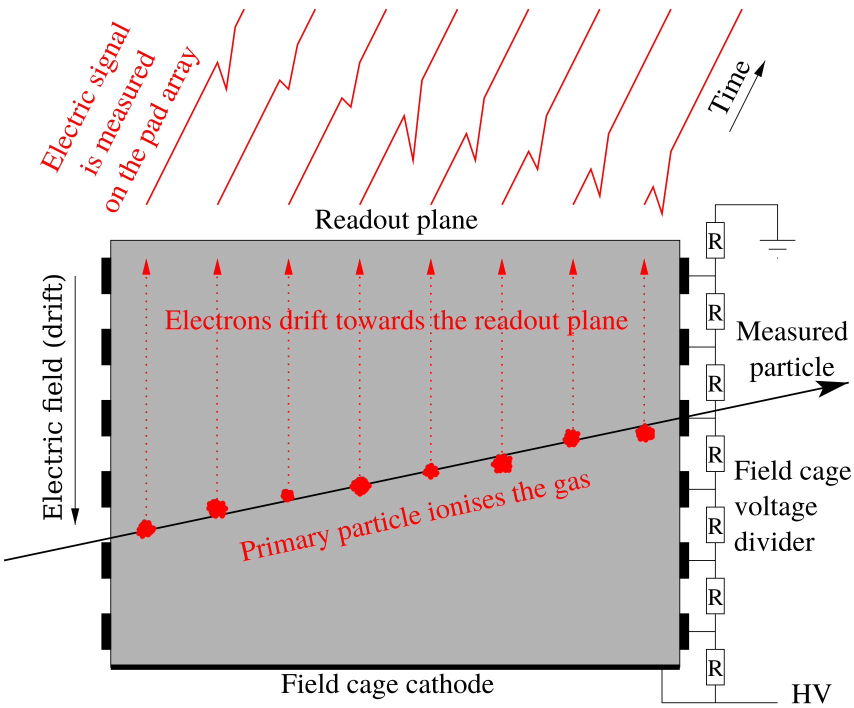

Fig. 2.5: Scheme presenting the principle of the Time Projection Chamber operation. Schematic based on Ref. [56]

the medium, presented in the figure 2.5 in the grey colour, surrounded with field shaping electrodes, so-called field cage, terminated with a cathode plate on one end (*bottom*) and an end-cap chamber with readout plane on the other end (*top*).

In particle physics, the most common are TPCs filled with gaseous medium, which is usually based on noble gases (e.g. Ar, Ne) with a contribution of so-called a quenching gas (e.g. CH_4, CO_2). The exact proportions of the gas mixture components are usually selected to satisfy such requirements like:

- production of a large number of electrons in the primary ionisation,

- low content of electronegative components (e.g. O_2), which have tendency to attract electrons towards itself and decrease the ionisation charge density,
- stable gas amplification, protecting from excessive and uncontrolled growth of the electron avalanches,
- low electron diffusion coefficient, preventing from a charge cluster bulking,
- high drift velocity at moderate electric fields, allowing to collect the charge from the whole TPC volume within the event readout period.

Since, even small variations of the gas mixture composition can change the detection properties of TPCs, the gas mixture stability has to be ensured. More information about gas mixture choice can be found in references [57–59].

The voltage on the field cage strips changes gradually by voltage interval given as a difference of the potentials between the cathode and the end-cap chamber divided by the number of strips to ensure possibly uniform electric field inside the active volume. Charge particles passing through TPC ionise the medium on their trajectory. Electrons released by ionisation at time t_0 create primary ionisation clusters (shown as red clouds in fig. 2.5), which drift under the influence of the electric field toward readout plane, in which they are detected at time t_1.

Since the number of primary electrons is relatively small (from several to several hundred per cm for relativistic particles), a readout plane is usually preceded with an amplification section, for example Multi-Wire Proportional Chamber (MWPC), like in NA61/SHINE TPCs, or Gas Electron Multiplier foils, as planned for ALICE TPCs after LHC Long Shutdown 2 (LS2) [60]. An example of the amplification section based on MWPC, as one installed in NA61/SHINE TPCs, is presented in the figure 2.6. The MWPC consists of two parallel cathode planes and one anode plane

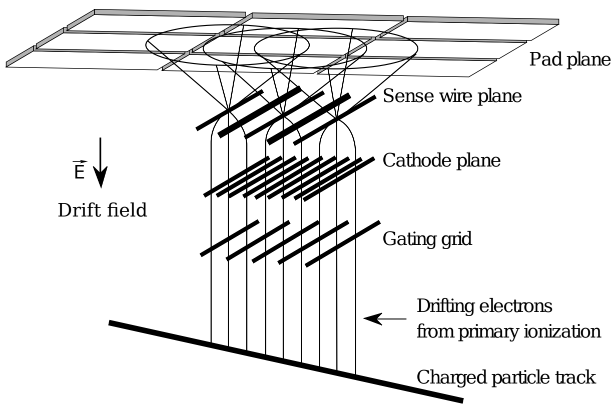

Fig. 2.6: Scheme of the MWPC presenting the charge amplification and signal readout section. Example based on NA61/SHINE time projection chambers. Figure taken from Ref. [55].

(sense wire plane) in between. MWPC volume can be isolated from the drift volume by an extra plane, so-called gating grid. In such MWPC design, one of the cathodes, made with a plate subdivided into small segments (*pads*), serves as a readout plane. The other cathode plane, the sense wire plane and the gating grid are built with thin parallel wires. The electric field inside the end-cap chamber is shaped as presented in the figure 2.7. The gating grid voltage setting has two modes – "closed" gating grid mode, when the voltage is adjusted in the way that the drifting charge is collected before entering the amplification section, and "opened" gating grid mode, when the voltage is adjusted to so-called offset voltage allowing the drifting electrons to enter the amplification section. During TPC operation the gating grid voltage settings are controlled by the trigger system. The gating grid remains open for the charge collection time, or drift time of the electrons, and closes for dead time of

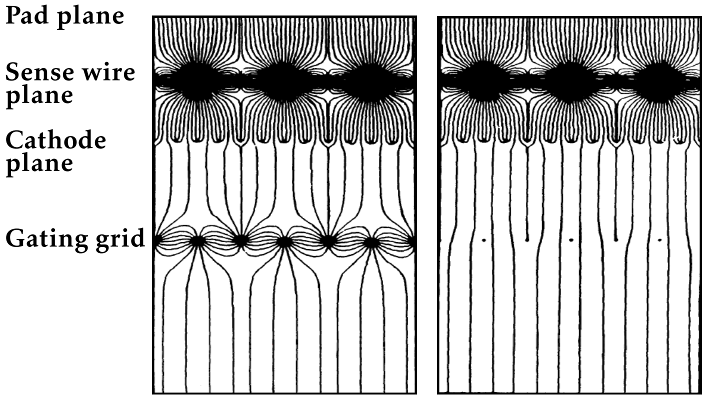

Fig. 2.7: Simulation of electric field inside and-cap chamber: *left* – "closed" gating grid (primary electrons cannot enter the amplification section; *right* – "opened" gating grid (primary electrons can enter the amplification section). Figures taken from Ref. [61].

the detection setup. Sense wires voltage generate a high gradient electric field, in which drifting electrons accelerate and collide with gas atoms causing the secondary ionisation. The process repeats creating an avalanche of electrons, which develops until all the electrons are collected on the anode wire. The sense wire voltage is adjusted to gain proportional multiplication of electrons (typical signal amplification is of the order of 10^4). The disappearance of the electrons and movement of the positive gas ions repelled from the anode wire induce an electromagnetic pulse on the pad plane, which is readout periodically in short consecutive time intervals, so-called *time-slices*.

The cluster position in the readout plane is know due to readout plane segmentation, while the distance of the clusters from the readout plane, s, can be obtained from the drift time measurement $\Delta t = t_1 - t_0$ when knowing the velocity of the drifting electrons, v_D, in a given conditions (gas mixture composition, drift field, temperature, pressure):

$$s = \Delta t \cdot v_D \, . \tag{2.1}$$

Both allow for full 3-dimensional reconstruction of the cluster position in the TPC active volume.

A pulse generated on the particular pad is proportional to the energy deposit corresponding to the single cluster. The energy deposit distribution in cluster is usually parametrised with the Landau distribution [57], which example is presented in the left panel of Fig. 2.8. The energy-losses strongly fluctuate along the particle trajectory, occasionally it is very large, which results in the characteristic long tail of the distribution. In order to reduce the impact of the fluctuations on the mean energy-loss value calculation, the extreme values are omitted. The example of so-called truncation procedure is demonstrated in the right panel of Fig. 2.8. Such procedure increases a resolution of particle identification based on the particle energy-loss (usually referred as dE/dx - an energy-loss per unit length) measurement.

The mean rate of energy-loss of moderately relativistic charged particle ($0.5 < \beta\gamma < 500$) is described by the Bethe-Bloch formula [62]:

$$\left\langle -\frac{dE}{dx} \right\rangle = Kz^2 \frac{Z}{A} \frac{1}{\beta^2} \left[\frac{1}{2} \ln \frac{2m_e c^2 \beta^2 \gamma^2 W_{\max}}{I^2} - \beta^2 - \frac{\delta(\beta\gamma)}{2} \right] \tag{2.2}$$

where $\gamma = (1-\beta^2)^{-1/2}$, $\beta = v/c$, v - velocity of the particle, c - speed of light, x - distance covered by the particle, z - charge of the incident particle in electron units,

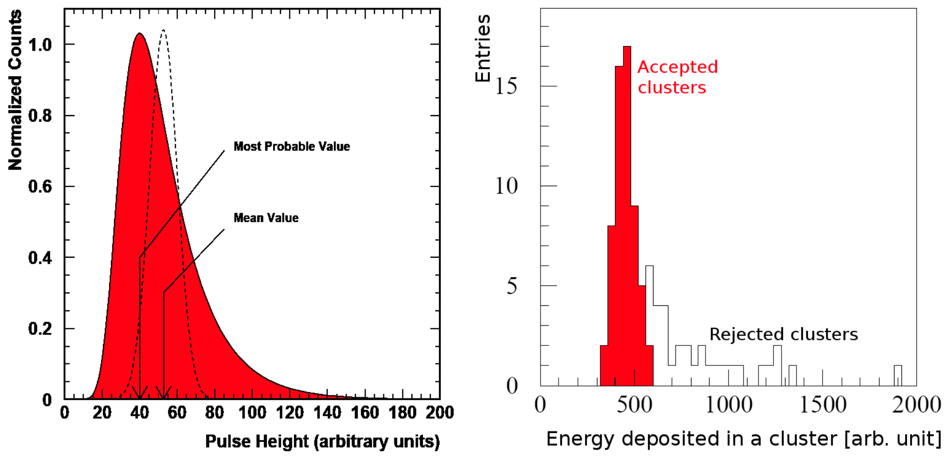

Fig. 2.8: *Left*: Simulation of a Landau distribution (*in red colour*) and a Gaussian distribution (*the dashed line*) for comparison The mean values and peak widths are similar. *Right*: example distribution of many measurements (called "clusters" in the figure) of the energy lost by a single particle. The red area shows the truncated distribution. Figures taken from Ref. [56].

Z - atomic number and A - atomic mass of absorber, m_e - mass of the electron, $W_{\max}$ - maximum energy that can be transfered to an electron in a single collision, I - mean excitation energy of absorber, $K = 0.307075$ MeV mol^{-1} cm^2 (constant), $\delta(\beta\gamma)$ - density effect correction to ionization energy-loss.

The mean energy-loss of the particle, as it is presented by formula 2.2 and figure 2.9, is a function of particle velocity β. Particles of the same momentum but different mass will have different β:

$$\beta = \frac{p}{mc}, \tag{2.3}$$

where p is momentum and m is mass of the particle. Therefore, energy-loss and momentum measurements enable reconstruction of the particle's mass (identification of its type). An example of an experimental measurement of energy-loss as a function of particle momentum is presented in the figure 2.10. The black lines show Bethe-Bloch parametrisation for different particle types. While for particles with momenta of several GeV/c and more the Bethe-Bloch curves are well separated, below 5 GeV/c curves approach and cross each other and it becomes difficult to distinguish particles of a different type (e.g. protons and kaons).

NA61/SHINE TPCs

The basic parameters of the NA61/SHINE TPCs are overviewed in table 2.2. The TPCs readout consists of over 18 000 channels. The pad array is organised as shown in Fig. 2.11: the TPCs are divided into sectors, where the readout pads are located along the padrows perpendicular to the beam line. The number of padrows determines the maximum number of clusters that can be measured on a track passing through the whole TPC length. The signal in the NA61/SHINE TPCs is sampled 256 times during the 50 μs charge collection time (with possibility to increase the sampling rate up to 512 samples per 50 μs charge collection time [55]).

The drift volume and amplification section in each NA61/SHINE TPC are separated with grounded MWPC cathode plane preceded by the gating grid plane. Both

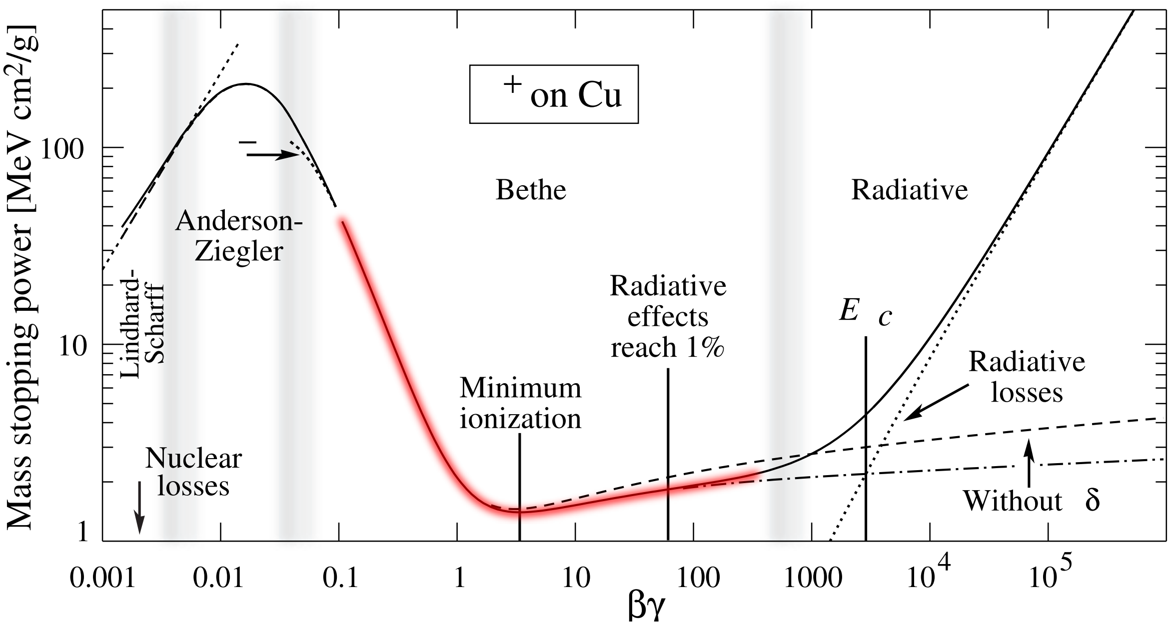

Fig. 2.9: Mass stopping power, dE/dx, for positively charged muons in copper. The thick red line marks the region relevant for TPCs in high-energy physics experiments. The decrease proportional to $1/\beta^2$ at the low energies, a minimum at $\beta\gamma \approx 3$ and a slow increase at the higher energies is observed for this region. Figure taken from Ref. [62].

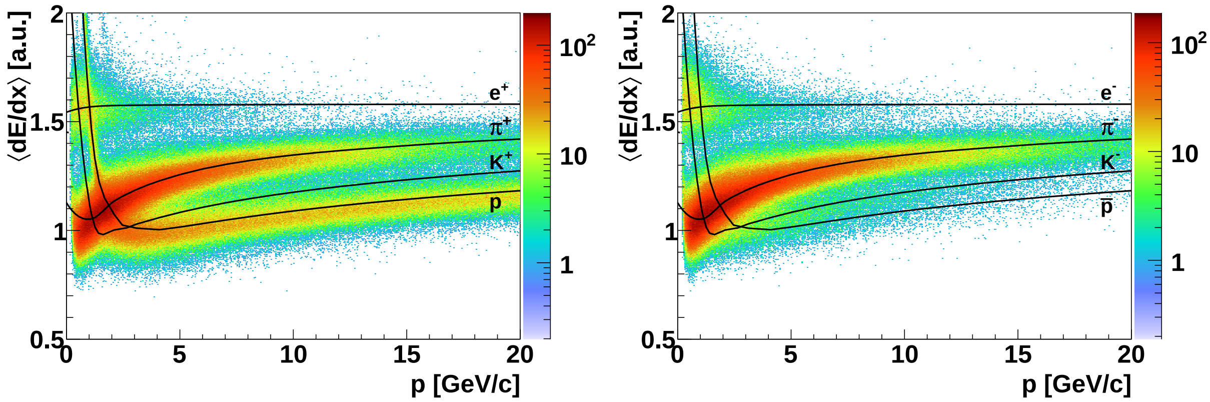

Fig. 2.10: Particle energy-loss as a function of particle momentum measured by NA61/SHINE TPCs for ^{7}Be+^{9}Be collision at 40A Gev/c. Each entry on the *left* histogram corresponds to a single positively charged particle, whereas on the *right* histogram - to a single negatively charged particle.The black lines show theoretical Bethe-Bloch curves for electrons, pions, kaons and protons.

planes are constructed with 75 μm thick gold-plated copper wires spaced by 1 mm. During the charge collection, the gating grid offset voltage is adjusted to about -115 V, while beyond the charge collection periods an additional voltage of about ±45 V (±60 V in case of FTPCs) is applied to each second wire of the gating grid. Two functions of the gate electrode are: collecting the electrons originating from particles arriving beyond time window correlated with the trigger and reducing migration of the slowly drifting positively charged ions created by the gas multiplication inside the amplification region towards drift volume, which prevents a drift field distortions. The sense wires plane consist of 20 μm gold-plated tungsten

	VTPC-1/2	MTPC-L/R	GAP-TPC	FTPC-1/2/3
Size (L×W×H) [cm]	250 × 200 × 98	390 × 390 × 180	30 × 81.5 × 70	60×71 (81)×160
Drift length [cm]	66.60	111.74	58.97	101.40
Drift velocity [cm/μs]	1.4	2.3	1.3	2.1
Drift field [V/cm]	195	170	173	171
Drift voltage [kV]	13	19	10.2	17.3
Gas mixture Ar/CO_2	90/10	95/5	90/10	94/6
No. of pads/TPC	27648	63360	672	1536
Pad size [mm]	3.5 × 28(16)	3.6 × 40, 5.5 × 40	4 × 28	4 × 40, 6.6 × 40
Pad angles [°]	3–55°	0°, 15°	0°	0°
No. of sectors	2 × 3	5 × 5	1	1
No. of padrows	72	90	7	12
pads/padrow	192	192, 128	96	128, 160, 96

Tab. 2.2: Parameters of NA61/SHINE Time Projection Chambers. The pad length of 16 mm in the VTPC-1 is installed in the two upstream sectors. In the MTPCs the five sectors closest to the beam have narrower pads and correspondingly more pads per padrow. The pads of a width of 6.6 mm are installed in 6 most downstream padrows of FTPC-2/3. FTPC-2/3 are also 10 cm wider that FTPC-1.

anode wires, so-called amplification wires, at the electric potential of about +1 kV, interspaced by 125 μm gold plated copper field wires at the ground potential. Such arrangement helps to shape the electric field for the gas amplification. The distance between neighbouring anode wires is 4 mm. The same spacing of field wires is employed. The separation of the MWPC cathodes (wire cathode and readout plane) is 6 mm (4 mm in VTPC-2 and 5 sectors of each MTPCs adjacent to the beamline). The distance between the cathodes and a sense wire plane is 3 mm (2 mm in VTPC-2 and 5 sectors of each MTPCs adjacent to the beamline) [55], and of order of 5 mm between wire cathode and the gating grid plane.

The MTPCs are the active volumes of 3.9×3.9 m^2 top surface area and 1.1 m drift length each. The signals of ionisation electrons are read out by 25 MWPCs per chamber, providing up to 90 measured clusters along the charge particle trajectory. The granularity of pads is more dense in the MWPCs in the sectors adjacent to the beamline, in so-called High-Resolution (HR) sectors, built with 3.6 mm wide pads. Remaining 20 sectors, so-called Standard Resolution (SR) sectors, are formed with 5.5 mm wide pads. The accuracy of the measurement of the average ionization energy-loss for a single particle in the MTPCs is of order of 4%.

VTPCs consist of 6 MWPCs each. Due to expected very high track density in the forward region the active sections of VTPCs are separated by a 25.5 cm wide gap along the beam axis, in which neither charge amplification, nor readout are provided. Readout pads in the two upstream sectors of the VTPC-1 (sectors 1 and 4 in figure 2.11) are shorter (16 mm) than in other four sections and whole VTPC-2 (28 mm). The size of VTPC-1 and VTPC-2 is limited by the gap between two coils of the superconducting magnets, VERTEX-1 and VERTEX-2, respectively. They cover of 2.5×2.0 m^2 top surface and 0.666 m drift length each.

Track angles with respect to the beam direction vary from a few degrees in the extreme forward direction at high momentum to a maximum of about 50° for the lowest accepted momenta at around 1 GeV/c in VTPC-1. The MTPCs and VTPCs

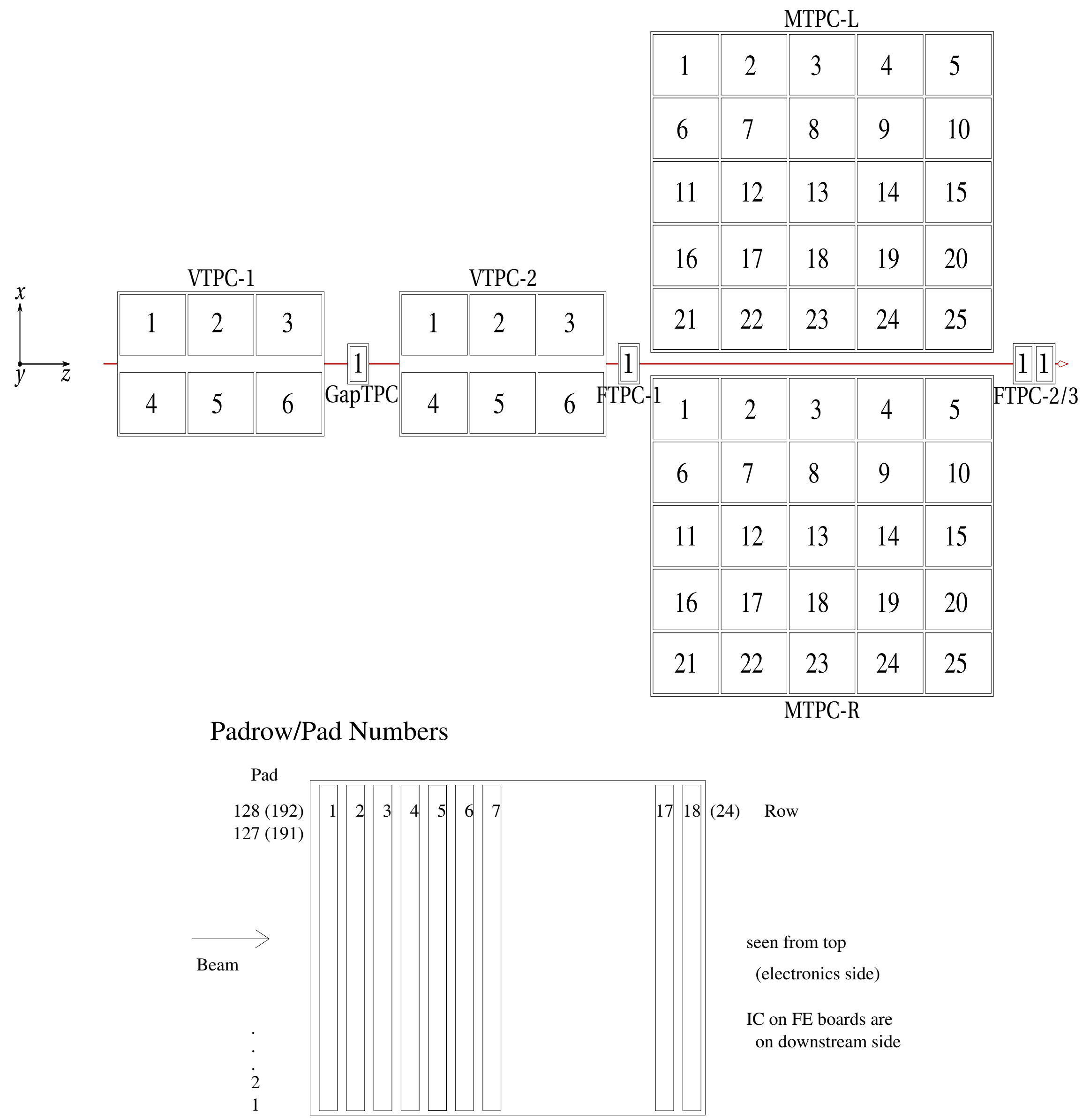

Fig. 2.11: *Top*: Scheme of NA61/SHINE TPC sector numbering convention. *Bottom*: Scheme of NA61/SHINE TPC padrows and pads numbering convention within a single sector. Drawing taken from Ref [63]

pads are tilted with respect to the beam axis in the various detector sectors to minimise the angle between a particle track and the longer edge of a pad. Therefore, the TPCs space resolution is determined by the limit given by electron diffusion only, both in vertical (drift) and horizontal (bending) direction. The two-track resolution in the MTPCs and VTPCs is in order of about 1 cm [55].

The GapTPC is a small gas box of a width of 81.5 cm, a length of 30 cm and a height of 70 cm, with the almost 59 cm high field cage inside. The width and length of the field cage fit to one readout sector consists of 7 padrows with 96 pads each. The pad dimensions are 28 mm by 4 mm.

FPTC-1 is composed of one readout sector with 128 pads devided into twelve padrows. The sector in FTPC-2/3 is divided into HR and SR regions. The HR is built with six padrows with 160 pads, whereas SR with six padrows with 96 pads. The FTPC-1 and FTPC-2/3 HR pads are 4 mm wide and 40 mm long, while the dimensions of the FTPC-2/3 SR pads are 6.6 mm in width and 40 mm in length. Due to different readout plane design, the FPTC-2 and FTPC-3 are 10 cm wider that FTPC-1. The drift length in all FTPCs is of order of 1 m.

The GapTPC and FTPCs are extending the spectrometer acceptance to the smallest production angles in low multiplicity collisions of hadrons and light nuclei. They are centred in the beamline. The pads in these chambers are parallel to the beamline. GapTPC and FTPC-1/2/3 work as two tandems: GapTPC/FTPC-1 as one and FTPC-2/FTPC-3 as the other one. They are designed in the way, that the drift direction is opposite in both chambers of the tandem (e.g. electrons drift towards positive y in GapTPC and towards negative y in the FTPC-1). Such arrangement simplifies rejection of particles not correlated with the trigger.

Each TPC in the NA61/SHINE is connected to a separate gas system, which constantly supplies the chamber with the appropriate gas mixture and also provide monitoring of the gas mixture parameters and quality (e.g. electron drift velocity, temperature and pressure of the gas, oxygen and water content in the gas mixture). Description of the gas system can be found in Appendix D.

2.4 Time of Flight detectors

The NA61/SHINE particle identification system based on TPCs is complemented with an additional identification method by ToF detectors. The NA61/SHINE detection system is equipped with three ToF detectors, in jargon called ToF Walls: left (ToF-L), forward (ToF-F) and right (ToF-R). The ToF-L and ToF-R are pixel detectors inherited from NA49 while ToF-F was additionally constructed to supplement the ToF acceptance in a forward region for reactions with a low multiplicity of produced particles. During a realisation of the NA61/SHINE strong interactions physics programme, ToF-F is removed from the detection setup.

2.4.1 Principle of operation

The ToF particle identification method is based on particle time-of-flight measurement performed by high time resolution (typically several tens of ps) detectors (e.g. scintillators). The detectors register the particles arrival time, so-called *stop signal*, with respect to some general reference (e.g. trigger), so-called *start signal*. The particle mass is obtained by combining the information from particle time-of-flight measurement, $tof = t_{stop} - t_{start}$, with measured track length, l, and momentum, p:

$$m^2 = \left(\frac{p}{c}\right)^2 \left(\frac{c^2 (tof)^2}{l^2} - 1\right). \tag{2.4}$$

2.4.2 NA61/SHINE ToF-L/R

Two Time of Flight walls in the NA61/SHINE, of 4.4 m^2 total area, are placed behind MTPCs symmetrically with respect to the beamline (see fig. 2.1). Schematic layout of the ToF-R wall is presented in the figure 2.12. Each wall is built with 891 individual

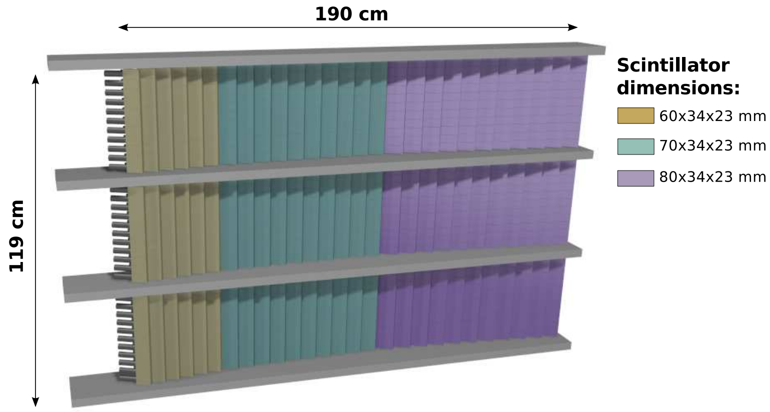

Fig. 2.12: Schematic layout of the ToF-R wall. The layout of ToF-L wall is a mirror reflection with respect to the beamline plane. Figure taken from Ref. [54].

plastic scintillators (TOF-R: Bicron BC-418, TOF-L: similar scintillator produced at JINR Dubna/Russia). The scintillators have a cuboidal shape and are placed next to each other in 33 rows and 27 columns. The wall is divided into three sections (symbolised in the figure 2.12 with different colours) consisting of scintillators of various widths. The scintillators have a thickness of 23 mm, a height of 34 mm and widths of 60, 70 or 80 mm. They are adjusted accordingly to the local track density, thus the narrowest scintillators positioned closest to the beamline. Particles measured by ToF-L/R, hit the largest side of the scintillator, while a photomultiplier (TOF-R: Philips XP-2972, TOF-L: FEU-87 MELZ) is glued directly to the smallest side of each crystal. Scintillation detectors will be further called pixels or tiles.

Each PMT output signal is split: one signal is fed into constant-fraction discriminator (CDF) module followed by a time-to-digital converter (TDC) and the second one to a charge-to-digital converter (QDC). The start signal reference for the TDCs is provided by the S1 beam counter while the stop signal comes from the CFDs if their input is above an arbitrary threshold.

The direct measurement of tof can be flawed for the incident particle hit position in the scintillator. At first, the hit position is assigned arbitrarily to the center of the scintillator (in both: S1 and any of ToF pixel). Then, in the calibration process, real hit position is calculated.

S1 scintillator has 4 PMTs (S11, S12, S13, S14) attached to each side parallel to the beamline. The time difference between S11 signal and other three PMTs (S12, S13 and S14) is used to calculate the beam particle position in the S1 scintillator. In the case of ToF-L/R tiles, the real position is obtained from the particle trajectory reconstructed via procedures described in the sec. 3.1. Then, knowing that hit displacement in the scintillator of order of 1 mm cause the time measurement discrepancy of order of 3 ps, the tof measurement dependence on the position of incident beam particle is removed. The final time resolution of the tof measurement is pf order of 100 ps for ToF-L and 80 ps for ToF-R. The difference in resolution is determined by the type of used PMTs and readout modules.

Such resolution is sufficient to separate pions and kaons for momenta up to 3 GeV/c and for even higher momenta if the tof information is combined with dE/dx

measurement. The distribution of the particle squared mass versus momentum measured in ^{7}Be+^{9}Be collisions at 40 GeV/c is presented in the Fig. 2.13 (*top*). Left

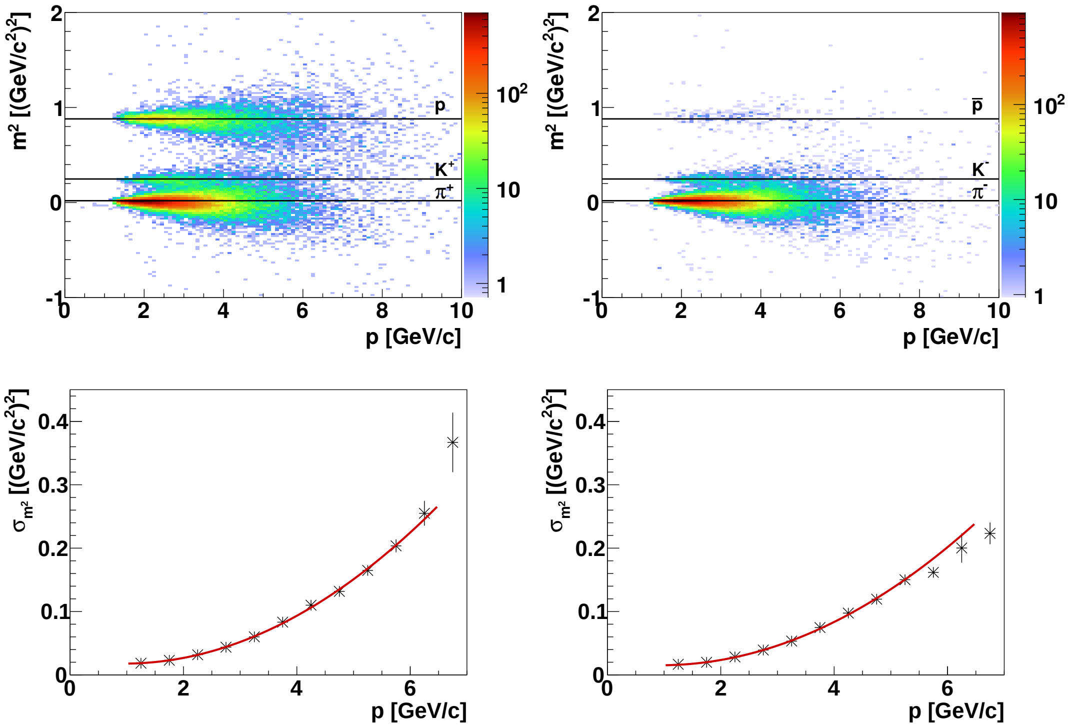

Fig. 2.13: *Top*: Mass squared versus momentum measured by ToF-L (*left*) and ToF-R (*right*) for B+Be collision at 40A Gev/c. Bold lines show the expected mass squared values for different charged hadrons. *Bottom*: The resolution of the m^2 measurement as a function of particle momentum for the ToF-L (*left*) and ToF-R (*right*).

panel represents the performance of ToF-L while right panel - ToF-R. The mass determination resolution is plotted as a function of momentum in Fig. 2.13 (*bottom*).

2.4.3 ToF-F

Measurements of hadron production for the T2K neutrino oscillation experiment required particle identification in a phase space region which is not covered by the ToF-L/R. Therefore, an additional time-of-flight detector, ToF-F, was constructed to provide a full time-of-flight detector coverage behind MTPCs. Originally, ToF-F consisted of 80 plastic scintillator bars of 120 cm length, 10 cm width 2.5 cm thickness oriented vertically. They are staggered with 1 cm overlap. The scintillations are registered on both sides of the ToF-F bars with two photomultipliers (Fast-Hamamatsu R1828) and were digitised by simple TDC modules. After FTPC-2/3 installation, ToF-F consists of 32 scintillators placed on both sides of the FTPC-2/3 and each ToF-F PMT is readout with Domino Ring Sampling (DRS4) based electronics.

2.5 Projectile Spectator Detector

The most downstream element of the NA61/SHINE detection setup is a zero-degree hadronic calorimeter, PSD. The calorimeter measures the energy deposited by those projectile nucleons, which did not interact in the nuclear collision, further called the forward energy (E_F). In simple approach, the higher E_F is registered, the less nucleons has interacted in the collision. Therefore, the PSD is employed to tag central collisions during data taking at the trigger level. Then, a comprehensive event-by-event analysis of the E_F is used to estimate the number of interacting nucleons from the projectile with the precision of one nucleon.

The incident particle, a hadron, interacting with material of the calorimeter engender the particle cascade, as example presented in the left panel of Fig. 2.14. Various processes, like inelastic interaction, ionisation, excitation, take part in the

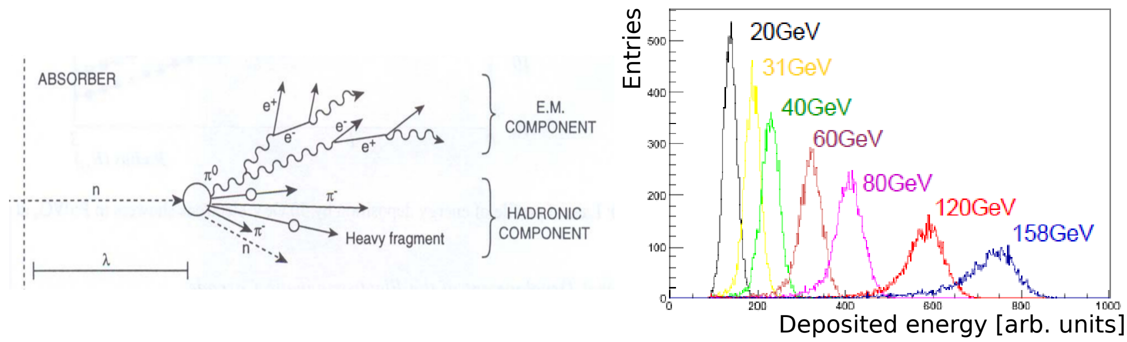

Fig. 2.14: *Left*: An example of particle cascade generated by single neutron. The cascade consists of hadronic part and electromagnetic part. Figure taken from Ref: [10]. *Right*: Energy deposit spectra of proton beam at different energies. Figure taken from Ref. [64]

cascade development, thus the particle cascade consist of hadronic component but also electromagnetic component. The energy deposited inside the calorimeter is probed by the PSD active material, scintillators. An example of the amplitude spectrum corresponding to the energy deposit of protons (summed over the whole calorimeter) is presented in the right panel of Fig. 2.14.

The PSD calorimeter consists of 44 modules covering a transverse area of 120x120 cm^2 in total. A schematic front view of the PSD is shown in Fig. 2.15 (*left*). The

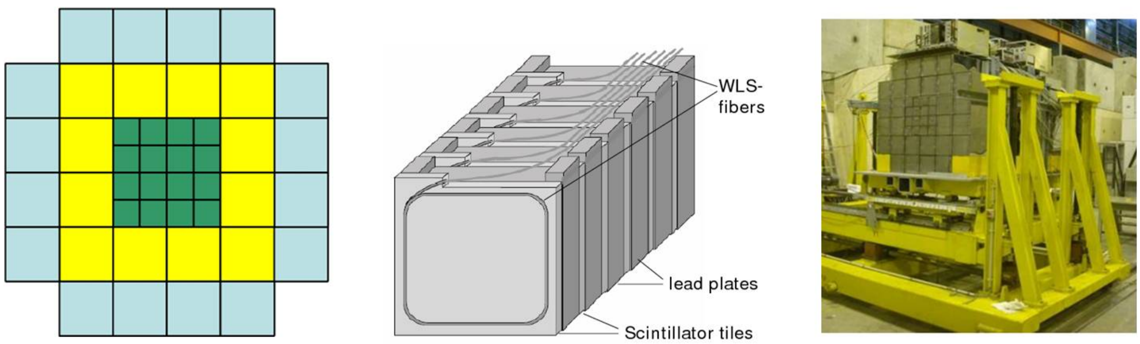

Fig. 2.15: The PSD: schematic front view (*left*), schematic view of single module (*center*) and the fully assembled detector (*right*). Figures taken from Ref. [54]

central part of the calorimeter is built with 16 small modules with a transverse area of 10x10 cm^2, whereas peripheral part of the PSD is constructed with 28 large modules with transverse dimensions of 20x20 cm^2. Each module consists of 60 pairs lead plates and scintillator plates with 16 mm and 4 mm thickness, respectively, creating a structure of a sampling calorimeter. The schematic layout of the module is presented in Fig. 2.15 (*center*). The longitudinal length of each module, 120 cm, corresponds to 5.7 nuclear interaction lengths. Scintillation light from each scintillator plate is transmitted by wave-length-shifter (WLS) fibres to the micro-pixel avalanche photodiodes, MAPDs. Each MAPD has $3{\times}3$ mm^2 active area with a pixel density of 10^3 pixels/mm^2, which fits well the size of the WLS-fiber bunch from six consecutive scintillators. Signals from the calorimeter are digitised by the FPGA based front-end-electronics. A photograph of the calorimeter is shown in Fig.2.15 (*right*).

Depending on the depth, at which the cascade starts, the energy is deposited in smaller or large amount of the detector. If the cascade starts just at the beginning of the PSD module, it develops through a large number of scintillator/lead plates. Then, the total energy carried by the cascade is deposited and reconstructed, as opposed to the case, in which the cascade starts in more downstream part of the module. On average, 10% of the energy carried by the cascade leaks longitudinally through the downstream side of the calorimeter. Moreover, due to the transversal development of the cascade some information about the energy it carries can lost. On the assumption that the cascade starts in the centre of a single module (the most idealistic scenario), the transversal energy leak from the large module is of order of 4% and even 13% in case of small module. Nevertheless, since the PSD has a modular construction and its position is adjusted in the way that the collision spectators hit the center part of the calorimeter, the cascade leakege from a single module is measured by neighbouring modules. Therefore, the total energy leakage in the transversal plane is of order of 0.1%. The cascade profiles in longitudinal and transversal plane, as well as the energy leakege are estimated with MC simulation and taken into account during calibration procedures.

2.6 Small Acceptance Vertex Detector

Construction of a high-resolution vertex detector is motivated by the possibility of the first direct measurements of open charm meson (D^0) production in heavy-ion collisions in the SPS energy range. Currently, a limited version of the Vertex Detector, SAVD, is installed in the NA61/SHINE detection setup. This device covers 35% of the acceptance of the final version which is foreseen to operate after LHC LS2.

The SAVD consists of two spectrometer arms composed with four detector stations, which are located 5, 10, 15 and 20 cm downstream the NA61/SHINE target. It is based on 16 ultra-light, 50 μm thick, MIMOSA-26AHR silicon sensors of $1.06{\times}2.13$ cm^2 active surface each, which provide a very fine pixel pitch of $18.4{\times}18.4$ μm^2 (over 650 thousands of pixels per sensor). The readout and a slow control of the pixel are realised with a Trigger Readout Boars 3 (TRBv3).

The detector was uses for the first physics data taking in autumn 2018, for Pb+Pb collisions at 150A GeV/c beam momenta.

Chapter 3

Data production and Monte Carlo simulation

All data registered with NA61/SHINE detection setup are reconstructed and calibrated. For this purpose dedicated algorithms are used. Moreover, experimental results are corrected for various effects, like, for example the detector geometry and response, reconstruction software inefficiencies, with Monte Carlo (MC) simulation. The first section of this chapter briefly describes the so-called *data production* procedure, which consists of a few steps for particle trace reconstruction and a few stages of calibration. Then, description of the NA61/SHINE MA simulation chain follows in the second section of this chapter.

3.1 Data production

3.1.1 Reconstruction

Each registered trigger is stored in a single record called *event*. This entity contains the digitised signals from all NA61/SHINE detectors, which are translated to particle trajectories and particle energy deposits in the reconstruction process. An example of a reconstructed ^{7}Be+^{9}Be collision is presented in figure 3.1. Event reconstruction concerns trajectories and characteristics of particles produces in the collision and requires several consecutive steps:

- **Cluster finding in the TPCs**. In the first step, the reconstruction software searches for any signals registered by pads in any time-slices. The signals registered in the first time-slice are rejected to minimise the impact of the electronic noise on the reconstruction. The signal on adjacent pads and in the consecutive time-slices are merged and assigned as so-called *potential clusters*. Then, in the case, that arbitrary requirements on the cluster properties, like number of fired pads, number of consecutive time-slices and ADC values, are fulfilled, the potential cluster becomes a so-called *real cluster*. The 3D position of the real cluster (point) is calculated with the centre of gravity method taking into account the amount of charge measured by a given pad in a given time-slice.
- **Local tracking in TPCs.** The tracking algorithm searches for clusters adjacent to each other, like in consecutive padrows and/or time-slices. The neighbouring clusters are merged into segments of tracks in each TPC, into so-called

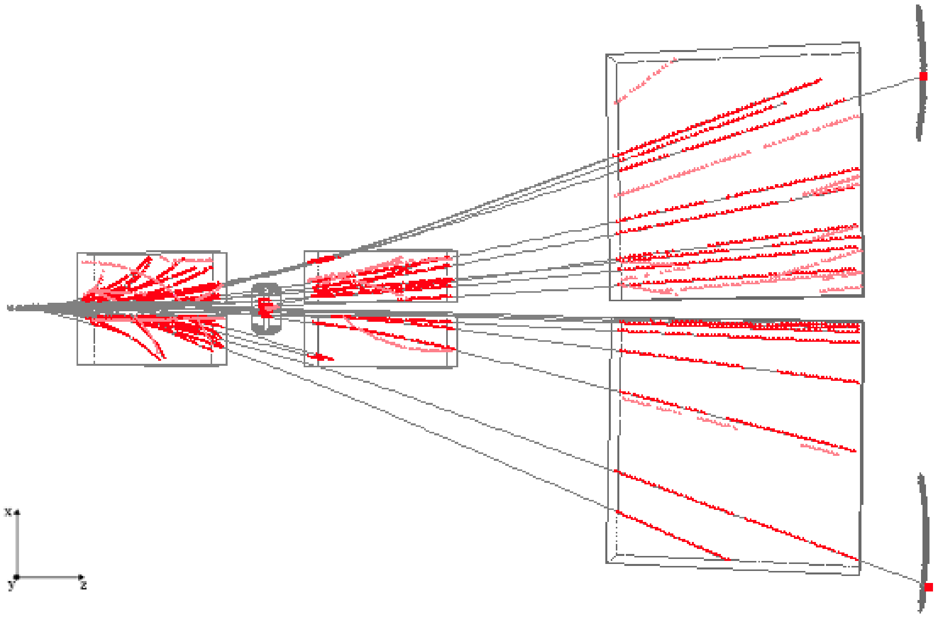

Fig. 3.1: An example of a reconstructed event of ^{7}Be+^{9}Be collision at 150A GeV/c. In the picture red lines symbolise measured clusters in TPCs and signal observed in TOF walls and grey lines - the extrapolated traces.

local tracks. In the MTPCs segments of the track are fitted with straight lines, whereas in VTPCs curved track segments are processed with a dedicated software class called *MagneticFieldTracker* (MFT), due to the magnetic field.

- **Global tracking in TPCs.** Track segments in consecutive TPCs are merged into a common track, so-called *global track*, and fitted again. This procedure allows for determining important parameters of a particle, like momentum and electric charge sign (accordingly to their curvature in the magnetic field), the length of the particle path and also the number of clusters measured along the particle trajectory, which allows to calculate the specific energy loss using the truncation procedure.
- **Primary vertex determination.** The fitting algorithm extrapolates all tracks to the approximate target plane, at $z = -580$ cm in the NA61/SHINE coordinate system, to find one common vertex, so-called *primary* or *interaction vertex*. The exact z coordinate of the primary vertex position is determined by the TPC tracks extrapolation, while the x and y coordinates of the primary vertex are identified by extrapolation to the target plane of the beam trajectory measured by BPDs.
- **Secondary vertices determination.** Moreover, each pair of particle traces is processed by the reconstruction algorithm in search of secondary vertices. Secondary vertices distant from the target area can indicate particles produced in weak decays (e.g. K^0_s, Λ), secondary interactions or off-target interactions.
- **ToF hits matching with track**. Finally, the reconstruction algorithm extrapolates all tracks from the primary vertex towards the ToF detectors and perform matching each track with the signals (so-called *hit*) in a particular ToF tile.

As a result of the complex reconstruction procedure, each track has assigned characteristic parameters crucial for further analysis, like momentum vector, electric charge sign, specific energy-loss, path length, number of clusters reconstructed in the TPC as well as time-of-flight and mass if the ToF hit was registered. Collision centrality for each event is estimated in the dedicated analysis briefly described in chapter 5 and presented in details in Ref. [65].

3.1.2 Calibration

The calibration procedure is provided to optimise time-dependent corrections (e.g. electron drift velocity or specific energy loss per length unit). The calibration procedure is realised sequentially for each calibration constant.

One of the most important stages of the calibration concerns the electron drift velocity. The v_D in a particular gas mixture is monitored by a dedicated device in the gas circulation circuit of each NA61/SHINE TPC (more detail can be found in Appendix D). It is measured in similar conditions of drift field, gas temperature and pressure, to those in a given TPC. The exact conditions in both, TPC and a drift velocity monitor, are registered. For the gas mixtures and drift fields used in NA61/SHINE, the drift velocity is scalable with E, p and T (proportional to E and T, inversely proportional to p). Thus, the drift velocity of electrons in a given TPC is calculated using the measured one and monitored values of E, p and T. The accurate reconstruction require the precision of the v_D in TPC estimation of order of 1‰. The precision of the v_D calculation is verified by the reconstruction software in the global tracking procedure. In the case the estimated v_D value deviate from the real value, the vertical offset between local tracks selected for the global track construction is observed. Since the 1‰ precision of the v_D calculation is difficult to achieve directly from the v_D measurements (only after the drift monitoring system upgrade in 2014 the measurement resolution is enough to achieve such precision), the real v_D value is calibrated with experimental data using the so-called *bottom-point method*. This procedure requires the event-by-event selection of the produced particles, which trajectories intersect with the TPC cathode plane. Since the drift length is well-known, the arrival time measurement of the electrons released close to the drift field cathode allows for the precise calculation of the real electron drift velocity in the particular TPC. Employment of the bottom-point method needs events of a high mean particle multiplicity.

Other data-driven calibration procedures concerning, for example, energy-loss (explained in details in Ref. [66]) or time-of-flight measurements are applied afterwards.

3.2 Monte Carlo simulation

The collisions measured by the NA61/SHINE have been studied with MC generators and the detection setup response was simulated using MC techniques. Several MC models have been tested on p+p interactions. Taking into account the agreement between experimental results and the model predictions, and also continuous support from the developers, the EPOS 1.99 model [67, 68] was selected as a particle generator (brief description of the model is contained in Appendix C). The particles passage through the detection setup is simulated with the GEometry ANd Tracking (GEANT) 3.21 software [69]. The MC simulation is used to correct the reconstructed data for various effects related to detector geometry and response, reconstruction algorithm inefficiency, as well as a contribution of particles produced in secondary interactions and weak decays of short-lived particles. The simulation procedure consists of the following steps:

- generation of inelastic ion-ion (e.g. ^{7}Be+^{9}Be) collisions using the EPOS 1.99 model,
- propagation of the produced particles through the NA61/SHINE detection, setup using the GEANT 3.21 package, taking into account relevant physics processes (e. g. particle decays, secondary interactions, γ conversion), with assigning the simulated cluster position and total charge,
- reconstruction of the simulated events with the same reconstruction chain used for experimental data,
- storing simulated events in the same format as raw experimental data,
- identification of the reconstructed tracks with so-called *matching procedure* (at the analysis level).

The MC simulation provides two sets of events: generated inelastic collisions ($MCgen$), which contain information of the type, momentum and trajectories of generated particles, and its subset – simulated events, which were reconstructed with the NA61/SHINE reconstruction chain ($MCrec$).

In the last step of the MC procedure, reconstructed MC tracks are identified via matching procedure. For each reconstructed MC track, the matching algorithm attempts to find the best candidate among the generated MC tracks. The generated MC track candidate with the highest number of generated MC points geometrically common with reconstructed MC clusters is selected as a matched track. Then, the MC particle number [70] of the matched generated MC track is assigned to the reconstructed MC track. The matching procedure provides also very important feedback about the possible contribution of so-called *feed down* – secondary particles wrongly reconstructed as primary ones.

Centrality determination of the simulated collision is based on the comparison between simulated and measured forward energy distributions. For each MC event, the energy deposit is simulated in each module of the PSD calorimeter. Next, the E_F distributions are compared with the reference distributions obtained with complex analysis of experimental data. The details of this procedure are described in chapter 5.

ToF response simulation is data-driven and involves the data-based efficiency calculation. Efficiency constants for each ToF pixel are calculated individually, separately for each dataset. Details of this procedure are presented in chapter 5. In the simulation, each track extrapolated from MTPCs towards ToF Walls is weighted by the efficiency constant of the pixel it has indicated.

Chapter 4

Characterisation of the data set

The data on ^{7}Be+^{9}Be collisions were collected in 2011 and 2013 by the NA61/SHINE experiment. Data registration was performed in two campaigns - the first, so-called *high-energy data taking*, for beam momenta $p_{\text{lab}} = 40A, 75A$ and $150A$ GeV/c, and the second, so-called *low-energy data taking*, for $p_{\text{lab}} = 13A, 19A$ and $30A$ GeV/c. During each campaign the dedicated trigger and the beam detectors configuration were used. Moreover, between these two data taking periods, ToF-R underwent maintenance (electric and light connections in 96 ToF-R pixels were fixed). This chapter describes properties of the beam, trigger and target employed in the recording of the experimental data for beam momenta from $30A$ to $150A$ GeV/c. The properties of the data sets collected at $13A$ and $19A$ GeV/c beam momenta are not studied in the framework of this thesis.

4.1 Trigger

Data were collected with a few specific on-line trigger configurations, in proportions defined by so-called *pre-scaling factors*. Each recorded event was tagged with a appropriate trigger label. For low-energy data taking, four trigger definitions were used: *identified beam*, *identified central interaction*, *unidentified beam* and *unidentified minimum bias interaction*. For high-energy data taking, three definitions were set up: *identified beam*, *identified central interaction* and *unidentified beam*. Typically, pre-scaling factors are set to record mostly central and semi-central inelastic collision of beryllium ions, which is defined as *identified central interaction*. A relatively small number of events was collected with the other trigger configurations for cross-section determination and beam monitoring purposes. The schematic layout of beam and trigger detectors configuration is presented in Fig. 4.1 and trigger definitions are given in table 4.1 for high-momentum data taking and in table 4.2 for low-momentum data taking. The *unidentified beam trigger* was defined using beam detectors: those counting the beam particles (e.g. S1, S2) and those limiting the beam transverse size (e.g. V0, V1). On top of that, the signal from Z-detector with threshold adjusted to select ^{7}Be ions was added to define the *identified beam trigger*. A tag for the *central interaction trigger* was defined using an integrated analogue signal from the PSD calorimeter. Additionally, for low momenta data taking, the S4 scintillator was employed. The threshold on the S4 signal was set to an arbitrary ADC value, below those generated by ^{7}Be ions. The S4 was used to tag the beam interaction in the *central interaction trigger* and *unidentified minimum bias interaction*

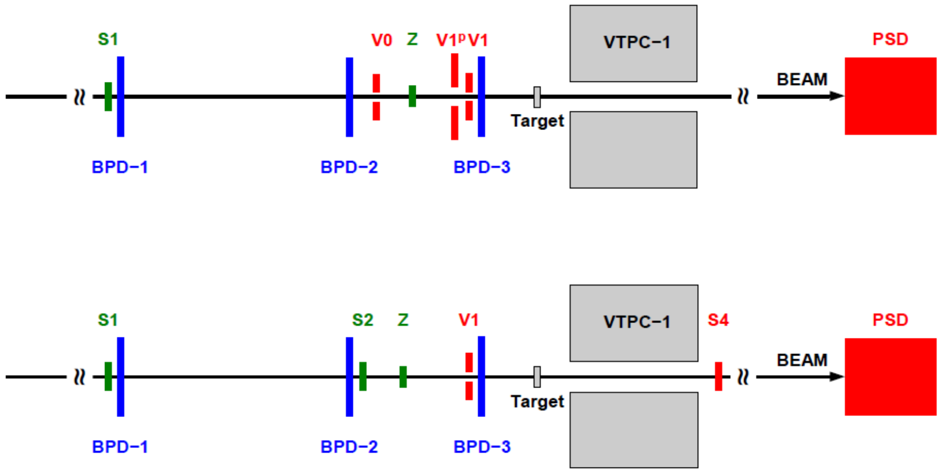

Fig. 4.1: Schematic layout of the beam and trigger detectors for a high momentum data taking (*top*) and a low momentum data taking (*bottom*). The red colour marks elements working in the veto mode, the green – in the coincidence mode.

Name	Description	Definition
T1	Ident. beam	$S1 \cdot \overline{V0} \cdot \overline{V1} \cdot \overline{V1'} \cdot Z(Be)$
T2	Ident. central interaction	$S1 \cdot \overline{V0} \cdot \overline{V1} \cdot \overline{V1'} \cdot Z(Be) \cdot \overline{PSD}$
T3	-	-
T4	Unident. beam	$S1 \cdot \overline{V0} \cdot \overline{V1} \cdot \overline{V1'}$

Tab. 4.1: The trigger definitions for a high momentum data taking campaign.

Name	Description	Definition
T1	Ident. beam	$S1 \cdot S2 \cdot \overline{V1} \cdot Z(Be)$
T2	Ident. central interaction	$S1 \cdot S2 \cdot \overline{V1} \cdot Z(Be) \cdot \overline{S4} \cdot \overline{PSD}$
T3	Unident. beam	$S1 \cdot S2 \cdot \overline{V1}$
T4	Unident. minimum bias interaction	$S1 \cdot S2 \cdot \overline{V1} \cdot \overline{S4}$

Tab. 4.2: The trigger definitions for a low momentum data taking campaign.

trigger. None minimum bias interaction trigger was used during the high momentum data taking campaign.

4.2 Beam properties

The ^{7}Be beam was a component of the secondary beam produced by $Pb82^{+}$ primary beam fragmentation on a thick (180 mm) beryllium target placed 535 m ahead of the NA61/SHINE production target. The secondary beam, delivered to the

NA61/SHINE experiment via the H2 beamline, consisted of various light fragments of the primary beam. The set of NA61/SHINE beam detectors measured the beam properties, like the beam particle arrival time, position and energy deposit, which allows to determine the beam particle charge.

The advantage of using a ^{7}Be beam for this study is that ^{7}Be has no long-lived neighbours and thus allows to make an isotopically pure beryllium beam. The closest neighbours to ^{7}Be, i.e. ^{8}Be and ^{6}Be and the nuclei with a charge difference of one and a similar mass-to-charge ratio (e.g. ^{5}Li, ^{9}B), are short-lived nuclei ($T_{1/2} < 10^{-15}$ s [71]).

4.2.1 Beam composition

The H2 beamline was used as a fragment separator, which allowed to select beam ions based on their rigidity. Fragment separator was tuned such that the fraction of the ^{7}Be-to-all ions reaching the NA61/SHINE interaction target was maximised. ^{7}Be beam intensity at the NA61/SHINE apparatus was of order of several thousands of ions per few seconds (per spill), which is only a few percent of the total beam intensity. The average beryllium content in the beam for each dataset is reported in table 4.3.

Beam momenta [GeV/c]	particles per spill	spill length [s]	content of ^{7}Be [%]
30A	150k	9	6.3
40A	130k	8	11.2
75A	170k	9	6.9
150A	150k	6	4.0

Tab. 4.3: The number of ions per spill, spill length and fraction of ^{7}Be content in the beam.

Impurities present in the beam reaching the NA61/SHINE target consist mainly of deuterons and helium ions with a smaller contribution of other stable or long-lived nuclei with mass-to-charge ratio $A/Z \leq 2$. The unidentified beam charge spectrum measured by Z-detector is presented in Fig. 4.2. The result of the ^{7}Be ions on-line selection with Z-detector (the identified beam trigger) is shown in Fig. 4.2 with the blue colour. The additional off-line analysis of the charge spectra obtained with Cherenkov light measurement by Z-detector and energy-loss measurements by other beam detectors was performed and reported in Chapter 5.

4.2.2 Beam time structure

The beam was delivered to the NA61/SHINE detector in spills, typically lasting several seconds. The incoming beam ions were counter by the S1 detector. The average number of the beam particles delivered per spill and the typical spill length for each data set are listed in table 4.3. Additionally, the S1 signals appearing within the ± 25 μs time window with respect to the triggering beam particle were registered by Multi-Hit Time Digital Converter (MHTDC). Such monitoring is used in the NA61/SHINE to reject those events, in which more than one beam particle could have interacted within the registered event (for details see Sec. 5.1.1). The examples of the beam particles time distribution registered by the MHTDC are presented in

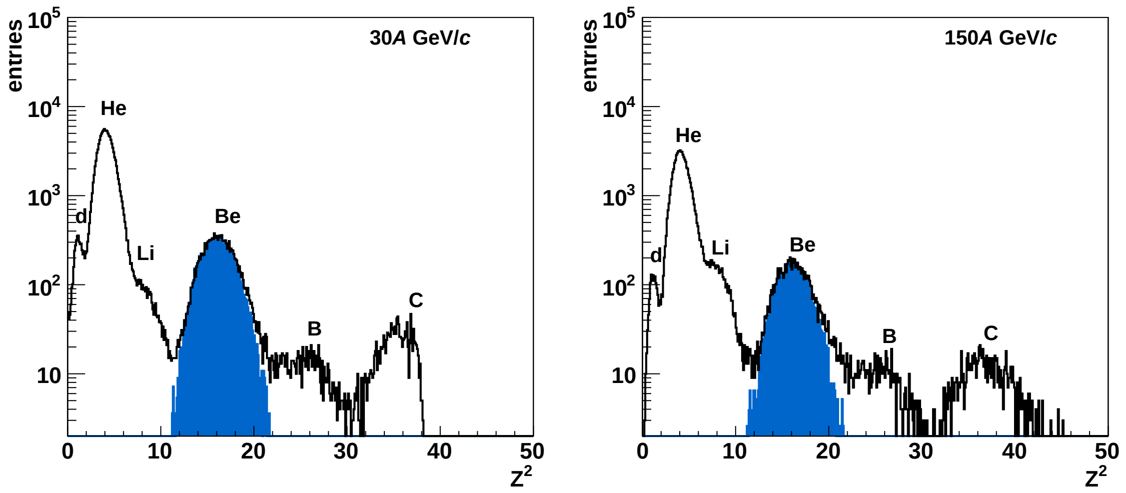

Fig. 4.2: Beam particles charge spectrum for 30*A* GeV/*c* (*left*) and 150*A* GeV/*c* (*right*) beam momentum measured by the Z-detector. The ^{7}Be content is marked in the blue colour. Contents of deuterium and carbon in these plots are underestimated due to arbitrary thresholds set on the signal from S1 counter.

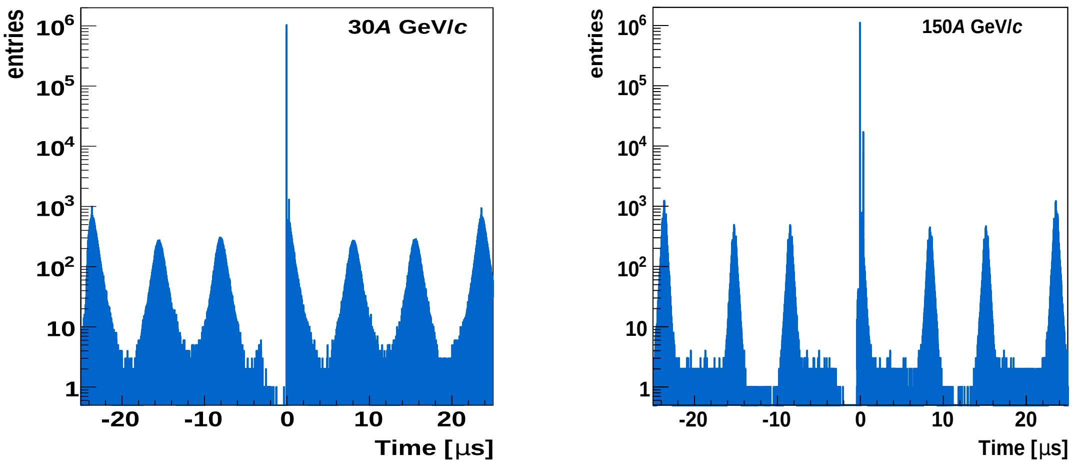

Fig. 4.3: The time distribution of the unidentified beam particles closest to the triggering one, which arrives at $t = 0$ μs, for 30*A* GeV/*c* (*left*) and 150*A* GeV/*c* (*right*) beam momentum before off-time particles rejection.

figure 4.3. In the MHTDC time distribution, the sharp spike at $t = 0$ corresponds to the triggering particle. The particles arriving before or after the trigger are called *off-time particles*. Maxima in the distribution (e.g. $\pm 9\mu s$) creating the bunch-like structure are related to the bursts of the primary lead beam injected to the SPS. The gap just before the triggering particle is an outcome of the hardware mechanism, so-called *fast clear*, which requires that for about 2 μs before the actual trigger no beam particles are registered by the S1 counter. Due to the fact that signals received from the S1 counter (after discrimination in the trigger logic) have width of about 120 ns, within the first 120 ns after the trigger the MHTCD does not register any off-time particles, which had to be considered in the data analysis.

4.2.3 Beam profile

The trajectory of the beam particles was measured by the set of the beam position detectors. The top row of figure 4.4 presents he beam particles position registered by BPD-3 set close to the target, while the bottom row – the beam divergence. Due to

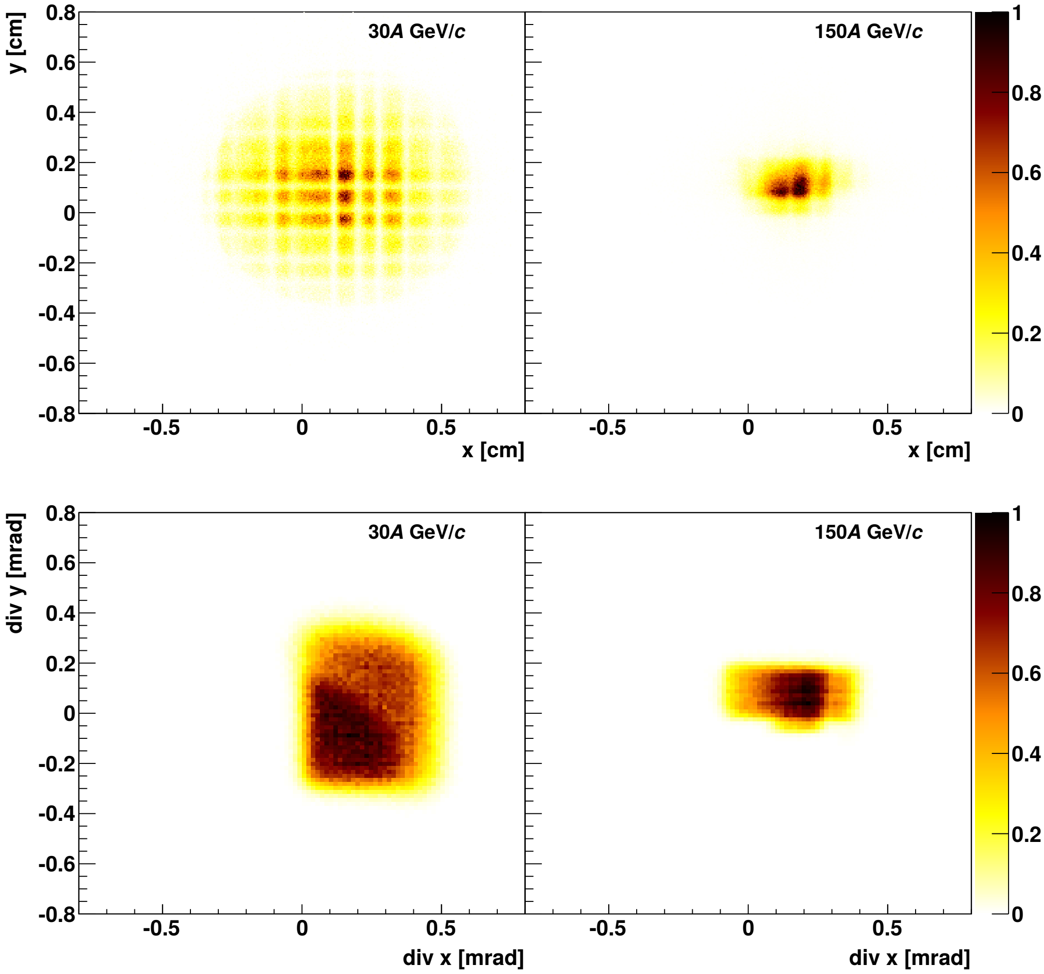

Fig. 4.4: Beam position measured by BPD3 (*top row*) for 30*A* (*left*) and 150*A* (*right*) Gev/*c*. Structures visible in the plots reflect the readout strips configuration of the BPD3. The circular outline of the distribution corresponds to shape of the hole in the V1 counter. Beam divergence measured by the set of BPDs (*bottom row*) for 30*A* (*left*) and 150*A* (*right*) Gev/*c*. Histograms were normalized to the maximum of the distributions to facilitate the comparison between their shape.

the SPS and H2 beamline characteristics, the beam profile strongly differs with beam momentum. For lower momentum (here 30*A* GeV/*c*) beam is broader and more divergent than for high momentum (150*A* GeV/*c*). In the top left panel of Fig. 4.4 the shape of the V1 counter is clearly visible, implying that the actual beam width was even larger than the width of the accepted beam fraction. Mesh-like structures visible in the top plots reflect the granularity of the BPD readout strips.

4.3 Target

The beryllium target had a cuboidal shape with dimension 25 × 25 mm in the transversal direction with respect to the beam axis and 12 mm along the beam axis. The thickness of the target was optimised to obtain high interaction probability while minimising secondary interactions rate. ^{7}Be+^{9}Be inelastic interaction probability was estimated in [65], values are shown in table 4.4.

Beam momenta [Ge/c]	Interaction probability [%]
30A	9.36 ± 0.10
40A	9.73 ± 0.39
75A	9.67 ± 0.12
150A	9.62 ± 0.33

Tab. 4.4: The inelastic interaction probability in ^{7}Be+^{9}Be collisions [65].

The target consisted of high-purity beryllium, which was verified with WDXRF method in Jan Kochanowski University in Kielce, Poland. ^{9}Be content in the target was in the order of 99.62%. Major contribution to target impurity comes from ^{56}Fe (0.12%), ^{16}O (0.09%), ^{24}Mg (0.04%), ^{27}Al (0.04%), ^{55}Mn (0.03%) and ^{48}Ti (0.02%). Low abundance of heavy elements in the target was crucial for minimising the probability of the "non-beryllium interactions".

Data were registered for two target configurations – *target inserted* (target IN) and *target removed* (target OUT). The majority of the data, approximately 90% of the total statistics, was collected in target IN configuration. Target OUT data, about 10% of the total statistics, were registered in order to correct the results for beam particles interaction with non-target material (e.g. Mylar windows or scintillators). Table 4.5 presents the total number of events registered with target inserted and

Beam momenta [Ge/c]	Target IN	Target OUT
30A	3894k	364k
40A	2858k	288k
75A	3936k	421k
150A	2828k	290k

Tab. 4.5: The number of events collected with target inserted and target removed configuration.

target removed configuration. For analysis purposes only part of the total statistics was used because of events quality selection (see Chapter 5).

Chapter 5

Analysis

Spectra of K^+, K^-, π^+, π^-, p and $\overline{p}$, produced in the central ^{7}Be+^{9}Be collisions at beam momenta of 30*A*, 40*A*, 75*A* and 150*A* GeV/*c*, were obtained with the so-called *tof-dE/dx* identification method based on measurements of energy-loss per length unit (dE/dx) via TPCs and a time-of-flight (tof) with ToF walls.

The results presented in chapter 6 stand for the mean number of identified particles produced per single event in a given bin of a two-dimensional phase-space in the rapidity y and the transverse momentum p_T. Examples of the acceptance in $y - p_T$ phase-space for various particles are presented in Fig. 5.1 with the binning scheme. The histogram binning was optimised to cover large area of the phase-space and minimises the statistical uncertainties.

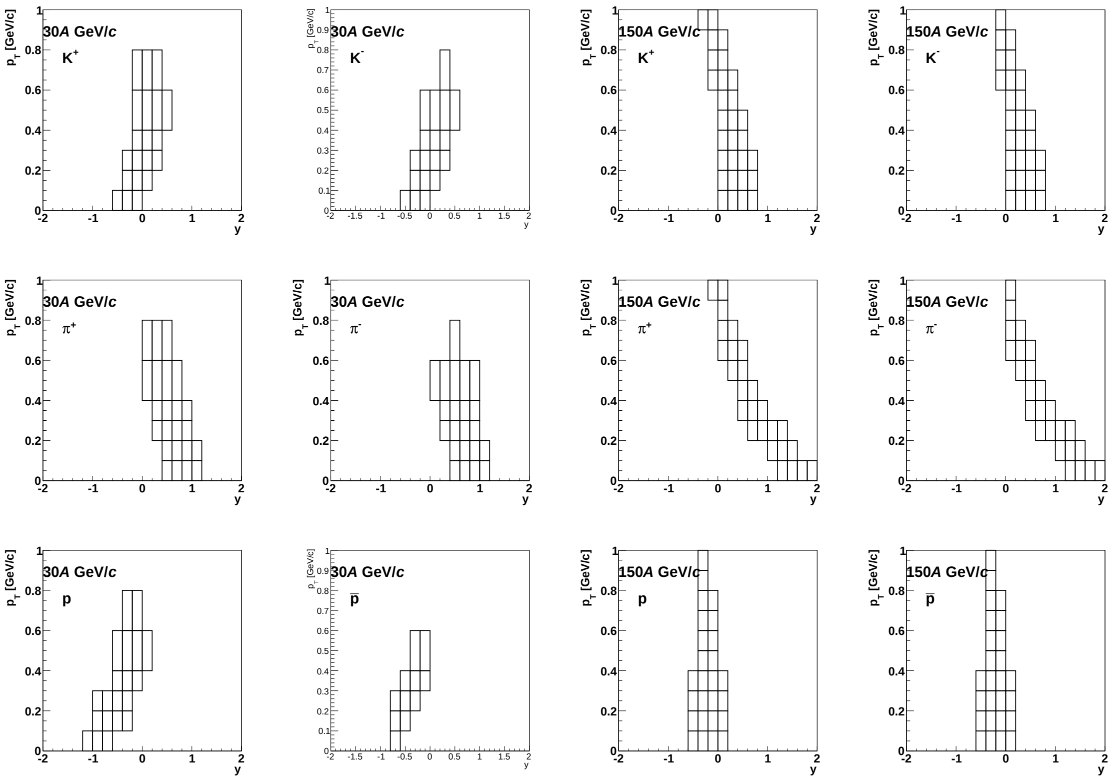

Fig. 5.1: Schematic acceptance in $y - p_T$ phase-space for K^+, K^-, π^+, π^-, p and $\overline{p}$ for 30*A* GeV/*c* (*two left columns*) and 150*A* GeV/*c* (*two right columns*) momentum.

The acceptances of the particle spectra are limited due to the geometry of the devices used in data registration and slightly varies with the collision energy. By that reasons, sparsely populated bins occurs at the edges of the spectra. Bin population was studied with a MC simulation taking into account geometrical acceptance of the analysis method. The factor c_{acc} derived for each bin as the:

$$c_{acc} = \frac{number\ of\ particles\ accepted\ by\ ToF\ geometry\ in\ y - p_{\mathrm{T}}\ bin}{total\ number\ of\ particles\ in\ y - p_{\mathrm{T}}\ bin} \tag{5.1}$$

was used to determine the final acceptance of the method. Bins with $c_{acc} < 50\%$ were not considered in further analysis.

The procedure of data analysis applied in this work consists of the following steps:

(i) event (Sec. 5.1) and track (Sec. 5.2) selection,
(ii) particles identification with *tof-dE/dx* method (Sec. 5.3) and calculation of the particle spectra,
(iii) estimation and application of the corrections to the particle spectra (Sec. 5.4),
(iv) estimation of the statistical and systematic uncertainties (Sec. 5.5).

The results in this work were obtained using SHINE (version 1, revisions from 5 to 8) [72] and ROOT 5.34 [73] frameworks.

5.1 Event selection

The analysed subsample of the collected statistics contains of T2 trigger events only, in other words – central collisions of ^{7}Be beam. There are two kinds of event selection criteria - biasing ones and non-biasing ones. The first ones concern mainly capabilities of the reconstruction software, off-target interactions and also detector performance, whereas the other ones are mainly related to the beam properties. Selection criteria were applied sequentially according to the enumeration given in subsections 5.1.1 and 5.1.2.

5.1.1 Non-biasing event cuts

Non-biasing cuts are the first ones applied in the analysis:

(i) beam position,
(ii) beam particle identification,
(iii) beam off-time (counted as a non-biasing due to the negligibly small impact of the off-time particles on this analysis).

These cuts were used to ensure that selected events subsample contain information of a single ^{7}Be ion interaction and that the trajectory of that ion points to the target.

Beam position

All accepted events must have well defined beam trajectory, which is measured by the set of three BPDs. Correct signals in both X and Y planes of the BPD-3 and at least one X and one Y planes measured by any of BPD-1 and BPD-2 were required in the beam-position cut. Figure 5.2 presents examples of the beam particles position

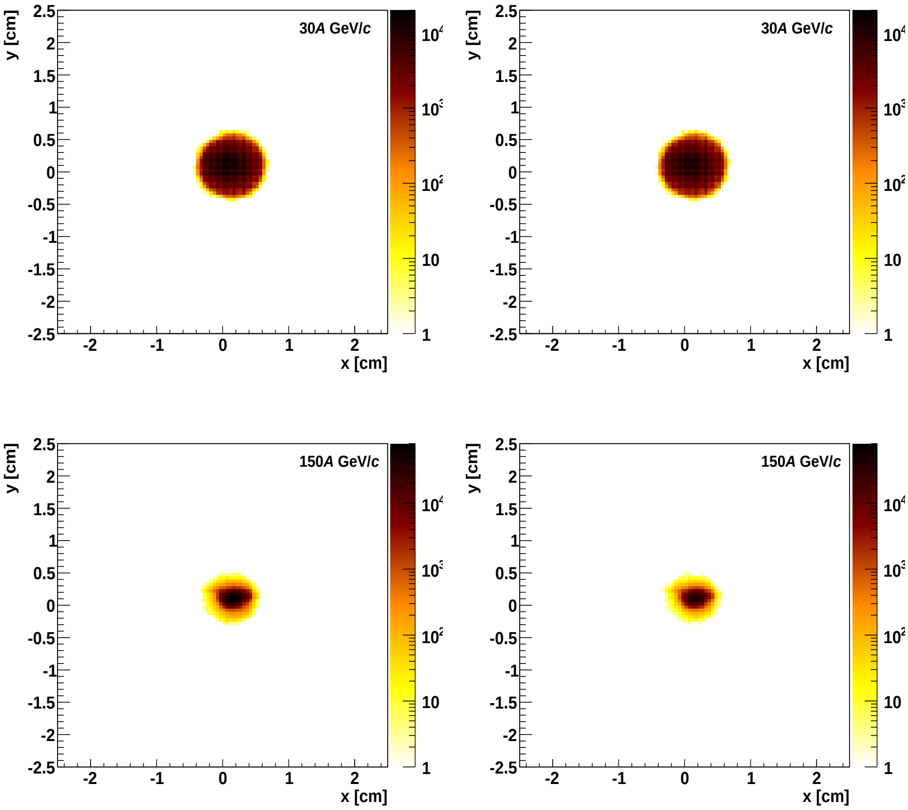

Fig. 5.2: Examples of the beam particles position distribution measured by BPD-3 (closest one to the target) for 30*A* (*top*) 150*A* (*bottom*) GeV/*c* before (*left*) and after (*right*) beam position cut.

distribution registered by BPD-3 for the lowest and highest beam momentum. The beam quality (focusing) dependence on the momentum can be observed (the width of the beam becomes narrower with the beam momentum). For the lowest beam momentum (top panel of Fig. 5.2) the circular shape of the V1 counter hole is visible. Since the core of the beam was efficiently selected by the trigger counters (e.g. V1, V0) and those beam particles accepted by the trigger had trajectories pointing to the target, the improvement of the beam position distribution after the *beam position cut* is not clearly visible in figure 5.2.

Beam composition

The on-line trigger system was set to select ^{7}Be ions from the secondary beam using the Z-detector. After on-line selection, the beam still contained up to 0.5% of ions other than ^{7}Be. Event triggered with non-beryllium beam particles were removed in off-line analysis based on charge spectra from S1, S2 and BPD3. Examples of correlation of charge spectra obtained with various beam detectors are presented in figure 5.3. The black lines show the contours of the graphical cuts called the *beam composition cuts*. With such selection, collisions of the ^{7}Be ions, which signals occur inside the contours, are accepted, while those of the beam impurities (e.g. d, He, Li, B, C) are removed from further analysis.

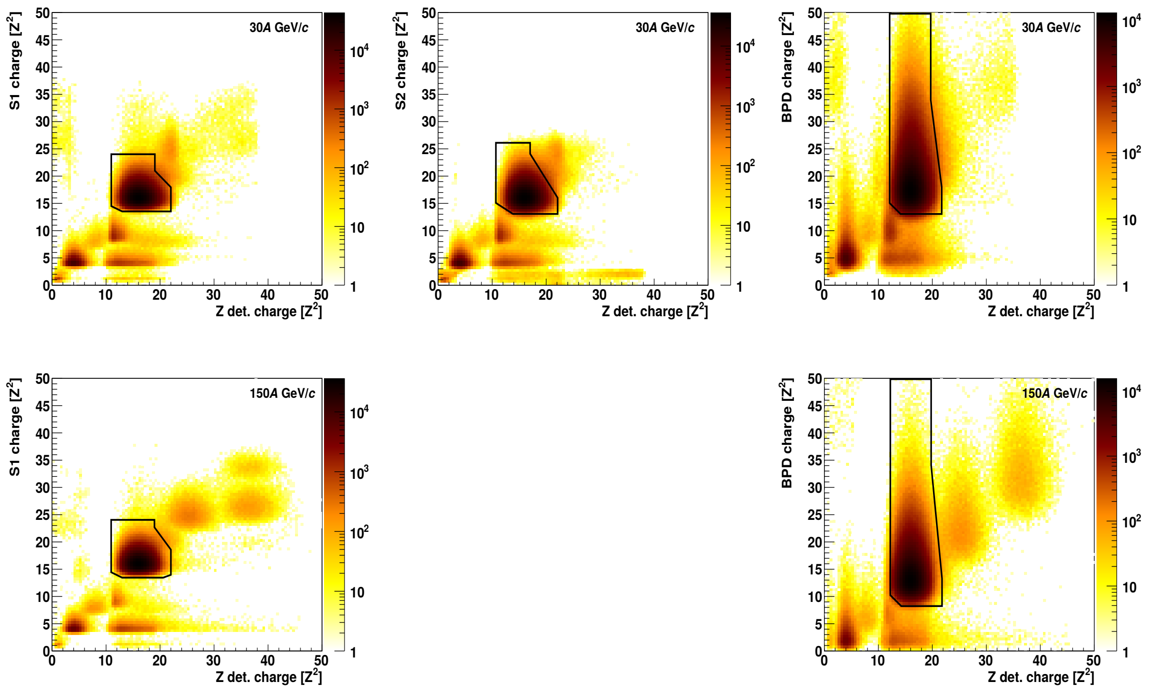

Fig. 5.3: Examples of correlations of charge measured by various beam detectors in the beryllium beam at 30*A* (*top*) and 150*A* GeV/*c* (*bottom*): S1 vs Z (*left*), S2 vs Z (*middle*) and BPD vs Z (*right*). The S2 counter was used only for ^{7}Be+^{9}Be collisions at 30*A* GeV/*c*. Limits of the cuts are marked with black line.

Beam off-time

The *beam off-time cut* is in general necessary to limit the possibility that more than one beam particle interacts within one registered event. Rejection of the off-time beam particles in ^{7}Be+^{9}Be data sets is briefly described in this subsection and in details in Ref. [65].

In the first step the off-time particles rejection involved setting limits on MHTDC measurement. The measured time structure along with off-time rejection are presented in figure 5.4. The *time structure cut* rejects events, in which any off-time particle appears within a ±4.5 μs window adjacent to the trigger and all events, in which off-time particle interacted within a ±25 μs window around the trigger.

Since it was impossible to register particles coming within ±120 ns around the trigger, an additional cut based on the charge measurement by Z-detector was developed. Z-detector signal was split in two, both were independently digitised, but one of them was delayed. The delay was set so, that both, Z and Z-delayed, signals associated with the trigger were registered within the Z-detector ADC gate. In the case of off-time particles, the Z-delayed signal was partially beyond the gate. In the left panel of figure 5.5 a charge correlation of both signals from the Z counter is presented. Z-detector signals visible below the diagonal are caused by off-time particles. The right panel of figure 5.5 shows the difference of charge collected in both signals from Z-detector. Only events with the appropriate charge difference were analysed. In the case of 30*A* and 40*A* GeV/*c*, the cut accepts the events with the difference from -0.7 to 0.7, for 75*A* GeV/*c* – from -0.4 to 0.6 and for 150*A* GeV/*c*, from -0.4 to 0.7. Since beam characteristic and Z-detector timing varied with the

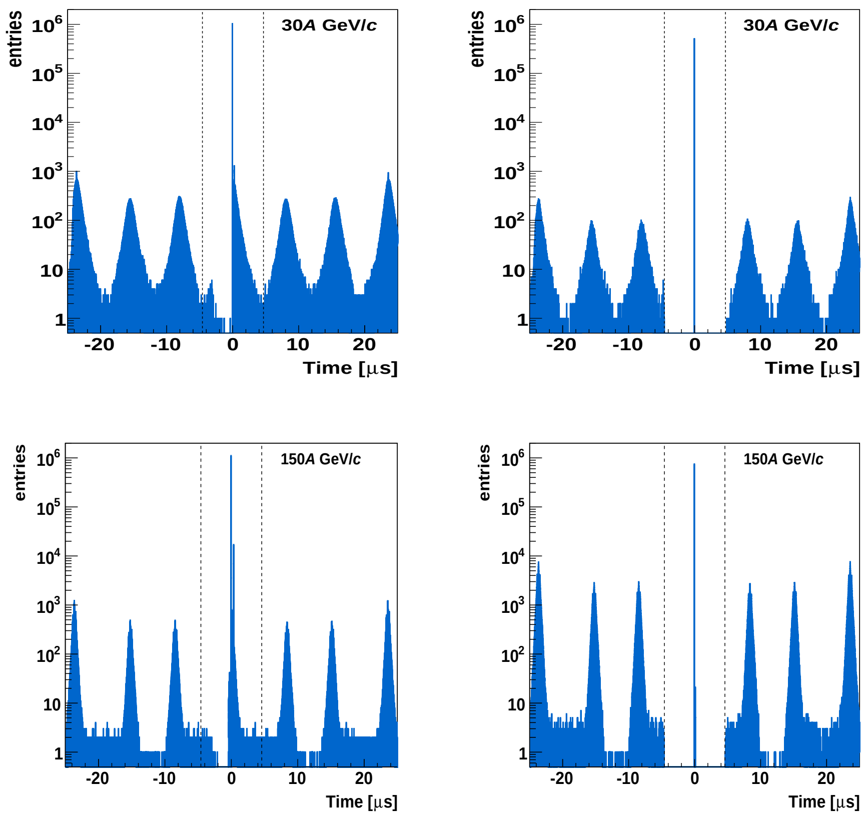

Fig. 5.4: Examples of beam time distribution for 30*A* GeV/*c* (*top row*) and 150*A* GeV/*c* (*bottom row*) beam momentum before (*left*) and after (*rught*) cuts. Triggering particle arrives at $t = 0\ \ \mu s$. Dashed lines symbolise cut limits ($\pm 4.5\ \ \mu s$).

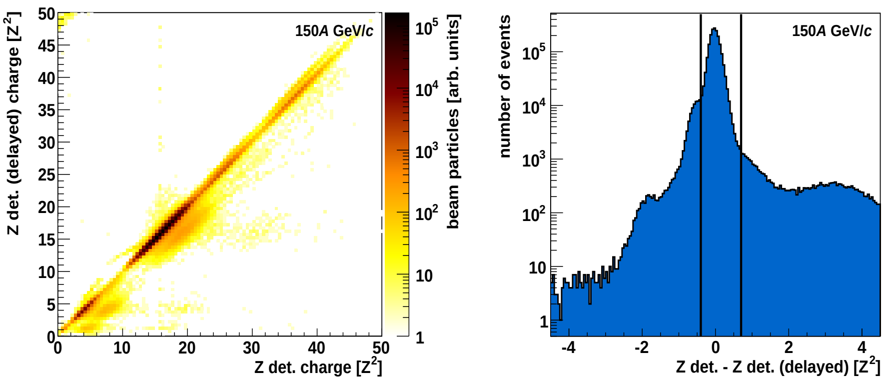

Fig. 5.5: Example of correlation of both signals from the Z-detector (*left*) and their difference (*right*) for ^{7}Be+^{9}Be collision at 150*A* GeV/*c*. The limits on the charge difference are marked with the black lines.

beam momenta, selection limits on Z-detector signals had to be adjusted accordingly. This cut was applied after beam position, beam composition cuts and also simple cut on the beam time structure.

Even though, the number of events with off-time beam particles is considerable (several percent of total statistics), the impact of the off-time particles on the particle identification via *tof-dEdx* analysis method is negligibly small. Important advantage of the *tof-dEdx* analysis method is the fact that hadrons produced in off-time interaction do not fulfill the quality requirements described in Sec. 5.2 (e.g. correctly reconstructed mass or track originating in the primary vertex). The only off-time beam particles able to bias the results obtained with this method have to interact with the target within narrow (< 5 ns) time window after the triggering beam particle. The time window is determined by ToF TDC range. The maximal possible bias caused by the beam off-time particles in *tof-dEdx* analysis is equal to their interaction probability in the 5 ns long time window. It was estimated using a subsample of the T2 trigger events passing primary vertex quality cuts only (described in sec. 5.1.2), without using any of the beam off-time selection criteria. The bias estimation was based on a simple exponential fit and extrapolation from the measured beam time structure (see figure 5.6) and inelastic interaction probability (see table 4.4). The

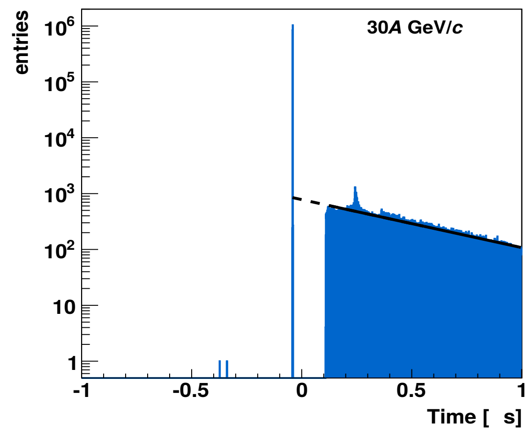

Fig. 5.6: A fit (*solid line*) and an extrapolation (*dashed line*) of the off-time particle background in the first 120 ns after the triggering particle for ^{7}Be+^{9}Be collisions at 30*A* GeV/*c*.

extrapolation results in a rough estimation of the number of off-time particles in the 5 ns long time window, $N_{off-time}$, per number of registered events, N_{all}. The values are listed in table 5.1. The ratio of off-time particles and total number of events was

p_{beam} [GeV/c]	$N_{off-time}$	N_{all}	$\frac{N_{off-time}}{N_{all}}$	Off-time particles interaction probability [%]
30*A*	4206 ± 17	1990174	0.0021	0.020 ± 0.002
40*A*	1692 ± 17	1144833	0.0015	0.014 ± 0.006
75*A*	4416 ± 18	1479499	0.0030	0.029 ± 0.006
150*A*	10964 ± 33	1120567	0.0098	0.094 ± 0.031

Tab. 5.1: Possible bias caused by the beam off-time particles in 5 *ns* long time window for ^{7}Be+^{9}Be collisions at various beam momenta.

multiplied by inelastic interaction probability (see table 4.4), which allowed for an estimate of the off-time particles interaction probability in the 5 ns long time window. Uncertainties of the bias estimate are propagated from uncertainties of the fit and the inelastic interaction probability calculation.

Even though the interactions of the off-time particles would have caused negligible bias in the particle identification method described in this thesis, below 1‰, the beam off-time cuts were used to ensure cuts consistency between various analysis methods for ^{7}Be+^{9}Be data in the NA61/SHINE experiment.

5.1.2 Biasing event cuts

The biasing cuts concern background interactions, capabilities of the reconstruction software and performance of the PSD calorimeter used for the centrality determination. Since, they can affect the results, a careful study on the possible bias was performed and is presented in section 5.5 concerning the systematic uncertainties. The biasing cuts considered are:

(iv) existence of the primary vertex and its fit quality,
(v) primary vertex position along the beamline,
(vi) centrality selection.

Primary vertex cuts

This thesis focuses on the yields of particles produced only in primary interactions, therefore selection criteria related to the primary vertex of the interaction were developed.

The first primary vertex cut requires that the primary vertex of the interaction was assigned in the reconstruction procedure and the primary particles momentum vector fit at the interaction vertex has converged.

The second primary vertex cut requires that the position of the reconstructed primary vertex is situated in the target area. Events, in which the reconstructed primary vertex placed within ±15 cm range adjacent to the actual target position along the beamline, are accepted for the further analysis. The limits on the primary vertex position are marked with solid vertical black lines in Fig. 5.7.

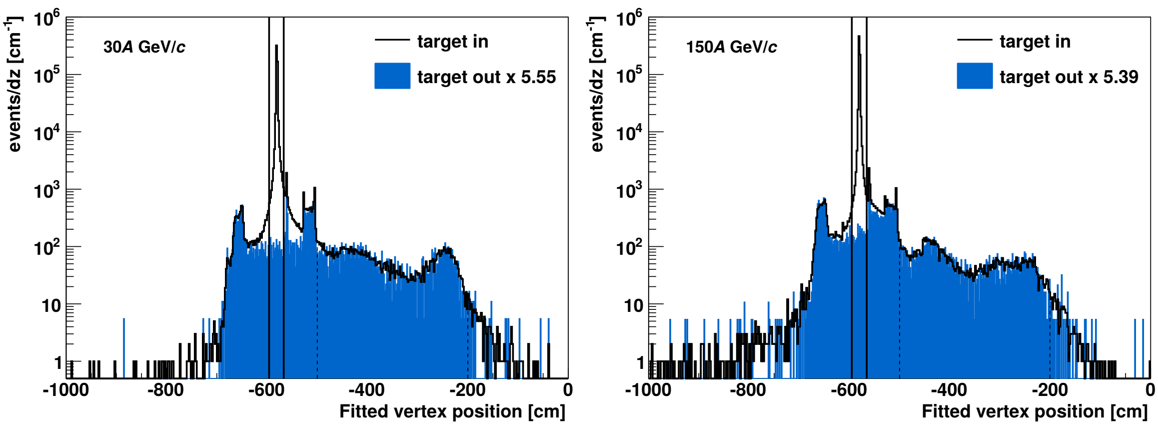

Fig. 5.7: Primary vertex position along the beamline for 30*A* GeV/*c* (*left*) and 150*A* GeV/*c* (*right*) momentum. The black curve represents target-inserted, and the blue area symbolises target-removed events. The target removed event are scaled up with a normalisation factor established in the region from -500 cm to -200cm, marked with dashed lines.

The black curve represents the distribution of the primary vertex position for the target-inserted events, and the blue area – for the target-removed events. The target removed distribution is scaled up with a normalisation factor established in the region from -500 cm to -200cm, marked with dashed lines.

Centrality selection

The ^{7}Be+^{9}Be energy scan was the first data taking campaign with PSD installed in the NA61/SHINE detection system [54]. The calorimeter measured the energy deposit of projectile spectators (nuclear fragments, protons and neutrons) as well as hadrons produced in the collision, which reach the calorimeter. At the stage of data taking, the integrated signal from the calorimeter roughly estimating the collision centrality was included in the trigger logic (see Sec. 4.1). Off-line analysis of the measured energy deposit in the calorimeter was used for more precise collision-centrality determination [65,74].

The first step of the centrality analysis required choosing the set of the PSD modules to be used for centrality determination. This selection was motivated by the fact that the energy deposit in some of the calorimeter modules can be dominated not by the collision spectators but by the particles produced in the collision. The set of PSD modules selected for centrality determination in the case of low beam momenta data sets involved the full detector, while in the case of higher beam momenta data sets – only 16 small, central modules and their 12 neighbouring large modules were used, see Fig. 5.8. The PSD module selection was based on the minimum bias MC

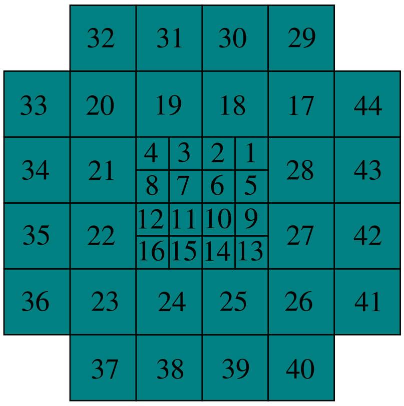

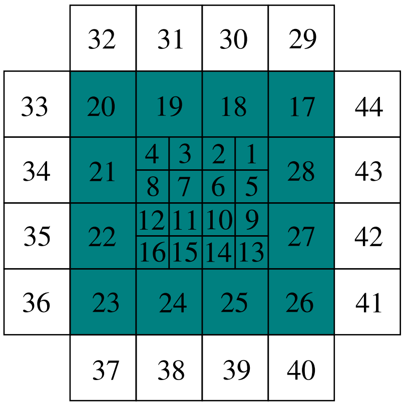

Fig. 5.8: The two different PSD module selections used for the centrality determination in ^{7}Be+^{9}Be collisions at 30A GeV/c (*left*) and 40A, 75A and 150A GeV/c (*right*).

simulation. Trajectories of the collision spectators were simulated and used to point to specific PSD modules. Modules indicated by the trajectories of the spectators were selected for the centrality determination. The simulation was verified studying the correlation between the energy deposit measured by a given PSD module and the multiplicity of particles registered in the TPC. An example of correlations between these two quantities is presented in figure 5.9 for an internal (*left*) and an external (*right*) module of the calorimeter. The negative slope of the correlation of the energy deposit visible in the left panel of figure 5.9 denotes that for the internal module the energy deposit is dominated by the projectile spectators, whereas the correlation in the right panel of figure 5.9 suggests considerable contribution of particles produced in the collision.

The actual centrality determination required a dedicated analysis based on minimum bias data (T1 trigger data subset) [65,74]. From this minimum bias data set, the subset of events in which an interaction had happened, was selected. This subset was sorted with respect to the energy deposited in PSD. Examples of energy deposit distribution normalised to the number of events are presented in figure

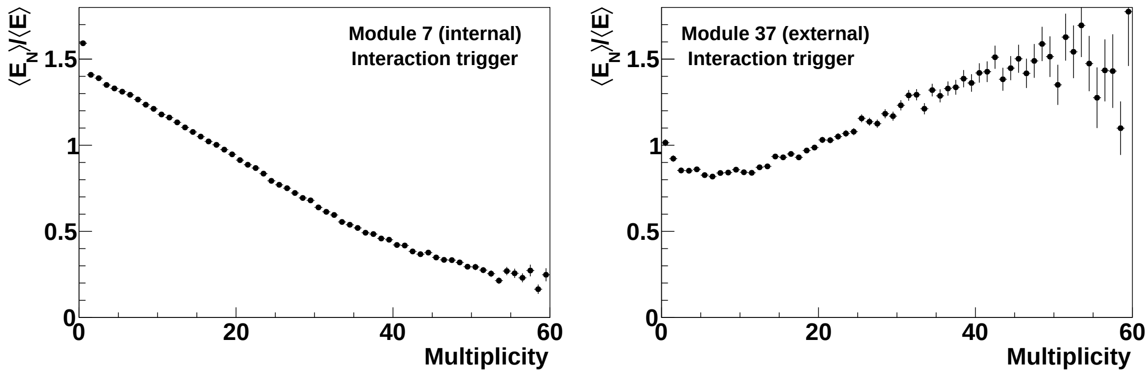

Fig. 5.9: Mean energy deposit measured by module 7 (internal, see numbering scheme in Fig. 5.8) (*left*) and module 37 (external, see numbering scheme in Fig. 5.8) (*right*) as a function of particle multiplicity for ^{7}Be+^{9}Be collisions at 150*A* GeV/*c*. The mean energy deposit associated with given number of particles registered in TPCs was normalised to the mean energy deposited in the particular module.

5.10 (*top row*). Subsequently, the collision centrality was estimated as the percent of events of a given fraction of E_F taking into account interaction cross-section and correction for target OUT interactions. Examples of the cumulative distribution functions of E_F normalised to the total probability of inelastic interactions along with E_F classes (5%, 10%, 15% and 20%) are presented in figure 5.10 (*bottom row*).

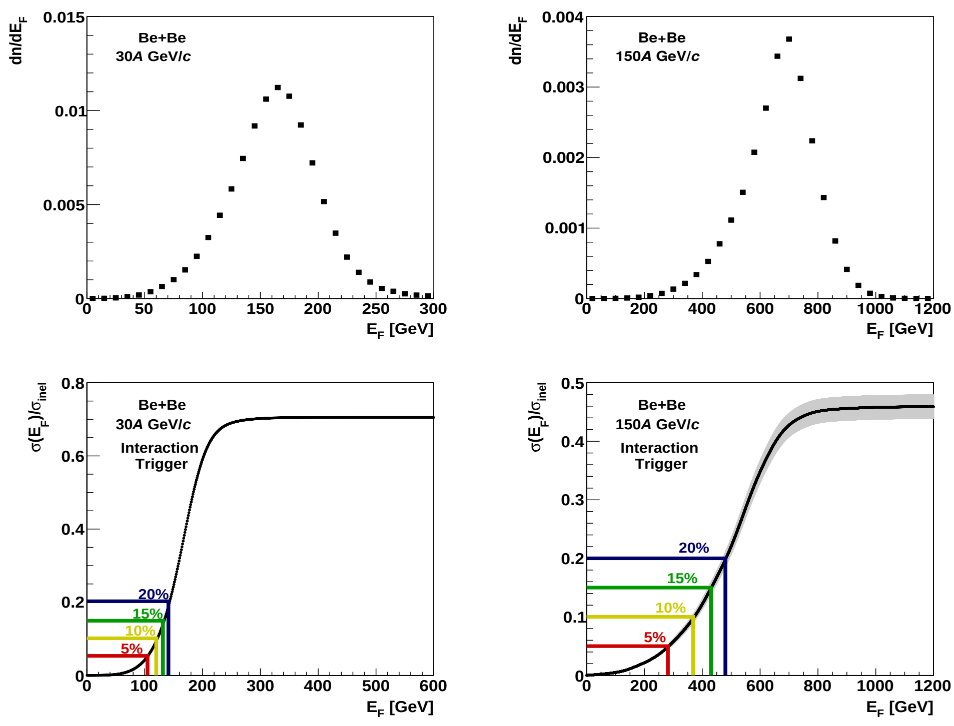

Fig. 5.10: Examples of the forward energy deposit distributions (*top row*) in PSD for 30*A* GeV/*c* (*left*) and 150*A* GeV/*c* (*right*) momentum along with cumulative distribution functions of E_F normalised to total probability of inelastic interaction (*bottom row*). Colour lines in the bottom plots mark forward energy classes (centrality classes).

For example, 5% of the most central events assumes $E_F < 282$ GeV measured by PSD in ^{7}Be+^{9}Be collisions at 150A GeV/c. Table 5.2 contains the number of events assigned to defined forward-energy classes for the analysed data sets. The

p_{beam} [GeV/c]	Forward energy class (centrality) 0–5%	5%–10%	10%–15%	15%–20%
30A	37658	35778	36326	38255
40A	98411	99306	99388	99597
75A	99685	100079	99922	99832
150A	80738	81667	81560	81642

Tab. 5.2: Number of events in a given forward energy class for analysed data sets. Statistics presented after all event-selection criteria.

results presented in this thesis are obtained for a broad forward energy class (0-20%), summarisisng all defined centrality intervals.

Event cuts presented in this section were applied to target-inserted and target-removed data. The same biasing cuts were applied also to reconstructed MC events. Table 5.3 contains the statistics of the events before and after consecutive event cuts in absolute numbers as well as the percentage of total statistics and the percentage with respect to the previous cut. Note that the number of target OUT events was scaled by the normalisation factor (see fig. 5.7). The selection criteria reject the majority of the target OUT events. For this reason, the possible bias caused by the off-target interactions in final results was neglected.

5.2 Track selection

For each event selected, the particle tracks are examined. Among all registered particles, those which were produced in the primary interaction beginning at the primary vertex and fulfilling the selection criteria described in this section, are selected for further analysis.

Track selection criteria can be subdivided into two classes. Firstly, so-called *standard track cuts* are applied. Those selection criteria are common for all types of analysis in the NA61/SHINE experiment performed with use of the ^{7}Be+^{9}Be data. The *tof-dE/dx* analysis method of particle identification required dedicated selection criteria concerning ToF performance. Those are further called the *non-standard track cuts*.

5.2.1 Standard track cuts

The standard selection criteria are following:

(i) impact point,
(ii) total number of clusters,
(iii) number of VTPCs and GapTPC clusters,
(iv) track topology.

cut	Target inserted			Target removed			EPOS		
				$p_{beam} = 30A$ GeV/c					
–	3 814 k	(100.0)	–	2 015 k	(100.0)	–	15.0 M	(100.0)	–
(i)	2 793 k	(73.2)	[73.2]	1 237 k	(61.4)	[61.4]	–	–	–
(ii)	2 431 k	(63.7)	[87.0]	949 k	(47.1)	[76.7]	–	–	–
(iii)	2 053 k	(53.8)	[84.5]	788 k	(39.1)	[83.0]	–	–	–
(iv)	583 k	(15.3)	[28.4]	27 k	(1.4)	[3.4]	14.6 M	(97.3)	[97.3]
(v)	550 k	(14.4)	[94.3]	1.5 k	(0.07)	[5.6]	14.3 M	(95.2)	[97.9]
(vi)	148 k	(3.9)	[26.9]	0.3 k	(0.02)	[21.1]	2.9 M	(19.3)	[20.3]
				$p_{beam} = 40A$ GeV/c					
–	2 919 k	(100.0)	–	1 712 k	(100.0)	–	19.4 M	(100.0)	–
(i)	2 428 k	(83.2)	[83.2]	1 361 k	(79.5)	[79.5]	–	–	–
(ii)	2 239 k	(76.7)	[92.2]	1 231 k	(71.9)	[90.4]	–	–	–
(iii)	1 890 k	(64.7)	[84.4]	1 026 k	(59.9)	[83.3]	–	–	–
(iv)	859 k	(29.4)	[45.4]	42 k	(2.5)	[4.1]	18.6 M	(95.9)	[95.9)
(v)	810 k	(27.7)	[94.3]	2.6 k	(0.15)	[6.2]	18.2 M	(93.8)	[97.9]
(vi)	397 k	(13.6)	[49.0]	1.0 k	(0.06)	[38.2]	3.6 M	(18.6)	[19.8]
				$p_{beam} = 75A$ GeV/c					
–	3 112 k	(100.0)	–	2 234 k	(100.0)	–	14.9 M	(100.0)	–
(i)	2 671 k	(85.8)	[85.8]	1 541 k	(69.0)	[69.0]	–	–	–
(ii)	2 492 k	(80.1)	[93.3]	1 415 k	(63.3)	[91.8]	–	–	–
(iii)	2 231 k	(71.7)	[89.5]	1 255 k	(56.2)	[88.7]	–	–	–
(iv)	975 k	(31.3)	[43.7]	45 k	(2.0)	[3.6]	14.5 M	(97.3)	[97.3]
(v)	923 k	(29.7)	[94.7]	3.2 k	(0.14)	[7.1]	14.2 M	(95.3)	[97.7]
(vi)	400 k	(12.9)	[43.3]	1.1 k	(0.05)	[34.4]	3.1 M	(20.8)	[21.8]
				$p_{beam} = 150A$ GeV/c					
–	2 662 k	(100.0)	–	1 445 k	(100.0)	–	19.9 M	(100.0)	–
(i)	2 025 k	(76.1)	[76.1]	1 035 k	(71.6)	[71.6]	–	–	–
(ii)	1 750 k	(65.7)	[86.4]	884 k	(61.2)	[85.4]	–	–	–
(iii)	1 531 k	(57.5)	[87.5]	765 k	(52.9)	[86.5]	–	–	–
(iv)	794 k	(29.8)	[51.9]	43 k	(3.0)	[5.6]	19.3 M	(97.0)	[97.0]
(v)	750 k	(28.2)	[94.5]	2.6 k	(0.18)	[6.0]	18.9 M	(95.0)	[97.9]
(vi)	326 k	(12.0)	[43.5]	0.8 k	(0.06)	[32.5]	5.4 M	(27.1)	[28.6]

Tab. 5.3: Number of events selected for analysis after consecutive selection criteria for target inserted, removed and EPOS MC. Numbers are given in thousands (k = 10^3) or millions (M = 10^6). The numbers in round brackets give the percentage of total statistics, and numbers in the square brackets give the percentage with respect to the previous cut.

Impact point

The impact point selection criterion applies to the distance between the track extrapolated to the transverse plane at $z = z_{target}$ and the reconstructed position of the interaction vertex. The distance was required to be smaller than 4 cm along the horizontal axis (b_x) and smaller than 2 cm along the vertical (b_y) axis. Examples of b_x amd b_y distributions are shown in Fig. 5.11

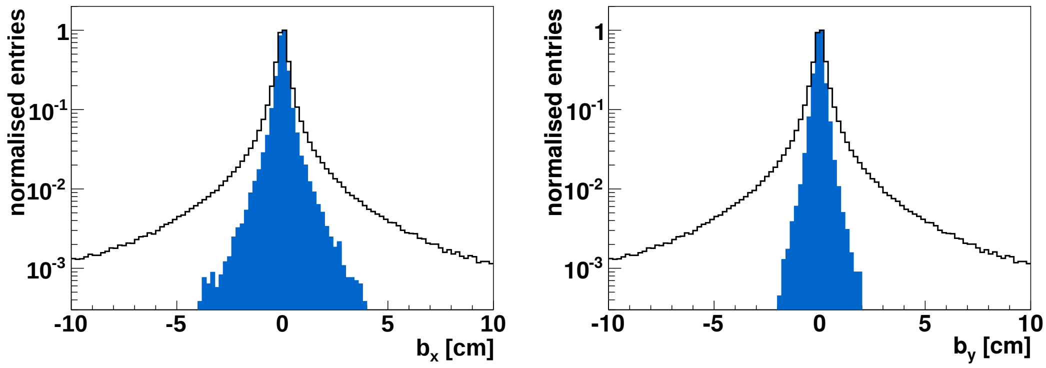

Fig. 5.11: Examples of a b_x (*left*) and b_y (*right*) distribution for particles produced in ^{7}Be+^{9}Be collisions at 30*A* GeV/*c* before (*black line*) and after (*blue area*) applying the impact point selection criterion. Histograms are normalised to their maxima.

Total number of clusters and number of VTPCs and GapTPC clusters

The threshold on the total number of clusters measured in the NA61/SHINE TPCs was set to 30 clusters. It concerns clusters registered in all TPC detectors and ensures that the mean value of particle energy loss per path unit is well reconstructed.

The requirement on the number of VTPCs and GapTPC clusters was set to minimum 15 clusters. This cut ensures that the momentum of the particle is well reconstructed since VTPCs and GapTPC are placed inside superconducting magnets.

Track topology

The reconstructed tracks are classified as *right side tracks* (RST) and *wrong side tracks* (WST). Particles with the RST topology are selected for the analysis.

For the NA61/SHINE magnetic field polarisation the RST satisfy equation 5.2:

$$q \cdot p_x > 0\,, \tag{5.2}$$

where q is the electric charge, and p_x is the x component of the momentum vector, whereas for the WST the product of equation 5.2 is negative. An example of WST is shown in the Fig. 5.12, marked with a blue arrow. In this figure the wrong side track is positively charged. It has a negative initial p_x, but the magnetic field bends it towards positive x.

As explained in sec. 2.3.2, NA61/SHINE TPC readout pads are tilted with respect to the beamline to minimise the average angle between RST and a given pad in the horizontal plane ($x - z$). This optimisation reduces width of the measured clusters the on the padrows, reduces the impact of the ionisation fluctuations along the particle trajectory and ensures constant dE/dx sensitivity.

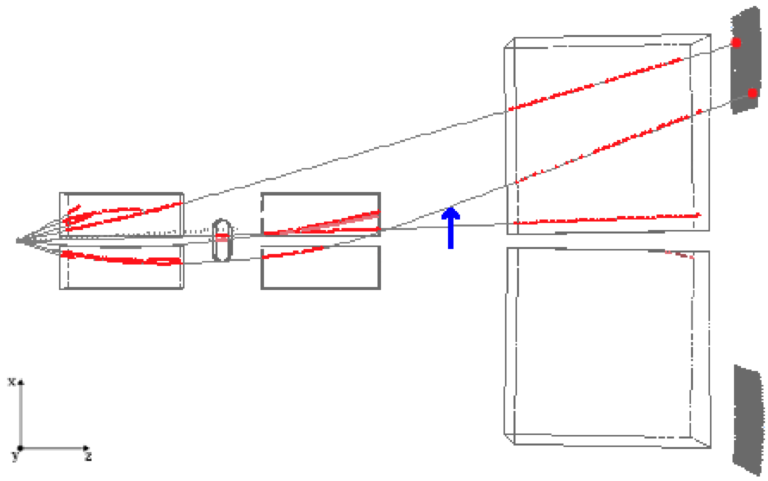

Fig. 5.12: Example of a wrong side track, marked with the blue arrow.

5.2.2 Non-standard track cuts

The non-standard cuts, developed for the *tof-dE/dx* analysis of the ^{7}Be+^{9}Be data are:

(i) the last point in the TPCs,
(ii) track in ToF acceptance,
(iii) ToF TDC and QDC signals,
(iv) pixels efficiency.

Last point in the TPCs

Trajectories of the particles registered in the TPCs are extrapolated towards the ToF detectors. The extrapolation is provided from a straight line fit of the last 10 clusters measured in MTPCs. The last cluster of the particle track is required to be measured by the most downstream sectors of the MTPC-L or MTPC-R, at $z > 650$ cm in the NA61/SHINE coordinate system (see Appendix A). This cut ensures an efficient tracking between MTPCs and ToF detectors. The same extrapolation procedure was used in both – experimental data and MC simulation.

Track in ToF acceptance

In the case that particle track extrapolated to the ToF Walls crosses the geometrical position of any of the ToF scintillator, it was assumed to be so-called *potential hits* in a given ToF tile. For each potential hit, the index number of the indicated ToF pixel was extracted. Then, it was check if the signals form a ToF pixel with this particular index number are stored in a given event, in other words if the potential hit matches the real hit in the corresponding ToF tile. Examples of correlation between potential and real hits in ToF-L/R are presented in figure 5.13. For each scintillator of ToF-R, the potential hits match the real hits, which is presented with a clear diagonal correlation in the right panel of Fig.5.13. In the case of 14 scintillators of ToF-L, potential hits do not match the real hits, which is exhibited by local maxima beyond the main diagonal correlation in the left panel of Fig.5.13. Those ToF-L pixel, for which potential-real hits matching is unclear, are excluded from the ToF-L

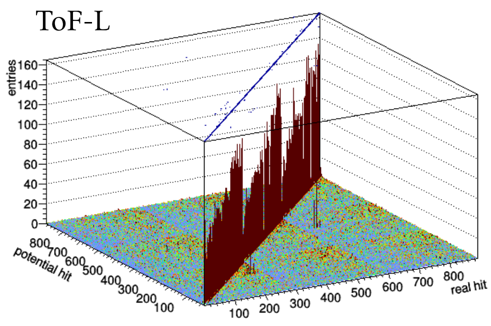

Fig. 5.13: Correlation between potential and real hits in ToF-L (*left*) and ToF-R (*right*) for ^{7}Be+^{9}Be collisions at 40A GeV/c.

acceptance (in both, experimental data analysis and MC simulation). Therefore, the particles with tracks pointing to those 14 scintillators of ToF-L, are not considered in the further analysis.

ToF TDC and QDC signals

The ToF detector provided two quantities, time and charge, through TDC and QDC signals, respectively. The *time-of-flight* based particle identification method required a systematic study of signal quality in each ToF tile and for each data set separately. In the first step, it was checked that both signals (TDC and QDC) from a particular scintillator were registered over all statistics. In the case that any of signals was missing in a given pixel, all particles, which trajectories point to such pixel, were rejected from the analysis.

QDC distributions were eye-scanned and grouped into 5 signal classes. Figures 5.14 and 5.15 show example distributions for ToF-L and ToF-R respectively.

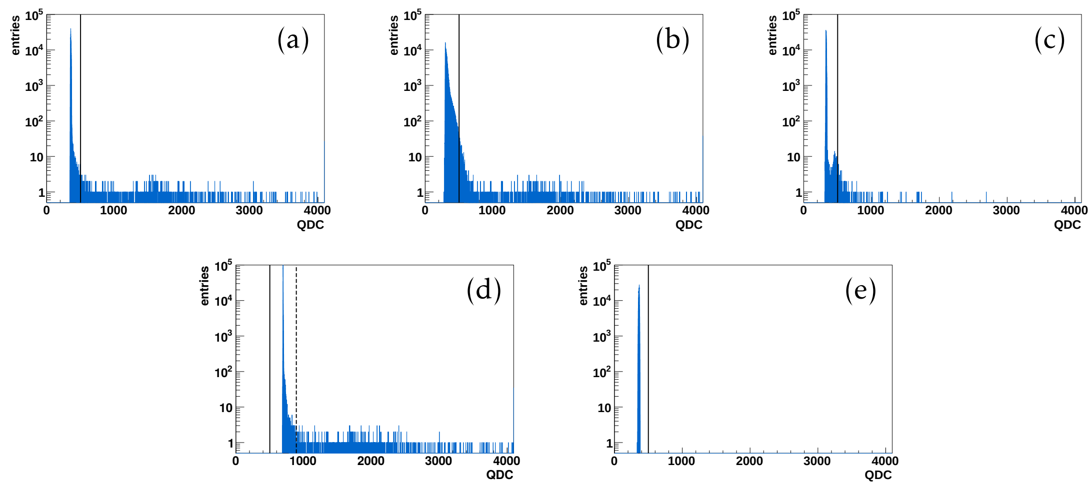

Fig. 5.14: Examples of QDC distribution for ToF-L: (a) – “healthy” distribution; (b) – distribution with smeared pedestal; (c) – too low HV; (d) – too high HV; (e) – pedestal only. The black solid vertical line marks a limit of natural ADC offset. The black dashed vertical line marks a readjusted limit of ADC offset.

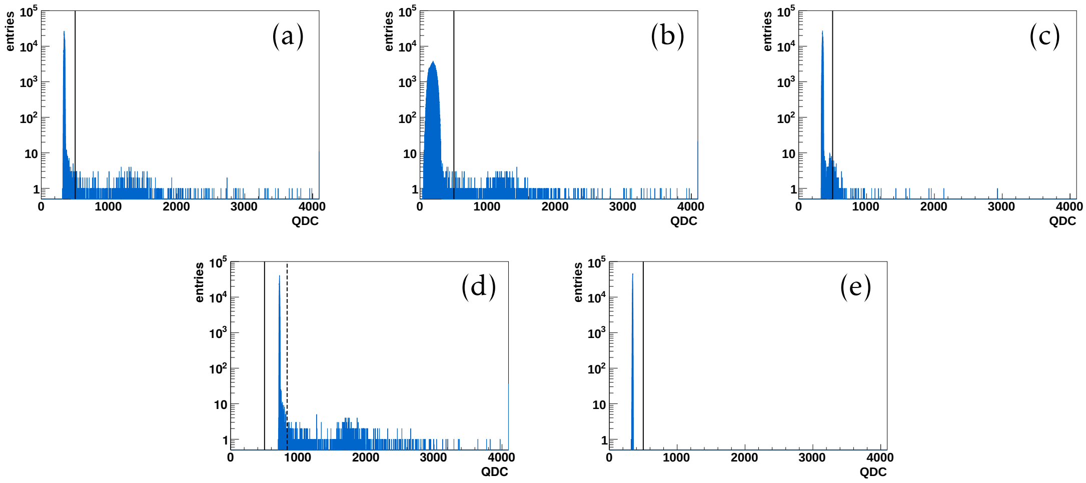

Fig. 5.15: Examples of QDC distribution for ToF-R: (a) – "healthy" distribution; (b) – distribution with smeared pedestal; (c) – too low HV; (d) – too high HV; (e) – pedestal only. The black solid vertical line marks a limit of natural ADC offset. The black dashed vertical line marks a readjusted limit of ADC offset.

The plots presented in panel (a), demonstrate "healthy" QDC distributions, where full charge information is registered along with natural ADC offset (<500 ADC counts). In panels (b) a smeared ADC offset, caused by a damaged readout module, can be observed. Distributions in panels (c) indicate to low HV setting of the pixel photomultiplier, which results in a charge signal incorporation into ADC offset and loss of the information. Distributions, as in panels (d), are shifted towards larger ADC values. This effect is caused by additional and accidental voltage offset of the QDC channel. In this case, some information for the highest ADC counts, associated with multiple hits in a ToF tile or heavy fragments registration, is lost. Still, multiple hits or heavy fragments cannot be analysed due to problems with unambiguous time-of-flight measurement. Therefore, for such cases as in panels (d), the pedestal offset was readjusted and charge information was retrieved. Plots placed in panels (e), show the pedestal only signal, coming from not working PMTs. Only particles, which trajectories point to the pixel with characteristic similar to one in (a) or (d) with readjusted pedestal offset are considered in further analysis.

Pixel efficiency

Charge signal (QDC) was normalised to the mean ADC value measured in a particular pixel (ignoring pedestal contribution). Only particles with normalised charge value from 0.5 to 2.0 were accepted in further analysis. Such selection rejects the contribution from multiple hits in ToF tile (high normalised QDC values) and particles hitting the very edge of the scintillator in the $x-y$ plane (low normalised QDC values). The figure 5.16 presents example distributions of normalised charge for ToF-L and ToF-R.

Selection criteria on the ToF TDC signals were set such, that particles with signal value from 900 to 3200 counts in ToF-L or from 600 to 2900 TDC counts in ToF-R were accepted in further analysis. This cut rejects particles with wrongly reconstructed momentum and possible contribution from off-time particles. The limits on TDC signals for ToF-L and ToF-R had to be adjusted individually, due to a

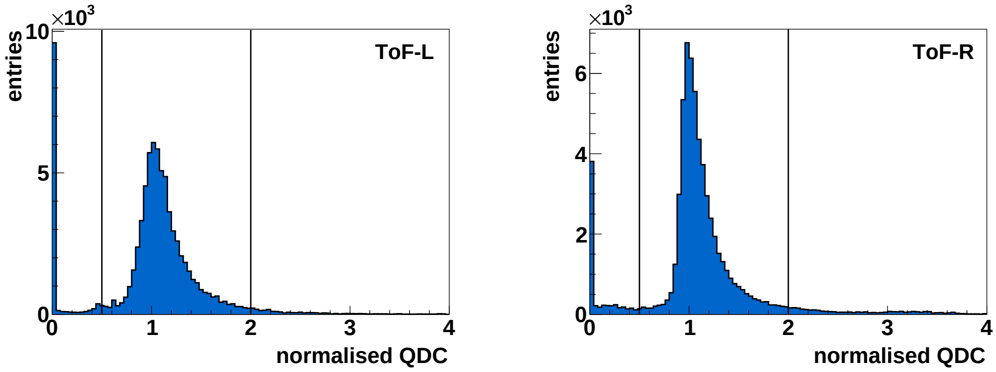

Fig. 5.16: Examples of normalised charge distributions for all ToF-L scintillators (*left*) and all ToF-R scintillators (*right*) in ^{7}Be+^{9}Be collisions at 75*A* GeV/*c*. Quality cuts limits are marked with the black vertical lines.

different length of the start signal cable for both detectors. Example distributions of the ToF-L/R TDC are presented in figure 5.17. The triple-maxima structure visible in the TDC distributions originates from the three different lengths of the cables transmitting information from the ToF-L/R scintillators toward the readout modules.

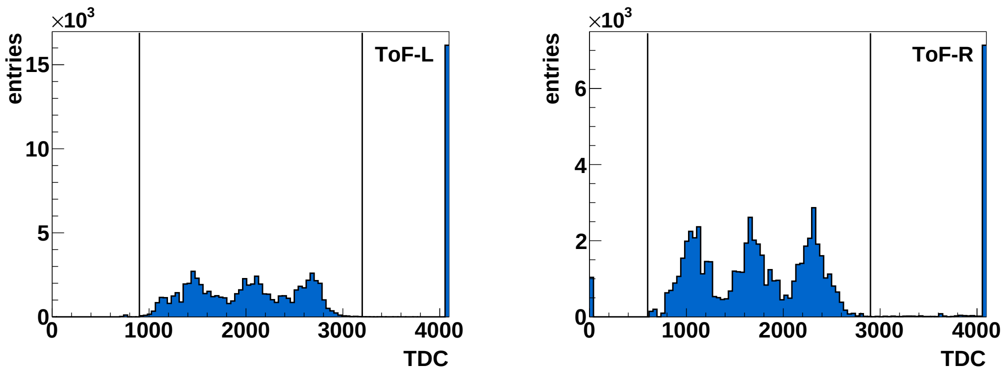

Fig. 5.17: Example TDC distributions for ToF-L (*left*) and ToF-R (*right*) pixels in ^{7}Be+^{9}Be collisions at 75*A* GeV/*c*. Quality cuts limits are marked with the black vertical lines.

TDC and QDC signals were used to estimate ToF pixels efficiency. The k–pixel efficiency ε_k is defined as in equation 5.3 below:

$$\varepsilon_k = \frac{ToFhit_{good}}{ToFhit_{all}}, \tag{5.3}$$

where the denominator of the fraction corresponds to a number of all tracks extrapolated to the particular pixel and the numerator contains a sub-sample of this track which fulfills normalised QDC and TDC signals quality requirements. Fig. 5.18 presents an example of the ToF walls efficiency extracted from ^{7}Be+^{9}Be collisions at 75*A* GeV/*c*. Pixels with efficiency lower that 50% are assumed as not working, thus the particles, which trajectories point to such pixel, are excluded from the analysis. Calculated efficiency factors were used in MC corrections (see Sec. 5.4).

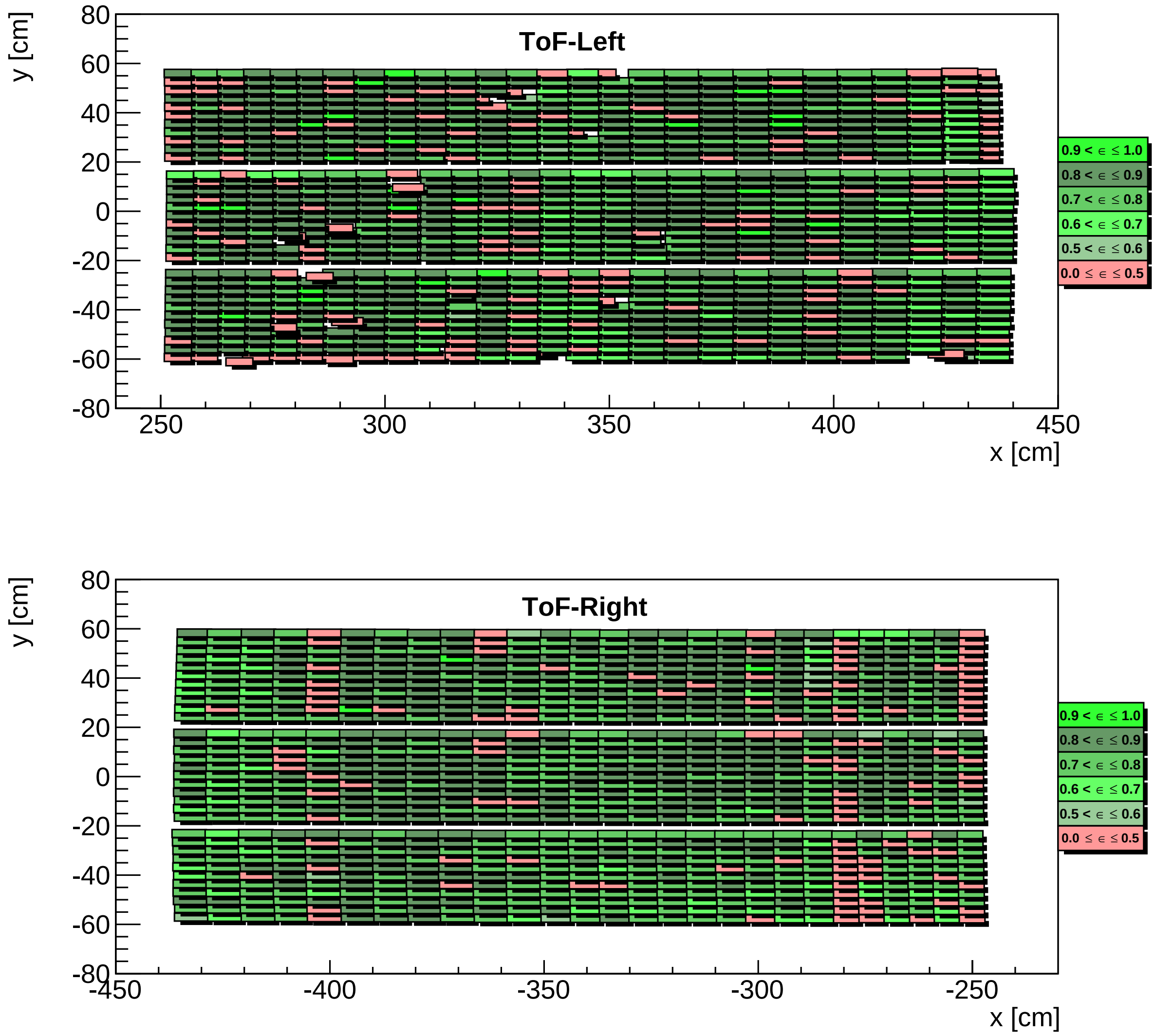

Fig. 5.18: An example of ToF-L (*top*) and ToF-R (*bottom*) pixels efficiency in ^{7}Be+^{9}Be collisions at 75A GeV/c. Pixels rejected from the analysis due to low efficiency are marked with red colour.

All track selection criteria explained in section 5.2 can bias the results thus a careful study on this effect is provided and described in Sec. 5.5.

5.3 Particle identification

5.3.1 *tof-dE/dx* method

In this work, the identification of K^{+}, K^{-}, π^{+}, π^{+}, p, $\overline{\text{p}}$ was based on combining the measurements of the mean particle energy loss in TPCs (dE/dx) and time of flight by ToF detectors (tof), used for particles mass calculation (m^2). An example of the m^2 versus dE/dx distribution in ^{7}Be+^{9}Be collisions at 40A GeV/c is presented in figure 5.19. Four groups of entries visible in the m^2 versus dE/dx distribution are directly associated with registered particle type.

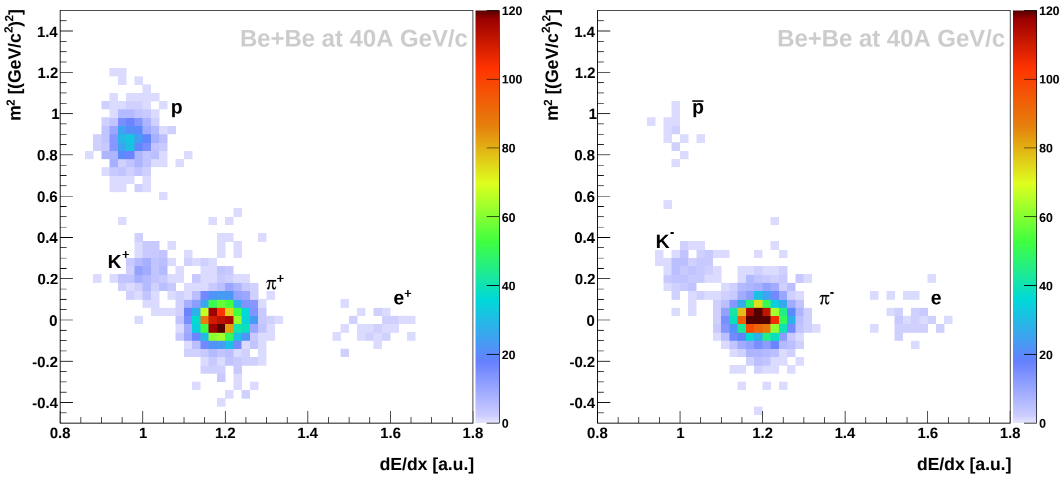

Fig. 5.19: The distribution of m^2 versus dE/dx for positively- (*left*) and negatively- (*right*) charged particles with 3 GeV/c < p_{tot} < 4 GeV/c and 0.3 GeV/c < p_{T} < 0.4 GeV/c measured by NA61/SHINE in ^{7}Be+^{9}Be collisions at 40A GeV/c.

The data sample was divided into smaller subsamples in the $p - p_{\mathrm{T}}$ phase-space with bins of 1 GeV/c in total momentum and 0.1 GeV/c (or 0.2 GeV/c for $p_{\mathrm{T}} >$ 0.4 GeV/c in the case of 30A GeV/c data set) in transverse momentum (see binnig scheme in Fig. 5.1). The analysis is performed for each $p - p_{\mathrm{T}}$ bin separately and independently for positively and negatively charged particles. Each two-dimensional histogram is described by the function $\rho(x,y)$:

$$\begin{aligned} \rho(x,y) &= \sum_{j=p,\pi,K,e} \rho_j(x,y) \\ &= \sum_j \frac{N_j}{2\pi\ \sigma_x}\ e^{-\frac{(x-x_j)^2}{2\sigma_x^2}} \left(\frac{f}{\sigma_{y_1}}\ e^{\frac{(y^2-y_j^2)^2}{2\sigma_{y1}^2}} + \frac{(1-f)}{\sigma_{y_2}}\ e^{\frac{(y^2-y_j^2)^2}{2\sigma_{y2}^2}} \right), \end{aligned} \tag{5.4}$$

where: N_j describes the yield of a given j particle kind, f is a weighting factor, σ_{y_1} and σ_{y_2} stand for standard deviations of weighted Gaussian distributions. The fitted function, equation 5.4, is the sum of two weighted two-dimensional Gaussian distributions with three standard deviations. For simplicity of notation in the formula, x stands for the measured dE/dx value and y denotes the calculated m^2 value. The use of two weighted Gaussian distributions was necessary to describe the m^2 distribution (broadening with momentum as visible in the Fig. 2.13). One Gaussian distribution, characterised by σ_{y_1}, describes the main content of the distribution, whereas the other one, characterised by σ_{y_2}, is used to describe only tails of the distribution. Hence, the value of σ_{y_2} is larger than σ_{y_1}. The total yield of all kinds particles is required to be equal to the integral of the fitted histogram. An example of the $m^2 - dE/dx$ distribution fitted with function 5.4 is presented in Fig. 5.20. The *tof-dE/dx* method in NA61/SHINE is ideally suited for kaon identification in the mid-rapidity region.

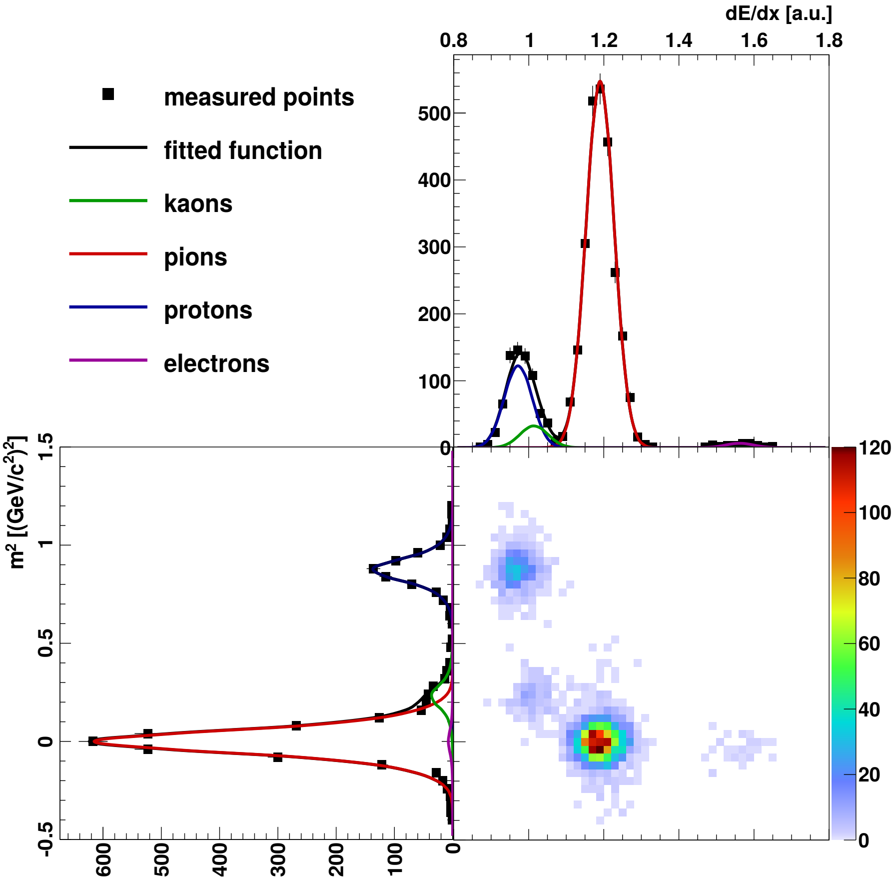

Fig. 5.20: An example of the m^2 versus dE/dx distribution fitted with *tof-dE/dx* function (Eq. 5.4) in a single phase-space bin ($3 < p_{tot} < 4$ GeV/c and $0.3 < p_{\mathrm{T}} < 0.4$ GeV/c) for positively-charged particles produced in ^{7}Be+^{9}Be collision at 40A GeV/c.

5.3.2 Identity method and raw spectra

The particle identification described above was performed in $p - p_{\mathrm{T}}$ bins. Since transformation between momentum and rapidity is not trivial, the identification based on probabilities, so-called *identity method* [75,76], was used.

The method for calculating the particle yield is based on the estimate of the probability of being a j–kind (proton, pion, kaon or electron) particle for each track. Tracks (entries in the fitted histogram) are characterised by measured momentum (p_x, p_y and p_z used for p and p_{T} calculation), m^2 and dE/dx values. Therefore, the identity procedure can be expressed by formula 5.5:

$$P_j = \frac{\rho_j(p, p_{\mathrm{T}}, m^2, dE/dx)}{\rho(p, p_{\mathrm{T}}, m^2, dE/dx)}, \tag{5.5}$$

where P_j is the estimated probability, j indicates the kind of a particle, ρ is the value of the fitted function (Eq. 5.4) in a particular $p - p_{\mathrm{T}}$ bin for the corresponding value of energy-loss (dE/dx) and squared mass (m^2) of a given particle.

Examples of the probability estimate as the sum over all fitted $p - p_{\mathrm{T}}$ bins for positively and negatively charged particles measured in ^{7}Be+^{9}Be collisions at 40A GeV/c are presented in figure 5.21. They were used for particle yield calculation in

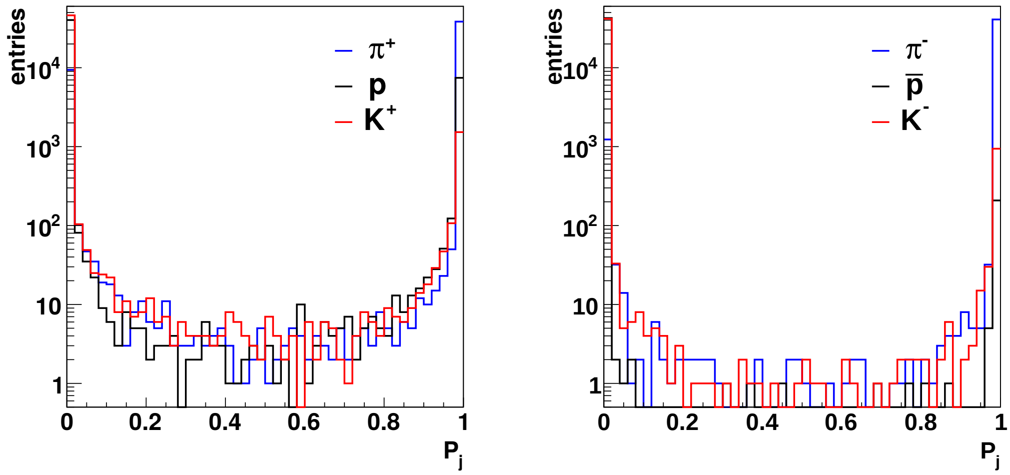

Fig. 5.21: Example of the probability distribution of track identification as a kaon, pion or proton for positively (*left*) and negatively (*right*) charged particles produced in ^{7}Be+^{9}Be collisions at 40A GeV/c.

different ranges of rapidity and transverse momentum.

Raw spectra of the j-kind particle multiplicity are derived in the bins of $y - p_{\mathrm{T}}$ as a sum of probabilities:

$$n_{j=K^{+},\,K^{-},\,\pi^{+},\,\pi^{-},\,p,\,\overline{p}} = \sum_{i=1}^{i=n'} P_j \;, \tag{5.6}$$

where n is number of particles type j, whereas n' represents number of tracks. Raw spectra of charged hadrons were normalised to the number of analysed events as well as the bin size of the y and p_{T} phase-space.

5.4 Corrections to the spectra

The corrections based on MC simulations were developed:

(i) detector effects, ε_{geo},
(ii) ToF inefficient pixels exclusion, $\varepsilon_{dead\ pixels}$,
(iii) Tof pixels efficiency, $\varepsilon_{efficiency}$,
(iv) weak deacays, ε_{decay}.

MC corrections are applied one after the other, bin-by-bin in $y - p_{\mathrm{T}}$ phase space (for each bin of the spectrum separately) and for each j-kind particle (j = K^{+}, K^{-}, π^{+}, π^{-}, p and $\overline{p}$) individually.

The partial corrections, after applying sequential selection criteria, are presented in $p - p_{\mathrm{T}}$ phase space corresponding to the kinematic acceptance of the ToF walls, due to the fact that the $tof - dE/dx$ analysis method has different $y - p_{\mathrm{T}}$ acceptance for particles of different kind (as presented in fig. 5.1).

The first correction, ε_{geo}, comes from the geometrical acceptance of the detection setup (TPCs and ToF-L/R), reconstruction efficiency as well as biasing selection criteria (biasing event cuts and track cuts: (i)–(vi)). It is defined as the ratio between reconstructed MC tracks multiplicity ($(n)_{geo}^{MCrec}$) – after applying the biasing cuts and extrapolation to ToF detectors with respect to its geometrical limits and the multiplicity of all generated particles ($(n)^{MCgen}$):

$$\varepsilon_{geo} = \frac{(n)^{MCrec}_{geo}}{(n)^{MCgen}} . \tag{5.7}$$

An example of such geometrical correction estimation is presented in Fig. 5.22. Quantitative differences between corrections for various particles originate from

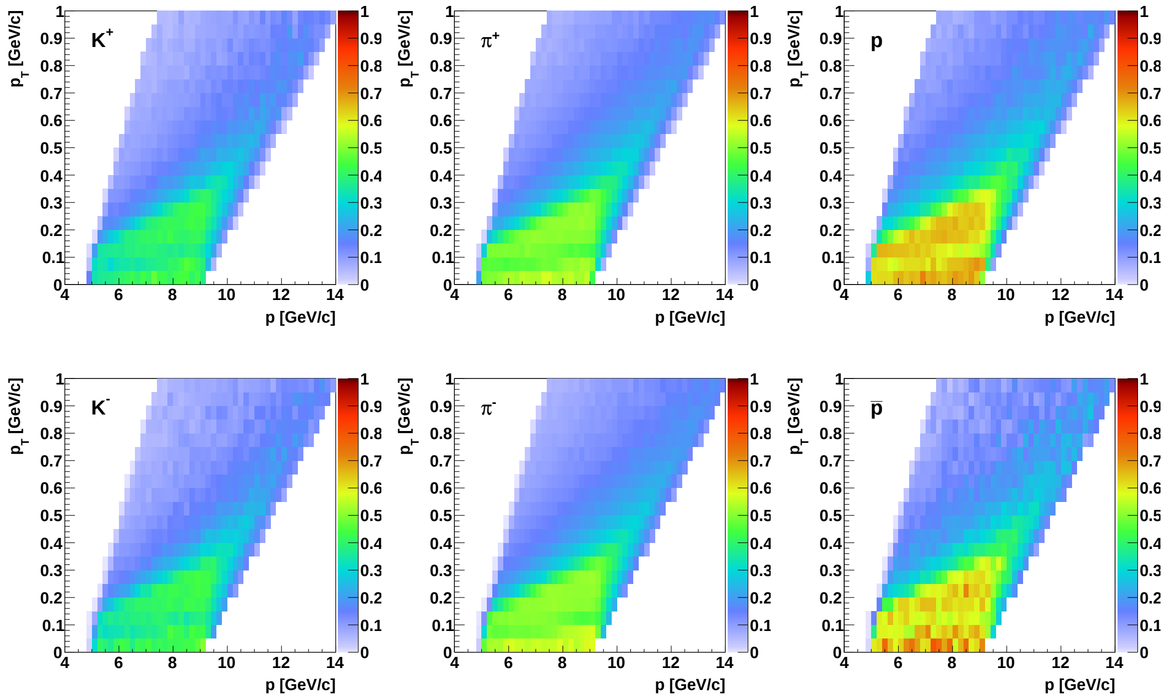

Fig. 5.22: MC correction for the geometrical acceptance of the detection system for various particles produced in ^{7}B+^{9}Be collision at 150A GeV/c.

various processes (e.g. K and π decays, interactions with the detector material).

The two following corrections were developed to revise the performance of the ToF detector. The efficiency of the ToF pixels was estimated pixel-by-pixel from experimental data and the efficiency coefficients are used for a pixel performance evaluation (for details on efficiency determination see Sec. 5.2.2). The *dead pixels* correction, $\varepsilon_{dead\ pixels}$, is defined as:

$$\varepsilon_{dead\ pixels} = \frac{(n)^{MCrec}_{dead\ pixels}}{(n)^{MCrec}_{geo}}, \tag{5.8}$$

where $(n)^{MCrec}_{dead\ pixels}$ stands for MC tracks multiplicity excluding those tracks reaching pixels of efficiency lower that 50%. An example of the correction impact with respect to the previous correction is presented in figure 5.23. The structures visible in the plots (strips of lower correction ratio) correspond to groups of not-working pixels.

After the exclusion of inefficient pixels, the correction for the ToF efficiency, $\varepsilon_{efficiency}$, was applied. Each particle trace, extrapolated towards ToF walls, was weighted by the efficiency factor of the pixel reached. The formula describing

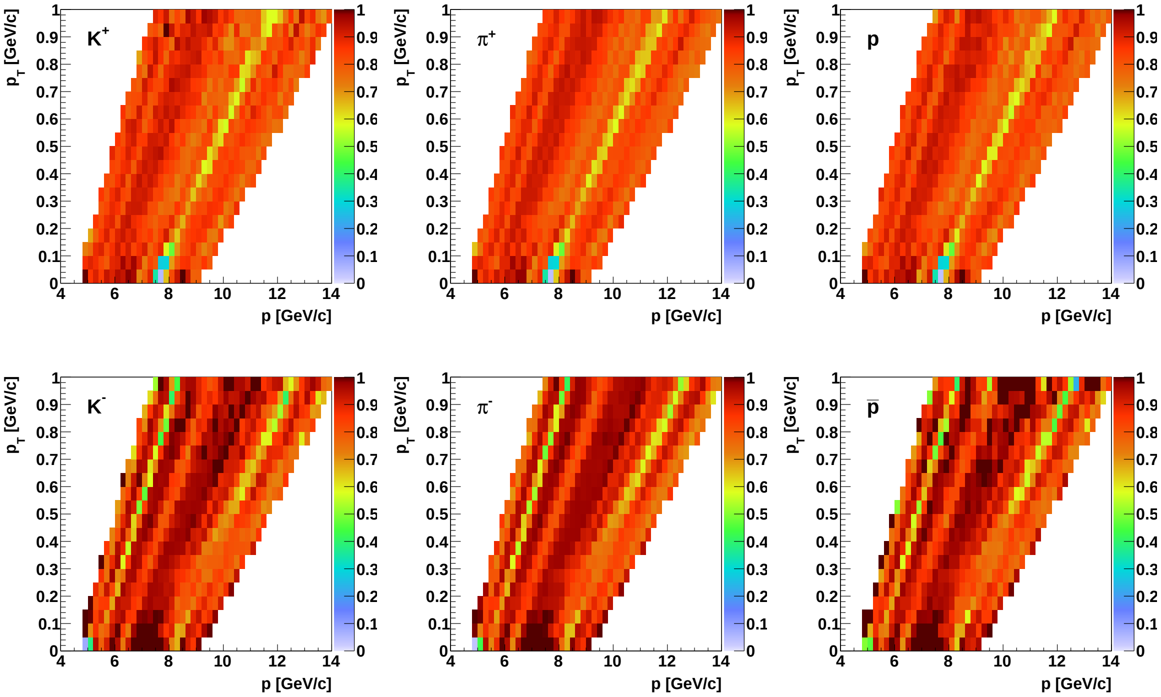

Fig. 5.23: MC correction for the inefficient pixels exclusion for various particles produced in ^{7}B+^{9}Be collision at 150*A* GeV/*c*.

efficiency correction is:

$$\varepsilon_{efficiency} = \frac{(n)^{MCrec}_{efficiency}}{(n)^{MCrec}_{dead\ pixels}}. \tag{5.9}$$

$(n)^{MCrec}_{efficiency}$ conveys the multiplicity of the reconstructed MC tracks, in which each track is weighted with the efficiency factor of the pixels it points to. The impact of the correction with respect to the previous correction is shown in figure 5.24.

The last correction, ε_{decay}, estimates the impact of particle decays and interactions between the downstream edge of the MTPC and ToF detectors. The correction factor is defined as follows:

$$\varepsilon_{decay} = \frac{(n)^{MCrec}_{decay}}{(n)^{MCrec}_{efficiency}}, \tag{5.10}$$

where $(n)^{MCrec}_{decay}$ mean reconstructed MC tracks which have neither decayed nor interacted before reaching the ToF detectors (multiplicity is weighted by efficiency factor). The impact of this correction is presented in Fig. 5.25.

The generated and reconstructed MC multiplicity spectra used for correction definition were normalised to the number of simulated and reconstructed events, respectively, as well as to the size of histogram bins in y and p_T. The overall multiplicative correction factor can be written as:

$$\varepsilon = \varepsilon_{geo} \times \varepsilon_{dead\ pixels} \times \varepsilon_{efficiency} \times \varepsilon_{decay} \tag{5.11}$$

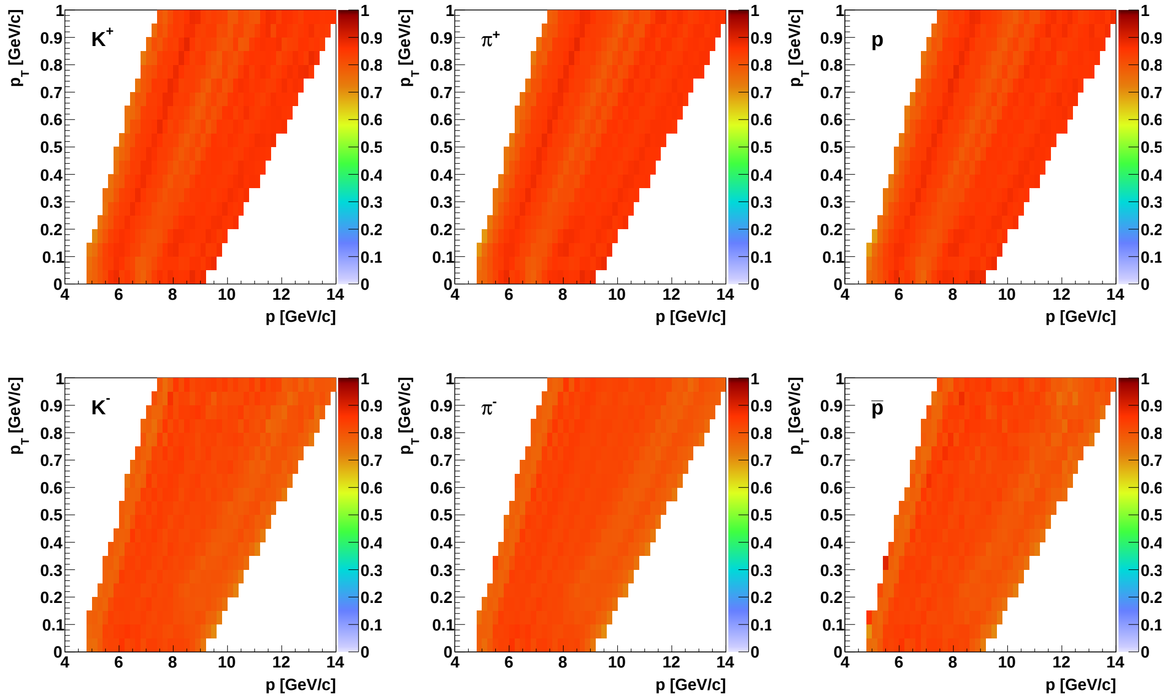

Fig. 5.24: MC correction for the ToF efficiency for various particles produced in ^{7}B+^{9}Be collision at 150A GeV/c.

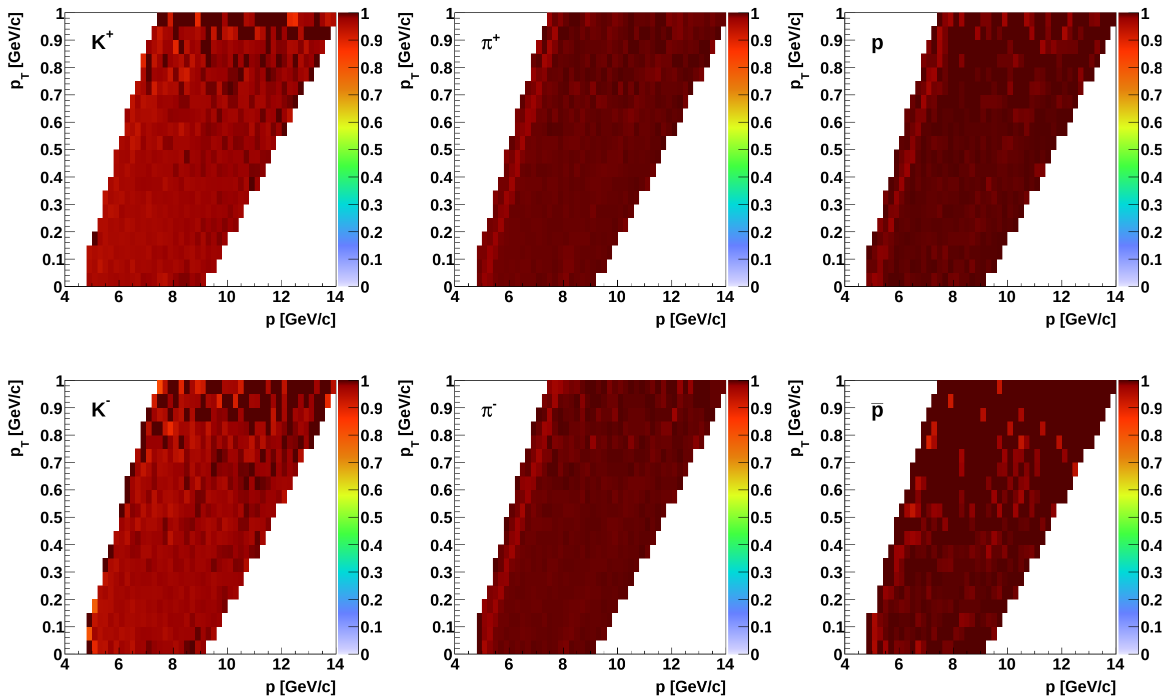

Fig. 5.25: MC correction for decays and interactions between the last two padrows of MTPC and ToF detectors for various particles produced in ^{7}B+^{9}Be collision at 150A GeV/c.

Figure 5.26 presents examples of generated MC spectra ($(n)^{MCgen}$) for various kinds of particles (*left panel*), the spectra of reconstructed MC tracks with selection criteria applied (*middle panel*) and correction factors (*right panel*).

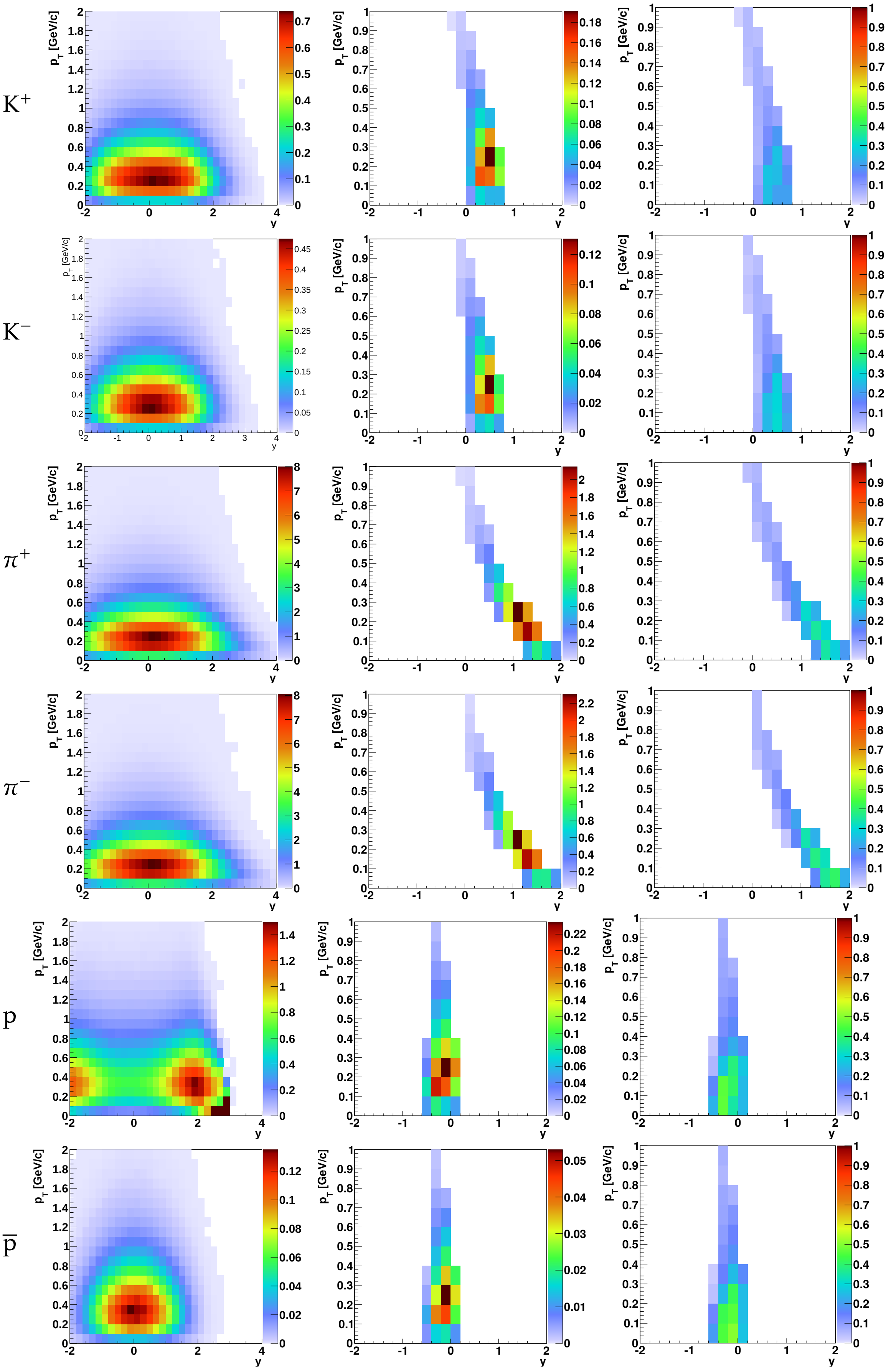

Fig. 5.26: Examples of simulated MC spectra (left panel), reconstructed MC spectra after applying selection criteria (middle panel) and correction factors (right panel) for various particles produced in ^{7}B+^{9}Be collisions at 150A GeV/c. Highly populated (off-scale) forward rapidity region ($2.4 < y < 3.0$) in proton MC spectrum is related to simulated beam particles.

Final spectra of particle kind j, $n_{j\ corrected}$, are obtained by multiplication of the raw normalised spectra, $n_{j\ normalised}$, by the correction factor ε calculated for a particle j (ε_j):

$$n_{j\ corrected} = n_{j\ normalised} \cdot \frac{1}{\varepsilon_j} \tag{5.12}$$

5.5 Statistical and systematic uncertainties

5.5.1 Statistical uncertainties

Statistical uncertainties are due to finite statistics of experimental data as well as simulated events used in the correction factors determination. Errors on the raw spectra were calculated bin-by-bin under the assumption that there is no correlation between tracks produced in separate events and spectra depend on Poisson distribution. The error on the identification (fitting procedure) is neglected in statistical uncertainties. It will be considered in systematic uncertainties estimation as the uncertainty on the identification method. The statistical error of raw spectra is therefore:

$$\sigma_{n_j} = \sqrt{\sum_{i=1}^{i=n'} P_j^2}, \tag{5.13}$$

where σ_{n_j} stands for the statistical uncertainty of n particles of type j and n' is the number of tracks.

Raw normalised spectra are obtained by scaling each bin in the spectra by the normalisation factor. The uncertainties are assumed to be scalable in the same way.

Uncertainties for the MC correction factor were calculated in each bin of the $y - p_{\mathrm{T}}$ phase space. Hence, since n_j^{MCrec} is a subset of the n_j^{MCgen}, the statistical uncertainties of correction factors were estimated with the binomial distribution. If we assume σ_{ε_j} as the statistical uncertainty of the correction factor, then the total statistical uncertainty of corrected spectra in that bin is defined as:

$$\sigma_{n_{j\ corrected}} = \sqrt{(\sigma_{n_{j\ normalised}} \cdot \frac{1}{\varepsilon_j})^2 + (n_{j\ normalised} \cdot \sigma_{\varepsilon_j})^2} \tag{5.14}$$

An example of the relative statistical uncertainties for charged hadrons produced in ^{7}B+^{9}Be collisions at 150A GeV/c is presented in the figure 5.27.

5.5.2 Systematic uncertainties

The analysis method along with the event and track selection criteria result in a systematic bias of the final results. The systematic bias was estimated in the following steps:

- the repetition of the analysis procedure (event and track selection, identification, and MC corrections) varying the biasing cuts on events and tracks,
- the comparison of the final spectra with the results obtained by varying the biasing cuts,

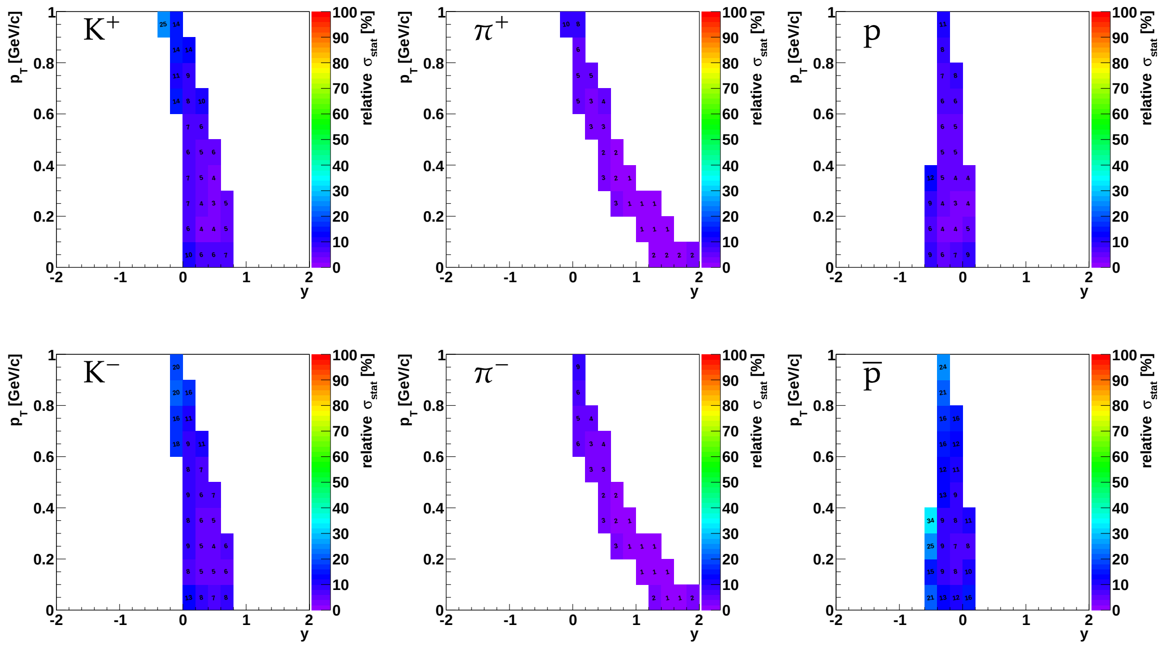

Fig. 5.27: An example of statistical uncertainty estimation for charged hadrons produced in ^{7}B+^{9}Be collisions at 150A GeV/c.

- the calculation of the absolute difference between the final spectra and the results obtained by varying the biasing cuts (for each $y - p_{\mathrm{T}}$ bin individually),
- the assigning the largest difference as the systematic uncertainty generated by particular biasing cut.

The main contributions to systematic errors are listed below.

(i) Bias due to event centrality class determination. The impact of this effect was estimated varying the number and of the PSD modules selected for the forward energy class determination. All module selections for this study are presented in figure 5.28.

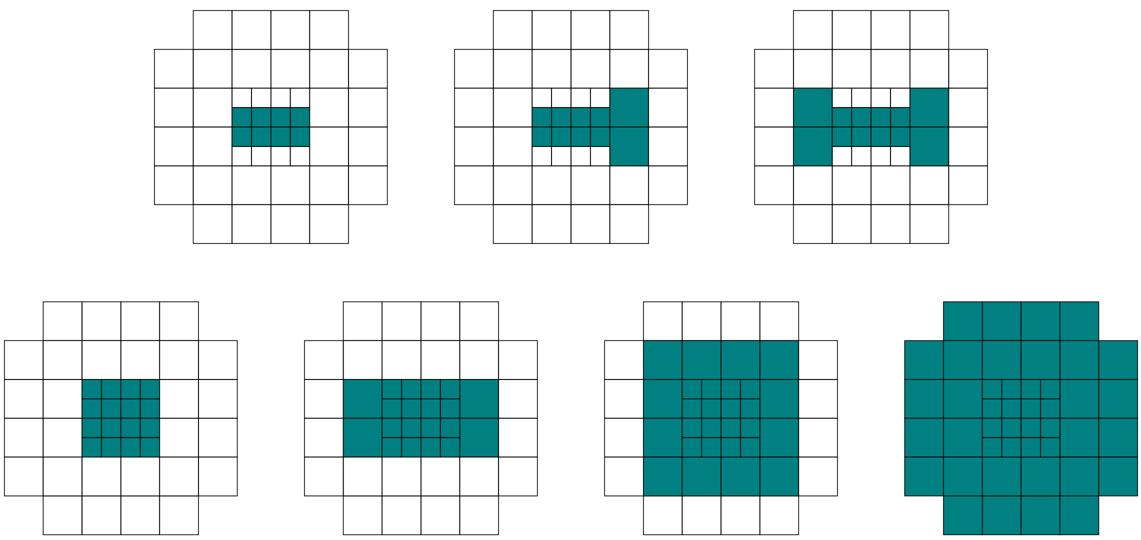

Fig. 5.28: Various module selections used to estimate of systematic uncertainty related to centrality definition.

(ii) Bias due to event and track selection criteria. Effect of selection criteria was calculated varying the biasing cuts within the most broad range, which do not cause increase of the statistical uncertainties by the factor more than 0.25. Considered selection criteria are:

- position of the fitted vertex along z-axis – studied within ±25 cm range with respect to the target position,
- position of the fitted interaction point – checked within ranges from -3.2 cm to +2.0 cm for x-axis and from -1.2 cm to +3.0 cm for y-axis with respect to the nominal values of the cuts on impact point,
- requirement on the number of measured points in the magnetic field (points in VTPCs and GapTPC) - checked within range of ±10 points in respect to the nominal requirement on the number of points.

(iii) Bias due to ToF detectors performance, which can be caused by two related reasons:

- efficiency determination based on the ToF signals selection criteria - checked for loose and tight thresholds on the QDC and TDC signals:

ToF signal	ToF-L				ToF-R			
selection	QDC		TDC		QDC		TDC	
criteria	*min*	*max*	*min*	*max*	*min*	*max*	*min*	*max*
loose	0.4	2.2	500	4000	0.4	2.2	500	4000
tight	0.6	1.8	900	3000	0.6	1.8	800	2800

Tab. 5.4: Thresholds on ToF signals due to systematic uncertainties study.

- inefficient pixels rejection - checked for ±10% variation of the nominal exclusion limit.

(iv) Bias due to particle identification techniques was studied by the shifting the mean (x_j and y_j) of the two-dimensional Gaussians (eq: 5.4) fitted to the $m^2 - dE/dx$ distributions by ±1%.

Total systematic uncertainty was calculated according to formula:

$$\sigma_{sys} = \sqrt{\sigma_i^2 + \sigma_{ii}^2 + \sigma_{iii}^2 + \sigma_{iv}^2} \tag{5.15}$$

The systematic uncertainty estimation was also provided bin-by-bin in the $y - p_\mathrm{T}$ phase space for each kind of identified hadrons separately. Figure 5.29 presents an example of the relative overall systematic uncertainties for charged hadrons produced in ^{7}B+^{9}Be collisions at 150A GeV/c, while figure 5.30 presents an example of the overall uncertainties (statistical and systematic) for positively- and negatively-charged kaon spectra in mid-rapidity along with partial contributions.

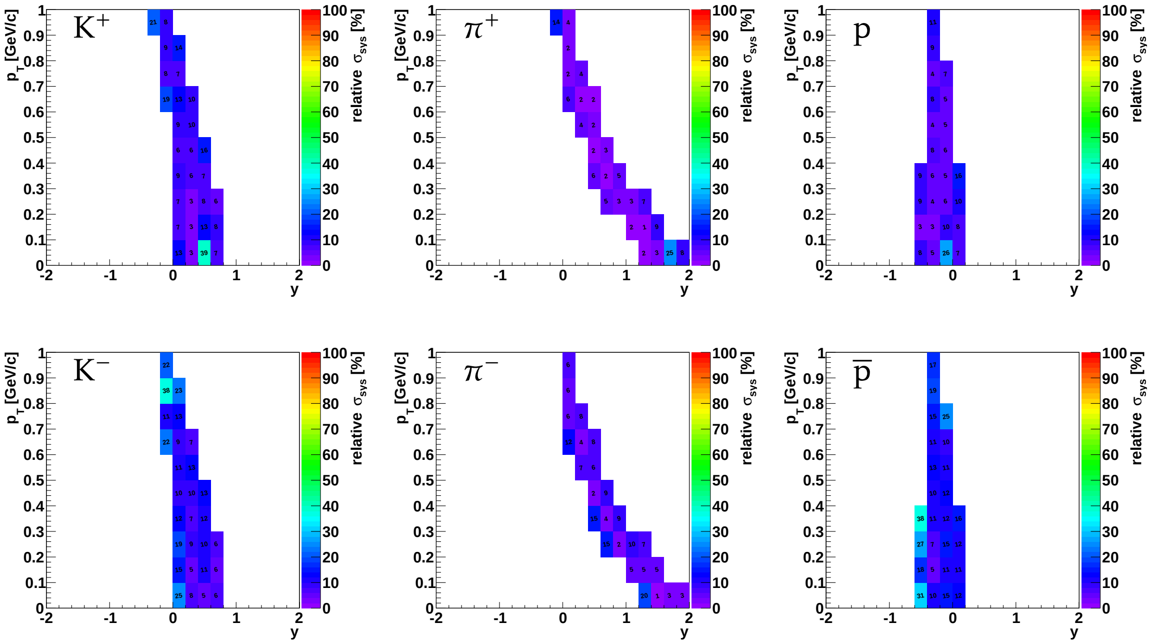

Fig. 5.29: An example of relative systematic uncertainty estimation for charged hadrons produced in ^{7}B+^{9}Be collisions at 150*A* GeV/*c*.

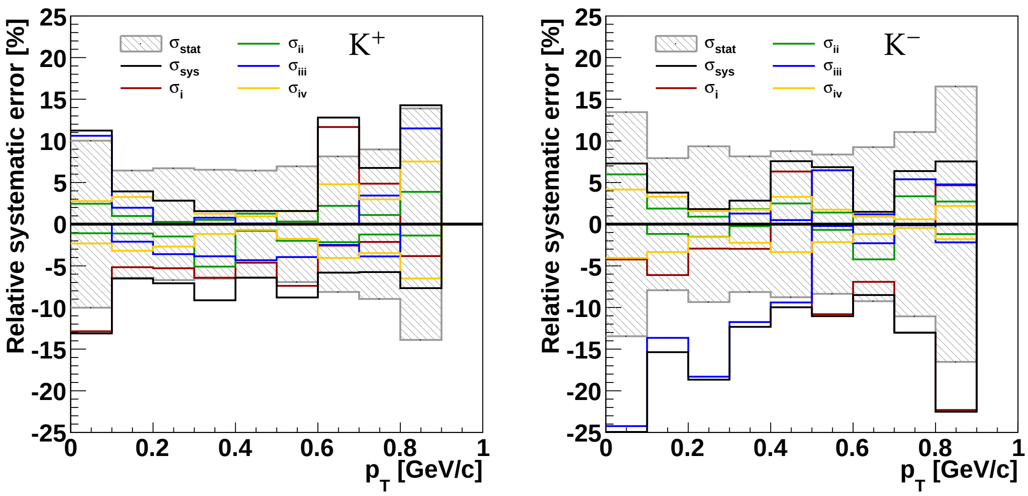

Fig. 5.30: Relative contributions of systematic uncertainties and statistical uncertainty in the background for mid-rapidity spectra of positively (*left*) and negatively (*right*) charged kaons obtained at 150*A* GeV/*c*.

Chapter 6

Results

This chapter contains experimental results on inclusive spectra of the identified hadrons produced in ^{7}Be+^{9}Be collision measured for the first time in SPS energy range. They were obtained using the methods described in chapter 5.

Two-dimensional spectra of K^+, K^-, π^+, π^-, p and $\overline{p}$, measured at incident projectile momenta of 30A, 40A, 75A, 150A GeV/c, are presented in the rapidity versus transverse momentum phase space. The results are corrected for detector acceptance and performance, detection and reconstruction efficiency as well as weak decays and secondary interactions.

I this chapter, the data on identified particle spectra are presented first. They are followed by the study of the onset of deconfinement with charged kaon spectra in the mid-rapidity presented along with results on p+p interactions by NA61/SHINE [27, 28], central Pb+Pb collisions by NA49 [20, 29–31] and world result on heavy ion collisions [21, 25, 26, 35, 38–41, 77], and finally the comparison with calculations performed with EPOS [67, 68], UrQMD [78, 79] and HiJING [80] theoretical models.

6.1 Charged hadron multiplicities as double differential spectra

Multiplicities of K^+, K^-, π^+, π^-, p and $\overline{p}$ produced in ^{7}Be+^{9}Be collisions at 30A, 40A, 75A, 150A GeV/c beam momenta were calculated in bins of transverse momentum and rapidity $d^2n/(dydp_{\mathrm{T}})$. The procedures for particle identification, application of corrections and uncertainties estimation are described in details in the chapter 5. The spectra were normalised to the bin size in the $y - p_{\mathrm{T}}$ phase space and to the number of analysed events. The value of a particular bin content corresponds to the multiplicity of a given kind particle in given rapidity and transverse momentum range. Double-differential spectra are presented in figures 6.1 -6.6. The spectra are grouped by particle kind in the following way:

- Fig. 6.1 – spectra of positively-charged kaons,
- Fig. 6.2 – spectra of negatively-charged kaons,
- Fig. 6.3 – spectra of positively-charged pions,
- Fig. 6.4 – spectra of negatively-charged pions,
- Fig. 6.5 – spectra of protons,
- Fig. 6.6 – spectra of anti-protons

for various beam momenta in SPS energy range.

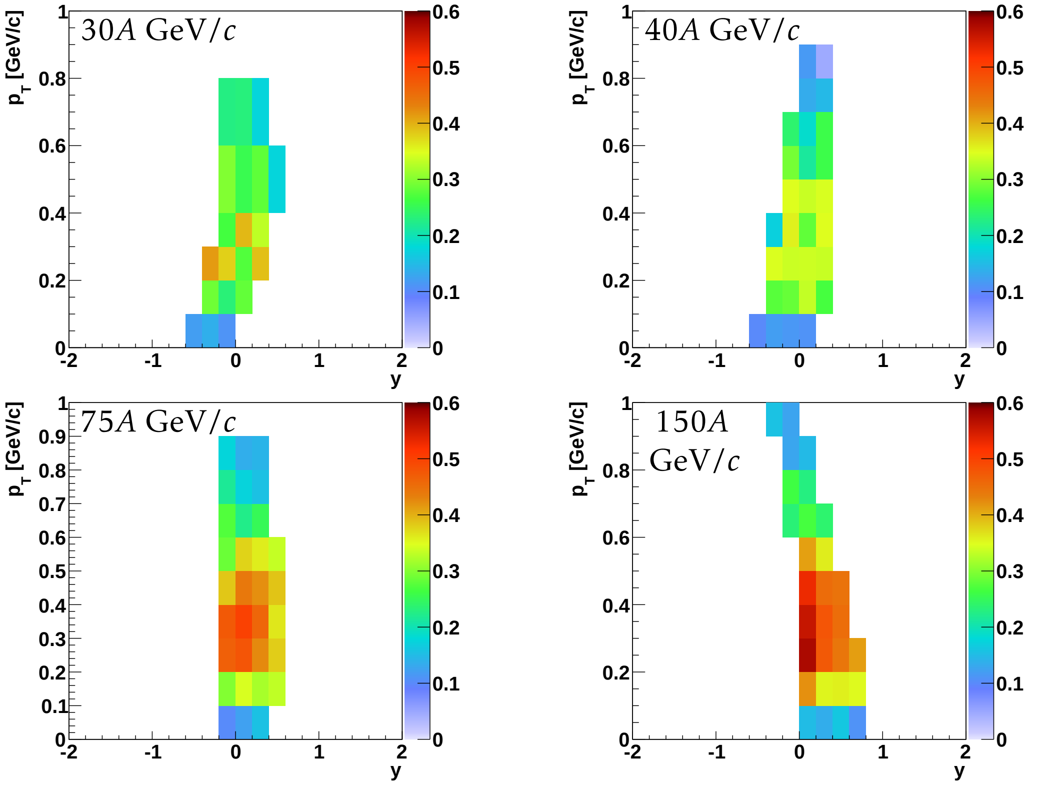

Fig. 6.1: The double differential spectra of positively-charged kaons produced in ^{7}Be+^{9}Be collisions at 30*A*, 40*A*, 75*A* and 150*A* GeV/*c*.

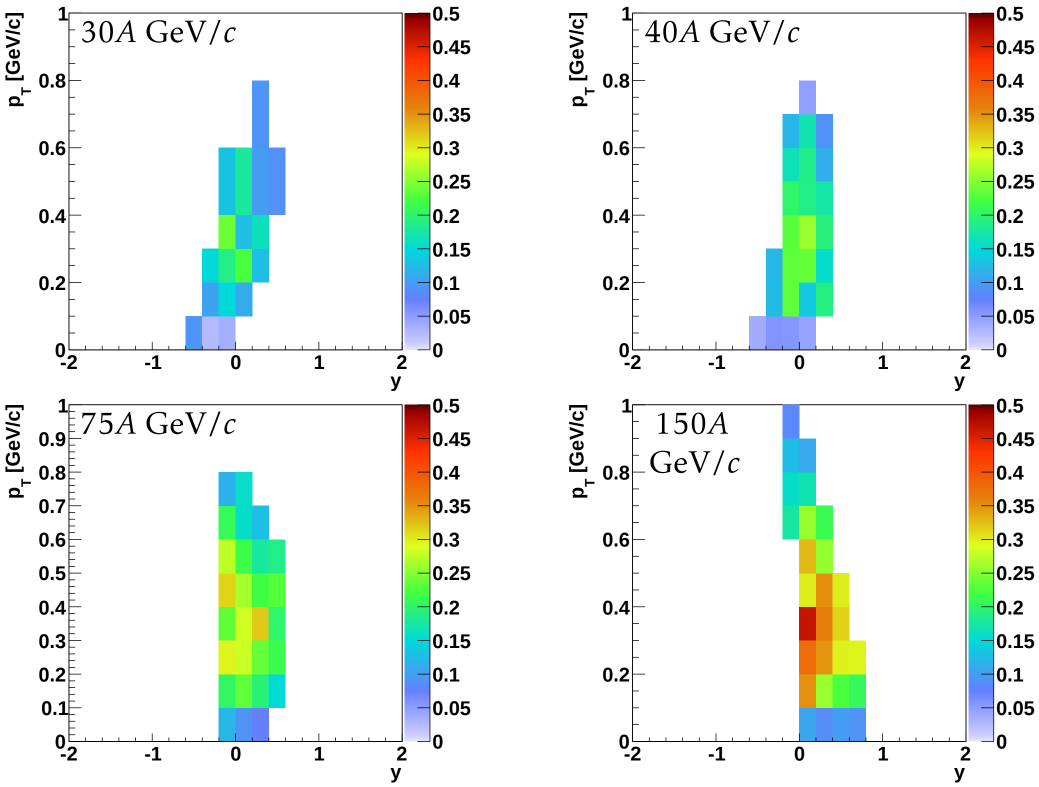

Fig. 6.2: The double differential spectra of negatively-charged kaons produced in ^{7}Be+^{9}Be collisions at 30*A*, 40*A*, 75*A* and 150*A* GeV/*c*.

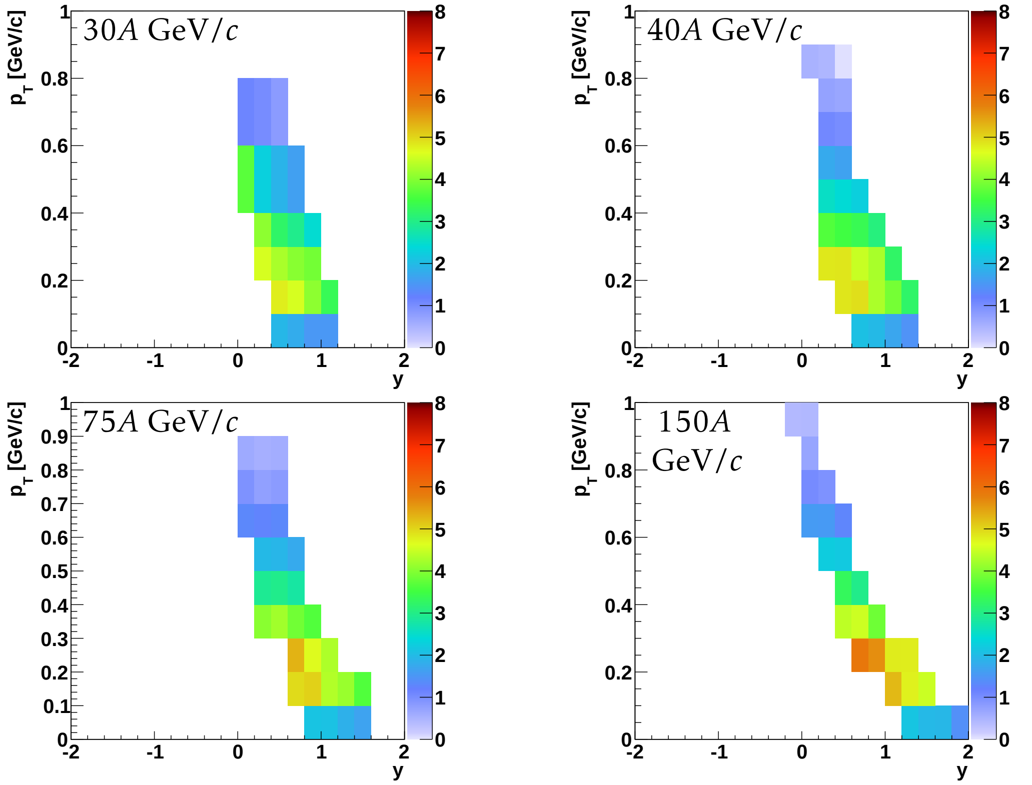

Fig. 6.3: The double differential spectra of positively-charged pions produced in ^{7}Be+^{9}Be collisions at 30*A*, 40*A*, 75*A* and 150*A* GeV/*c*.

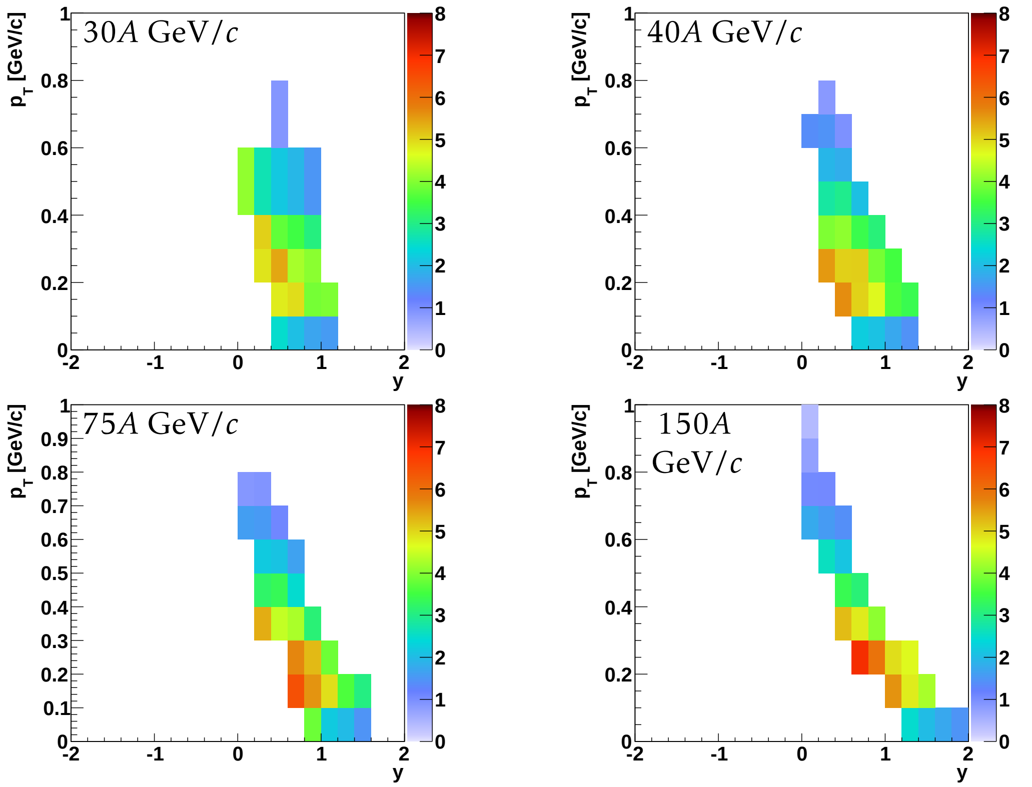

Fig. 6.4: The double differential spectra of negatively-charged pions produced in ^{7}Be+^{9}Be collisions at 30*A*, 40*A*, 75*A* and 150*A* GeV/*c*.

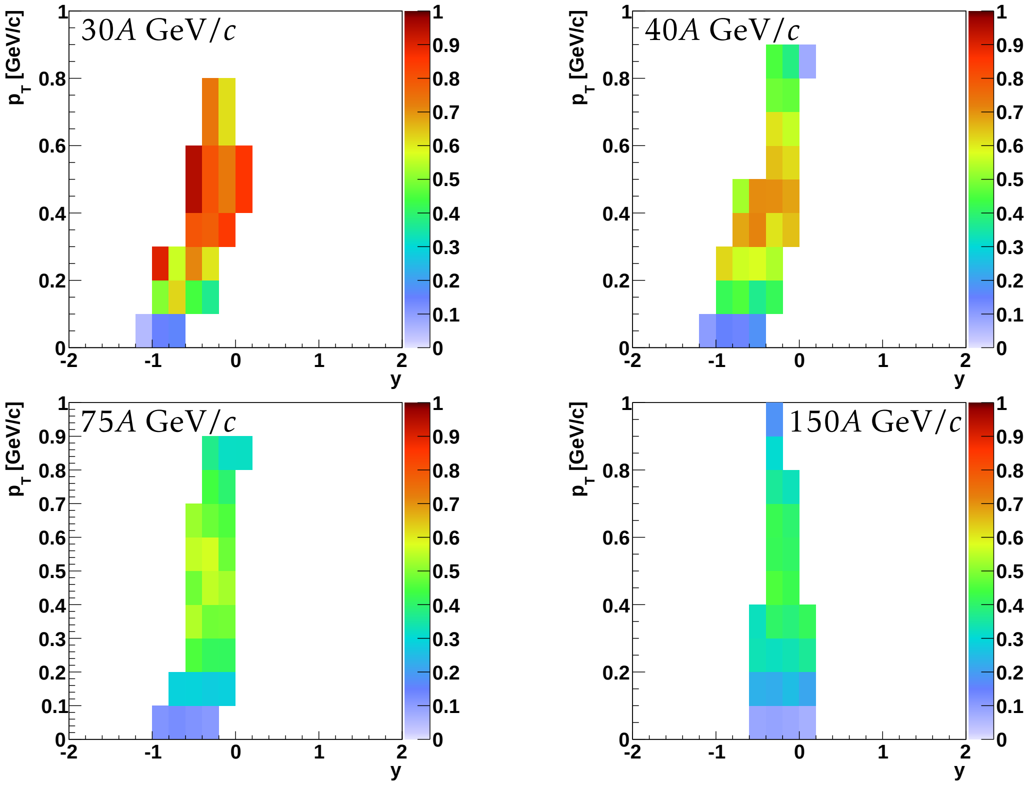

Fig. 6.5: The double differential spectra of protons produced in ^{7}Be+^{9}Be collisions at 30*A*, 40*A*, 75*A* and 150*A* GeV/*c*.

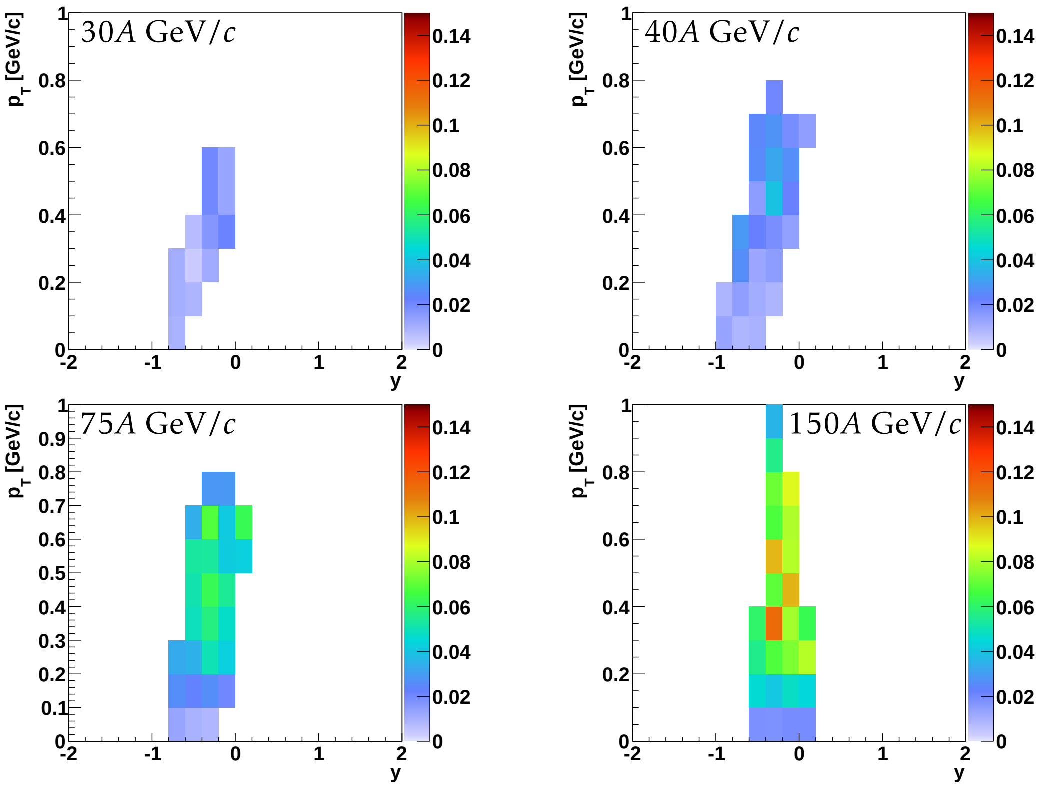

Fig. 6.6: The double differential spectra of anti-protons produced in ^{7}Be+^{9}Be collisions at 30*A*, 40*A*, 75*A* and 150*A* GeV/*c*.

Numerical values of the charged hadron multiplicities presented in figures 6.1-6.6 are tabulated along with statistical and systematic uncertainties in Appendix B.

6.2 Transverse momentum spectra of charged kaons in the mid-rapidity

The goal of the analysis described in this thesis was to derive transverse momentum spectra of the charged K mesons in the mid-rapidity region. These results give important insights for the study of the onset of deconfinement [14]. The p_{T} spectra were derived as a projection of the double differential spectra of kaons to the p_{T}–axis in a particular rapidity region, selected for each beam momentum separately due to slightly different acceptance in the $y_{\mathrm{K}} - p_{\mathrm{T}}$ phase space. Rapidity regions assigned as the mid-rapidity are specified in table 6.1. The mid-rapidity region selection

Beam momentum	lower mid-rapidity limit	upper mid-rapidity limit
30*A* GeV/*c*	-0.2	0.0
40*A* GeV/*c*	0.0	0.2
75*A* GeV/*c*	0.0	0.2
150*A* GeV/*c*	0.0	0.2

Tab. 6.1: Definition of the mid-rapidity region int this thesis for various beam momenta.

was studied with the EPOS 1.99 model. The generated spectra are symmetric with respect to $y = 0$ within 1% accuracy.

The transverse momentum spectra in the mid-rapidity are presented in figure 6.7. They were parametrised with the function:

$$\frac{d^2 n}{dp_{\mathrm{T}} dy} = \frac{S\ p_{\mathrm{T}}}{\mathrm{T}^2 + \mathrm{T}\ m_{\mathrm{K}}}\ exp(-\frac{\sqrt{p_{\mathrm{T}}^2 + m_{\mathrm{K}}^2} - m_{\mathrm{K}}}{\mathrm{T}}), \tag{6.1}$$

where: T is the inverse slope parameter, m_{K} is the mass of the K meson and S is a normalisation factor. The spectra presented in figure 6.7 were scaled for better display. Statistical error bars are drawn, still they are mostly smaller than the point marker. Shadowed envelopes show systematic uncertainties. Solid lines illustrate the spectra parametrisation with the function 6.1, which was also used to extrapolate the spectra in transverse momentum up to 1.0 GeV/c. The experimental results along with the extrapolation allowed to estimate the kaon ($\frac{dn}{dy}$) multiplicity in the mid-rapidity range. The obtained charged K meson yields and K^+/K^- ratio in the mid-rapidity range are given in table 6.2 and compared with theoretical models in section 6.4.

Furthermore, the function 6.1 yields the inverse slope parameter of transverse momentum spectra of kaons, which stands for an important observable in the study on the onset of deconfinement. Values of the inverse slope parameter of transverse momentum K^+ and K^- spectra in the mid-rapidity region can be found in table 6.3.

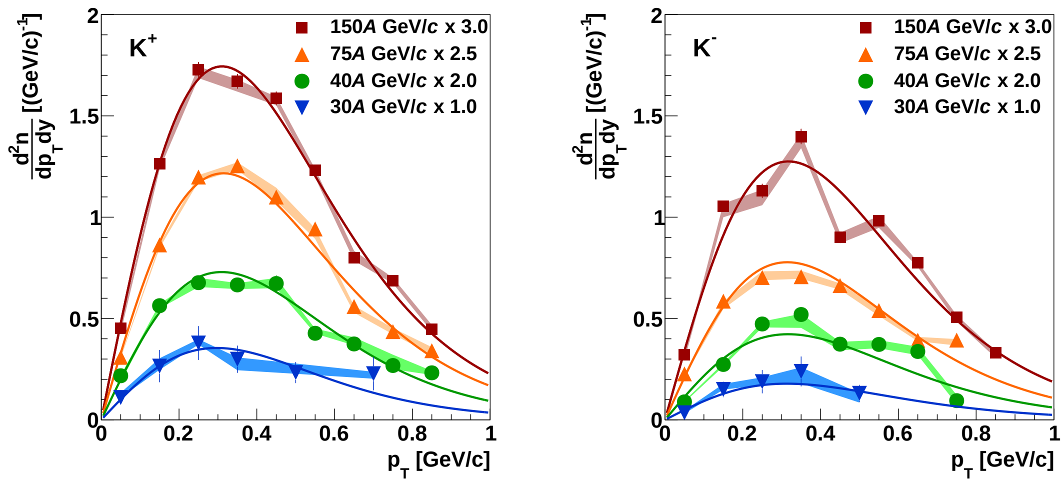

Fig. 6.7: The transverse momentum spectra of K^+ (left) and K^- (right) produced in ^{7}Be+^{9}Be collisions at 30*A*, 40*A*, 75*A* and 150*A* GeV/*c*. Shadow envelopes show systematic uncertainties of the spectra. The lines to the fit with function 6.1.

p_{beam} [GeV/c]	$K^+ \left(\frac{dn}{dy}\right)_{y\approx0}$			$K^- \left(\frac{dn}{dy}\right)_{y\approx0}$			$\frac{K^+}{K^-}\ y\approx0$		
30*A*	0.209	±0.025	±0.009	0.111	±0.019	±0.007	1.882	±0.396	±0.153
40*A*	0.220	±0.009	±0.008	0.136	±0.007	±0.008	1.620	±0.111	±0.105
75*A*	0.288	±0.009	±0.007	0.182	±0.007	±0.006	1.586	±0.073	±0.068
150*A*	0.338	±0.008	±0.009	0.254	±0.008	±0.013	1.330	±0.053	±0.075

Tab. 6.2: Values of charged K mesons yields and K^+/K^- ratio (*first element*) in the mid-rapidity region with statistical (*second element*) and maximum systematic uncertainties (*third element*).

p_{beam} [GeV/c]	T_{K^+} [MeV]			T_{K^-} [MeV]		
30*A*	152.87	±16.91	±12.41	167.52	±23.72	±14.64
40*A*	164.33	±6.93	±5.70	170.64	±11.32	±12.64
75*A*	168.67	±5.70	±4.59	168.81	±9.28	±4.70
150*A*	165.33	±5.18	±6.97	171.73	±7.07	±12.27

Tab. 6.3: Values of the inverse slope parameter of the transverse momentum K meson spectra in the mid-rapidity region (*first element*) with statistical (*second element*) and maximum systematic uncertainties (*third element*).

6.3 Study of onset of deconfinement

6.3.1 Inverse slope parameter of m_T spectra – *step*

One of the signatures of the quarks deconfinement and phase transition studied in this thesis is the energy dependence of the inverse slope parameter of the transverse mass (m_T) spectra of charged kaons. The exponential parametrisation of the p_T spectra of positively and negatively-charged kaons in the mid-rapidity (function 6.1 and figure 6.7) yields the inverse slope parameter, which energy dependence is presented with world data in figure 6.8. Results on the inverse slope parameter

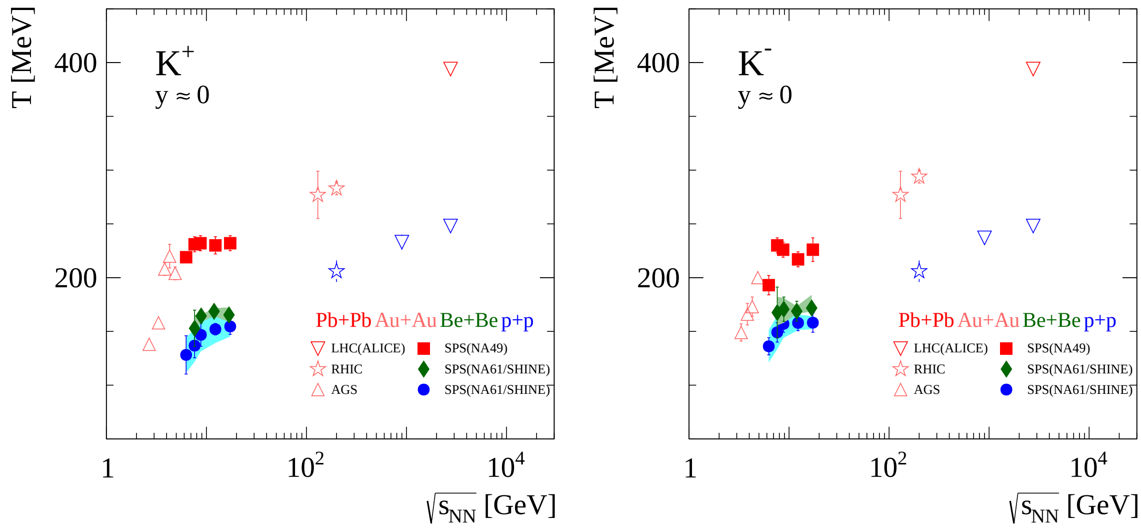

Fig. 6.8: The energy dependence of the inverse slope parameter T of transverse mass spectra of charged kaons in the mid-rapidity for central ^{7}Be+^{9}Be, Pb+Pb and Au+Au collisions and inelastic p+p interactions [20, 21, 28–31, 33–38, 40].

from ^{7}Be+^{9}Be collisions follow the trend presented by Pb+Pb points. T values from ^{7}Be+^{9}Be collisions are about 6-12% higher than those from p+p interactions, which can be associated with a slightly higher kinetic freeze-out temperature [14] or/and some collective transverse effects (also observed in m_{T} spectra of negatively-charged pions from ^{7}Be+^{9}Be collisions [81]).

6.3.2 Kaon to pion ratio – *horn*

Another indication of the onset of deconfinement studied in this thesis is the energy dependence of the strangeness-to-entropy ratio. The rapid changes of the K/π energy dependence in the SPS energy range are attributed to the phase transition of the strongly interacting matter [20].

The acceptance of the NA61/SHINE identification methods used by NA61/SHINE does not cover the mid-rapidity region of the positively-charged pions. The spectra of the negatively-charged pions were derived by so-called h^- identification method (for the detail see Ref. [27, 65]) in a broad region of the forward hemisphere, including the mid-rapidity. Hence, the calculation of the K^-/π^- ratio is straightforward, using the K$^-$ yield obtained with the analysis presented in this thesis and π^- yields from h^- analysis [65].

Nevertheless, the total numbers of protons and neutrons in the ^{7}Be+^{9}Be colliding system are equal. Thus, since the isospin symmetry has to be conserved, the same production of π^+ and π^- can be assumed. The isospin symmetry effect was studied with theoretical models (for details see section C.5 in appendix C). Models suggest π^+/π^- ratio close to 1 with few percent variations. Therefore, the K^+ yields obtained with the analysis presented in this thesis is divided by π^- yields taken from from the h^- analysis. The variations in π^+/π^- ratio were taken into account in systematic uncertainty of the K^+/π^+ ratio estimation. Results on the energy dependence of th K^+/π^+ and K^-/π^- ratios compared with world data are presented in figure 6.9.

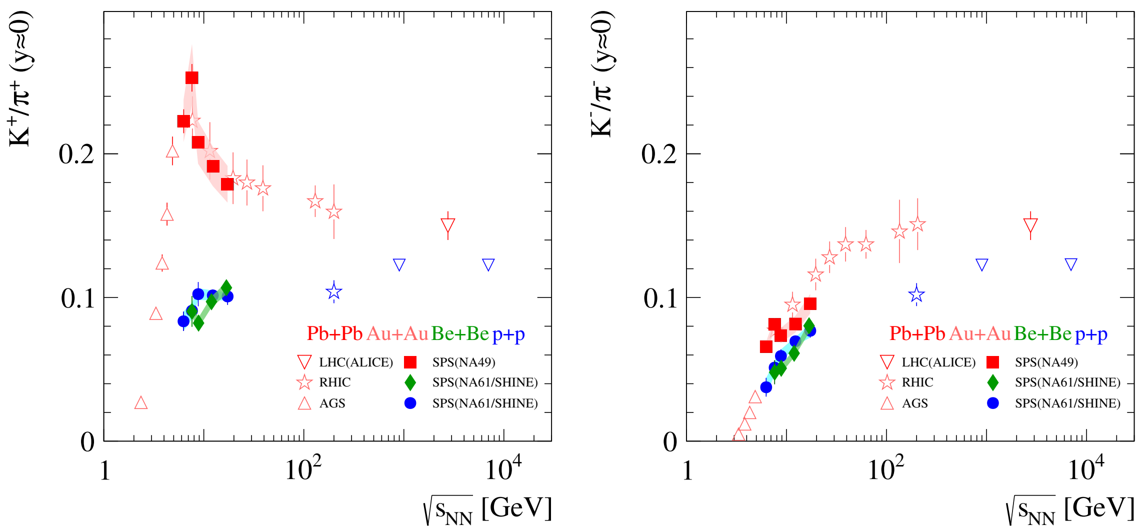

Fig. 6.9: The energy dependence of the K/π particle yields ratio in the mid-rapidity of positively (*left*) and negatively (*right*) charged hadrons for central ^{7}Be+^{9}Be, Pb+Pb and Au+Au collisions and inelastic p+p interactions [20, 21, 25, 26, 28–31, 33, 34, 36–39, 41].

Results from ^{7}Be+^{9}Be collisions show the increase of the K^+/π^+ ratio with the collision energy (within statistical uncertainties). Furthermore, the NA61/SHINE results show that the strangeness-to-entropy production ratio in ^{7}Be+^{9}Be collisions is similar to those in p+p interactions (firmly visible in the energy dependence of the K^-/π^- ratio), in contradiction to the SMES model predictions [19] and HRG model calculations [42, 44, 45].

6.4 Theoretical models

The charged K meson spectra in the mid-rapidity and the results derived from them (e. g. K^+/π^+ ratio) were compared with few theoretical models, namely EPOS 1.99, UrQMD 3.4 and HIJING 1.411 (see sections C.2). A brief description of those models and the numerical values of the theoretical calculations of p_T spectra in y bins for each beam momentum are included in appendix C.

Figures 6.10 and 6.11 present the comparison of the experimental p_T spectra of charged K mesons in the mid-rapidity with theoretical models. The full points present the experiment with shadowed band showing systematic uncertainties, while open points - the predictions of the theoretical models . The lines show the fit to the data and simulation points obtained using function 6.1. Comparison of the $d^2n/dp_T dy$ spectra of K^+ and K^- shows that all the tested models qualitatively describe p_T spectra. In the case of positively-charged particles, the UrQMD model agrees also quantitatively well with the experiment, while neither EPOS nor HIJING can reproduce the quantitative picture of the K^+ p_T spectra. None of the tested models can quantitatively recreate the K^- multiplicity in mid-rapidity, still the UrQMD is in the best agreement with the experiment.

Figures 6.12 - 6.17 present the comparison of the energy dependence of various observables, namely $K^\pm$ yields, $K^\pm/\pi^\pm$ ratios and T, in the mid-rapidity for central ^{7}Be+^{9}Be collisions with predictions of theoretical models. In the right panels of these

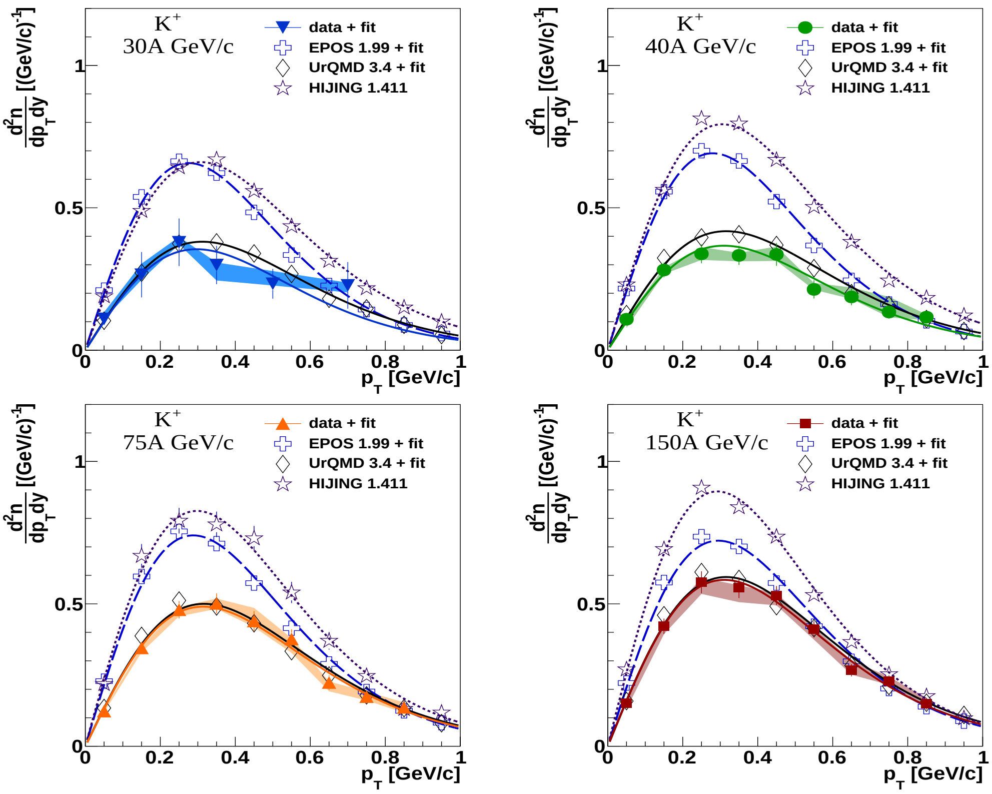

Fig. 6.10: Comparison of the transverse momentum spectra of K^+ produced in ^{7}Be+^{9}Be collisions at 30*A*, 40*A*, 75*A* and 150*A* GeV/*c* with theoretical models.

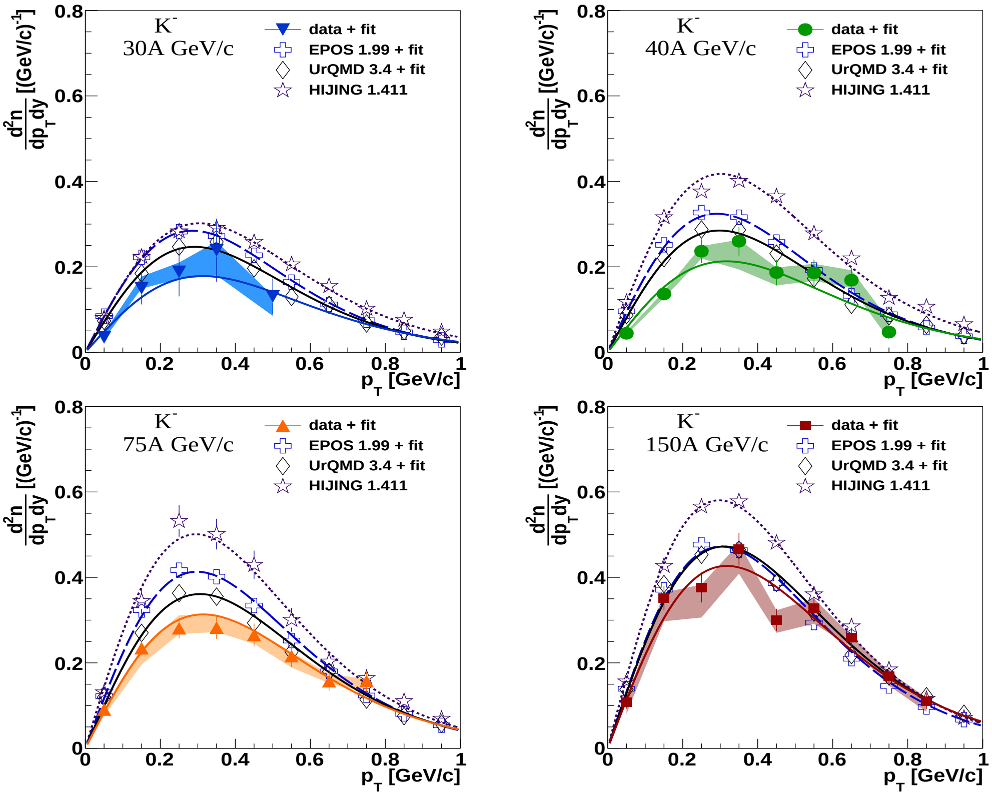

Fig. 6.11: Comparison of the transverse momentum spectra of K^- produced in ^{7}Be+^{9}Be collisions at 30*A*, 40*A*, 75*A* and 150*A* GeV/*c* with theoretical models.

figures, the relative difference of the theoretical models with respect to experimental data is presented. Such presentation allows to show the agreement between models and experimental results within a given number of total experimental uncertainty.

Charged K meson yields were calculated as described in Sec. 6.2. The obtained values were compared with model calculations, where $K^{\pm}$ yields were obtained by integration of the $d^2n/dp_T dy$ spectra for $0.0 < p_T < 1.0$ GeV/c range.

Figures 6.12 and 6.13 show the energy dependence of K^+ and K^- yields, respectively.

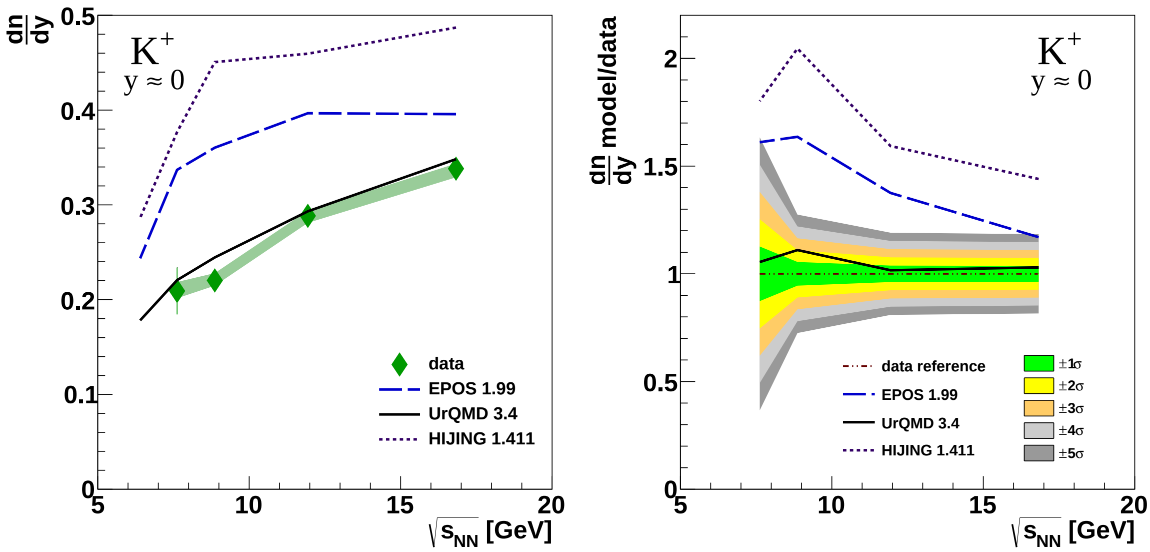

Fig. 6.12: *Left*: comparison of the energy dependence of K^+ yields in the mid-rapidity for central ^{7}Be+^{9}Be collisions with theoretical models: EPOS 1.99 (*blue dashed line*), UrQMD 3.4 (*black solid line*) and HIJING 1.411 (*violet doted line*). *Right*: relative difference of simulated K^+ yields with respect to experimental data. Coloured bands correspond to multiples of σ_{tot} of the experimental data.

The energy dependence of K^+ yields in the mid-rapidity can be described with UrQMD (within 2σ agreement). Again, for the energy dependence of K^- yields in the mid-rapidity in the SPS energy range, UrQMD provide the best estimate among the tested models (2.5σ agreement). Neither EPOS nor HIJING can characterise the energy dependence of K^+ and K^- yields in ^{7}Be+^{9}Be collisions in SPS energy range that well.

The observables of the onset of deconfinement studied as a function of the collision energy were also tested against theoretical models.

Figures 6.14 and 6.15 show the comparison of the energy dependence of the experimental and simulated inverse slope parameter of kaon p_T spectra in the mid-rapidity for positively- and negatively-charged mesons, respectively. The energy dependence of the inverse slope parameter of p_T spectra of positively-charged kaons in the mid-rapidity is in agreement with the UrQMD simulation within statistical uncertainties. EPOS simulation reveals a similar tendency as in the experimental results, still it predicts smaller values of the T parameter than it was measured (3σ difference). HIJING presents a rather different energy dependence with respect to the experimental results. The experimental results on the inverse slope parameter of p_T spectra of negatively-charged kaons are burdened by a significant total uncertainty

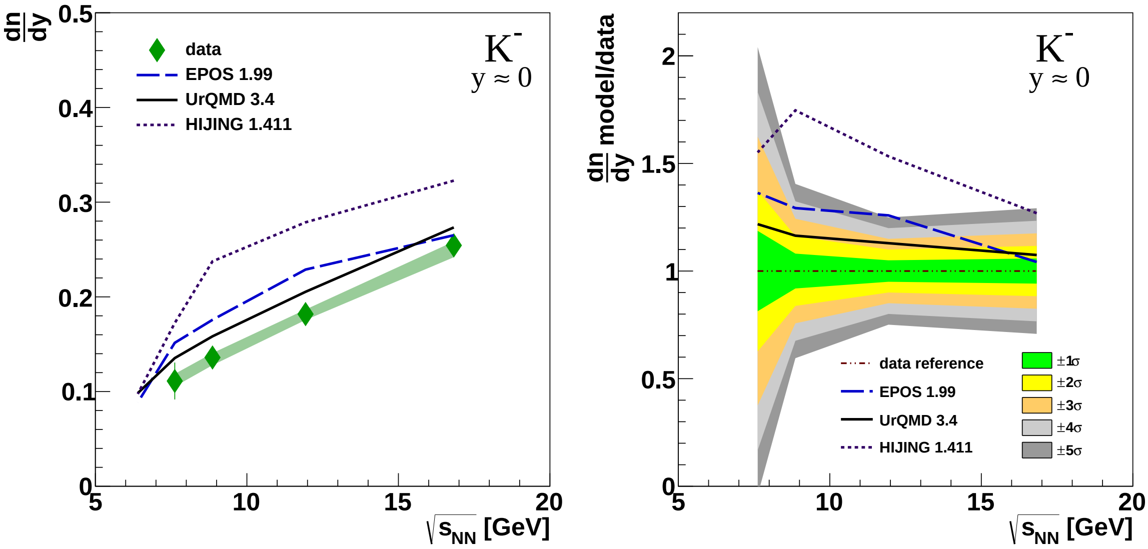

Fig. 6.13: *Left*: comparison of the energy dependence of K^- yields in the mid-rapidity for central ^{7}Be+^{9}Be collisions with theoretical models: EPOS 1.99 (*blue dashed line*), UrQMD 3.4 (*black solid line*) and HIJING 1.411 (*violet doted line*). *Right*: relative difference of simulated K^- yields with respect to experimental data. Coloured bands correspond to multiples of σ_{tot} of the experimental data.

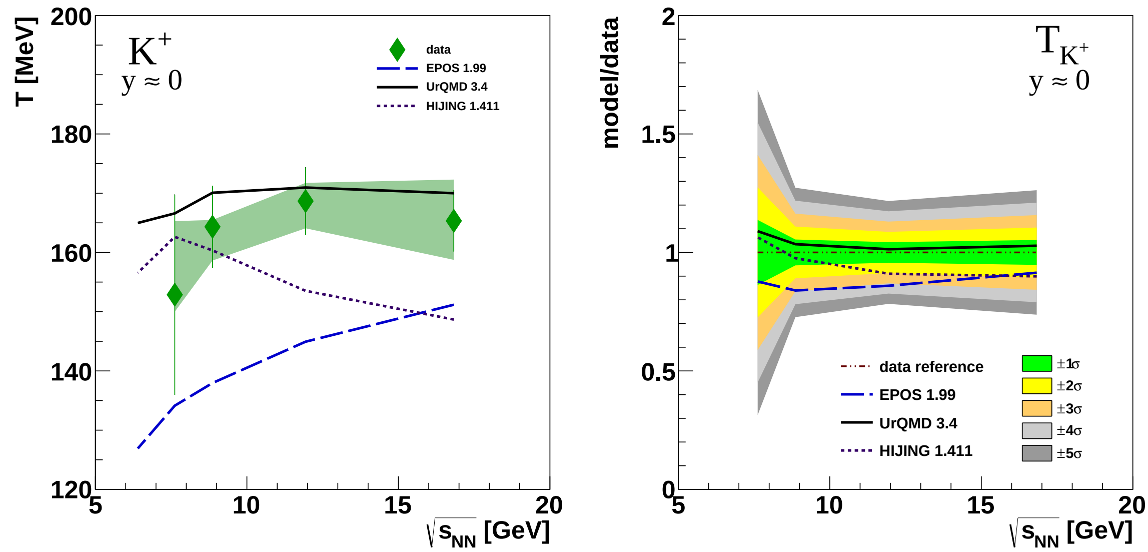

Fig. 6.14: *Left*: comparison of the energy dependence of the inverse slope parameter of K^+ spectra in the mid-rapidity for central ^{7}Be+^{9}Be collisions with theoretical models: EPOS 1.99 (*blue dashed line*), UrQMD 3.4 (*black solid line*) and HIJING 1.411 (*violet doted line*). *Right*: relative difference of simulated T with respect to experimental data. Coloured bands correspond to multiples of σ_{tot} of the experimental data.

($\sigma_{tot} > 10\%$), which shows an agreement within 2σ between the experiment and the tested models. UrQMD diverges the least from the results (agreement within 1σ).

The most notable signature of the onset of deconfinement has been the energy dependence of K^+/π^+ ratio. Experimental results on K/π ratio were obtained with

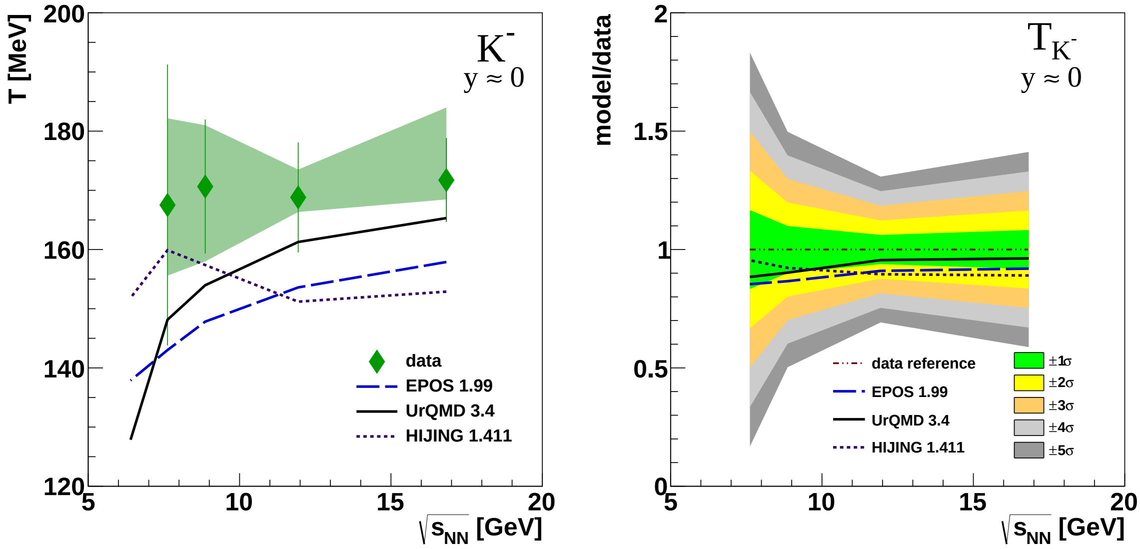

Fig. 6.15: *Left*: comparison of the energy dependence of the inverse slope parameter of K^- spectra in the mid-rapidity for central ^{7}Be+^{9}Be collisions with theoretical models: EPOS 1.99 (*blue dashed line*), UrQMD 3.4 (*black solid line*) and HIJING 1.411 (*violet doted line*). *Right*: relative difference of simulated T with respect to experimental data. Coloured bands correspond to multiples of σ_{tot} of the experimental data.

the procedure described in section 6.3. Figures 6.16 and 6.17 contain the comparison of the results with theoretical models. Simulated π yields were obtained via integration of the $d^2n/dp_{\rm T}dy$ spectra of positively- and negatively-charged pions in the 0.0< $p_{\rm T}$ <1.0 GeV/c range. The models that gives predictions quantitatively

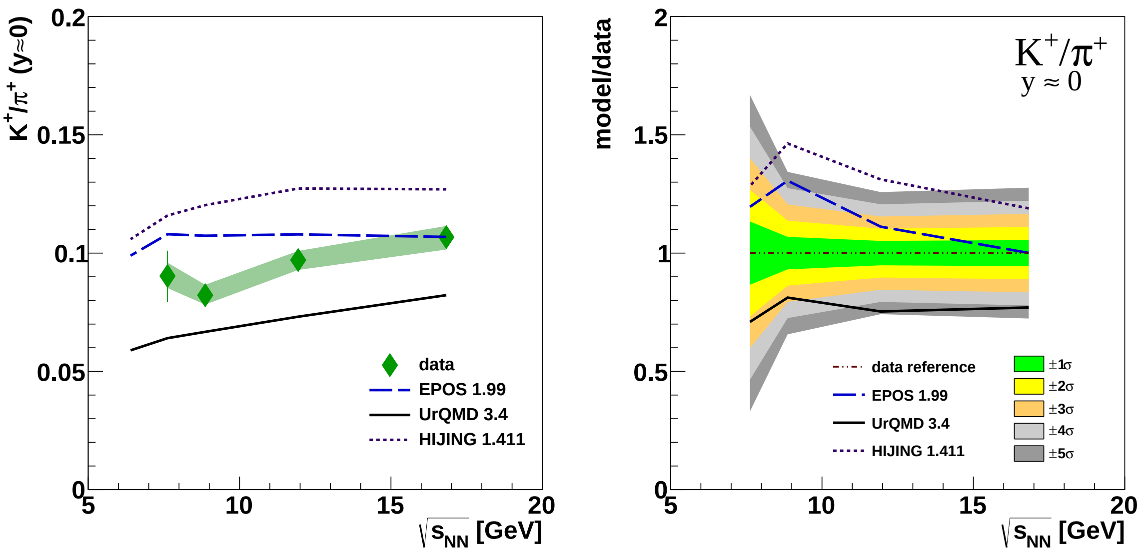

Fig. 6.16: *Left*: comparison of the energy dependence of K^+/π^+ yields ratio in the mid-rapidity for central ^{7}Be+^{9}Be collisions with theoretical models: EPOS 1.99 (*blue dashed line*), UrQMD 3.4 (*black solid line*) and HIJING 1.411 (*violet doted line*). *Right*: relative difference of simulated K^+/π^+ ratio with respect to experimental data. Coloured bands correspond to multiples of σ_{tot} of the experimental data.

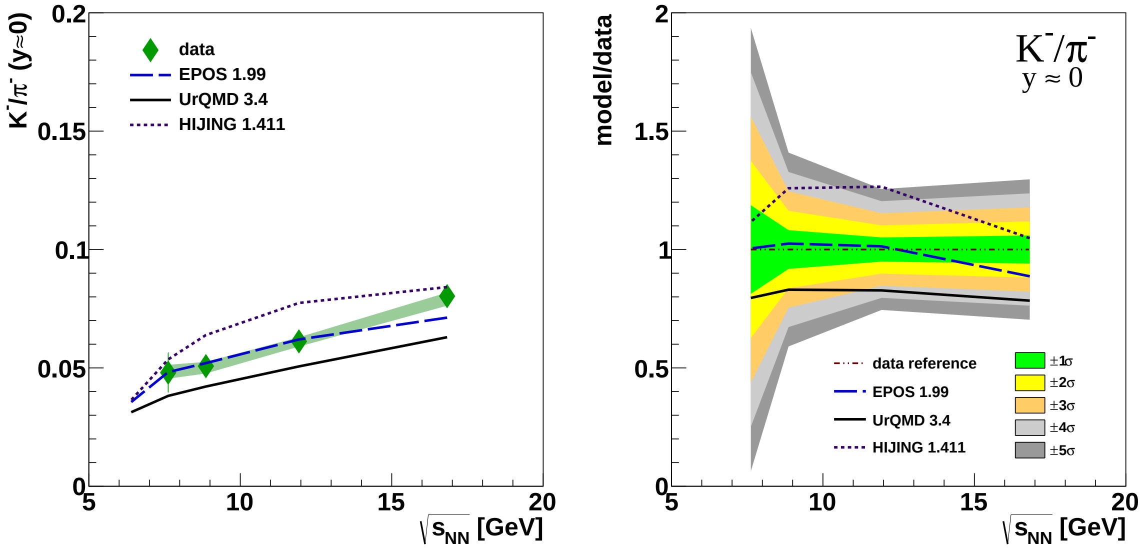

Fig. 6.17: *Left*: comparison of the energy dependence of K^-/π^- yields ratio in the mid-rapidity for central ^{7}Be+^{9}Be collisions with theoretical models: EPOS 1.99 (*blue dashed line*), UrQMD 3.4 (*black solid line*) and HIJING 1.411 (*violet doted line*). *Right*: relative difference of simulated K^-/π^- ratio with respect to experimental data. Coloured bands correspond to multiples of σ_{tot} of the experimental data.

closest to the experimental results is EPOS. The agreement of the model calculations and the experimental energy dependence of the K^+/π^+ ratio varies with the energy from 1σ to 5σ. In the case of the K^-/π^- ratio, the EPOS model describes the experimental results reasonably well. The most significant divergence occurs at the highest NA61/SHINE energy. Still, the model agrees well with the data (within 2σ). Two other models show less compliance with the experimental data for energy dependency of the K^+/π^+ ratio as well as K^-/π^- ratio.

Surprisingly, even though UrQMD is the best model to parameterise p_{T} spectra and yields of charged kaons in the mid-rapidity, EPOS works better for the a calculation of the produced particle ratios.

Chapter 7

Summary and outlook

This thesis presents experimental results on inclusive spectra of charged hadrons, K^+, K^-, π^+, π^+, p, $\overline{p}$, for ^{7}Be+^{9}Be collisions at four beam momenta: 30*A*, 40*A*, 75*A* and 150*A* GeV/*c*. The measurements were performed by the NA61/SHINE collaboration using a large acceptance hadron spectrometer located at CERN SPS. For the first time, Be+Be collisions at SPS energy range were measured and the spectra of identified-hadrons produced in such collisions were studied.

Two-dimensional particle spectra were obtained with the analysis technique based on the combination of the time-of-flight and energy-loss measurements and defined in rapidity and transverse momentum phase-space. The identified-particle multiplicities were corrected for the detector effects, reconstruction efficiency and contribution of the particles originating from the weak decays and secondary interactions. Further, statistical and systematic uncertainties were calculated and presented along with the final results.

The main goal of this thesis was studying the multiplicity of charged K meson in mid-rapidity. The K mesons, next to the Λ barion, are the most populated strange hadrons produced in ion-ion collisions in the SPS energy range, i.e. at high barion density. The strangeness production gives insight into the transition between confineg matter and QGP.

The charged kaon p_T spectra were parametrised, then the K meson yields in mid-rapidity were obtained. The K meson yields in mid-rapidity increase with the collision energy from $dn/dy = 0.209 \pm 0.025_{(stat)} \pm 0.009_{(sys)}$ to $dn/dy = 0.338 \pm 0.008_{(stat)} \pm 0.009_{(sys)}$ for positively-charged and from $dn/dy = 0.111 \pm 0.019_{(stat)} \pm 0.007_{(sys)}$ to $dn/dy = 0.254 \pm 0.008_{(stat)} \pm 0.013_{(sys)}$ for negatively-charged K mesons.

The ratio of charged kaon yield to charged pion yield in mid-rapidity was calculated and compared with all available results from (ultra-)relativistic heavy-ion collisions. Strangeness production normalised to the entropy production is one of the most notable signatures of the onset of deconfinement anticipated by the SMES. This model predicts non-monotonic changes of the energy dependence of the strangeness-to-entropy ratio due to canonical suppression of strangeness production while QGP appears. It also suggests that the strangeness-to-entropy ratio rapidly increases with the number of participants, or colliding-system size. The K^+/π^+ ratio in mid-rapidity from ^{7}Be+^{9}Be collisions changes with the collision energy from $0.090 \pm 0.011_{(stat)} \pm 0.005_{(sys)}$ up to $0.107 \pm 0.003_{(stat)} \pm 0.005_{(sys)}$: it increases monotonically within the total error bars. The discussed K^+/π^+ energy dependence is at the level of that from p+p interactions, they vary from each other for 5-20%. This means that the results on K^+/π^+ ratio in mid-rapidity from ^{7}Be+^{9}Be collisions are far below the predictions of statistical models, like SMES and HRG. The K^-/π^- ratio in mid-rapidity increases from $0.048 \pm 0.008_{(stat)} \pm 0.004_{(sys)}$ to $0.080 \pm 0.003_{(stat)} \pm 0.005_{(sys)}$ with the energy and agrees within total error bars with the one from p+p interactions. The results on strangeness-to-entropy ratio presented in this thesis indicate that Be+Be collisions are similar to binary p+p interactions.

Characteristics of the p_T spectra of charged kaons in mid-rapidity, namely the inverse slope parameters, T_{K^+} and T_{K^-}, were extracted from the spectra parametrisation and compared with all available data in (ultra-)relativistic energy range. The energy dependence of the inverse slope parameter in central ^{7}Be+^{9}Be collisions qualitatively resembles the one from the most central Pb+Pb collisions observed by the NA49 experiment and those predicted by SMES due to the existence of the confined-deconfined mixed phase of strongly interacting matter. The inverse slope parameter increases with the collision energy, for positively-charged kaons from $152.87 \pm 16.91_{(stat)} \pm 12.41_{(sys)}$ to $165.33 \pm 5.18_{(stat)} \pm 6.97_{(sys)}$, and negatively-charged kaons from $167.523 \pm 23.7199_{(stat)} \pm 14.6376_{(sys)}$ to $171.726 \pm 7.07145_{(stat)} \pm 12.265_{(sys)}$. The results on the T parameter from ^{7}Be+^{9}Be are about 6-12% higher than those from p+p interactions, which can be associated with a slightly higher kinetic freeze-out temperature [14] or/and some collective transverse effects pronounced more in heavier systems.

The results on K^+ and K^- p_T spectra in mid-rapidity, their parametrisation and yields, as well as the strangeness-to-entropy ratio, were compared with calculations of the microscopic models EPOS 1.99, UrQMD 3.4 and HIJING 1.411. All the models tested qualitatively reproduce p_T spectra of charged kaons in mid-rapidity. The one that gives results quantitatively compatible with the experiment is UrQMD. This model also describes the $K^{+/-}$ yield within 2σ and $T_{K^{+/-}}$ within 1σ, while the two other models show less compliance with the data. In the case of strangeness-to-entropy ratio, EPOS gives predictions closest to the experimental results. The agreement of the model calculations with the experimental energy dependence of the K/π ratio varies with the energy from 1σ to 5σ. The comparison between the experimental results and theoretical predictions presented in this thesis suggests that there is still a need to improve theories describing the collisions of small systems at high energies.

The comparison of the results presented in this thesis with world data, as well as a preliminary comparison of the results stemming from other observables of hadron-production properties, which are not discussed in this thesis, like, e.g. multiplicity fluctuations, studied as a function of the system size, show that ^{7}Be+^{9}Be results are very close to those from p+p interactions independently of the collision energy. Moreover, the data indicate a jump of the observable values when going from light (p+p, Be+Be) to intermediate/heavy (Ar+Sc, Pb+Pb) systems, which can be interpreted as the beginning of creation of large clusters of strongly interacting matter - the *onset of fireball* [82].

The interpretation of the results reported in this work requires the comparison with hadron spectra produced in ^{7}Be + ^{9}Be collisions at beam momentum of 13*A* and 20*A* GeV/c, which are going to be analysed separately, not in the framework of this dissertation, as well as final results from the ongoing analyses of Ar+Sc, Xe+La and Pb+Pb collisions collected by NA61/SHINE at the SPS energies, also not part of this dissertation. The two-dimensional scan of the phase-space performed by the NA61/SHINE experiment was completed at the end of 2018. Hence, the overall comparison of the results obtained from all the systems studied, as well as the subsequent deeper understanding of the strongly interacting matter phase transition, might be possible in the mid-term future. The theoretical understanding of the properties of the phase transition is still rather poor and the NA61/SHINE results present challenges for theoretical models.

The future NA61/SHINE physics program, focused on the study of charm production, is a natural extension of the previous studies of the phase transition to the quark-gluon plasma. It, among others, addresses the question of the mechanism of charm production and the impact of the onset of deconfinement on charm production. The data on the mean number of charm–anti-charm quark pairs, $\langle c\bar{c} \rangle$, produced in the full phase-space of heavy-ion collisions do not exist yet and NA61/SHINE aims at providing them in 2022-2024. For this purpose, a significant modification of the NA61/SHINE spectrometer is planned during the LS2 at CERN (2019-2020), which concerns a tenfold increase of the data taking rate (to about 1 kHz), construction of the Large Acceptance Vertex Detector and upgrade of the PSD. Moreover, new ToF detectors are planned to be constructed for particle identification at mid-rapidity, which is mainly motivated by possible future measurements related to the extension of the measurements of strangeness production.

The studies of the properties of nuclear matter in the region close to the maximum baryonic density are progressing at SIS18 (GSI), SPS (CERN) and RHIC (BNL). Furthermore, new projects like NICA (JINR), RHIC-fixed target (BNL) and SIS100 (GSI) are planned for the next following years. They should shed more light on: properties of hadrons and the nuclear matter equation of state, the onset of deconfinement and/or chiral symmetry restoration, signals of a phase transition and the critical point, and also provide means to verify and interpret the results contained in this dissertation.

Appendix A

Coordinate system and kinematic variables

A.1 Introduction

This appendix introduces the standard detector coordinate system of the NA61/SHINE experiment and the definition of the kinematic variables used in this thesis.

A.2 NA61/SHINE coordinate system

The coordinate system used in NA61/SHINE and this thesis is shown in Fig. 2.1. The origin of the coordinate system is located in the centre of VTPC-2, on the beamline. The system is right-handed and organised as follows:

- z axis is horizontal, coincidental with the beam line,
- x axis is horizontal, perpendicular to the z axis,
- y axis is vertical, pointing up.

The azimuthal angle, ϕ, is defined in the x–y plane in the way that $\phi = 0$ rad corresponds to the x axis and $\phi = \pi$ rad to the y axis. It is defined as follows:

$$\phi \equiv atan\frac{p_y}{p_x} \,. \tag{A.1}$$

The ϕ angle ranges form 0 to 2π rad. The polar angle, θ, is the angle from the z axis:

$$\theta \equiv asin\frac{p_{\mathrm{T}}}{p} \,. \tag{A.2}$$

The θ angle ranges from 0 to π rad and $\theta = 0$ corresponds to particles produced parallel to the beam particle, in the forward direction.

A.3 Kinematic variables

A.3.1 Total momentum and transverse variables

The total momentum is defined by the sum of all components of the momentum vector:

$$p = \sqrt{p_x^2 + p_y^2 + p_z^2}\,, \tag{A.3}$$

where p_x and p_y are the particle momentum components in the plane transverse to the beam axis (z), while p_z is a particle momentum component parallel to the beam axis (z). Hence, the z coordinate is defined along the beam axis, the transverse momentum, p_{T}, which is perpendicular to the beam axis and defined as:

$$p_{\mathrm{T}} = \sqrt{p_x^2 + p_y^2}\,. \tag{A.4}$$

The transverse mass is defined as:

$$m_{\mathrm{T}} = \sqrt{p_{\mathrm{T}}^2 c^{-2} + m^2}\,, \tag{A.5}$$

where m is an invariant mass of a given particle.

A.3.2 Rapidity

The rapidity definition is following:

$$y = \frac{1}{2} ln \frac{E + p_z c}{E - p_z c}\,, \tag{A.6}$$

where E is energy of the particle and p_z is its momentum component parallel to the beam line.

Rapidity is a dimensionless variable, invariant to the Lorentz transformation. It can be easily transformed from the laboratory frame to the centre-of-mass frame:

$$y_{CMS\ frame} = y_{LAB\ frame} + y_{CMS}\,, \tag{A.7}$$

where

$$y_{CMS} = atanh \frac{p_{beam} c}{E_{beam} + m_p c^2}\,. \tag{A.8}$$

p_{beam} is the beam momentum, $E_{beam} = \sqrt{p_{beam}^2 c^2 + m_p^2 c^4}$ stands for the beam energy and m_p is the mass of a nucleon (proton). In this thesis rapidity is always given in the centre-of-mass frame.

The so-called *mid-rapidity* region is defined as the one close to $y = 0$. It corresponds to particles produced perpendicularly to the beam line in the centre of mass system. The regions at $y > 0$ and $y < 0$ are called *forward* and *backward* rapidities, respectively.

A.4 Collision energy

In the collision of two particles of masses m_{beam} and m_{target}, respectively, the total center-of-mass energy is be expressed in the Lorentz-invariant form

$$\sqrt{s} = \sqrt{(E_{beam} + E_{target})^2 - (p_{beam} + p_{target})^2} \tag{A.9}$$

In a high-energy collision, usually the centre-of-mass energy per nucleon pair, $\sqrt{s_{NN}}$, further called collisions energy, is given as a reference. For $\sqrt{s_{NN}}$ masses m_{beam} and m_{target} are equal to the mass of the nucleon. In a fixed-target experiment, like NA61/SHINE, $p_{target} = 0$ and E_{target} is simply the mass of the ion used as a target.

Appendix B

Tabulated results

B.1 Introduction

This appendix summarises the numerical values of the double differential spectra

$$\frac{d^2n}{dy\,dp_T} \;[(\mathrm{GeV}/c)^{-1}] \tag{B.1}$$

of charged K^+, K^-, π^+, π^-, p and $\overline{p}$ produced in ^{7}Be+^{9}Be collisions at 30*A*, 40*A*, 75*A* and 150*A* GeV/*c*. For each bin content value the statistical (σ_{stat}) and systematic uncertainties (σ_{sys}) are given as a percent fraction of the value.

B.2 K^+ spectra

$p_{beam} = 30$ GeV/c

y		p_T [GeV/c]											
		$0.0 < p_T < 0.1$			$0.1 < p_T < 0.2$			$0.2 < p_T < 0.3$			$0.3 < p_T < 0.4$		
min	max	$\frac{d^2n}{dydp_T}$	σ_{stat}	σ_{sys}	$\frac{d^2n}{dydp_T}$	σ_{stat}	σ_{sys}	$\frac{d^2n}{dydp_T}$	σ_{stat}	σ_{sys}	$\frac{d^2n}{dydp_T}$	σ_{stat}	σ_{sys}
-0.6	-0.4	0.1206	38.6	45.9		–			–			–	
-0.4	-0.2	0.1381	23.2	12.9	0.2884	27.5	12.0	0.4142	38.2	18.4		–	
-0.2	0.0	0.1100	20.3	21.5	0.2651	30.0	14.7	0.3790	22.1	5.1	0.2990	22.5	18.1
0.0	0.2		–		0.2818	16.6	5.0	0.2731	20.0	6.1	0.3950	18.8	14.4
0.2	0.4		–			–		0.3896	19.7	10.5	0.3304	16.3	7.7

y		$0.4 < p_T < 0.6$			$0.6 < p_T < 0.8$		
min	max	$\frac{d^2n}{dydp_T}$	σ_{stat}	σ_{sys}	$\frac{d^2n}{dydp_T}$	σ_{stat}	σ_{sys}
-0.2	0.0	0.2333	22.4	19.1	0.2276	36.0	10.9
0.0	0.2	0.2547	17.0	14.0	0.2310	18.0	17.4
0.2	0.4	0.2801	13.0	4.2	0.1754	19.4	14.4
0.4	0.6	0.1760	32.6	9.8		–	

Tab. B.1: Numerical values $\frac{d^2n}{dydp_T}$ spectra of K^+ produced in ^{7}Be+^{9}Be collisions at 30 GeV/c.

$p_{\mathrm{beam}} = 40$ GeV/c

y		p_T [GeV/c]											
		$0.0 < p_T < 0.1$			$0.1 < p_T < 0.2$			$0.2 < p_T < 0.3$			$0.3 < p_T < 0.4$		
min	max	$\frac{d^2n}{dydp_T}$	σ_{stat}	σ_{sys}	$\frac{d^2n}{dydp_T}$	σ_{stat}	σ_{sys}	$\frac{d^2n}{dydp_T}$	σ_{stat}	σ_{sys}	$\frac{d^2n}{dydp_T}$	σ_{stat}	σ_{sys}
-0.6	-0.4	0.1005	27.4	16.8		–			–			–	
-0.4	-0.2	0.1213	13.2	12.6	0.2767	15.6	8.8	0.3462	23.8	14.7	0.1708	50.1	33.5
-0.2	0.0	0.1145	10.3	8.6	0.2846	10.9	6.7	0.3374	12.3	15.1	0.3568	12.6	12.1
0.0	0.2	0.1088	12.7	27.9	0.2817	12.0	5.0	0.3384	9.8	7.0	0.3329	7.7	6.3
0.2	0.4		–		0.2668	15.7	12.7	0.3363	9.6	19.0	0.3484	8.9	4.1

y		$0.4 < p_T < 0.5$			$0.5 < p_T < 0.6$			$0.6 < p_T < 0.7$			$0.7 < p_T < 0.8$		
min	max	$\frac{d^2n}{dydp_T}$	σ_{stat}	σ_{sys}	$\frac{d^2n}{dydp_T}$	σ_{stat}	σ_{sys}	$\frac{d^2n}{dydp_T}$	σ_{stat}	σ_{sys}	$\frac{d^2n}{dydp_T}$	σ_{stat}	σ_{sys}
-0.2	0.0	0.3487	14.1	9.3	0.2922	18.7	41.9	0.2387	17.9	30.3		–	
0.0	0.2	0.3364	11.9	8.2	0.2135	14.9	10.7	0.1872	15.7	17.6	0.1340	17.8	39.8
0.2	0.4	0.3450	9.1	7.9	0.2587	11.4	10.8	0.2583	11.2	9.2	0.1476	15.5	14.4

y		$0.8 < p_T < 0.9$		
min	max	$\frac{d^2n}{dydp_T}$	σ_{stat}	σ_{sys}
0.0	0.2	0.1160	19.5	9.0
0.2	0.4	0.0468	24.5	26.4

Tab. B.2: Numerical values $\frac{d^2n}{dydp_T}$ spectra of K^+ produced in ^{7}Be+^{9}Be collisions at 40 GeV/c.

$p_{\mathrm{beam}} = 75$ GeV/c

y		p_T [GeV/c]											
		$0.0 < p_T < 0.1$			$0.1 < p_T < 0.2$			$0.2 < p_T < 0.3$			$0.3 < p_T < 0.4$		
min	max	$\frac{d^2n}{dydp_T}$	σ_{stat}	σ_{sys}	$\frac{d^2n}{dydp_T}$	σ_{stat}	σ_{sys}	$\frac{d^2n}{dydp_T}$	σ_{stat}	σ_{sys}	$\frac{d^2n}{dydp_T}$	σ_{stat}	σ_{sys}
-0.2	0.0	0.1019	9.3	9.1	0.2994	9.6	5.2	0.4666	10.4	5.8	0.4742	10.8	10.9
0.0	0.2	0.1234	7.4	4.4	0.3453	5.7	4.5	0.4793	6.4	4.8	0.5015	7.0	3.8
0.2	0.4	0.1557	6.1	5.7	0.3186	4.6	5.5	0.4259	5.4	6.2	0.4598	5.9	3.7
0.4	0.6		–		0.3317	8.1	4.3	0.3810	7.2	10.0	0.3639	8.2	3.9

y		$0.4 < p_T < 0.5$			$0.5 < p_T < 0.6$			$0.6 < p_T < 0.7$			$0.7 < p_T < 0.8$		
min	max	$\frac{d^2n}{dydp_T}$	σ_{stat}	σ_{sys}	$\frac{d^2n}{dydp_T}$	σ_{stat}	σ_{sys}	$\frac{d^2n}{dydp_T}$	σ_{stat}	σ_{sys}	$\frac{d^2n}{dydp_T}$	σ_{stat}	σ_{sys}
-0.2	0.0	0.3850	11.6	11.7	0.2859	13.9	11.6	0.2732	12.1	13.7	0.2165	15.7	14.6
0.0	0.2	0.4397	8.0	10.5	0.3768	9.0	13.1	0.2237	11.3	13.8	0.1741	12.9	10.1
0.2	0.4	0.4216	6.4	4.6	0.3603	7.0	8.0	0.2515	8.6	12.3	0.1556	12.6	34.4
0.4	0.6	0.3869	9.7	8.6	0.3345	12.7	20.3		–			–	

y		$0.8 < p_T < 0.9$		
min	max	$\frac{d^2n}{dydp_T}$	σ_{stat}	σ_{sys}
-0.2	0.0	0.1764	15.6	16.9
0.0	0.2	0.1364	13.8	13.7
0.2	0.4	0.1434	13.3	18.8

Tab. B.3: Numerical values $\frac{d^2n}{dydp_T}$ spectra of K^+ produced in ^{7}Be+^{9}Be collisions at 75 GeV/c.

$p_{beam} = 150$ GeV/c

y		p_T [GeV/c]										
		$0.0 < p_T < 0.1$			$0.1 < p_T < 0.2$			$0.2 < p_T < 0.3$			$0.3 < p_T < 0.4$		
min	max	$\frac{d^2n}{dydp_T}$	σ_{stat}	σ_{sys}	$\frac{d^2n}{dydp_T}$	σ_{stat}	σ_{sys}	$\frac{d^2n}{dydp_T}$	σ_{stat}	σ_{sys}	$\frac{d^2n}{dydp_T}$	σ_{stat}	σ_{sys}
0.0	0.2	0.1504	10.0	13.1	0.4213	6.4	6.5	0.5757	6.7	7.1	0.5568	6.5	9.1
0.2	0.4	0.1360	6.3	3.1	0.3547	3.8	2.7	0.4750	4.1	3.2	0.4788	4.7	6.0
0.4	0.6	0.1625	6.2	39.4	0.3584	3.8	13.3	0.4421	3.3	7.5	0.4517	3.8	7.1
0.6	0.8	0.1092	7.5	6.8	0.3512	4.6	8.2	0.4119	4.9	5.7		–	

y		$0.4 < p_T < 0.5$			$0.5 < p_T < 0.6$			$0.6 < p_T < 0.7$			$0.7 < p_T < 0.8$		
min	max	$\frac{d^2n}{dydp_T}$	σ_{stat}	σ_{sys}	$\frac{d^2n}{dydp_T}$	σ_{stat}	σ_{sys}	$\frac{d^2n}{dydp_T}$	σ_{stat}	σ_{sys}	$\frac{d^2n}{dydp_T}$	σ_{stat}	σ_{sys}
-0.2	0.0		–			–		0.2339	14.1	18.6	0.2620	11.0	7.5
0.0	0.2	0.5287	6.4	6.4	0.4104	6.9	8.8	0.2668	8.1	12.8	0.2286	9.0	6.8
0.2	0.4	0.4534	5.3	6.1	0.3601	6.2	9.7	0.2387	10.0	9.5		–	
0.4	0.6	0.4455	5.8	15.7		–			–			–	

y		$0.8 < p_T < 0.9$			$0.9 < p_T < 1.0$		
min	max	$\frac{d^2n}{dydp_T}$	σ_{stat}	σ_{sys}	$\frac{d^2n}{dydp_T}$	σ_{stat}	σ_{sys}
-0.2	0.0	0.1289	14.3	9.4	0.1273	14.2	8.4
0.0	0.2	0.1490	13.9	14.3		–	

Tab. B.4: Numerical values $\frac{d^2n}{dydp_T}$ spectra of K^+ produced in ^{7}Be+^{9}Be collisions at 150 GeV/c.

B.3 K^- spectra

$p_{beam} = 30$ GeV/c

y		p_T [GeV/c]											
		$0.0 < p_T < 0.1$			$0.1 < p_T < 0.2$			$0.2 < p_T < 0.3$			$0.3 < p_T < 0.4$		
min	max	$\frac{d^2n}{dydp_T}$	σ_{stat}	σ_{sys}	$\frac{d^2n}{dydp_T}$	σ_{stat}	σ_{sys}	$\frac{d^2n}{dydp_T}$	σ_{stat}	σ_{sys}	$\frac{d^2n}{dydp_T}$	σ_{stat}	σ_{sys}
-0.6	-0.4	0.1206	38.6	45.9		–			–			–	
-0.4	-0.2	0.1381	23.2	12.9	0.2884	27.5	12.0	0.4142	38.2	18.4		–	
-0.2	0.0	0.1100	20.3	21.5	0.2651	30.0	14.7	0.3790	22.1	5.1	0.2990	22.5	18.1
0.0	0.2		–		0.2818	16.6	5.0	0.2731	20.0	6.1	0.3950	18.8	14.4
0.2	0.4		–			–		0.3896	19.7	10.5	0.3304	16.3	7.7

y		$0.4 < p_T < 0.6$			$0.6 < p_T < 0.8$		
min	max	$\frac{d^2n}{dydp_T}$	σ_{stat}	σ_{sys}	$\frac{d^2n}{dydp_T}$	σ_{stat}	σ_{sys}
-0.2	0.0	0.2333	22.4	19.1	0.2276	36.0	10.9
0.0	0.2	0.2547	17.0	14.0	0.2310	18.0	17.4
0.2	0.4	0.2801	13.0	4.2	0.1754	19.4	14.4
0.4	0.6	0.1760	32.6	9.8		–	

Tab. B.5: Numerical values $\frac{d^2n}{dydp_T}$ spectra of K^- produced in ^{7}Be+^{9}Be collisions at 30 GeV/c.

$p_{beam} = 40$ GeV/c

y		p_T [GeV/c]											
		$0.0 < p_T < 0.1$			$0.1 < p_T < 0.2$			$0.2 < p_T < 0.3$			$0.3 < p_T < 0.4$		
min	max	$\frac{d^2n}{dydp_T}$	σ_{stat}	σ_{sys}	$\frac{d^2n}{dydp_T}$	σ_{stat}	σ_{sys}	$\frac{d^2n}{dydp_T}$	σ_{stat}	σ_{sys}	$\frac{d^2n}{dydp_T}$	σ_{stat}	σ_{sys}
-0.6	-0.4	0.1005	27.4	16.8		–			–			–	
-0.4	-0.2	0.1213	13.2	12.6	0.2767	15.6	8.8	0.3462	23.8	14.7	0.1708	50.1	33.5
-0.2	0.0	0.1145	10.3	8.6	0.2846	10.9	6.7	0.3374	12.3	15.1	0.3568	12.6	12.1
0.0	0.2	0.1088	12.7	27.9	0.2817	12.0	5.0	0.3384	9.8	7.0	0.3329	7.7	6.3
0.2	0.4		–		0.2668	15.7	12.7	0.3363	9.6	19.0	0.3484	8.9	4.1

y		$0.4 < p_T < 0.5$			$0.5 < p_T < 0.6$			$0.6 < p_T < 0.7$			$0.7 < p_T < 0.8$		
min	max	$\frac{d^2n}{dydp_T}$	σ_{stat}	σ_{sys}	$\frac{d^2n}{dydp_T}$	σ_{stat}	σ_{sys}	$\frac{d^2n}{dydp_T}$	σ_{stat}	σ_{sys}	$\frac{d^2n}{dydp_T}$	σ_{stat}	σ_{sys}
-0.2	0.0	0.3487	14.1	9.3	0.2922	18.7	41.9	0.2387	17.9	30.3		–	
0.0	0.2	0.3364	11.9	8.2	0.2135	14.9	10.7	0.1872	15.7	17.6	0.1340	17.8	39.8
0.2	0.4	0.3450	9.1	7.9	0.2587	11.4	10.8	0.2583	11.2	9.2	0.1476	15.5	14.4

y		$0.8 < p_T < 0.9$		
min	max	$\frac{d^2n}{dydp_T}$	σ_{stat}	σ_{sys}
0.0	0.2	0.1160	19.5	9.0
0.2	0.4	0.0468	24.5	26.4

Tab. B.6: Numerical values $\frac{d^2n}{dydp_T}$ spectra of K^- produced in ^{7}Be+^{9}Be collisions at 40 GeV/c.

p_{beam} = 75 GeV/c

y min	y max	$0.0 < p_T < 0.1$ $\frac{d^2n}{dydp_T}$	σ_{stat}	σ_{sys}	$0.1 < p_T < 0.2$ $\frac{d^2n}{dydp_T}$	σ_{stat}	σ_{sys}	$0.2 < p_T < 0.3$ $\frac{d^2n}{dydp_T}$	σ_{stat}	σ_{sys}	$0.3 < p_T < 0.4$ $\frac{d^2n}{dydp_T}$	σ_{stat}	σ_{sys}
-0.2	0.0	0.1019	9.3	9.1	0.2994	9.6	5.2	0.4666	10.4	5.8	0.4742	10.8	10.9
0.0	0.2	0.1234	7.4	4.4	0.3453	5.7	4.5	0.4793	6.4	4.8	0.5015	7.0	3.8
0.2	0.4	0.1557	6.1	5.7	0.3186	4.6	5.5	0.4259	5.4	6.2	0.4598	5.9	3.7
0.4	0.6		–		0.3317	8.1	4.3	0.3810	7.2	10.0	0.3639	8.2	3.9

y min	y max	$0.4 < p_T < 0.5$ $\frac{d^2n}{dydp_T}$	σ_{stat}	σ_{sys}	$0.5 < p_T < 0.6$ $\frac{d^2n}{dydp_T}$	σ_{stat}	σ_{sys}	$0.6 < p_T < 0.7$ $\frac{d^2n}{dydp_T}$	σ_{stat}	σ_{sys}	$0.7 < p_T < 0.8$ $\frac{d^2n}{dydp_T}$	σ_{stat}	σ_{sys}
-0.2	0.0	0.3850	11.6	11.7	0.2859	13.9	11.6	0.2732	12.1	13.7	0.2165	15.7	14.6
0.0	0.2	0.4397	8.0	10.5	0.3768	9.0	13.1	0.2237	11.3	13.8	0.1741	12.9	10.1
0.2	0.4	0.4216	6.4	4.6	0.3603	7.0	8.0	0.2515	8.6	12.3	0.1556	12.6	34.4
0.4	0.6	0.3869	9.7	8.6	0.3345	12.7	20.3		–			–	

y min	y max	$0.8 < p_T < 0.9$ $\frac{d^2n}{dydp_T}$	σ_{stat}	σ_{sys}
-0.2	0.0	0.1764	15.6	16.9
0.0	0.2	0.1364	13.8	13.7
0.2	0.4	0.1434	13.3	18.8

Tab. B.7: Numerical values $\frac{d^2n}{dydp_T}$ spectra of K^- produced in ^{7}Be+^{9}Be collisions at 75 GeV/c.

p_{beam} = 150 GeV/c

y min	y max	$0.0 < p_T < 0.1$ $\frac{d^2n}{dydp_T}$	σ_{stat}	σ_{sys}	$0.1 < p_T < 0.2$ $\frac{d^2n}{dydp_T}$	σ_{stat}	σ_{sys}	$0.2 < p_T < 0.3$ $\frac{d^2n}{dydp_T}$	σ_{stat}	σ_{sys}	$0.3 < p_T < 0.4$ $\frac{d^2n}{dydp_T}$	σ_{stat}	σ_{sys}
0.0	0.2	0.1504	10.0	13.1	0.4213	6.4	6.5	0.5757	6.7	7.1	0.5568	6.5	9.1
0.2	0.4	0.1360	6.3	3.1	0.3547	3.8	2.7	0.4750	4.1	3.2	0.4788	4.7	6.0
0.4	0.6	0.1625	6.2	39.4	0.3584	3.8	13.3	0.4421	3.3	7.5	0.4517	3.8	7.1
0.6	0.8	0.1092	7.5	6.8	0.3512	4.6	8.2	0.4119	4.9	5.7		–	

y min	y max	$0.4 < p_T < 0.5$ $\frac{d^2n}{dydp_T}$	σ_{stat}	σ_{sys}	$0.5 < p_T < 0.6$ $\frac{d^2n}{dydp_T}$	σ_{stat}	σ_{sys}	$0.6 < p_T < 0.7$ $\frac{d^2n}{dydp_T}$	σ_{stat}	σ_{sys}	$0.7 < p_T < 0.8$ $\frac{d^2n}{dydp_T}$	σ_{stat}	σ_{sys}
-0.2	0.0		–			–		0.2339	14.1	18.6	0.2620	11.0	7.5
0.0	0.2	0.5287	6.4	6.4	0.4104	6.9	8.8	0.2668	8.1	12.8	0.2286	9.0	6.8
0.2	0.4	0.4534	5.3	6.1	0.3601	6.2	9.7	0.2387	10.0	9.5		–	
0.4	0.6	0.4455	5.8	15.7		–			–			–	

y min	y max	$0.8 < p_T < 0.9$ $\frac{d^2n}{dydp_T}$	σ_{stat}	σ_{sys}	$0.9 < p_T < 1.0$ $\frac{d^2n}{dydp_T}$	σ_{stat}	σ_{sys}
-0.2	0.0	0.1289	14.3	9.4	0.1273	14.2	8.4
0.0	0.2	0.1490	13.9	14.3		–	

Tab. B.8: Numerical values $\frac{d^2n}{dydp_T}$ spectra of K^- produced in ^{7}Be+^{9}Be collisions at 150 GeV/c.

B.4 π^+ spectra

$p_{\mathrm{beam}} = 30$ GeV/c

y		p_T [GeV/c] $0.0 < p_T < 0.1$			$0.1 < p_T < 0.2$			$0.2 < p_T < 0.3$			$0.3 < p_T < 0.4$		
min	max	$\frac{d^2n}{dydp_T}$	σ_{stat}	σ_{sys}	$\frac{d^2n}{dydp_T}$	σ_{stat}	σ_{sys}	$\frac{d^2n}{dydp_T}$	σ_{stat}	σ_{sys}	$\frac{d^2n}{dydp_T}$	σ_{stat}	σ_{sys}
0.2	0.4		–			–		4.5827	9.5	8.7	4.0609	7.4	2.7
0.4	0.6	1.9501	13.5	19.9	4.7903	5.4	3.9	4.2662	4.5	3.5	3.2286	5.1	2.7
0.6	0.8	1.7944	4.2	7.7	4.5883	3.5	4.1	4.0352	4.0	1.9	2.9578	4.4	2.2
0.8	1.0	1.5280	3.7	6.5	4.0625	3.1	2.7	3.8778	3.8	1.8	2.4563	7.5	4.5
1.0	1.2	1.5267	3.6	10.5	3.3582	4.0	1.2		–			–	

y		$0.4 < p_T < 0.6$			$0.6 < p_T < 0.8$		
min	max	$\frac{d^2n}{dydp_T}$	σ_{stat}	σ_{sys}	$\frac{d^2n}{dydp_T}$	σ_{stat}	σ_{sys}
0.0	0.2	3.6921	10.4	15.3	1.1287	11.5	8.7
0.2	0.4	2.2752	4.7	3.4	1.0239	6.8	2.9
0.4	0.6	1.9015	4.6	1.9	0.8215	7.4	2.3
0.6	0.8	1.6304	4.7	1.5		–	

Tab. B.9: Numerical values $\frac{d^2n}{dydp_T}$ spectra of π^+ produced in ^{7}Be+^{9}Be collisions at 30 GeV/c.

$p_{\mathrm{beam}} = 40$ GeV/c

y		p_T [GeV/c] $0.0 < p_T < 0.1$			$0.1 < p_T < 0.2$			$0.2 < p_T < 0.3$			$0.3 < p_T < 0.4$		
min	max	$\frac{d^2n}{dydp_T}$	σ_{stat}	σ_{sys}	$\frac{d^2n}{dydp_T}$	σ_{stat}	σ_{sys}	$\frac{d^2n}{dydp_T}$	σ_{stat}	σ_{sys}	$\frac{d^2n}{dydp_T}$	σ_{stat}	σ_{sys}
0.2	0.4		–			–		4.8422	5.8	6.6	3.6428	3.5	4.1
0.4	0.6		–		4.8539	3.9	7.2	4.8542	2.4	2.8	3.5031	2.8	3.4
0.6	0.8	2.0721	2.8	10.1	4.9180	2.0	3.0	4.4819	2.1	3.3	3.3763	2.4	3.0
0.8	1.0	1.9778	1.9	13.3	4.2804	1.8	2.2	4.2568	1.9	3.8	3.0692	4.0	5.0
1.0	1.2	1.7216	1.7	7.5	3.8939	1.7	3.5	3.2353	6.3	3.4		–	
1.2	1.4	1.4535	3.0	11.9	3.2209	7.9	8.2		–			–	

y		$0.4 < p_T < 0.5$			$0.5 < p_T < 0.6$			$0.6 < p_T < 0.7$			$0.7 < p_T < 0.8$		
min	max	$\frac{d^2n}{dydp_T}$	σ_{stat}	σ_{sys}	$\frac{d^2n}{dydp_T}$	σ_{stat}	σ_{sys}	$\frac{d^2n}{dydp_T}$	σ_{stat}	σ_{sys}	$\frac{d^2n}{dydp_T}$	σ_{stat}	σ_{sys}
0.2	0.4	2.5432	3.6	3.9	1.7643	4.3	6.2	1.0742	5.6	5.9	0.7303	6.7	6.6
0.4	0.6	2.4226	3.3	2.9	1.6618	4.0	4.5	1.0125	4.9	4.3	0.6781	7.1	6.5
0.6	0.8	2.2731	3.2	4.2		–			–			–	
14.4													

y		$0.8 < p_T < 0.9$		
min	max	$\frac{d^2n}{dydp_T}$	σ_{stat}	σ_{sys}
0.0	0.2	0.5108	8.8	4.5
0.2	0.4	0.4626	8.4	9.3
0.4	0.6	0.0348	30.3	13.3

Tab. B.10: Numerical values $\frac{d^2n}{dydp_T}$ spectra of π^+ produced in ^{7}Be+^{9}Be collisions at 40 GeV/c.

$p_{\text{beam}} = 75$ GeV/c

y		p_T [GeV/c]											
		$0.0 < p_T < 0.1$			$0.1 < p_T < 0.2$			$0.2 < p_T < 0.3$			$0.3 < p_T < 0.4$		
min	max	$\frac{d^2n}{dydp_T}$	σ_{stat}	σ_{sys}	$\frac{d^2n}{dydp_T}$	σ_{stat}	σ_{sys}	$\frac{d^2n}{dydp_T}$	σ_{stat}	σ_{sys}	$\frac{d^2n}{dydp_T}$	σ_{stat}	σ_{sys}
0.2	0.4		–			–			–		4.0400	4.4	6.5
0.4	0.6		–			–			–		4.2081	2.2	3.2
0.6	0.8		–		4.9553	3.4	3.2	5.3059	1.7	3.5	3.8699	1.9	3.3
0.8	1.0	2.1220	4.2	4.7	5.0490	1.5	3.0	4.6728	1.5	2.1	3.6379	1.8	1.7
1.0	1.2	2.0843	1.4	3.1	4.3258	1.2	2.2	4.2976	1.5	2.5		–	
1.2	1.4	1.8568	1.5	2.1	4.1512	1.1	2.0		–			–	
1.4	1.6	1.6657	1.7	2.4	3.6329	3.2	2.8		–			–	

y		$0.4 < p_T < 0.5$			$0.5 < p_T < 0.6$			$0.6 < p_T < 0.7$			$0.7 < p_T < 0.8$		
min	max	$\frac{d^2n}{dydp_T}$	σ_{stat}	σ_{sys}	$\frac{d^2n}{dydp_T}$	σ_{stat}	σ_{sys}	$\frac{d^2n}{dydp_T}$	σ_{stat}	σ_{sys}	$\frac{d^2n}{dydp_T}$	σ_{stat}	σ_{sys}
0.0	0.2		–			–		1.3150	5.0	3.4	0.9520	6.1	3.8
0.2	0.4	2.9124	3.1	3.8	1.9717	3.5	2.1	1.2508	4.3	5.4	0.7585	5.4	6.5
0.4	0.6	2.9659	2.5	4.4	1.9236	3.0	2.3	1.3074	3.5	3.5	0.8206	6.0	2.5
0.6	0.8	2.7974	2.2	3.5	1.7627	3.5	4.6		–			–	

y		$0.8 < p_T < 0.9$		
min	max	$\frac{d^2n}{dydp_T}$	σ_{stat}	σ_{sys}
0.0	0.2	0.6167	6.9	5.4
0.2	0.4	0.5480	6.2	4.4
0.4	0.6	0.5698	7.9	10.0

Tab. B.11: Numerical values $\frac{d^2n}{dydp_T}$ spectra of π^+ produced in ^{7}Be+^{9}Be collisions at 75 GeV/c.

$p_{\text{beam}} = 150$ GeV/c

y		p_T [GeV/c]											
		$0.0 < p_T < 0.1$			$0.1 < p_T < 0.2$			$0.2 < p_T < 0.3$			$0.3 < p_T < 0.4$		
min	max	$\frac{d^2n}{dydp_T}$	σ_{stat}	σ_{sys}	$\frac{d^2n}{dydp_T}$	σ_{stat}	σ_{sys}	$\frac{d^2n}{dydp_T}$	σ_{stat}	σ_{sys}	$\frac{d^2n}{dydp_T}$	σ_{stat}	σ_{sys}
0.4	0.6		–			–			–		4.4095	3.2	5.9
0.6	0.8		–			–		5.8892	2.7	4.6	4.5092	1.6	1.8
0.8	1.0		–			–		5.6347	1.3	2.6	3.8503	1.5	5.1
1.0	1.2		–		5.2584	1.1	1.7	4.8119	1.0	2.8		–	
1.2	1.4	2.1274	2.0	1.5	4.7627	1.0	1.3	4.8007	1.2	7.5		–	
1.4	1.6	1.9673	1.5	2.5	4.4949	1.1	9.3		–			–	
1.6	1.8	1.9417	1.7	24.9		–			–			–	
1.8	2.0	1.4249	2.4	8.2		–			–			–	

0.0	0.2		–			–		1.5744	5.2	6.5	1.0372	4.9	2.2
0.2	0.4		–		2.2333	3.2	4.3	1.5581	3.4	1.9	0.9491	4.7	4.4
0.4	0.6	3.3134	2.2	1.8	2.1782	2.6	2.3	1.2863	4.4	1.6		–	
0.6	0.8	2.9720	2.0	3.0		–			–			–	

y		$0.8 < p_T < 0.9$			$0.9 < p_T < 1.0$		
min	max	$\frac{d^2n}{dydp_T}$	σ_{stat}	σ_{sys}	$\frac{d^2n}{dydp_T}$	σ_{stat}	σ_{sys}
0.0	0.2	0.6956	5.7	2.1	0.4269	8.2	3.5

Tab. B.12: Numerical values $\frac{d^2n}{dydp_T}$ spectra of π^+ produced in ^{7}Be+^{9}Be collisions at 150 GeV/c.

B.5 π^- spectra

$p_{\text{beam}} = 30$ GeV/c

y		p_T [GeV/c]											
		$0.0 < p_T < 0.1$			$0.1 < p_T < 0.2$			$0.2 < p_T < 0.3$			$0.3 < p_T < 0.4$		
min	max	$\frac{d^2n}{dydp_T}$	σ_{stat}	σ_{sys}	$\frac{d^2n}{dydp_T}$	σ_{stat}	σ_{sys}	$\frac{d^2n}{dydp_T}$	σ_{stat}	σ_{sys}	$\frac{d^2n}{dydp_T}$	σ_{stat}	σ_{sys}
0.2	0.4		–			–		4.5827	9.5	8.7	4.0609	7.4	2.7
0.4	0.6	1.9501	13.5	19.9	4.7903	5.4	3.9	4.2662	4.5	3.5	3.2286	5.1	2.7
0.6	0.8	1.7944	4.2	7.7	4.5883	3.5	4.1	4.0352	4.0	1.9	2.9578	4.4	2.2
0.8	1.0	1.5280	3.7	6.5	4.0625	3.1	2.7	3.8778	3.8	1.8	2.4563	7.5	4.5
1.0	1.2	1.5267	3.6	10.5	3.3582	4.0	1.2		–			–	

y		$0.4 < p_T < 0.6$			$0.6 < p_T < 0.8$		
min	max	$\frac{d^2n}{dydp_T}$	σ_{stat}	σ_{sys}	$\frac{d^2n}{dydp_T}$	σ_{stat}	σ_{sys}
0.0	0.2	3.6921	10.4	15.3	1.1287	11.5	8.7
0.2	0.4	2.2752	4.7	3.4	1.0239	6.8	2.9
0.4	0.6	1.9015	4.6	1.9	0.8215	7.4	2.3
0.6	0.8	1.6304	4.7	1.5		–	

Tab. B.13: Numerical values $\frac{d^2n}{dydp_T}$ spectra of π^- produced in ^{7}Be+^{9}Be collisions at 30 GeV/c.

$p_{\text{beam}} = 40$ GeV/c

y		p_T [GeV/c]											
		$0.0 < p_T < 0.1$			$0.1 < p_T < 0.2$			$0.2 < p_T < 0.3$			$0.3 < p_T < 0.4$		
min	max	$\frac{d^2n}{dydp_T}$	σ_{stat}	σ_{sys}	$\frac{d^2n}{dydp_T}$	σ_{stat}	σ_{sys}	$\frac{d^2n}{dydp_T}$	σ_{stat}	σ_{sys}	$\frac{d^2n}{dydp_T}$	σ_{stat}	σ_{sys}
0.2	0.4		–			–		4.8422	5.8	6.6	3.6428	3.5	4.1
0.4	0.6		–		4.8539	3.9	7.2	4.8542	2.4	2.8	3.5031	2.8	3.4
0.6	0.8	2.0721	2.8	10.1	4.9180	2.0	3.0	4.4819	2.1	3.3	3.3763	2.4	3.0
0.8	1.0	1.9778	1.9	13.3	4.2804	1.8	2.2	4.2568	1.9	3.8	3.0692	4.0	5.0
1.0	1.2	1.7216	1.7	7.5	3.8939	1.7	3.5	3.2353	6.3	3.4		–	
1.2	1.4	1.4535	3.0	11.9	3.2209	7.9	8.2		–			–	

y		$0.4 < p_T < 0.5$			$0.5 < p_T < 0.6$			$0.6 < p_T < 0.7$			$0.7 < p_T < 0.8$		
min	max	$\frac{d^2n}{dydp_T}$	σ_{stat}	σ_{sys}	$\frac{d^2n}{dydp_T}$	σ_{stat}	σ_{sys}	$\frac{d^2n}{dydp_T}$	σ_{stat}	σ_{sys}	$\frac{d^2n}{dydp_T}$	σ_{stat}	σ_{sys}
0.2	0.4	2.5432	3.6	3.9	1.7643	4.3	6.2	1.0742	5.6	5.9	0.7303	6.7	6.6
0.4	0.6	2.4226	3.3	2.9	1.6618	4.0	4.5	1.0125	4.9	4.3	0.6781	7.1	6.5
0.6	0.8	2.2731	3.2	4.2		–			–			–	

y		$0.8 < p_T < 0.9$		
min	max	$\frac{d^2n}{dydp_T}$	σ_{stat}	σ_{sys}
0.0	0.2	0.5108	8.8	4.5
0.2	0.4	0.4626	8.4	9.3
0.4	0.6	0.0348	30.3	13.3

Tab. B.14: Numerical values $\frac{d^2n}{dydp_T}$ spectra of π^- produced in ^{7}Be+^{9}Be collisions at 40 GeV/c.

$p_{\text{beam}} = 75$ GeV/c

y		p_T [GeV/c] $0.0 < p_T < 0.1$			$0.1 < p_T < 0.2$			$0.2 < p_T < 0.3$			$0.3 < p_T < 0.4$		
min	max	$\frac{d^2n}{dydp_T}$	σ_{stat}	σ_{sys}	$\frac{d^2n}{dydp_T}$	σ_{stat}	σ_{sys}	$\frac{d^2n}{dydp_T}$	σ_{stat}	σ_{sys}	$\frac{d^2n}{dydp_T}$	σ_{stat}	σ_{sys}
0.2	0.4		–			–			–		4.0400	4.4	6.5
0.4	0.6		–			–			–		4.2081	2.2	3.2
0.6	0.8		–		4.9553	3.4	3.2	5.3059	1.7	3.5	3.8699	1.9	3.3
0.8	1.0	2.1220	4.2	4.7	5.0490	1.5	3.0	4.6728	1.5	2.1	3.6379	1.8	1.7
1.0	1.2	2.0843	1.4	3.1	4.3258	1.2	2.2	4.2976	1.5	2.5		–	
1.2	1.4	1.8568	1.5	2.1	4.1512	1.1	2.0		–			–	
1.4	1.6	1.6657	1.7	2.4	3.6329	3.2	2.8		–			–	

y		$0.4 < p_T < 0.5$			$0.5 < p_T < 0.6$			$0.6 < p_T < 0.7$			$0.7 < p_T < 0.8$		
min	max	$\frac{d^2n}{dydp_T}$	σ_{stat}	σ_{sys}	$\frac{d^2n}{dydp_T}$	σ_{stat}	σ_{sys}	$\frac{d^2n}{dydp_T}$	σ_{stat}	σ_{sys}	$\frac{d^2n}{dydp_T}$	σ_{stat}	σ_{sys}
0.0	0.2		–			–		1.3150	5.0	3.4	0.9520	6.1	3.8
0.2	0.4	2.9124	3.1	3.8	1.9717	3.5	2.1	1.2508	4.3	5.4	0.7585	5.4	6.5
0.4	0.6	2.9659	2.5	4.4	1.9236	3.0	2.3	1.3074	3.5	3.5	0.8206	6.0	2.5
0.6	0.8	2.7974	2.2	3.5	1.7627	3.5	4.6		–			–	

y		$0.8 < p_T < 0.9$		
min	max	$\frac{d^2n}{dydp_T}$	σ_{stat}	σ_{sys}
0.0	0.2	0.6167	6.9	5.4
0.2	0.4	0.5480	6.2	4.4
0.4	0.6	0.5698	7.9	10.0

Tab. B.15: Numerical values $\frac{d^2n}{dydp_T}$ spectra of π^- produced in ^{7}Be+^{9}Be collisions at 75 GeV/c.

$p_{\text{beam}} = 150$ GeV/c

y		p_T [GeV/c] $0.0 < p_T < 0.1$			$0.1 < p_T < 0.2$			$0.2 < p_T < 0.3$			$0.3 < p_T < 0.4$		
min	max	$\frac{d^2n}{dydp_T}$	σ_{stat}	σ_{sys}	$\frac{d^2n}{dydp_T}$	σ_{stat}	σ_{sys}	$\frac{d^2n}{dydp_T}$	σ_{stat}	σ_{sys}	$\frac{d^2n}{dydp_T}$	σ_{stat}	σ_{sys}
0.4	0.6		–			–			–		4.4095	3.2	5.9
0.6	0.8		–			–		5.8892	2.7	4.6	4.5092	1.6	1.8
0.8	1.0		–			–		5.6347	1.3	2.6	3.8503	1.5	5.1
1.0	1.2		–		5.2584	1.1	1.7	4.8119	1.0	2.8		–	
1.2	1.4	2.1274	2.0	1.5	4.7627	1.0	1.3	4.8007	1.2	7.5		–	
1.4	1.6	1.9673	1.5	2.5	4.4949	1.1	9.3		–			–	
1.6	1.8	1.9417	1.7	24.9		–			–			–	
1.8	2.0	1.4249	2.4	8.2		–			–			–	

y		$0.4 < p_T < 0.5$			$0.5 < p_T < 0.6$			$0.6 < p_T < 0.7$			$0.7 < p_T < 0.8$		
min	max	$\frac{d^2n}{dydp_T}$	σ_{stat}	σ_{sys}	$\frac{d^2n}{dydp_T}$	σ_{stat}	σ_{sys}	$\frac{d^2n}{dydp_T}$	σ_{stat}	σ_{sys}	$\frac{d^2n}{dydp_T}$	σ_{stat}	σ_{sys}
0.0	0.2		–			–		1.5744	5.2	6.5	1.0372	4.9	2.2
0.2	0.4		–		2.2333	3.2	4.3	1.5581	3.4	1.9	0.9491	4.7	4.4
0.4	0.6	3.3134	2.2	1.8	2.1782	2.6	2.3	1.2863	4.4	1.6		–	
0.6	0.8	2.9720	2.0	3.0		–			–			–	

y		$0.8 < p_T < 0.9$			$0.9 < p_T < 1.0$		
min	max	$\frac{d^2n}{dydp_T}$	σ_{stat}	σ_{sys}	$\frac{d^2n}{dydp_T}$	σ_{stat}	σ_{sys}
0.0	0.2	0.6956	5.7	2.1	0.4269	8.2	3.5

Tab. B.16: Numerical values $\frac{d^2n}{dydp_T}$ spectra of π^- produced in ^{7}Be+^{9}Be collisions at 150 GeV/c.

B.6 Proton spectra

$p_{\text{beam}} = 30$ GeV/c

y		p_T [GeV/c]											
		$0.0 < p_T < 0.1$			$0.1 < p_T < 0.2$			$0.2 < p_T < 0.3$			$0.3 < p_T < 0.4$		
min	max	$\frac{d^2n}{dydp_T}$	σ_{stat}	σ_{sys}	$\frac{d^2n}{dydp_T}$	σ_{stat}	σ_{sys}	$\frac{d^2n}{dydp_T}$	σ_{stat}	σ_{sys}	$\frac{d^2n}{dydp_T}$	σ_{stat}	σ_{sys}
-1.2	-1.0	0.0500	22.0	34.6		–			–			–	
-1.0	-0.8	0.1480	9.4	26.7	0.4998	11.9	25.9	0.8990	29.2	25.5		–	
-0.8	-0.6	0.1595	9.2	16.7	0.6254	7.6	32.0	0.5622	11.2	12.2		–	
-0.6	-0.4		–		0.4428	7.8	5.6	0.7127	8.1	4.0	0.7978	9.2	6.3
-0.4	-0.2		–		0.3680	20.6	6.0	0.6074	8.5	3.7	0.7824	8.0	4.5
-0.2	0.0		–			–			–		0.8491	9.7	4.8

y		$0.4 < p_T < 0.6$			$0.6 < p_T < 0.8$		
min	max	$\frac{d^2n}{dydp_T}$	σ_{stat}	σ_{sys}	$\frac{d^2n}{dydp_T}$	σ_{stat}	σ_{sys}
-0.6	-0.4	0.9502	8.5	5.7		–	
-0.4	-0.2	0.8033	6.7	4.4	0.7395	8.4	4.5
-0.2	0.0	0.7344	6.0	5.0	0.6146	7.8	2.3
0.0	0.2	0.8568	12.4	9.5		–	

Tab. B.17: Numerical values $\frac{d^2n}{dydp_T}$ spectra of p produced in ^{7}Be+^{9}Be collisions at 30 GeV/c.

$p_{\text{beam}} = 40$ GeV/c

y		p_T [GeV/c]											
		$0.0 < p_T < 0.1$			$0.1 < p_T < 0.2$			$0.2 < p_T < 0.3$			$0.3 < p_T < 0.4$		
min	max	$\frac{d^2n}{dydp_T}$	σ_{stat}	σ_{sys}	$\frac{d^2n}{dydp_T}$	σ_{stat}	σ_{sys}	$\frac{d^2n}{dydp_T}$	σ_{stat}	σ_{sys}	$\frac{d^2n}{dydp_T}$	σ_{stat}	σ_{sys}
-1.2	-1.0	0.1014	12.1	40.0		–			–			–	
-1.0	-0.8	0.1521	5.5	13.2	0.4195	7.7	24.3	0.6240	19.6	18.0		–	
-0.8	-0.6	0.1411	5.1	10.8	0.4522	4.9	7.1	0.5652	6.1	8.0	0.6774	8.8	7.6
-0.6	-0.4	0.1811	6.6	11.7	0.3689	4.6	4.7	0.5758	5.1	4.2	0.7167	5.4	1.8
-0.4	-0.2		–		0.4183	7.6	6.8	0.5384	4.6	5.2	0.6103	5.1	7.2
-0.2	0.0		–			–			–		0.6490	6.5	6.6

y		$0.4 < p_T < 0.5$			$0.5 < p_T < 0.6$			$0.6 < p_T < 0.7$			$0.7 < p_T < 0.8$		
min	max	$\frac{d^2n}{dydp_T}$	σ_{stat}	σ_{sys}	$\frac{d^2n}{dydp_T}$	σ_{stat}	σ_{sys}	$\frac{d^2n}{dydp_T}$	σ_{stat}	σ_{sys}	$\frac{d^2n}{dydp_T}$	σ_{stat}	σ_{sys}
-0.8	-0.6	0.5276	21.2	25.3		–			–			–	
-0.6	-0.4	0.7064	6.3	6.3		–			–			–	
-0.4	-0.2	0.7042	5.6	5.2	0.6494	6.4	7.3	0.6105	6.8	5.2	0.4806	9.9	12.0
-0.2	0.0	0.6814	5.1	8.9	0.6192	5.6	5.4	0.5573	6.4	4.5	0.4695	7.5	6.3

y		$0.8 < p_T < 0.9$		
min	max	$\frac{d^2n}{dydp_T}$	σ_{stat}	σ_{sys}
-0.4	-0.2	0.4488	9.3	13.2
-0.2	0.0	0.3789	8.7	5.8
0.0	0.2	0.0767	19.1	23.7

Tab. B.18: Numerical values $\frac{d^2n}{dydp_T}$ spectra of p produced in ^{7}Be+^{9}Be collisions at 40 GeV/c.

$p_{\text{beam}} = 75$ GeV/c

y		p_T [GeV/c]												
		$0.0 < p_T < 0.1$			$0.1 < p_T < 0.2$			$0.2 < p_T < 0.3$			$0.3 < p_T < 0.4$			
min	max	$\frac{d^2n}{dydp_T}$	σ_{stat}	σ_{sys}	$\frac{d^2n}{dydp_T}$	σ_{stat}	σ_{sys}	$\frac{d^2n}{dydp_T}$	σ_{stat}	σ_{sys}	$\frac{d^2n}{dydp_T}$	σ_{stat}	σ_{sys}	
-1.0	-0.8	0.1154	20.2	14.2		–			–			–		
-0.8	-0.6	0.1271	5.2	7.7	0.2879	6.5	4.2		–			–		
-0.6	-0.4	0.1162	5.1	3.1	0.2898	4.2	2.4	0.4506	4.8	3.8	0.5398	5.4	3.9	
-0.4	-0.2	0.1066	5.3	4.1	0.2798	3.5	2.8	0.4135	4.2	4.0	0.4815	4.9	2.0	
-0.2	0.0		–		0.2850	6.6	3.8	0.4133	4.4	6.4	0.4852	4.1	3.1	

y		$0.4 < p_T < 0.5$			$0.5 < p_T < 0.6$			$0.6 < p_T < 0.7$			$0.7 < p_T < 0.8$		
min	max	$\frac{d^2n}{dydp_T}$	σ_{stat}	σ_{sys}	$\frac{d^2n}{dydp_T}$	σ_{stat}	σ_{sys}	$\frac{d^2n}{dydp_T}$	σ_{stat}	σ_{sys}	$\frac{d^2n}{dydp_T}$	σ_{stat}	σ_{sys}
-0.6	-0.4	0.4812	6.7	6.2	0.5553	8.4	42.2	0.5201	9.1	5.5		–	
-0.4	-0.2	0.5527	5.2	6.2	0.5700	5.7	4.8	0.4770	6.7	4.1	0.4399	7.4	6.5
-0.2	0.0	0.5288	4.3	3.3	0.4775	5.1	4.4	0.4514	5.8	7.7	0.3966	6.6	6.6

y		$0.8 < p_T < 0.9$		
min	max	$\frac{d^2n}{dydp_T}$	σ_{stat}	σ_{sys}
-0.4	-0.2	0.3714	8.3	4.2
-0.2	0.0	0.3190	7.7	11.9
0.0	0.2	0.3199	9.1	8.0

Tab. B.19: Numerical values $\frac{d^2n}{dydp_T}$ spectra of p produced in ^{7}Be+^{9}Be collisions at 75 GeV/c.

$p_{\text{beam}} = 150$ GeV/c

y		p_T [GeV/c]											
		$0.0 < p_T < 0.1$			$0.1 < p_T < 0.2$			$0.2 < p_T < 0.3$			$0.3 < p_T < 0.4$		
min	max	$\frac{d^2n}{dydp_T}$	σ_{stat}	σ_{sys}	$\frac{d^2n}{dydp_T}$	σ_{stat}	σ_{sys}	$\frac{d^2n}{dydp_T}$	σ_{stat}	σ_{sys}	$\frac{d^2n}{dydp_T}$	σ_{stat}	σ_{sys}
-0.6	-0.4	0.0845	8.8	8.1	0.2324	6.3	2.9	0.3332	9.0	8.9	0.3244	12.1	8.6
-0.4	-0.2	0.0893	5.9	4.6	0.2255	3.8	3.3	0.3234	4.1	4.4	0.4040	4.7	5.9
-0.2	0.0	0.0825	6.9	26.3	0.2534	3.7	9.9	0.3344	3.3	5.6	0.3867	4.0	5.1
0.0	0.2	0.0674	9.1	6.6	0.2150	5.0	7.9	0.3595	3.8	10.4	0.4150	4.3	15.7

y		$0.4 < p_T < 0.5$			$0.5 < p_T < 0.6$			$0.6 < p_T < 0.7$			$0.7 < p_T < 0.8$		
min	max	$\frac{d^2n}{dydp_T}$	σ_{stat}	σ_{sys}	$\frac{d^2n}{dydp_T}$	σ_{stat}	σ_{sys}	$\frac{d^2n}{dydp_T}$	σ_{stat}	σ_{sys}	$\frac{d^2n}{dydp_T}$	σ_{stat}	σ_{sys}
-0.4	-0.2	0.4513	5.1	7.6	0.4184	5.9	4.1	0.4233	6.3	8.2	0.3581	7.1	4.4
-0.2	0.0	0.4263	4.5	5.7	0.4072	5.2	5.1	0.3982	6.0	5.2	0.3290	8.4	6.8

y		$0.8 < p_T < 0.9$			$0.9 < p_T < 1.0$		
min	max	$\frac{d^2n}{dydp_T}$	σ_{stat}	σ_{sys}	$\frac{d^2n}{dydp_T}$	σ_{stat}	σ_{sys}
-0.4	-0.2	0.3072	8.0	9.5	0.1822	10.7	10.9

Tab. B.20: Numerical values $\frac{d^2n}{dydp_T}$ spectra of p produced in ^{7}Be+^{9}Be collisions at 150 GeV/c.

B.7 $\overline{\mathrm{p}}$ spectra

$p_{\mathrm{beam}} = 30$ GeV/c

y		p_{T} [GeV/c]											
		$0.0 < p_{\mathrm{T}} < 0.1$			$0.1 < p_{\mathrm{T}} < 0.2$			$0.2 < p_{\mathrm{T}} < 0.3$			$0.3 < p_{\mathrm{T}} < 0.4$		
min	max	$\frac{d^2n}{dydp_{\mathrm{T}}}$	σ_{stat}	σ_{sys}	$\frac{d^2n}{dydp_{\mathrm{T}}}$	σ_{stat}	σ_{sys}	$\frac{d^2n}{dydp_{\mathrm{T}}}$	σ_{stat}	σ_{sys}	$\frac{d^2n}{dydp_{\mathrm{T}}}$	σ_{stat}	σ_{sys}
-1.2	-1.0	0.0500	22.0	34.6		–			–			–	
-1.0	-0.8	0.1480	9.4	26.7	0.4998	11.9	25.9	0.8990	29.2	25.5		–	
-0.8	-0.6	0.1595	9.2	16.7	0.6254	7.6	32.0	0.5622	11.2	12.2		–	
-0.6	-0.4		–		0.4428	7.8	5.6	0.7127	8.1	4.0	0.7978	9.2	6.3
-0.4	-0.2		–		0.3680	20.6	6.0	0.6074	8.5	3.7	0.7824	8.0	4.5
-0.2	0.0		–			–			–		0.8491	9.7	4.8

y		$0.4 < p_{\mathrm{T}} < 0.6$			$0.6 < p_{\mathrm{T}} < 0.8$		
min	max	$\frac{d^2n}{dydp_{\mathrm{T}}}$	σ_{stat}	σ_{sys}	$\frac{d^2n}{dydp_{\mathrm{T}}}$	σ_{stat}	σ_{sys}
-0.6	-0.4	0.9502	8.5	5.7		–	
-0.4	-0.2	0.8033	6.7	4.4	0.7395	8.4	4.5
-0.2	0.0	0.7344	6.0	5.0	0.6146	7.8	2.3
0.0	0.2	0.8568	12.4	9.5		–	

Tab. B.21: Numerical values $\frac{d^2n}{dydp_{\mathrm{T}}}$ spectra of $\overline{\mathrm{p}}$ produced in ^{7}Be+^{9}Be collisions at 30 GeV/c.

$p_{\mathrm{beam}} = 40$ GeV/c

y		p_{T} [GeV/c]											
		$0.0 < p_{\mathrm{T}} < 0.1$			$0.1 < p_{\mathrm{T}} < 0.2$			$0.2 < p_{\mathrm{T}} < 0.3$			$0.3 < p_{\mathrm{T}} < 0.4$		
min	max	$\frac{d^2n}{dydp_{\mathrm{T}}}$	σ_{stat}	σ_{sys}	$\frac{d^2n}{dydp_{\mathrm{T}}}$	σ_{stat}	σ_{sys}	$\frac{d^2n}{dydp_{\mathrm{T}}}$	σ_{stat}	σ_{sys}	$\frac{d^2n}{dydp_{\mathrm{T}}}$	σ_{stat}	σ_{sys}
-1.2	-1.0	0.1014	12.1	40.0		–			–			–	
-1.0	-0.8	0.1521	5.5	13.2	0.4195	7.7	24.3	0.6240	19.6	18.0		–	
-0.8	-0.6	0.1411	5.1	10.8	0.4522	4.9	7.1	0.5652	6.1	8.0	0.6774	8.8	7.6
-0.6	-0.4	0.1811	6.6	11.7	0.3689	4.6	4.7	0.5758	5.1	4.2	0.7167	5.4	1.8
-0.4	-0.2		–		0.4183	7.6	6.8	0.5384	4.6	5.2	0.6103	5.1	7.2
-0.2	0.0		–			–			–		0.6490	6.5	6.6

y		$0.4 < p_{\mathrm{T}} < 0.5$			$0.5 < p_{\mathrm{T}} < 0.6$			$0.6 < p_{\mathrm{T}} < 0.7$			$0.7 < p_{\mathrm{T}} < 0.8$		
min	max	$\frac{d^2n}{dydp_{\mathrm{T}}}$	σ_{stat}	σ_{sys}	$\frac{d^2n}{dydp_{\mathrm{T}}}$	σ_{stat}	σ_{sys}	$\frac{d^2n}{dydp_{\mathrm{T}}}$	σ_{stat}	σ_{sys}	$\frac{d^2n}{dydp_{\mathrm{T}}}$	σ_{stat}	σ_{sys}
-0.8	-0.6	0.5276	21.2	25.3		–			–			–	
-0.6	-0.4	0.7064	6.3	6.3		–			–			–	
-0.4	-0.2	0.7042	5.6	5.2	0.6494	6.4	7.3	0.6105	6.8	5.2	0.4806	9.9	12.0
-0.2	0.0	0.6814	5.1	8.9	0.6192	5.6	5.4	0.5573	6.4	4.5	0.4695	7.5	6.3

y		$0.8 < p_{\mathrm{T}} < 0.9$		
min	max	$\frac{d^2n}{dydp_{\mathrm{T}}}$	σ_{stat}	σ_{sys}
-0.4	-0.2	0.4488	9.3	13.2
-0.2	0.0	0.3789	8.7	5.8
0.0	0.2	0.0767	19.1	23.7

Tab. B.22: Numerical values $\frac{d^2n}{dydp_{\mathrm{T}}}$ spectra of $\overline{\mathrm{p}}$ produced in ^{7}Be+^{9}Be collisions at 40 GeV/c.

$p_{\mathrm{beam}} = 75$ GeV/c

y		p_T [GeV/c]											
		$0.0 < p_T < 0.1$			$0.1 < p_T < 0.2$			$0.2 < p_T < 0.3$			$0.3 < p_T < 0.4$		
min	max	$\frac{d^2n}{dydp_T}$	σ_{stat}	σ_{sys}	$\frac{d^2n}{dydp_T}$	σ_{stat}	σ_{sys}	$\frac{d^2n}{dydp_T}$	σ_{stat}	σ_{sys}	$\frac{d^2n}{dydp_T}$	σ_{stat}	σ_{sys}
-1.0	-0.8	0.1154	20.2	14.2		–			–			–	
-0.8	-0.6	0.1271	5.2	7.7	0.2879	6.5	4.2		–			–	
-0.6	-0.4	0.1162	5.1	3.1	0.2898	4.2	2.4	0.4506	4.8	3.8	0.5398	5.4	3.9
-0.4	-0.2	0.1066	5.3	4.1	0.2798	3.5	2.8	0.4135	4.2	4.0	0.4815	4.9	2.0
-0.2	0.0		–		0.2850	6.6	3.8	0.4133	4.4	6.4	0.4852	4.1	3.1

y		$0.4 < p_T < 0.5$			$0.5 < p_T < 0.6$			$0.6 < p_T < 0.7$			$0.7 < p_T < 0.8$		
min	max	$\frac{d^2n}{dydp_T}$	σ_{stat}	σ_{sys}	$\frac{d^2n}{dydp_T}$	σ_{stat}	σ_{sys}	$\frac{d^2n}{dydp_T}$	σ_{stat}	σ_{sys}	$\frac{d^2n}{dydp_T}$	σ_{stat}	σ_{sys}
-0.6	-0.4	0.4812	6.7	6.2	0.5553	8.4	42.2	0.5201	9.1	5.5		–	
-0.4	-0.2	0.5527	5.2	6.2	0.5700	5.7	4.8	0.4770	6.7	4.1	0.4399	7.4	6.5
-0.2	0.0	0.5288	4.3	3.3	0.4775	5.1	4.4	0.4514	5.8	7.7	0.3966	6.6	6.6

y		$0.8 < p_T < 0.9$		
min	max	$\frac{d^2n}{dydp_T}$	σ_{stat}	σ_{sys}
-0.4	-0.2	0.3714	8.3	4.2
-0.2	0.0	0.3190	7.7	11.9
0.0	0.2	0.3199	9.1	8.0

Tab. B.23: Numerical values $\frac{d^2n}{dydp_T}$ spectra of $\overline{p}$ produced in ^{7}Be+^{9}Be collisions at 75 GeV/c.

$p_{\mathrm{beam}} = 150$ GeV/c

y		p_T [GeV/c]											
		$0.0 < p_T < 0.1$			$0.1 < p_T < 0.2$			$0.2 < p_T < 0.3$			$0.3 < p_T < 0.4$		
min	max	$\frac{d^2n}{dydp_T}$	σ_{stat}	σ_{sys}	$\frac{d^2n}{dydp_T}$	σ_{stat}	σ_{sys}	$\frac{d^2n}{dydp_T}$	σ_{stat}	σ_{sys}	$\frac{d^2n}{dydp_T}$	σ_{stat}	σ_{sys}
-0.6	-0.4	0.0845	8.8	8.1	0.2324	6.3	2.9	0.3332	9.0	8.9	0.3244	12.1	8.6
-0.4	-0.2	0.0893	5.9	4.6	0.2255	3.8	3.3	0.3234	4.1	4.4	0.4040	4.7	5.9
-0.2	0.0	0.0825	6.9	26.3	0.2534	3.7	9.9	0.3344	3.3	5.6	0.3867	4.0	5.1
0.0	0.2	0.0674	9.1	6.6	0.2150	5.0	7.9	0.3595	3.8	10.4	0.4150	4.3	15.7

y		$0.4 < p_T < 0.5$			$0.5 < p_T < 0.6$			$0.6 < p_T < 0.7$			$0.7 < p_T < 0.8$		
min	max	$\frac{d^2n}{dydp_T}$	σ_{stat}	σ_{sys}	$\frac{d^2n}{dydp_T}$	σ_{stat}	σ_{sys}	$\frac{d^2n}{dydp_T}$	σ_{stat}	σ_{sys}	$\frac{d^2n}{dydp_T}$	σ_{stat}	σ_{sys}
-0.4	-0.2	0.4513	5.1	7.6	0.4184	5.9	4.1	0.4233	6.3	8.2	0.3581	7.1	4.4
-0.2	0.0	0.4263	4.5	5.7	0.4072	5.2	5.1	0.3982	6.0	5.2	0.3290	8.4	6.8

y		$0.8 < p_T < 0.9$			$0.9 < p_T < 1.0$		
min	max	$\frac{d^2n}{dydp_T}$	σ_{stat}	σ_{sys}	$\frac{d^2n}{dydp_T}$	σ_{stat}	σ_{sys}
-0.4	-0.2	0.3072	8.0	9.5	0.1822	10.7	10.9

Tab. B.24: Numerical values $\frac{d^2n}{dydp_T}$ spectra of $\overline{p}$ produced in ^{7}Be+^{9}Be collisions at 150 GeV/c.

Appendix C

Theoretical models

C.1 Introduction

This appendix contain the tables with the numerical values of the p_T spectra of charged kaons and pions in mid-rapidity calculated with theoretical models: EPOS 1.99, UrQMD 3.4 and HIJING 1.411, for ^{7}Be+^{9}Be collisions in SPS energy range.

C.2 Description of the models

EPOS model

The name of the model stands for: ***E**nergy conserving quantum mechanical multiple scattering approach, based on **P**artons (parton ladders), **O**ff-shell remnants and **S**plitting of parton ladders* [67, 68]. EPOS was designed to simulate proton-proton, proton-nucleus or nucleus-nucleus collisions. It is a microscopic string model, where the colour exchange between partons (from separate hadrons) leads to Pomeron (parton ladders) creation followed by hadronisation. In this model, a "parton ladder" consists of two parts: the hard one, obtained from perturbative QCD, and a soft phenomenological one, parametrised with Regge theory. Additionally, EPOS considers the remnants of the projectile and target to be colourless off-shell objects. Thus, particle production provided by EPOS has so-called "inner contributions" (from parton ladders), the most important for central rapidities, and so-called "outer contributions" (from remnants), supplying particle production mainly at large rapidities. The model includes such effects as splitting of parton ladders, transport of transverse momentum between parton ladders as well as ladders merging and ladders loops formation. Finally, EPOS allows for particles production via hadronisation of non-interacting (so-called "normal hadronisation") and interacting ladders (so-called "collective hadronisation"). Moreover, the model is able to treat the system evolution differently with respect to its density. In the case of the low-density part of the collision (hadron collisions, light nucleus collisions, hadron-nucleus collisions and peripheral nucleus collisions), the string segments dress up as hadrons, without further interactions. For the high-density part, particle production engine takes into account interactions of not only strings segments but of produced hadrons.

UrQMD model

***U**ltra**r**elativistic **Q**uantum **M**olecular **D**ynamics* (UrQMD) is a microscopic string model of transport used to simulate (ultra)relativistic heavy ion collisions in the energy range from about $\sqrt{s_{NN}}$ =2 GeV up to $\sqrt{s_{NN}}$ =200 GeV [78,79]. The generator contains a broad spectrum of baryon and meson species which can be produced in string decays or resonance decays (for excitations with masses higher than 2 GeV/c^2 a string picture is used). In this model, the colour string is created between partons from the same hadron when colliding hadrons (nuclei) are interacting only by exchange of the momenta (without colour transfer between colliding hadrons). Interaction leads to an increase of energy, string excitation and finally the colour string fragmentation. It is assumed that the string decays independently from both ends. Then a hadron is formed randomly on one of the end-points of the string. Moreover, a microscopic transport approach, which relies on the covariant Boltzmann equation, is implemented in the model. The UrQMD allows to study the full space-time evolution of all hadrons, resonances and their decay products in hadron-hadron or nucleus-nucleus collisions. Nevertheless, a phase transition to a quark-gluon state is not implemented into the model dynamics.

HIJING model

***H**eavy **I**on **J**et **I**nteraction **G**enerator* (HIJING) is a microscopic model designed to simulate multiple jets and particle production in p+p, p+A or A+A collisions in broad collision energy range [80]. The generator combines quantum chromo-dynamics inspired model for jet production with a phenomenological string model of hadronisation. It includes mini-jets production, soft excitation, nuclear shadowing of partons. For so-called soft nucleus-nucleus reactions at intermediate energies (5 GeV < $\sqrt{s_{NN}}$ < 20 GeV) HIJING adopts a variant of multiple string phenomenology. The basic idea is that multiple soft gluon exchanges between the constituent quarks in colliding hadrons (nucleons) can lead to longitudinal string-like excitations of those hadrons. The colour strings are assumed to decay independently via quark-antiquark creation followed by hadronisation, where the coloured partons are transformed into jets of colourless hadrons, photons and lepton. HIJING does not describe the interactions of produced hadrons in the final state of the collision.

C.3 Spectra of charged kaons in mid-rapidity

The tables in this section summarises the theoretical calculations of the p_T spectra of charged kaons in mid-rapidity, with statistical uncertainties, for Be+Be collisions in SPS energy range.

EPOS ($0.0 < y < 0.2$)

p_{T} [GeV/c]	p_{beam} [GeV/c] 20A	30A	40A	75A	150A
0.05	0.152 ± 0.001	0.211 ± 0.001	0.217 ± 0.001	0.229 ± 0.002	0.224 ± 0.001
0.15	0.400 ± 0.002	0.538 ± 0.002	0.558 ± 0.003	0.597 ± 0.003	0.578 ± 0.002
0.25	0.514 ± 0.002	0.664 ± 0.003	0.703 ± 0.003	0.755 ± 0.003	0.738 ± 0.003
0.35	0.460 ± 0.002	0.622 ± 0.003	0.663 ± 0.003	0.713 ± 0.003	0.703 ± 0.003
0.45	0.340 ± 0.002	0.482 ± 0.003	0.521 ± 0.003	0.574 ± 0.003	0.572 ± 0.002
0.55	0.231 ± 0.001	0.334 ± 0.002	0.368 ± 0.002	0.414 ± 0.002	0.422 ± 0.002
0.65	0.150 ± 0.001	0.227 ± 0.002	0.246 ± 0.002	0.290 ± 0.002	0.298 ± 0.002
0.75	0.097 ± 0.001	0.143 ± 0.002	0.162 ± 0.002	0.192 ± 0.002	0.201 ± 0.001
0.85	0.057 ± 0.001	0.088 ± 0.001	0.103 ± 0.002	0.124 ± 0.001	0.138 ± 0.001
0.95	0.034 ± 0.001	0.058 ± 0.001	0.065 ± 0.001	0.083 ± 0.001	0.088 ± 0.001

Tab. C.1: Numerical values $\frac{d^2n}{dy\,dp_{\mathrm{T}}}$ spectra of K^+ in mid-rapidity simulated for Be+Be collisions with EPOS 1.99.

EPOS ($0.0 < y < 0.2$)

p_{T} [GeV/c]	p_{beam} [GeV/c] 20A	30A	40A	75A	150A
0.05	0.050 ± 0.001	0.085 ± 0.001	0.097 ± 0.001	0.122 ± 0.001	0.141 ± 0.001
0.15	0.129 ± 0.001	0.222 ± 0.001	0.252 ± 0.002	0.323 ± 0.002	0.368 ± 0.002
0.25	0.167 ± 0.001	0.282 ± 0.002	0.327 ± 0.002	0.417 ± 0.002	0.474 ± 0.002
0.35	0.161 ± 0.001	0.272 ± 0.002	0.316 ± 0.002	0.401 ± 0.002	0.463 ± 0.002
0.45	0.133 ± 0.001	0.227 ± 0.002	0.258 ± 0.002	0.333 ± 0.002	0.384 ± 0.002
0.55	0.098 ± 0.001	0.164 ± 0.002	0.192 ± 0.002	0.253 ± 0.002	0.292 ± 0.002
0.65	0.068 ± 0.001	0.112 ± 0.001	0.131 ± 0.001	0.181 ± 0.002	0.212 ± 0.001
0.75	0.040 ± 0.001	0.075 ± 0.001	0.089 ± 0.001	0.124 ± 0.001	0.146 ± 0.001
0.85	0.024 ± 0.001	0.047 ± 0.001	0.058 ± 0.001	0.081 ± 0.001	0.097 ± 0.001
0.95	0.015 ± 0.001	0.029 ± 0.001	0.038 ± 0.001	0.054 ± 0.001	0.067 ± 0.001

Tab. C.2: Numerical values $\frac{d^2n}{dy\,dp_{\mathrm{T}}}$ spectra of K^- in mid-rapidity simulated for Be+Be collisions with EPOS 1.99.

UrQMD ($0.0 < y < 0.2$)

p_T	p_{beam} [GeV/c]				
[GeV/c]	20A	30A	40A	75A	150A
0.05	0.099 ± 0.001	0.104 ± 0.001	0.127 ± 0.001	0.134 ± 0.001	0.159 ± 0.001
0.15	0.226 ± 0.001	0.272 ± 0.002	0.324 ± 0.002	0.387 ± 0.002	0.460 ± 0.002
0.25	0.296 ± 0.002	0.374 ± 0.002	0.396 ± 0.002	0.512 ± 0.002	0.612 ± 0.002
0.35	0.301 ± 0.002	0.379 ± 0.002	0.407 ± 0.002	0.491 ± 0.002	0.587 ± 0.002
0.45	0.245 ± 0.002	0.340 ± 0.002	0.369 ± 0.002	0.432 ± 0.002	0.492 ± 0.002
0.55	0.237 ± 0.001	0.268 ± 0.002	0.288 ± 0.002	0.334 ± 0.002	0.415 ± 0.002
0.65	0.151 ± 0.001	0.181 ± 0.001	0.200 ± 0.001	0.248 ± 0.001	0.283 ± 0.002
0.75	0.109 ± 0.001	0.147 ± 0.001	0.158 ± 0.001	0.179 ± 0.001	0.212 ± 0.001
0.85	0.067 ± 0.001	0.089 ± 0.001	0.110 ± 0.001	0.134 ± 0.001	0.153 ± 0.001
0.95	0.049 ± 0.001	0.053 ± 0.001	0.067 ± 0.001	0.081 ± 0.001	0.110 ± 0.001

Tab. C.3: Numerical values $\frac{d^2n}{dy dp_T}$ spectra of K^+ in mid-rapidity simulated for Be+Be collisions with UrQMD 3.4.

UrQMD ($0.0 < y < 0.2$)

p_T	p_{beam} [GeV/c]				
[GeV/c]	20A	30A	40A	75A	150A
0.05	0.061 ± 0.001	0.073 ± 0.001	0.087 ± 0.001	0.120 ± 0.001	0.137 ± 0.001
0.15	0.147 ± 0.001	0.185 ± 0.001	0.220 ± 0.001	0.270 ± 0.002	0.384 ± 0.002
0.25	0.207 ± 0.002	0.247 ± 0.001	0.287 ± 0.002	0.363 ± 0.002	0.453 ± 0.002
0.35	0.195 ± 0.002	0.258 ± 0.002	0.286 ± 0.002	0.355 ± 0.002	0.465 ± 0.002
0.45	0.140 ± 0.001	0.196 ± 0.001	0.231 ± 0.001	0.293 ± 0.002	0.387 ± 0.002
0.55	0.096 ± 0.001	0.130 ± 0.001	0.173 ± 0.001	0.226 ± 0.001	0.318 ± 0.002
0.65	0.061 ± 0.001	0.111 ± 0.001	0.111 ± 0.001	0.179 ± 0.001	0.218 ± 0.001
0.75	0.042 ± 0.001	0.067 ± 0.001	0.084 ± 0.001	0.114 ± 0.001	0.168 ± 0.001
0.85	0.025 ± 0.001	0.049 ± 0.001	0.064 ± 0.001	0.075 ± 0.001	0.122 ± 0.001
0.95	0.010 ± 0.001	0.037 ± 0.001	0.040 ± 0.001	0.058 ± 0.001	0.081 ± 0.001

Tab. C.4: Numerical values $\frac{d^2n}{dy dp_T}$ spectra of K^- in mid-rapidity simulated for Be+Be collisions with UrQMD 3.4.

HIJING ($0.0 < y < 0.2$)

p_T	p_{beam} [GeV/c]				
[GeV/c]	20A	30A	40A	75A	150A
0.05	0.138 ± 0.001	0.190 ± 0.001	0.231 ± 0.001	0.219 ± 0.001	0.270 ± 0.002
0.15	0.380 ± 0.001	0.489 ± 0.002	0.563 ± 0.002	0.669 ± 0.002	0.692 ± 0.003
0.25	0.508 ± 0.002	0.642 ± 0.002	0.814 ± 0.003	0.792 ± 0.003	0.908 ± 0.003
0.35	0.528 ± 0.002	0.670 ± 0.003	0.796 ± 0.003	0.779 ± 0.003	0.840 ± 0.003
0.45	0.436 ± 0.002	0.559 ± 0.002	0.669 ± 0.002	0.731 ± 0.003	0.736 ± 0.003
0.55	0.321 ± 0.002	0.436 ± 0.002	0.503 ± 0.002	0.540 ± 0.002	0.531 ± 0.002
0.65	0.219 ± 0.001	0.314 ± 0.002	0.380 ± 0.002	0.370 ± 0.002	0.366 ± 0.002
0.75	0.156 ± 0.001	0.218 ± 0.001	0.245 ± 0.001	0.247 ± 0.002	0.253 ± 0.001
0.85	0.108 ± 0.001	0.150 ± 0.001	0.183 ± 0.001	0.131 ± 0.001	0.176 ± 0.001
0.95	0.070 ± 0.001	0.100 ± 0.001	0.122 ± 0.001	0.118 ± 0.001	0.098 ± 0.001

Tab. C.5: Numerical values $\frac{d^2n}{dydp_T}$ spectra of K^+ in mid-rapidity simulated for Be+Be collisions with HIJING 1.411.

HIJING ($0.0 < y < 0.2$)

p_T	p_{beam} [GeV/c]				
[GeV/c]	20A	30A	40A	75A	150A
0.05	0.044 ± 0.001	0.080 ± 0.001	0.118 ± 0.001	0.131 ± 0.001	0.157 ± 0.001
0.15	0.118 ± 0.001	0.224 ± 0.001	0.316 ± 0.002	0.345 ± 0.002	0.427 ± 0.002
0.25	0.168 ± 0.001	0.283 ± 0.002	0.376 ± 0.002	0.532 ± 0.002	0.566 ± 0.002
0.35	0.177 ± 0.001	0.291 ± 0.002	0.401 ± 0.002	0.501 ± 0.002	0.578 ± 0.002
0.45	0.145 ± 0.001	0.258 ± 0.002	0.365 ± 0.002	0.429 ± 0.002	0.481 ± 0.002
0.55	0.121 ± 0.001	0.206 ± 0.001	0.278 ± 0.002	0.301 ± 0.002	0.360 ± 0.002
0.65	0.089 ± 0.001	0.155 ± 0.001	0.220 ± 0.001	0.203 ± 0.001	0.286 ± 0.002
0.75	0.057 ± 0.001	0.102 ± 0.001	0.128 ± 0.001	0.165 ± 0.001	0.184 ± 0.001
0.85	0.035 ± 0.001	0.076 ± 0.001	0.107 ± 0.001	0.111 ± 0.001	0.116 ± 0.001
0.95	0.023 ± 0.001	0.049 ± 0.001	0.066 ± 0.001	0.069 ± 0.001	0.071 ± 0.001

Tab. C.6: Numerical values $\frac{d^2n}{dydp_T}$ spectra of K^- in mid-rapidity simulated for Be+Be collisions with HIJING 1.411.

C.4 Spectra of charged pions in mid-rapidity

The tables reported in this section contain the theoretical calculations of the p_T spectra of charged pions in mid-rapidity, with statistical uncertainties, for central Be+Be collisions in SPS energy range.

EPOS ($0.0 < y < 0.2$)

p_T	p_{beam} [GeV/c]				
[GeV/c]	20A	30A	40A	75A	150A
0.05	1.872 ± 0.002	2.439 ± 0.006	2.785 ± 0.006	3.140 ± 0.006	3.222 ± 0.008
0.15	4.932 ± 0.008	6.252 ± 0.010	6.691 ± 0.010	7.400 ± 0.010	7.502 ± 0.012
0.25	5.809 ± 0.008	7.191 ± 0.010	7.401 ± 0.010	8.008 ± 0.010	8.007 ± 0.012
0.35	4.756 ± 0.008	5.862 ± 0.008	6.034 ± 0.009	6.473 ± 0.009	6.446 ± 0.011
0.45	3.133 ± 0.007	3.936 ± 0.007	4.200 ± 0.008	4.541 ± 0.007	4.512 ± 0.009
0.55	1.889 ± 0.005	2.422 ± 0.006	2.713 ± 0.006	2.964 ± 0.006	2.976 ± 0.007
0.65	1.088 ± 0.004	1.450 ± 0.005	1.686 ± 0.005	1.869 ± 0.005	1.901 ± 0.006
0.75	0.606 ± 0.003	0.860 ± 0.004	1.038 ± 0.004	1.174 ± 0.004	1.214 ± 0.005
0.85	0.340 ± 0.002	0.499 ± 0.003	0.636 ± 0.003	0.729 ± 0.003	0.772 ± 0.004
0.95	0.193 ± 0.002	0.290 ± 0.002	0.385 ± 0.002	0.457 ± 0.002	0.487 ± 0.003

Tab. C.7: Numerical values $\frac{d^2n}{dy dp_T}$ spectra of π^+ in mid-rapidity simulated for central Be+Be collisions with EPOS 1.99.

EPOS ($0.0 < y < 0.2$)

p_T	p_{beam} [GeV/c]				
[GeV/c]	20A	30A	40A	75A	150A
0.05	1.845 ± 0.002	2.393 ± 0.006	2.782 ± 0.006	3.140 ± 0.006	3.235 ± 0.008
0.15	4.898 ± 0.008	6.280 ± 0.010	6.710 ± 0.010	7.437 ± 0.010	7.539 ± 0.012
0.25	5.870 ± 0.008	7.282 ± 0.010	7.443 ± 0.010	8.063 ± 0.010	8.065 ± 0.012
0.35	4.859 ± 0.008	5.924 ± 0.008	6.114 ± 0.009	6.519 ± 0.009	6.484 ± 0.011
0.45	3.213 ± 0.007	3.980 ± 0.007	4.255 ± 0.008	4.559 ± 0.007	4.555 ± 0.009
0.55	1.926 ± 0.005	2.449 ± 0.006	2.729 ± 0.006	2.965 ± 0.006	2.969 ± 0.007
0.65	1.109 ± 0.004	1.452 ± 0.005	1.703 ± 0.005	1.877 ± 0.005	1.905 ± 0.006
0.75	0.620 ± 0.003	0.862 ± 0.003	1.038 ± 0.004	1.167 ± 0.004	1.212 ± 0.005
0.85	0.350 ± 0.002	0.496 ± 0.003	0.633 ± 0.003	0.728 ± 0.003	0.764 ± 0.004
0.95	0.199 ± 0.002	0.298 ± 0.002	0.386 ± 0.002	0.447 ± 0.002	0.490 ± 0.003

Tab. C.8: Numerical values $\frac{d^2n}{dy dp_T}$ spectra of π^- in mid-rapidity simulated for central Be+Be collisions with EPOS 1.99.

UrQMD ($0.0 < y < 0.2$)

p_{T}	p_{beam} [GeV/c]				
[GeV/c]	20A	30A	40A	75A	150A
0.05	3.196 ± 0.006	3.475 ± 0.007	3.674 ± 0.007	4.147 ± 0.009	4.398 ± 0.009
0.15	6.562 ± 0.010	7.324 ± 0.010	7.798 ± 0.010	8.583 ± 0.012	9.285 ± 0.013
0.25	6.309 ± 0.010	7.177 ± 0.010	7.558 ± 0.010	8.410 ± 0.012	9.119 ± 0.013
0.35	4.811 ± 0.009	5.561 ± 0.008	5.928 ± 0.008	6.417 ± 0.011	6.833 ± 0.011
0.45	3.327 ± 0.007	3.942 ± 0.007	4.298 ± 0.008	4.649 ± 0.009	4.751 ± 0.009
0.55	2.303 ± 0.006	2.626 ± 0.006	2.946 ± 0.006	3.114 ± 0.007	3.112 ± 0.007
0.65	1.559 ± 0.005	1.815 ± 0.005	1.864 ± 0.005	2.012 ± 0.006	2.038 ± 0.006
0.75	1.006 ± 0.004	1.213 ± 0.005	1.187 ± 0.005	1.322 ± 0.005	1.333 ± 0.005
0.85	0.697 ± 0.003	0.791 ± 0.004	0.860 ± 0.004	0.848 ± 0.004	0.876 ± 0.004
0.95	0.470 ± 0.003	0.520 ± 0.003	0.538 ± 0.003	0.593 ± 0.003	0.607 ± 0.004

Tab. C.9: Numerical values $\frac{\mathrm{d}^2 n}{\mathrm{d}y \mathrm{d}p_{\mathrm{T}}}$ spectra of π^+ in mid-rapidity simulated for central Be+Be collisions with UrQMD 3.4.

UrQMD ($0.0 < y < 0.2$)

p_{T}	p_{beam} [GeV/c]				
[GeV/c]	20A	30A	40A	75A	150A
0.05	3.605 ± 0.007	3.952 ± 0.008	4.052 ± 0.008	4.405 ± 0.009	4.765 ± 0.009
0.15	7.216 ± 0.010	7.778 ± 0.011	8.285 ± 0.011	9.033 ± 0.013	9.726 ± 0.013
0.25	6.560 ± 0.010	7.295 ± 0.010	7.772 ± 0.010	8.541 ± 0.012	9.177 ± 0.013
0.35	4.757 ± 0.009	5.575 ± 0.008	5.911 ± 0.008	6.463 ± 0.010	6.860 ± 0.010
0.45	3.369 ± 0.007	3.960 ± 0.008	4.195 ± 0.008	4.522 ± 0.008	4.763 ± 0.008
0.55	2.274 ± 0.006	2.670 ± 0.007	2.894 ± 0.007	2.950 ± 0.007	3.195 ± 0.008
0.65	1.572 ± 0.005	1.806 ± 0.006	1.867 ± 0.006	1.975 ± 0.006	2.081 ± 0.006
0.75	1.042 ± 0.004	1.167 ± 0.005	1.253 ± 0.005	1.273 ± 0.005	1.375 ± 0.005
0.85	0.660 ± 0.004	0.763 ± 0.004	0.827 ± 0.004	0.854 ± 0.004	0.881 ± 0.005
0.95	0.402 ± 0.003	0.484 ± 0.003	0.522 ± 0.003	0.547 ± 0.003	0.592 ± 0.004

Tab. C.10: Numerical values $\frac{\mathrm{d}^2 n}{\mathrm{d}y \mathrm{d}p_{\mathrm{T}}}$ spectra of π^- in mid-rapidity simulated for central Be+Be collisions with UrQMD 3.4.

HIJING ($0.0 < y < 0.2$)

p_T [GeV/c]	p_{beam} [GeV/c] 20A	30A	40A	75A	150A
0.05	2.303 ± 0.006	2.759 ± 0.006	3.250 ± 0.007	2.962 ± 0.006	3.307 ± 0.007
0.15	5.832 ± 0.009	6.593 ± 0.009	7.365 ± 0.010	7.184 ± 0.010	7.524 ± 0.010
0.25	5.957 ± 0.009	6.749 ± 0.009	7.784 ± 0.011	7.544 ± 0.010	8.098 ± 0.011
0.35	4.482 ± 0.007	5.339 ± 0.008	6.203 ± 0.010	6.233 ± 0.010	6.650 ± 0.010
0.45	3.113 ± 0.007	3.909 ± 0.007	4.599 ± 0.008	4.348 ± 0.008	4.843 ± 0.008
0.55	2.077 ± 0.006	2.745 ± 0.006	3.179 ± 0.007	3.088 ± 0.008	3.224 ± 0.008
0.65	1.379 ± 0.005	1.858 ± 0.005	2.206 ± 0.006	2.070 ± 0.007	2.101 ± 0.006
0.75	0.911 ± 0.004	1.238 ± 0.005	1.416 ± 0.005	1.273 ± 0.005	1.312 ± 0.005
0.85	0.589 ± 0.004	0.808 ± 0.004	0.903 ± 0.005	0.828 ± 0.004	0.809 ± 0.005
0.95	0.390 ± 0.003	0.519 ± 0.004	0.562 ± 0.004	0.561 ± 0.004	0.493 ± 0.004

Tab. C.11: Numerical values $\frac{d^2n}{dydp_T}$ spectra of π^+ in mid-rapidity simulated for central Be+Be collisions with HIJING 1.411.

HIJING ($0.0 < y < 0.2$)

p_T [GeV/c]	p_{beam} [GeV/c] 20A	30A	40A	75A	150A
0.05	2.337 ± 0.006	2.693 ± 0.006	3.125 ± 0.007	2.929 ± 0.006	3.311 ± 0.007
0.15	5.674 ± 0.009	6.392 ± 0.009	7.298 ± 0.010	7.009 ± 0.010	7.633 ± 0.010
0.25	5.835 ± 0.009	6.609 ± 0.009	7.523 ± 0.010	7.472 ± 0.010	8.114 ± 0.011
0.35	4.445 ± 0.007	5.313 ± 0.008	6.154 ± 0.010	6.099 ± 0.010	6.614 ± 0.010
0.45	3.077 ± 0.007	3.927 ± 0.007	4.672 ± 0.008	4.638 ± 0.008	4.832 ± 0.008
0.55	2.127 ± 0.006	2.758 ± 0.006	3.216 ± 0.007	3.247 ± 0.008	3.189 ± 0.008
0.65	1.393 ± 0.005	1.898 ± 0.005	2.245 ± 0.006	1.934 ± 0.006	2.103 ± 0.006
0.75	0.894 ± 0.004	1.262 ± 0.005	1.391 ± 0.005	1.327 ± 0.005	1.262 ± 0.005
0.85	0.589 ± 0.004	0.808 ± 0.004	0.987 ± 0.005	0.797 ± 0.004	0.805 ± 0.005
0.95	0.392 ± 0.003	0.516 ± 0.004	0.575 ± 0.004	0.543 ± 0.004	0.493 ± 0.004

Tab. C.12: Numerical values $\frac{d^2n}{dydp_T}$ spectra of π^- in mid-rapidity simulated for central Be+Be collisions with HIJING 1.411.

C.5 Study of the isospin symmetry

The total number of protons and the total number neutrons in the colliding system of ^{7}Be+^{9}Be is even. Therefore, the conservation of the isospin symmetry in the collision is assumed and thus, the same mean number of π^- and π^+ produced is expected. The isospin effect was checked with theoretical models. In figure C.1 the comparison of the energy dependence of the π^+/π^- ratio calculated with theoretical models is presented. As expected, this ratio is close to 1. Surprisingly, EPOS and UrQMD

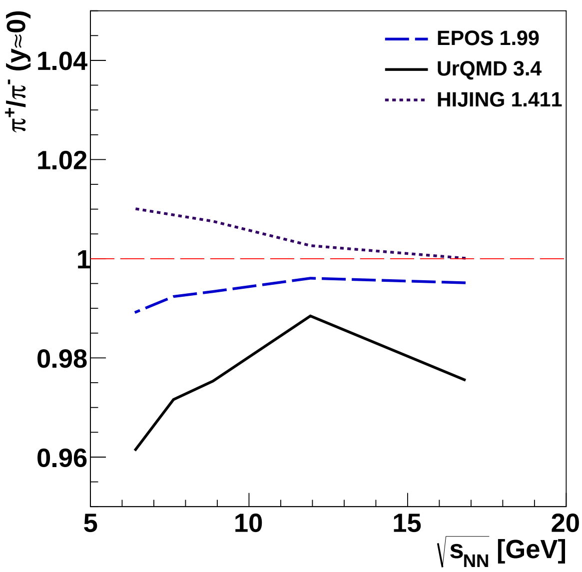

Fig. C.1: Energy dependence of π^+/π^- ratio calculated with EPOS 1.99 (*blue dashed line*), UrQMD 3.4 (*black solid line*) and HIJING (*violet doted line*).

favour production of π^- in the mid-rapidity region, in contrast to the HIJING model. The variation from unity (as the biggest difference) was taken into account in the estimation of the systematic uncertainty of the π^+ yield.

Appendix D

NA61/SHINE gas system

Each Time Projection Chamber in the NA61/SHINE experiment is equipped with a separate gas system supplying it with the appropriate gas mixture. The systems include also devices monitoring the quality and properties of the gas mixture, like drift velocity, gas amplification, water and oxygen content, pressure ant temperature. The choice of the gas mixture for the NA61/SHINE TPCs is discussed at first. Then, a description of the NA61/SHINE gas systems follows.

D.1 Gas mixture

Gas mixtures are usually characterised by two parameters: a drift velocity (v_D) and an electron diffusion coefficient (D). Both strongly depend on gas density, mean free path of the electron and the average electron collision time, and also an influence of external fields: magnetic (H) and electric (E), which increases the electron energy (thus modifying the electron interaction cross section) [57].

A base component of all NA61/SHINE gas mixtures in argon. It is characterised by a large number of electrons produced in the primary ionisation and high drift velocity. However, in argon, even at small values of E (a few V/cm), the electron energy is considerably increased, which can enhance the diffusion and lead to development of violent electron avalanches. Therefore, addition of so-called quenching gas is needed. Carbon dioxide is chosen as quenching gas in the NA61/SHINE detectors, which is also called "cool" gas. The main advantage of this gas is that it keeps the average electron energy at thermal values up to rather large electric fields (up to several hundred volts per centimetre). Thus CO_2 limits the electron diffusion, facilitates controlling of the gas amplification, but also decreases the drift velocity. The exact proportions of the gas mixture components are being optimised during the TPC maintenance phases; therefore they vary for each TPC and a data taking campaign. The rough Ar/CO_2 proportion are: 90/10 – GapTPC and VTPCs, 94/6 – FTPCs and 95/5 – MTPCs.

The NA61/SHINE TPCs operate at drift fields about 170 V/cm (195 V/cm in VTPCs). In this range, drift velocities are unsaturated, i.e. they increase almost linearly with the electric field. Drift velocities in the NA61/SHINE TPC are roughly: 1.3 cm/μs – GapTPC, 1.4 cm/μs – VTPCs, 2.1 cm/μs – FTPCs and 2.3 cm/μs – MTPCs. For the NA61/SHINE gas mixtures and drift fields the diffusion coefficients are favourable: in transverse plane $D_{\mathrm{T}} \approx 210\ \mu m/\sqrt{cm}$, in the drift direction $D_{\mathrm{L}} \approx 250\ \mu m/\sqrt{cm}$ [56].

D.2 MTPCs and VTPCs gas system

Gas systems for MTPCs and VTPCs are almost identical. Figure D.1 shows a schematic layout of the gas system of MTPC-L/R (both chambers have identical but separate gas systems). Symbols used in this layout are explained in Fig. D.2. In

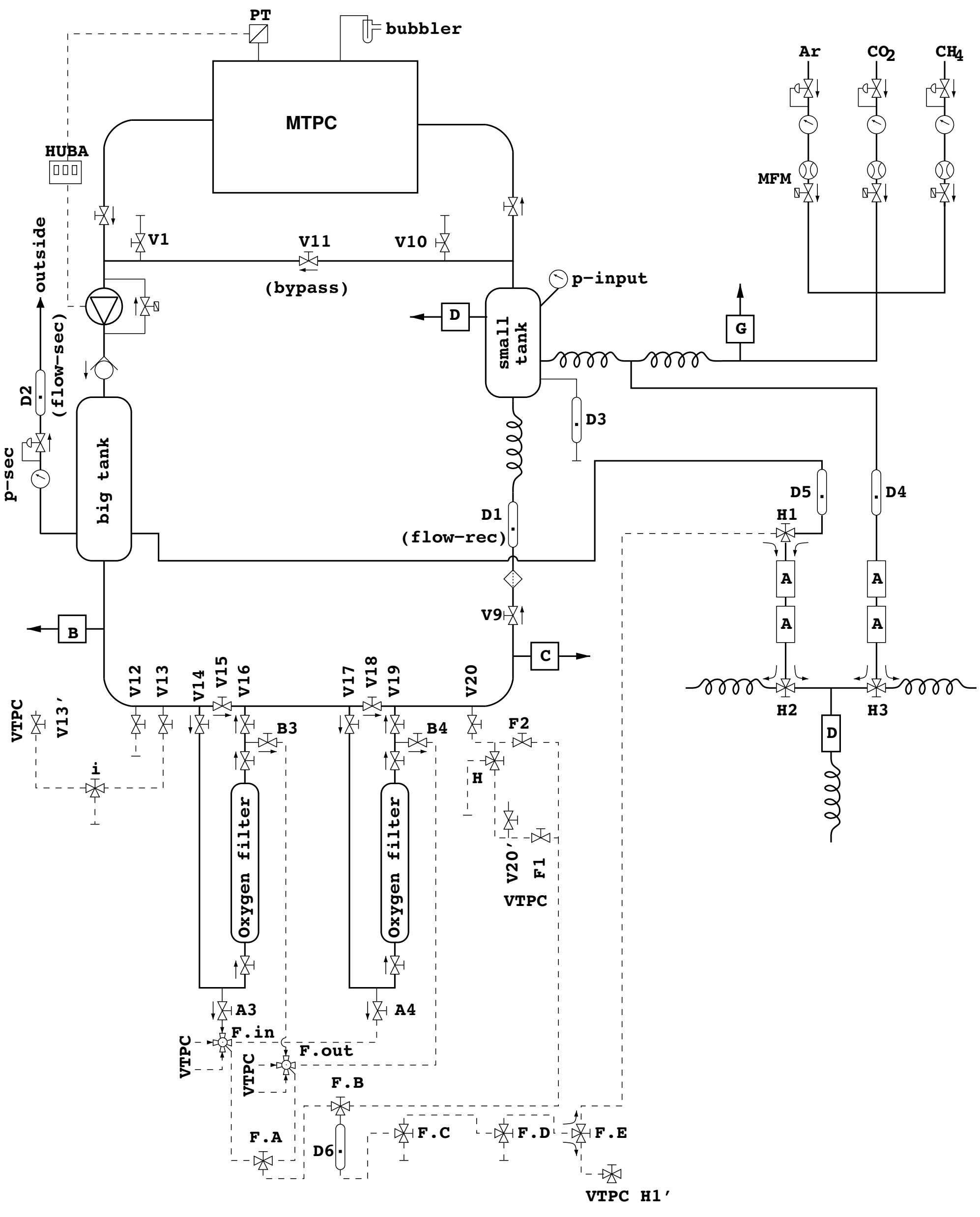

Fig. D.1: Schematic layout of the gas system of MTPC-L/R (both chambers have identical but separate gas systems). The legend for the symbols used is given in Fig. D.2. The main gas circulation path is marked with bold lines. Dashed lines symbolise parts of the gas system used for maintenance (not used in the regular operation modes). The gas supplying lines along with mixing system are shown in the upper right corner. The gas flow direction is marked by arrows next to the valves. Points labelled B, C, D and G symbolise gas lines where oxygen and water content measurements can be provided. The drift velocity and the gas amplification monitors are drawn on the right side, labelled D and A, respectively. Figure taken from [83].

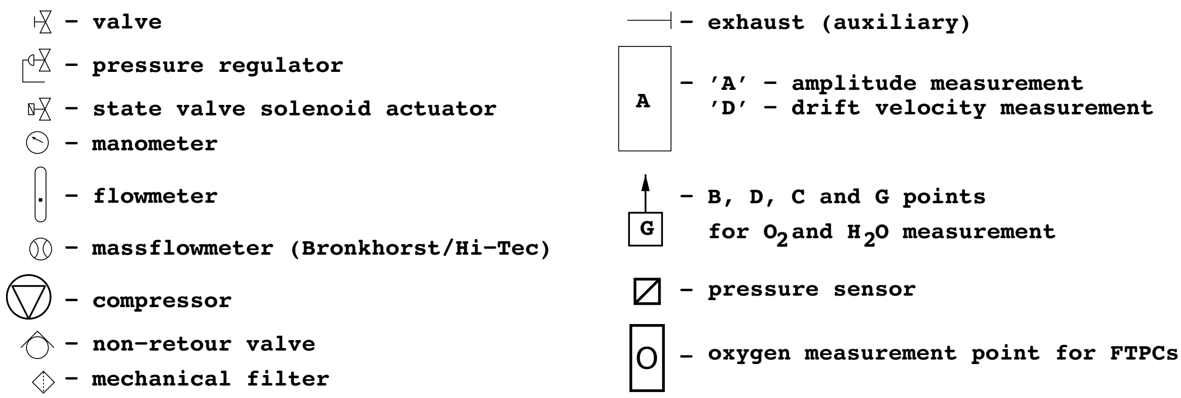

Fig. D.2: Description of symbols used in figures: D.1, D.5, D.6 and D.7. Updated figure from [83].

the scheme the main gas circulation is marked with bold line and gas flow direction is marked by arrows next to the valves. Each system circulates the gas with a compressor at a rate of about 20% of the detector volume per hour (0.9 m^3/h for VTPCs and 3 m^3/h for MTPCs). The gas supplying lines provide gas mixture the components, Ar and CO_2, to a gas mixing system (shown in the upper right corner of Fig. D.1) where the mixture is produced. The fresh gas mixture enters the small buffer tank and then the TPC. In normal operation, the supply of fresh gas corresponds to only about 3% detector volume per hour. During detector maintenance before data taking, in the so-called *purge mode*, the full recirculation rate is used. The gas circulation is forced with a compressor controlled by variable frequency drive. The compressor pumps the gas out of the TPC regulating the constant gas overpressure (0.50 ± 0.01 mbar), which additionally prevents contamination by air in case of a leak.

The recirculated gas is flushed through a filter made of activated copper, which reduces the gas contamination – oxygen content to about 5 ppm and water content to about 10-100 ppm. Oxygen filters are regenerated each 4–6 months of operation by flushing them with an Ar/H_2 (97/3) mixture at 200° C for a few days. The regeneration progress is monitored by measuring the humidity in the outgoing gas.

Thereafter, the gas mixture is circulated through an additional mechanical filter to remove possible contamination of solid particles from the gas.

Bypass lines allow isolating the TPC and oxygen filter from the gas circulation without stopping the system. Small amounts of gas are directed to monitoring units which measure water and oxygen content. The gas mixture can be monitored in a few points - the fresh gas (point G), gas entering the TPC (point D), gas exiting the TPC (point B), and filtered gas (point C). The schematic of the connection is presented in Fig. D.3. There are two sets of measuring devices. One is common for a pair of VTPC-1 and MTPC-L, the other one for a pair of VTPC-2 and MTPC-R. The gas from only one TPC from each pair is monitored at the time. Example of the oxygen and water content measurements is presented in the panel *(e)* of Fig. D.4.

Each MTPC and VTPC gas system is equipped with a system consisting of a drift velocity monitor and four amplitude monitors (shown in the middle right part of Fig. D.1). As its name indicates, the drift velocity monitor measures the drift velocity of the electrons in the gas mixture. The principle of the drift velocity measurement is described in sec. D.5. Example of the drift velocity measured by the drift velocity monitor in a selected period of time is shown in the panel *a* of Fig. D.4 with the

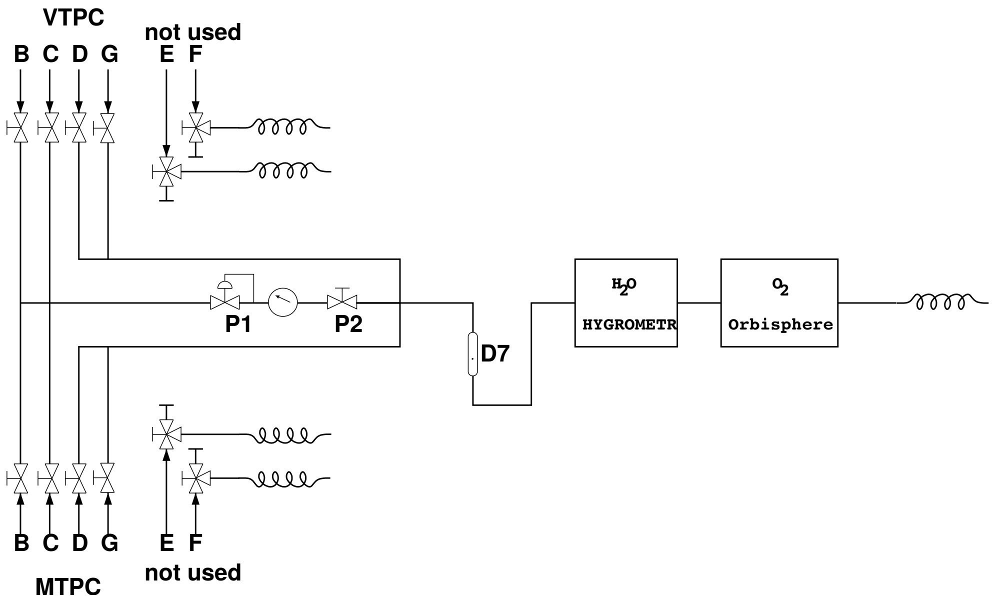

Fig. D.3: Schematic of the circuit leading the gas mixture to the oxygen and water meters. There are two pairs of the meters shared between MTPC-L/VTPC-1 and MTPC-R/VTPC-2. Gas can be taken from 4 points (B, C, G, D) of each system, but only one at the time. Figure taken from [83]. The legend for the symbols used is given in Fig. D.2.

red colour. Additionally, other parameters like, gas temperature and drift field, are monitored in both, drift velocity monitor and a given TPC (see panels *c* and *d* of Fig. D.4). The amplitude monitors, small proportional tubes equipped with a photon source (^{55}Fe), can measure the gas amplification achievable in the given gas mixture. They were used in the NA49 experiment to adjust the content of the quenching gases (CO_2 and CH_4) in the gas mixture. Since methane is not in use in NA61/SHINE, neither are the amplitude monitors. The quality of the gas mixture is monitored periodically during the gas system operation.

In addition to the active volume of the detector, gas needs to be provided also to the buffer volume between the two layers of the MTPCs and VTPCs walls. This volume is flushed with nitrogen, to prevent the TPC gas from air contamination by diffusion through the walls, or a potential leak. Moreover, the TPCs are equipped with safety bubblers protecting the chambers from excessive overpressure in case of compressor failure, or when the compressor is switched off.

D.3 GapTPC gas system

In contrast to the large volume TPCs, the GapTPC uses a simple gas system as presented in figure D.5. The GapTPC gas system circulates about 20 l/h of fresh (no recirculation) Ar/CO_2 gas mixture, which corresponds to about 10% of the detector volume per hour. The chamber operates with atmospheric pressure without overpressure stabilisation and is equipped with a safety bubbler. The outgoing gas from the TPC passes through a drift velocity monitor with a pressure sensor, which is described in section D.5. The drift velocity measurement in GapTPC was

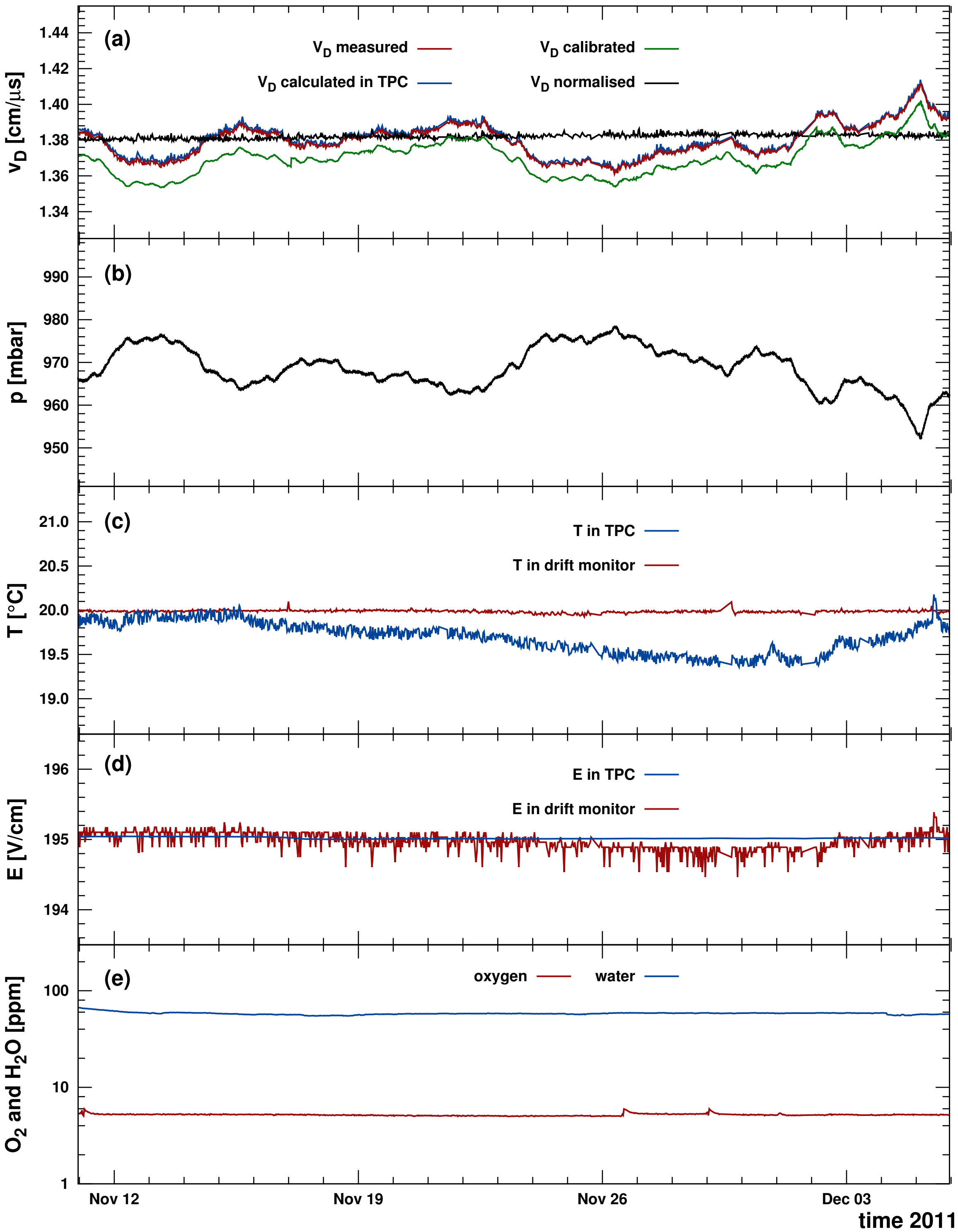

Fig. D.4: Parameter of the VTPC-1 gas mixture monitored in a selected period of time. Panel contain: *a* – drift velocity: measured in the drift monitor, normalised based on measurements of pressure, temperature and drift voltage, calculated in the TPC conditions and calibrateb with the bottom point method; *b* – atmospheric pressure; *c* – gas temperature: in the drift monitor and in the TPC; *d* – electric field: in the drift monitor and in the TPC; *e* – water and oxygen content in the VTPC-1 gas mixture.

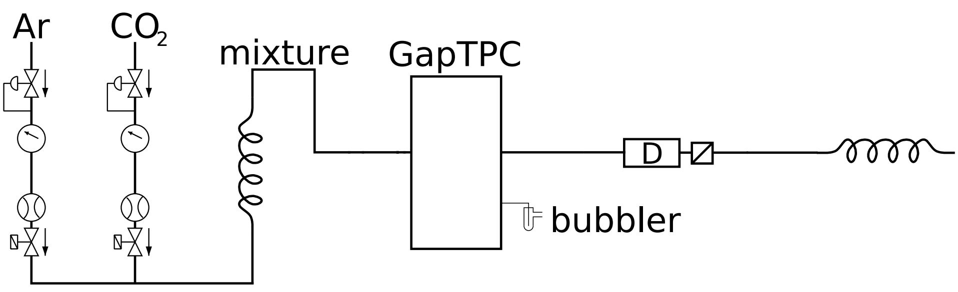

Fig. D.5: Schematic layout of the GapTPC gas system.

automatised in 2014, allowing for continuous monitoring in the following data taking campaigns.

D.4 FTPCs gas system

Each FTPC is equipped with a simple separate gas system as shown in figure D.6. FTPCs are supplied with fresh Ar/CO_2 gas mixture. The total gas flow is of order

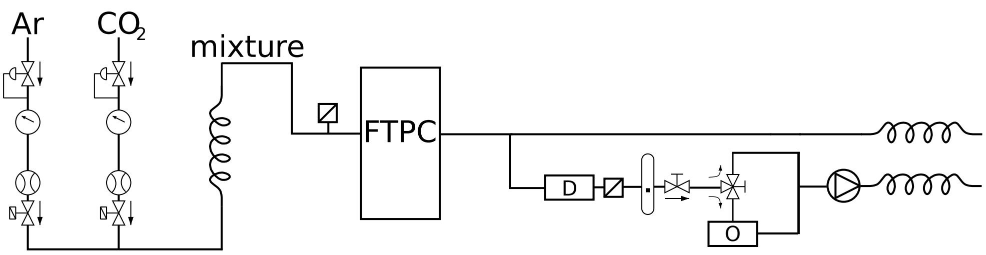

Fig. D.6: Schematic layout of the FTPC gas system.

of 100 l/h (13 – 15% of the detector volume per hour). Overpressure sensors are installed in the gas inlets of the chambers to measure FTPCs gas overpressure with respect to the atmospheric pressure.

Due to safety reasons concerning the use of open ^{241}Am sources in the drift velocity monitors (see section D.5), only about 10% (10 l/h) of the total flow is directed to the drift velocity monitor. The circulation through the drift velocity monitor as well as oxygen sensor (see Fig. D.7) is forced by a small pump. The needle

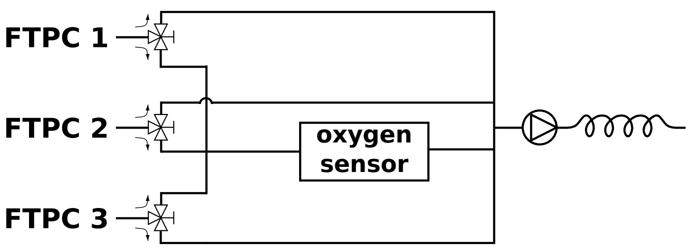

Fig. D.7: Schematic layout of the measurement point "O" (oxygen content monitoring), common for FTPC-1, FTPC-2 and FTPC-3.

valve between the monitor and the pump reduces pressure fluctuations caused by pump membrane rotation cycles. A glass tube flowmeter is used to monitor the approximate gas flow through the drift velocity monitor. The oxygen sensor is located in a junction of output pipes from all FTPC drift velocity monitors. The oxygen content is measured in each FTPC independently and the decision about for which TPC the oxygen content is measured, is obtained by using three three-way valves. The indication of the valve setting is registered automatically with inductive sensors.

D.5 Drift velocity monitoring

The drift velocity monitoring system is part of a bigger system called the Detector Control System (DCS). Values of the measured drift velocity and other important parameters from the whole detection system, in particular TPCs and gas system (e.g. temperature, pressure, drift voltage, oxygen and water content) are registered and sent to the data storage together with physics data.

Drift velocity is measured in a small drift monitor consisting of a drift chamber, three wire counters and two ^{241}Am sources. Figure D.8 presents a schematic design of the drift velocity monitor. Two alpha sources (^{241}Am) face the two wire detectors:

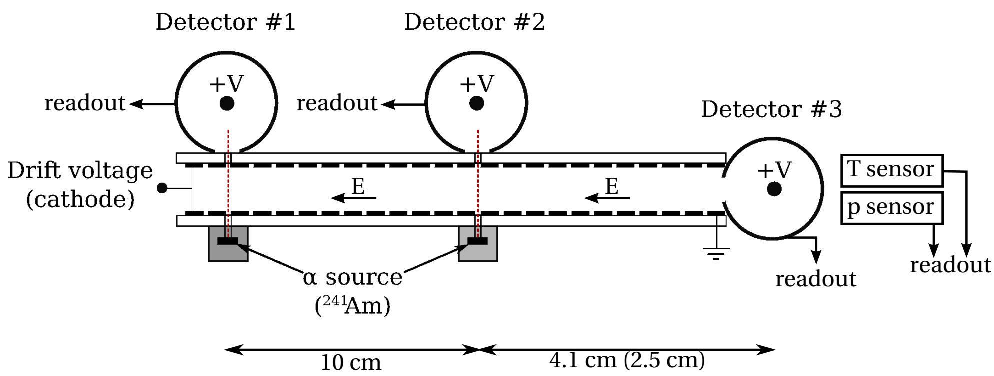

Fig. D.8: Schematic layout of the drift velocity monitor. Updated figure from [83].

#1, so-called *far detector*, and #2, so-called *close detector*. When one of the sources emits an α particle, it is registered by the far or by the close counter. α particle ionises the gas mixture not only inside a cell of close/far wire detector, but also in the drift chamber, which is built with two PCB boards segmented into 1.8 mm wide strips, perpendicular to the longer edge of the chamber, connected consecutively to each other via voltage divider. The drift voltage cathode and strips shape the electric field inside the drift chamber. Ionisation electrons travel through the drift chamber towards the last wire detector #3, so-called *pick-up*. Signals in the pick-up are registered after some drift time (t_c if the α particle has triggered the close counter and t_f – if the far counter). Signals from wire counters are amplified by a charge pre-amplifier and digitised by an oscilloscope (Picoscope 3406D; 200 MHz; 1 GS/s). The waveforms are sent along with the results of the gas temperature and atmospheric pressure measurements (as presented in panels *b* and *c* of Fig. D.4) to the DCS, see Fig. D.9. The drift time measurements and knowledge of the distance between the close and far counters, s =10 cm) are used for the drift velocity calculation:

$$v_D = \frac{s}{t_f - t_c} . \tag{D.1}$$

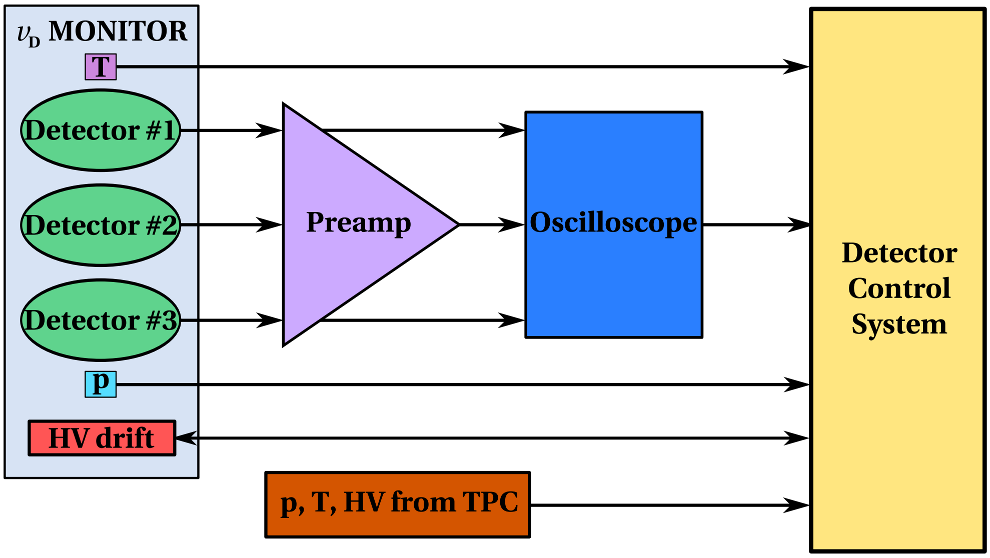

Fig. D.9: Diagram presenting the information flow within the drift velocity monitoring system.

The values of the drift velocity strongly depend on electric field, E and density of the gas mixture, which depends on pressure and temperature. The NA61/SHINE TPCs and the drift velocity monitors are placed in the conditions of stabilised temperature. Still, the pressure cannot be controlled and it follows changes of the atmospheric pressure, which can change by several per miles within several hours in case of fast weather changes. The drift field and gas density can be combined into reduced electric field:

$$\widetilde{E} = E \cdot \frac{T}{p} \,, \tag{D.2}$$

where T is the temperature in Kelvin, p is the pressure. In the NA61/SHINE, pressure is normalised to $p = 1000$hPa and temperature to $T = 20$°C. For the gas mixtures used in NA61/SHINE the drift velocity is almost linear function of reduced field as presented in the left panel of Fig. D.10. Any non-linear contribution to the drift velocity on the reduced electric field dependence is taken into account by the so-called E/p calibration, which is performed at least once per week during data taking period. It is based on systematic scan (~ 10 measurements) of the drift velocity as a function of $\widetilde{E}$ (see left panel of Fig. D.10). For each consecutive pair of points value of:

$$\frac{\Delta v}{v} / \frac{\Delta \widetilde{E}}{\widetilde{E}} \tag{D.3}$$

is calculated (see right panel of Fig. D.10) and fitted with 3rd order polynomial

$$\frac{\Delta v}{v} / \frac{\Delta \widetilde{E}}{\widetilde{E}} = \sum_{i=0}^{3} f_i \cdot (\widetilde{E})^i \,, \tag{D.4}$$

where the value of $f_0 = 1$ is fixed. This calibration is used to calculate the so-called *normalised* drift velocity, $v_{D_{norm}}$, and then also the one in a given TPC, $v_{D_{TPC}}$. The value of $v_{D_{norm}}$ is calculated for each single drift velocity measurement, $v_{D_{meas}}$, as

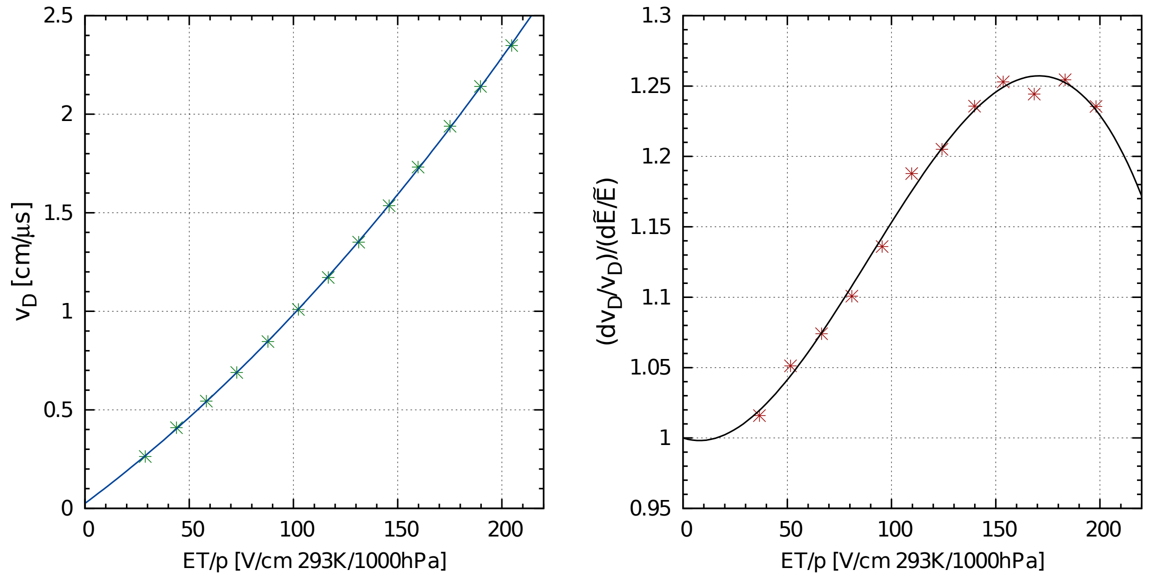

Fig. D.10: Example of the drift velocity as a function of reduced field and E/p calibration scan in MTPC-L during ^{7}Be+^{9}Be high beam momenta data-taking campaign.

follows:

$$v_{D_{norm}} = v_{D_{meas}} \cdot \frac{2+z}{2-z}, \tag{D.5}$$

where the parameter z is derived:

$$z = \frac{\widetilde{E}_{norm} - \widetilde{E}_{meas}}{(\widetilde{E}_{norm} + \widetilde{E}_{meas})/2} \cdot \left[\sum_{i=0}^{3} f_i \cdot \left(\frac{\widetilde{E}_{norm} + \widetilde{E}_{meas}}{2} \right)^i \right]. \tag{D.6}$$

The $v_{D_{TPC}}$ is calculated in similar way. The measured $v_{D_{meas}}$ is scaled to the conditions in a given TPC:

$$v_{D_{TPC}} = v_{D_{meas}} \cdot \frac{2+z_2}{2-z_2}, \tag{D.7}$$

with the z parameter, obtained with the normalised reduced electric field:

$$z_2 = \frac{\widetilde{E}_{norm} - \widetilde{E}_{TPC}}{(\widetilde{E}_{norm} + \widetilde{E}_{TPC})/2} \cdot \left[\sum_{i=0}^{3} f_i \cdot \left(\frac{\widetilde{E}_{norm} + \widetilde{E}_{TPC}}{2} \right)^i \right]. \tag{D.8}$$

For the gas mixtures used in NA61/SHINE the drift velocity is almost proportional (thus sensitive) to the gas density changes. Therefore, if the normalised conditions of p and T are assumed, very accurate information about the gas mixture composition can be extracted via calculation of the normalised drift velocity. For example, changes of order of 0.01% of the CO_2 content in the gas mixture modify the normalised v_D by about 0.013 cm/μs in the NA61/SHINE VTPCs and by about 0.019 cm/μs in the NA61/SHINE MTPCs. Example of the time dependence of various kinds of the drift velocity is presented in panel *a* of Fig. D.4). The red curve represents the $v_{D_{meas}}$ measured by the drift velocity monitor included in the VTPC-1 gas circulation circuit during ^{7}Be+^{9}Be high beam momenta data taking campaign. The $v_{D_{TPC}}$ calculated for the VTPC-1 in this period is shown in the blue colour, while calibrated $v_{D_{calib}}$ – with the green. All the three curves evince clear anti-correlation with the atmospheric pressure, while p increases the drift velocities drops. The black line in figure D.4, exhibiting the constant time dependence, presents values of the $v_{D_{norm}}$, indicating stable gas composition, in the period of the measurements.

The plot presented in the panel *c* of Fig. D.4 demonstrate that, there were severe problems with the temperature stabilisation around the NA61/SHINE TPCs in 2011. Instability of the temperature in this period was compensated with the adjustments of the drift field in the drift velocity monitors (see panel *d* of Fig. D.4). The interval of the drift field difference was calculated using the E/p calibration.

The drift velocity units in MTPCs, VTPCs and GapTPC and readout system were inherited from the NA49 experiment. The monitors are still operational. The readout of the drift velocity monitoring systems was upgraded in 2014, which enhanced the measurement precision from several percents up to few per milles (precision of 1‰ is achievable). Thereafter, three new measuring units with complete readout chain were installed at the NA61/SHINE in 2016. Their technical design was based on reverse engineering of the NA49 units. They monitor the drift velocity in FTPCs.

Acronyms

ADC	Analog-to-Digital Converter
ALICE	A Large Ion Collider Experiment
ATLAS	A Toroidal LHC ApparatuS experiment
BNL	Brookhaven National Laboratory
BPD	Beam Position Detector
CEDAR	Cherenkov Differential Counter with Achromatic Ring Focus
CERN	European Organization for Nuclear Research
CFD	Constant-Fraction Discriminator
CMOS	Complementary Metal-Oxide-Semiconductor technology
CMS	Compact Muon Solenoid experiment
CP	Critical Point
DCS	Detector Control System
DRS	Domino Ring Sampling
ECR	Electron Cyclotron Resonance
EPOS	Energy conserving quantum mechanical multiple scattering approach, based on Partons, Off-shell remnants and Splitting of parton ladders model
FPGA	Field-Programmable Gate Array
FTPC	Forward Time Projection Chamber
GapTPC	Gap Time Projection Chamber
GEANT	GEometry ANd Tracking simulation platform
HG	Hadron Gas
HIJING	Heavy-Ion Jet Interaction Generator
HR	High Resolution
HRG	Hadron-Resonance Gas
HV	High Voltage
LEIR	Low Energy Ion Ring
LHC	Large Hadron Collider
LHT	Liquid Hydrogen Target

LINIAC	Linear Accelerator
LS2	Long Shutdown 2
MAPD	Micro-pixel Avalanche AhotoDiodes
MC	Monte Carlo
MFT	Magnetic Field Tracker
MHTDC	Multi-Hit Time Digital Converter
MTPC	Main Time Projection Chamber
MWPC	Multi-Wire Proportional Chamber
NA49	49th experiment in CERN North Area
NA61/SHINE	61st experiment in CERN North Area/SPS Heavy Ion and Neutrino Experiment
NOνA	NuMI Off-axis ν_e Appearance experiment
PMT	Photomultiplier
PS	Proton Synchrotron
PSB	Proton Synchrotron Booster
PSD	Projectile Spectator Detector
QDC	Charge-to-Digital Converter
QGP	Quark-Gluon Plasma
RHIC	Relativistic Heavy Ion Collider
RST	Right-Side Track
SAVD	Small Acceptance Vertex Detector
SMES	Statistical Model of the Early Stage
SPS	Super Proton Synchrotron
SR	Standard Resolution
T2K	Tokai to Kamioka experiment
Target IN	target inserted
Target OUT	target removed
TDC	Time-to-Digital Converter
ToF	Time-of-Flight detector
tof	Analysis method based on time-of-flight measurement
ToF-F	Forward Time-of-Flight detector
ToF-L	Left Time-of-Flight detector
ToF-R	Right Time-of-Flight detector
TPC	Time Projection Chamber
TRB	Trigger Readout Board
UrQMD	Ultra-relativistic Quantum Molecular Dynamics model

VTPC	Vertex Time Projection Chamber
WDXRF	Wavelength Dispersive X-Ray Fluorescence
WLS	Wave-Length-Shifter
WST	Wrong-side track

Bibliography

[1] A. K. Wróblewski. *Historia Fizyki*. PWN, 1st edition, 2006.

[2] S. Weinberg. *The Making of the standard model. 50 years of Yang-Mills theory.* Eur. Phys. J., **C34**:5, 2004.

[3] M. Tanabashi et al. (Particle Data Group). *Quarks*. Phys. Rev. **D98**:030001, 2018.

[4] M. Tanabashi et al. (Particle Data Group). *Leptons*. Phys. Rev. **D98**:030001, 2018.

[5] M. Tanabashi et al. (Particle Data Group). *Gauge and Higgs bosons*. Phys. Rev. **D98**:030001, 2018.

[6] D. Griffiths. *Introduction to elementary particles*. Physics textbook. Wiley, New York, 2nd edition, 2008.

[7] J. Collins and M. J. Perry. *Superdense Matter: Neutrons or Asymptotically Free Quarks?* Phys. Rev. Lett. **34**:1353, 1975.

[8] M. I. Gorenstein. *Discovery of quark-gluon plasma in nucleus nucleus collisions at CERN SPS*. In *New trends in high-energy physics: Experiment, phenomenology, theory. Proceedings, International School-Conference, Crimea 2000, Yalta, Ukraine, May 27-June 4, 2000*, pages 128–134, 2000.

[9] T. Ludlam. *Experimental results from the early measurements at RHIC; hunting for the quark–gluon plasma*. Nucl. Phys. **A750**:9, 2005.

[10] K. Grebieszkow. *Lecture on Introduction to Heavy Ion Collisions 2017/2018*, http://if.pw.edu.pl/ kperl/hip/hip.html.

[11] F. Becattini, J. Cleymans, A. Keranen, E Suhonen, and K. Redlich. *Features of particle multiplicities and strangeness production in central heavy ion collisions between 1.7A-GeV/c and 158A-GeV/c*. Phys. Rev. **C64**:024901, 2001.

[12] F. Becattini, J. Manninen, and M. Gazdzicki. *Energy and system size dependence of chemical freeze-out in relativistic nuclear collisions*. Phys. Rev. **C73**:044905, 2006.

[13] K. Grebieszkow. *NA49 and NA61/SHINE experiments: Results and perspectives*. Acta Phys. Polon. **B41**:427, 2010.

[14] M. Gaździcki, M. Gorenstein, and P. Seyboth. *Onset of deconfinement in nucleus-nucleus collisions: Review for pedestrians and experts*. Acta Phys. Polon. **B42**:307, 2011.

[15] E. S. Bowman and J. I. Kapusta. *Critical Points in the Linear Sigma Model with Quarks*. Phys. Rev. **C79**:015202, 2009.

[16] M. A. Stephanov. *QCD phase diagram: An Overview*. PoS **LAT2006**:024, 2006.

[17] Z. Fodor and S. D. Katz. *Critical point of QCD at finite T and mu, lattice results for physical quark masses*. JHEP **04**:050, 2004.

[18] M. Gaździcki and M. I. Gorenstein. *On the early stage of nucleus-nucleus collisions*. Acta Phys. Polon. **B30**:2705, 1999.

[19] R. V. Poberezhnyuk, M. Gaździcki, and M. I. Gorenstein. *Statistical Model of the Early Stage of nucleus-nucleus collisions with exact strangeness conservation*. Acta Phys. Polon. **B46**:1991, 2015.

[20] C. Alt et al. *Pion and kaon production in central* Pb + Pb *collisions at 20A and 30A GeV: Evidence for the onset of deconfinement*. Phys. Rev. **C77**:024903, Feb 2008.

[21] L. Adamczyk et al. *Bulk Properties of the Medium Produced in Relativistic Heavy-Ion Collisions from the Beam Energy Scan Program*. Phys. Rev. **C96**:044904, 2017.

[22] Lokesh Kumar. *Systematics of Kinetic Freeze-out Properties in High Energy Collisions from STAR*. Nucl. Phys. **A931**:1114, 2014.

[23] E. V. Shuryak. *Quantum chromodynamics and the theory of superdense matter*. Phys. Rep. **61**:71, 1980.

[24] J. Cleymans, R.V. Gavai, and E. Suhonen. *Quarks and gluons at high temperatures and densities*. Phys. Rep. **130**:217, 1986.

[25] M. Gaździcki and D. Röhrich. *Pion multiplicity in nuclear collisions*. Z. Phys. **C65**:215, 1995.

[26] M. Gaździcki and D. Röhrich. *Strangeness in nuclear collisions*. Z. Phys. **C71**:55, 1996.

[27] N. Abgrall et al. *Measurement of negatively charged pion spectra in inelastic p+p interactions at p_{lab} = 20, 31, 40, 80 and GeV/c*. Eur. Phys. J. **C74**:2794, 2014.

[28] A. Aduszkiewicz et al. *Measurements of $\pi^{\pm}$, $K^{\pm}$, p and $\overline{p}$ spectra in proton-proton interactions at 20, 31, 40, 80 and 158 GeV/c with the NA61/SHINE spectrometer at the CERN SPS*. Eur. Phys. J. **C77**:671.

[29] S. V. Afanasiev et al. *Energy dependence of pion and kaon production in central* Pb + Pb *collisions*. Phys. Rev. **C66**:054902, Nov 2002.

[30] T. Anticic et al. *System-size and centrality dependence of charged kaon and pion production in nucleus-nucleus collisions at 40A GeV and 158A GeV beam energy*. Phys. Rev. **C86**:054903, Nov 2012.

[31] T. Anticic et al. *Inclusive production of charged kaons in p+p collisions at 158 GeV/c beam momentum and a new evaluation of the energy dependence of kaon production up to collider energies*. Eur. Phys. J. **C68**:1, 2010.

[32] L. Ahle et al. *Particle production at high baryon density in central Au+Au reactions at 11.6A GeV/c*. Phys. Rev. **C57**:R466, 1998.

[33] L. Ahle et al. *Centrality dependence of kaon yields in Si+A and Au+Au collisions at the AGS*. Phys. Rev. **C60**:044904, 1999.

[34] J. Adams and others. *Identified Particle Distributions in pp and* Au + Au *Collisions at* $\sqrt{s_{NN}} = 200$ GeV. Phys. Rev. Lett. **92**:112301, 2004.

[35] B. I. Abelev et al. *Systematic measurements of identified particle spectra in pp,* $d +$Au*, and* Au + Au *collisions at the STAR detector*. Phys. Rev. **C79**:034909, 2009.

[36] K. Adcox et al. *Single identified hadron spectra from* $\sqrt{s_{NN}} = 130$ GeV *Au+Au collisions*. Phys. Rev. **C69**:024904.

[37] S. S. Adler et al. *Identified charged particle spectra and yields in Au+Au collisions at* $\sqrt{s_{NN}} = 200$ GeV. Phys. Rev. **C69**:034909, 2004.

[38] K. Aamodt et al. *Production of pions, kaons and protons in pp collisions at* $\sqrt{s} =$ *900 GeV with ALICE at the LHC*. Eur. Phys. J. **C71**:1655, 2011.

[39] B. Abelev et al. *Pion, Kaon, and Proton Production in Central Pb-Pb Collisions at* $\sqrt{s_{\mathrm{NN}}}$=2.76 TeV. Phys. Rev. Lett. **109**:252301, 2012.

[40] B. Abelev et al. *Production of charged pions, kaons and protons at large transverse momenta in pp and Pb–Pb collisions at* $\sqrt{s_{\mathrm{NN}}} = 2.76$ *TeV*. Phys. Lett. **B736**:196, 2014.

[41] I. Arsene et al. *Centrality dependent particle production at* $y = 0$ *and* $y \sim 1$ *in Au+Au collisions at* $\sqrt{s_{NN}}$ *= 200 GeV*. Phys. Rev. **C72**:014908.

[42] V. Begun, *private communication*.

[43] Michał Naskręt. *Mean pion multiplicities in Ar+Sc collisions*. Acta Phys. Polon. Supp. **10**:693, 2017.

[44] V. V. Begun, V. Vovchenko, M. I. Gorenstein, and H. Stoecker. *Problems in statistical hadron-gas treatment of systems created in proton-proton interactions at CERN SPS*. arXiv:1805.01901, 2018.

[45] V. Vovchenko, V. V. Begun, and M. I. Gorenstein. *Hadron multiplicities and chemical freeze-out conditions in proton-proton and nucleus-nucleus collisions*. Phys. Rev. **C93**:064906, 2016.

[46] Y. Itow et al. *The JHF-Kamioka neutrino project*. In *Neutrino oscillations and their origin. Proceedings, 3rd International Workshop, NOON 2001, Kashiwa, Tokyo, Japan, December 508, 2001*, pages 239–248, 2001.

[47] K. Abe et al. *The T2K Experiment*. Nucl. Instrum. Meth. **A659**:106, 2011.

[48] N Abgrall. *NA61/SHINE plans beyond the approved program*. Technical Report CERN-SPSC-2012-022, CERN, Geneva, 2012.

[49] K. Abe et al. *T2K neutrino flux prediction*. Phys. Rev. **D87**:012001, 2013.

[50] J. Abraham et al. *Properties and performance of the prototype instrument for the Pierre Auger Observatory*. Nucl. Instrum. Meth. **A523**:50, 2004.

[51] T. Antoni et al. *The cosmic-ray experiment KASCADE*. Nucl. Instrum. Meth. **A513**:490, 2003.

[52] V. Khachatryan et al. *Evidence for collectivity in pp collisions at the LHC*. Phys. Lett. **B765**:193, 2017.

[53] J. Adam et al. *Enhanced production of multi-strange hadrons in high-multiplicity proton-proton collisions*. Nature Phys. **13**:535, 2017.

[54] N. Abgrall et al. *NA61/SHINE facility at the CERN SPS: beams and detector system*. JINST **9**:P06005, 2014.

[55] S. Afanasev et al. *The NA49 large acceptance hadron detector*. Nucl. Instrum. Meth. **A430**:210, 1999.

[56] R. Renfordt. *Introduction to NA61/SHINE Time Projection Chambers*, https://indico.cern.ch/event/515331/.

[57] F. Sauli. *Gaseous Radiation Detectors: Fundamentals and Applications*. Cambridge Monographs on Particle Physics, Nuclear Physics and Cosmology. Cambridge University Press, 2014.

[58] R Brockmann et al. *RD-32 final report: development of a time projection chamber with high two-track resolution capability for collider experiments*. Technical Report CERN-LHCC-96-016, CERN, Geneva, 1996.

[59] T. Alber, V. Eckardt, H. Fessler, S. Schönfelder, and P. Seyboth. *A study of argon, neon and helium based gas mixtures for improving the spatial resolution in time projection chambers*. Nucl. Instrum. Meth. **A349**:56, 1994.

[60] H. Appelshaeuser et al. *Upgrade of the ALICE Time Projection Chamber*. Technical Report CERN-LHCC-2013-020, 2013.

[61] S.R. Amendolia et al. *Ion trapping properties of a synchronously gated time projection chamber*. Nucl. Instrum. Meth. **A239**:192, 1985.

[62] C. Patrignani et al. (Particle Data Group). *Passage of particles through matter*. Chin. Phys. **C40**:100001, 2017.

[63] P. Seyboth. *Numbering conventions for NA49 TPC's*. NA49 internal note, 1994.

[64] A Aduszkiewicz et al. *Report from the NA61/SHINE experiment*. Technical Report CERN-SPSC-2015-036, CERN, Geneva, 2015.

[65] E. Kaptur. *Analysis of collision centrality and negative pion spectra in* $^{7}Be + {}^{9}Be$ *interactions at CERN SPS energy range*. PhD thesis, University of Silesia, 2017.

[66] A. Marcinek. *ϕ meson production in proton-proton collisions in the NA61/SHINE experiment at CERN SPS*. PhD thesis, Jagiellonian University, 2016.

[67] M. Bleicher K. Werner, L. Karpenko and T. Pierog. *The physics of EPOS*. EPJ Web of Conf. **52**:05001, 2013.

[68] K. Werner. *The hadronic interaction model EPOS*. Nucl. Phys. **B175**:81, 2008. Proceedings of the XIV International Symposium on Very High Energy Cosmic Ray Interactions.

[69] R Brun, R Hagelberg, M Hansroul, and J C Lassalle. *Simulation program for particle physics experiments, GEANT: user guide and reference manual*. Technical Report CERN-DD-78-2-REV, CERN, Geneva, 1978.

[70] L. Garren et al. (Particle Data Group). *Monte Carlo particle numbering scheme*. 2018.

[71] National Nuclear Data Center (Jul 4, 2018), https://www.nndc.bnl.gov/.

[72] SHINE framework documentation (2013-2018), http://shinedoc.web.cern.ch/.

[73] ROOT framework documentation (2013-2018), http://root.cern.ch/.

[74] E. Kaptur, *private communication*.

[75] M. I. Gorenstein. *Identity method for particle number fluctuations and correlations*. Phys. Rev. **C84**:024902, 2011.

[76] M. Gaździcki, K. Grebieszkow, M. Maćkowiak, and S. Mrówczyński. *Identity method to study chemical fluctuations in relativistic heavy-ion collisions*. Phys. Rev. **C83**:054907, 2011.

[77] M. Kliemant, B. Lungwitz, and M. Gaździcki. *Energy dependence of transverse mass spectra of kaons produced in $p+p$ and $p+\overline{p}$ interactions: A compilation*. Phys. Rev. **C69**:044903, 2004.

[78] M. Bleicher, E. Zabrodin, C. Spieles, S. A. Bass, C. Ernst, S. Soff, L. Bravina, M. Belkacem, H. Weber, H. Stöcker, and W. Greiner. *Relativistic hadron-hadron collisions in the ultra-relativistic quantum molecular dynamics model*. J. Phys. **G25**:1859, 1999.

[79] S. A. Bass, M. Belkacem, M. Bleicher, M. Brandstetter, L. Bravina, C. Ernst, L. Gerland, M. Hofmann, S. Hofmann, J. Konopka, G. Mao, L. Neise, S. Soff, C. Spieles, H. Weber, L.A. Winckelmann, and H. St˙ *Microscopic models for ultrarelativistic heavy ion collisions*. Prog. Part. Nucl. Phys. **41**:255, 1998.

[80] X. Wang and M. Gyulassy. *HIJING: A Monte Carlo model for multiple jet production in pp, pA, and AA collisions*. Phys. Rev. **D44**:3501, 1991.

[81] E. Kaptur. *Energy scan with Be+Be collisions: cross-section, centrality determination, pion spectra and mean multiplicities*. PoS **CPOD2014**:053, 2015.

[82] A Aduszkiewicz et al. *Report from the NA61/SHINE experiment at the CERN SPS*. Technical Report CERN-SPSC-2017-038, CERN, Geneva, 2017.

[83] A. Aduszkiewicz. *Operation and performance of Time Projection Chambers of SHINE/NA61 experiment at CERN*. Master's thesis, University of Warsaw, 2008.